INDIAN INSTITUTE OF TECHNOLOGY,

GANDHINAGAR

DOCTORAL THESIS

Interaction of intense femtosecond pulses with polyatomic molecules: probing the ultrafast dynamics

---

Author:

Rituparna Das

Supervisor:

Dr. Rajesh Kumar Kushawaha

A thesis submitted in fulfillment of the requirements

for the degree of Doctor of Philosophy

in the

March 24, 2023

Declaration

I declare that this written submission represents my ideas in my own words and where others' ideas or words have been included, I have adequately cited and referenced the original sources. I also declare that I have adhered to all principles of academic honesty and integrity and have not misrepresented or fabricated or falsified any idea/data/fact/source in my submission. I understand that any violation of the above will be cause for disciplinary action by the Institute and can also evoke penal action from the sources which have thus not been properly cited or from whom proper permission has not been taken when needed.

Rituparna Das

Signature

Name: Rituparna Das

(Roll No: 17330025)

Date: 20/03/2023

CERTIFICATE

It is certified that the work contained in the thesis titled **"Interaction of intense femtosecond pulses with polyatomic molecules: probing the ultrafast dynamics"** by Ms. Rituparna Das (Roll No. 17330025), has been carried out under my supervision and that this work has not been submitted elsewhere for a degree.

23-03-2023

Dr. Rajesh Kumar Kushawaha
Assistant Professor
Atomic, Molecular and Optical Physics Division,
Physical Research Laboratory,
Ahmedabad, India.

(Thesis Supervisor)

Date: 23-03-2023

Acknowledgements

My PhD journey has been the most profound and life-changing chapter of my life. The three years I spent in my group have transformed me completely as a person. Although it was my dream to become a scientist during one of the phases in my teenage years, I never completely knew what it meant to do a PhD until I did it. And now, when the journey is over, and I have reached the destination, I feel gratitude and an even greater thirst for knowledge and understanding – not only about my research area but much more. I would like to acknowledge each person I came across during this journey since they have directly or indirectly, knowingly or unknowingly shaped my journey.

I am grateful to my supervisor, Dr. Kushawaha, who has been my guide and mentor and showed faith in me, even in those most challenging times when I didn't have confidence in myself. Because of him, I believe anything can be achieved if you set your mind to it, and nothing is impossible. He taught me to be persistent, work hard while developing experimental setups, and keep trying no matter how often I failed. I am also thankful to Dr. Achim Czasch, Roentdek, without whom the development work during my PhD would not have been possible. Dr. Czasch patiently guided me over emails and video call sessions at each step of assembling the MCP and DLD during the RIMS setup development. Next, I would like to thank my collaborators, Dr. Dheeraj K. Singh and Deepak K. Pandey, who performed the quantum chemical calculations for all my experiments. Their work helped me to interpret my results with greater clarity and provided a better understanding of the fragmentation pathways.

I am grateful to my DSC members – Dr. Bhalamurugan Sivaraman, Dr. Naveen Chauhan, Dr. Sanjay K. Mishra and Prof. Angom Dilip Kumar Singh – who critically reviewed my work and asked numerous questions during my presentations, thereby pushing me to read more and develop a better understanding of strong-field physics. I thank the director of PRL, Dr. Anil Bhardwaj, whose constant support to our lab is evident from the fact that the Femtosecond laser lab in PRL is one of the

best facilities not only in India but also comparable to many international labs. I also thank Prof. R. P. Singh, who has provided much valuable knowledge in physics and supported me during difficult times.

I thank my lab members – Madhu, Pranav, Vinitha, Pooja, Sweta, Shameem, Prashant bhaiya and Nageshwar bhaiya – each of them has contributed to my PhD journey. I have learned a lot from my colleagues in the three years of my PhD tenure. I thank all group members for helping me during the development of the RIMS setup, without which it would have been impossible to develop the setup. I also thank Sweta for providing the MO-ADK data for obtaining the fit with the experimental results.

I thank everyone in the JRF/SRF batch of 2017 – we had some of the most unforgettable times, especially during our first year of PhD (like the sudden trip to Bhuj that was planned randomly at 11 pm and we boarded the train at 2 am!!). I thank all the residents of the Thaltej hostel, including my juniors and seniors. The three-month-long Covid lockdown in 2019 in the Thaltej hostel was one of the best times we had, which momentarily helped me escape the brutal reality of the effects of Covid. I must thank my gym buddies – Ankit, Abhay, Partha, and Hrushi. Our early morning workout sessions not only improved my physical fitness but also helped me deal with my anxiety, and stress, and improved my concentration and alertness. I also thank the PRL workshop, CMG, Richa ma'am, the housekeeping staff, the canteen staff, CISF, and others whose contributions to my day-to-day life have helped me complete my thesis work directly and indirectly.

Finally, I want to mention the angels in my life who have been my constant support and biggest cheerleaders – Ma, Rinky, and Hrushi. Your unending love for me, even when I was unlovable, has taught me the meaning of unconditional love. Thank you for understanding me and sacrificing so much for me, Ma. I will be forever grateful to my parents for giving me the wings to fly and inspiring me to dream big and work towards my goals continuously. Baba would have been very proud

of me if he could witness my journey from my BSc days to the end of my PhD journey. I hope I continue making him proud in every step of my life and prove that everything he did for us was worth it. A huge shout-out to Rinky, the best sister in the world. Thank you for inspiring me every day to work hard and never settle for anything but the best. Last but definitely not least, I thank my love (now husband), Hrushi, who has seen me through the highest of highs and lowest of lows during my PhD journey and yet never gave up on me. I do not think any of this would have been possible without your love, guidance, encouragement, and inspiration.

P.S.: I have to specially mention the four-legged loves of my life – Doggo, Goku, Chhutki, Mojo and Madhuri. I am extermely grateful to these fur babies for my daily dose of oxytocin. They always put a smile on my face and helped me to deal with stressful times during my PhD days. You angels make this world a better place – a place worth living.

Dedicated to Ma, Baba, Rinky and Hrushi

Abstract

Strong-field physics aims to understand the ultrafast nuclear and electron dynamics in atoms and molecules on their intrinsic timescale and eventually, control them. The development in laser technology made it possible to produce ultrashort (durations of few tens of fs or even shorter) bursts of light of intensities ranging from TW/cm^2 to PW/cm^2. Such intense fields are comparable to and sometimes stronger than the Coulomb potential in the atoms/molecules. To understand the ultrafast nuclear dynamics in polyatomic molecules using femtosecond laser pulses, the molecules are first ionized, thereby creating a molecular wavepacket in a ground or excited ionic state. Next, as the wavepacket evolves on the electronic state, the ion undergoes changes in its geometry leading to bond breakup, intramolecular migration of moieties and bond formation before it dissociates into fragments. Obtaining the complete kinematic information of the fragments in coincidence using a Recoil Ion Momentum Spectrometer (RIMS) reveals information about the excited-state dynamics of the molecular ion. For instance, the kinetic energy, momentum distribution and the angular distribution of the fragments provide information about the orbital from which ionization took place, the nature of the electronic state from which dissociation took place, the timescale of dissociation, and so on. Further, by shaping the laser pulses or tweaking the laser parameters, it is possible to manipulate these ultrafast nuclear dynamics and hence, control the yield of the dissociative pathways.

Although the control of light-induced reactions and molecular fragmentation has been studied extensively in the past decades, a complete understanding of H_2^+ and H_3^+ formation by the bond breakup, intramolecular H migration, and bond formation has not been achieved yet. Furthermore, the control of the H_2^+, H_3^+ yield by controlling the excited-state dynamics of the parent ion is of particular interest, as this will enable us to control bond breakup and bond formation in reactions.

In this thesis, we have investigated the strong-field ionization and fragmentation of polyatomic molecules (CH_3OH, CD_3OH, and CH_3Cl) induced by intense femtosecond laser pulses in our in-house developed RIMS and Velocity Map Imaging (VMI) spectrometers. We focused on the formation of H_2^+ and H_3^+, which involve the bond breakup, intramolecular H migration, and bond formation processes, as mentioned above. We first demonstrated the influence of laser parameters like intensity, pulse duration, wavelength, and polarization on their yield. Next, a few two-body fragmentation pathways (that produce H_n^+ and HCl^+) of a molecular dication (CH_3Cl^{2+}) using photoion-photoion coincidence were identified. The complete kinematic information of the fragments revealed the timescale of dissociation and the nature of the excited electronic states from which dissociation occurred. Using laser intensity and chirp, it was possible to control the excited-state dynamics of the parent dication and hence, its dissociation along the four pathways. Finally, the complex fragmentation dynamics of CH_3Cl^{2+} along three-body breakup pathways were investigated using Dalitz plots, Newton diagrams, and the native frame method. The momentum sharing between the fragments and the fragmentation mechanism for the pathways were investigated. The most dominant fragmentation pathways were found to be concerted, along with some sequential processes. Chirped pulses were found to influence the excited-state dynamics of the dication and hence, the fragmentation mechanism. I have, therefore, investigated and demonstrated the control of the ultrafast nuclear dynamics in polyatomic molecules and their dissociation along two- and three-body breakup pathways by using different intensities and pulse durations, which is a significant step in the control of reactions.

Contents

List of Figures

List of Tables

List of Abbreviations

SFI	Strong-field ionization
PES	Potential energy surface
IR	Infrared
MPI	Multiphoton ionization
TI	Tunneling ionization
SPIDER	Spectral Phase Interferometry for Direct Electric-field Reconstruction
HHG	High-harmonic generation
NSDI	Non-sequential double ionization
ATI	Above-threshold ionization
RESI	Recollision excitation with subsequent ionization
ADK	Ammosov-Delone-Krainov theory
SAE	Single active electron approximation
SFA	Strong-field approximation
HOMO	Highest occupied molecular orbital
CEP	Carrier envelope phase
RIMS	Recoil Ion Momentum Spectrometer
CPA	Chirped pulse amplification
GVD	Group velocity dispersion
SPA	Single pass amplifier
SPM	Self-phase modulation
FROG	Frequency Resolved Optical Gating
BBO	Barium β-borate
VMI	Velocity map imaging
TOF	Time-of-flight
MCP	Microchannel plate detector

DLD	Delay line detector
NIM	Nuclear Instrumentation module
FWHM	Full-width half-maximum
TTL	Transistor-transistor logic
KER	Kinetic energy release
COBOLD	COmputer Based Online offline Listmode Dataanalyzer
DAq	Data acquisition
DAn	Data analysis
AIMD	*ab-initio* molecular dynamics
CFD	Constant fraction discriminator
CREI	Charge resonance enhanced ionization
LP	Linear polarization
CP	Circular polarization
LUMO	Lowest unoccupied molecular orbital
CASSCF	Complete active space self-consistent field
PIPICO	Photoion-photoion coincidence
CE	Coulomb explosion

List of Publications

Included in thesis

1. **Rituparna Das**, Deepak Kumar Pandey, Swetapuspa Soumyashree, P Madhusudhan, Vinitha Nimma, Pranav Bhardwaj, Muhammed Shameem K M, Dheeraj Kumar Singh, and Rajesh Kumar Kushawaha, 2022. "Strong-field ionization of CH_3Cl: proton migration and association" *Physical Chemistry Chemical Physics* (doi: 10.1039/D2CP02494B).

2. **Rituparna Das**, Deepak Kumar Pandey, Vinitha Nimma, P Madhusudhan, Pranav Bhardwaj, Pooja Chandravanshi, Muhammed Shameem K M, Dheeraj Kumar Singh, and Rajesh Kumar Kushawaha, 2021. "Strong-field ionization of polyatomic molecules: ultrafast H atom migration and bond formation in the photodissociation of CH_3OH" *Faraday Discuss*. **228**, 432-450.

3. **Rituparna Das**, P Madhusudhan, Vinitha Nimma, Pranav Bhardwaj, and Rajesh Kumar Kushawaha, 2022. "Fragmentation dynamics of CH_3Cl^{2+} induced by femtosecond laser pulses" *Journal of Chemical Physics* **(under review)**.

Not included in thesis

1. Muhammed Shameem KM, P Madhusudhan, **Rituparna Das**, Pranav Bharadwaj, Nimma Vinitha, Swetapuspa Soumyashree, Rajesh Kumar Kushawaha, 2022. "Molecular emission dynamics from a femtosecond filament induced plasma plume" *Journal of Optics* **24** 044015.

2. **Rituparna Das**, P Madhusudhan, Vinitha Nimma, Pranav Bhardwaj, and Rajesh Kumar Kushawaha. "Fragmentation dynamics of *cis*- and *trans*-$C_2H_2Cl_2$: investigating the effect of molecular geometry" **(under preparation)**.

3. P Madhusudhan, **Rituparna Das**, Pranav Bhardwaj, Muhammed Shameem K M, Vinitha Nimma, Swetapuspa Soumyashree, and Rajesh K Kushawaha. "Strong-field ionization of N_2 and CO molecules using two-color laser field" **(under preparation)**.

Book Chapters

1. **Rituparna Das**, KM Muhammed Shameem, Vinitha Nimma, Swetapuspa Soumyashree, Prashant Kumar, Rajesh K Kushawaha, 2021. "Improving the Signal Strength and Detection Limits of Laser-Induced Breakdown Spectroscopy", Modern Techniques of Spectroscopy *Springer Nature* **13** 307-320.

2. P Madhusudhan, **Rituparna Das**, Pranav Bharadwaj, Pooja Chandravanshi, Swetapuspa Soumyashree, Vinitha Nimma, Rajesh K Kushawaha, 2021. "Modern Experimental Techniques in Ultrafast Atomic and Molecular Physics", Modern Techniques of Spectroscopy *Springer Nature* **13** 257-285.

3. Muhammed Shameem K M, Swetapuspa Soumyashree, P Madhusudhan, Vinitha Nimma, **Rituparna Das**, Pranav Bhardwaj, Prashant Kumar, and Rajesh K Kushawaha. "Nanosecond and Femtosecond Laser-Induced Breakdown Spectroscopy (LIBS): Fundamentals and Applications" **(accepted)**.

4. Muhammed Shameem K M, Swetapuspa Soumyashree, P Madhusudhan, Vinitha Nimma, **Rituparna Das**, Pranav Bhardwaj, Prashant Kumar, and Rajesh K Kushawaha. "Molecular species formation in laser produced plasma" **(accepted)**.

"Whatever makes you uncomfortable is your biggest opportunity for growth."

Bryant H. McGill

Chapter 1

Introduction

1.1 Background and Motivation

Humans have always been interested in understanding the various physical, chemical, and biological processes occurring around them. These phenomena are the result of sub-Angstrom scale events on a timescale of attoseconds (10^{-18} s) to femtoseconds (10^{-15} s). The building blocks of matter are atoms and molecules which, in turn, are comprised of electrons and nuclei in perpetual motion. In the semi-classical picture of an atom, the electrons revolve around the nucleus in circular orbits called stationary states. To get an idea about the timescale of electronic motion, we consider the electron in the 1s (Bohr) orbit of the hydrogen atom. Then, the time taken by the electron to complete one revolution around the nucleus is $\sim$ 152 as [1]. On the other hand, the nuclei which are $\sim$ 1800 times heavier than the electrons, move (translational, rotational and vibrational) on a much longer timescale (hundreds of femtoseconds to picoseconds). This means that in response to a field, the electrons move much more quickly compared to the nuclei. Due to their different timescales of motions, the Born-Oppenheimer approximation assumes that the electronic and nuclear motions can be treated independently. Understanding the ultrafast motion of electrons and nuclei on their natural timescale will deepen our understanding of the various physical, chemical, and biological processes around us. A few instances of light-induced processes in nature are the cis-trans isomerization of rhodopsin marking the first step in vision ($\sim$ 200 fs) [2, 3], the absorption of sunlight by photoactive pigments and the subsequent transfer of energy to the reaction center in photosynthesis (few tens to hundreds of fs) [4], DNA damage [5] and repair [6] following

interaction with UV radiation (few tens of fs). Capturing the ultrafast electron and nuclear dynamics in real-time will enable us to make a molecular movie and understand reactions.

The 20th century saw the development of numerous spectroscopic and diffraction techniques along with quantum mechanics, which deepened our understanding of matter. The foundation of quantum mechanics laid by Planck and Einstein in the early 1900s eventually explained the spectral lines of hydrogen atom. The phenomena of absorption and emission of radiation by atoms and molecules was now attributed to the transition of electrons from one energy level to another. This was possible due to the development of various spectroscopic techniques, based on light-matter interaction, which revealed the structure of atoms and even complex molecules like DNA, proteins and enzymes.

The interaction of light and matter results in a portion of the spectrum (depending on the constituent atoms and molecules) being absorbed, while the rest is emitted. Measuring the absorbed and emitted parts of the electromagnetic spectrum is termed molecular spectroscopy and they contain information about the molecular structure. Some of the spectroscopic techniques used to understand molecular structure are UV-visible spectroscopy, infrared spectroscopy, nuclear magnetic resonance, mass spectrometry, to name a few. Furthermore, various diffraction techniques based on the scattering of x-rays, electrons, and neutrons from molecules also reveal the molecular structures. However, during reactions the molecular structure changes continuously. Therefore, the next challenge was to capture the atoms and molecules as they evolve with time (dynamics), that is, capture their motion and understand the fragmentation dynamics. This was partially achieved by the ion or electron collision of atoms [7–9] and molecules [10–13]. The multiple ionization of molecules initiated by ion collisions, followed by the ultrafast excited-state dynamics of the parent ion leading to fragmentation were studied using 3D imaging of the fragments in coincidence [14, 15]. In addition, the multiphoton ionization of atoms and molecules was investigated using x-radiation that revealed the core-hole dynamics [16]. However, time-resolved studies of electron and nuclear dynamics

was possible only after the development in laser technology.

To capture the image of a moving object, we need a tool/event shorter than the timescale of the event to be measured. Our eyes can resolve events as short as 13 ms. The pioneering works of the English photographer Eadward Muybridge on the study of motion pictures (1878), and Harold Edgerton on flash photography, freezing the moment when a bullet (timescale of $\sim$ millisecond) passes through an apple (1900s), made it possible to see and capture events that our eyes cannot resolve. To capture the ultrafast motion of electrons and nuclei, the fastest event known to mankind was used – light. With the development in the laser technology in the 20th century, it was possible to produce short bursts of light (pulses) having durations of the order of nanoseconds to picoseconds. Such lasers enabled the time-resolved studies of the structure and dynamics of molecules, including biomolecules like proteins and nucleic acids by absorption and vibration spectroscopy [17, 18]. With the advent of solid state lasers in the 1980s, it was possible to generate "intense" (the laser field strength is strong enough to perturb the Coulomb potential of the atom/molecule) ultrashort pulses, as short as a few tens of femtoseconds or even shorter, thereby improving the resolution by 10 orders of magnitude. It is now possible to study nuclear and coupled electron-nuclear dynamics on their natural timescale. The field of femtochemistry pioneered by Zewail [19], for which he was awarded the Nobel prize in Chemistry in 1999, opened up the possibility of observing the time-resolved changes in the geometry of molecules in the intermediates and the transition states. For this purpose, a pulse pair was used, called the pump and probe, with a delay between them. The energy imparted by the pump pulse is redistributed among the various degrees of freedom. The subsequent nuclear dynamics in the excited state is probed by sending a delayed probe pulse, which probes the time-resolved changes in the molecule induced by the pump pulse. With such ultrashort bursts of light, it is now possible to take snapshots of processes like photosynthesis [20], binding of drugs with proteins [21], viral infections [22], and even fundamental processes in technology [23]. Using intense ultrashort laser pulses to study the rich physics in atoms and molecules is known as strong-field physics.

1.1.1 Strong-field ionization

As mentioned above, the Ti:sapphire lasers emit intense, ultrashort pulses of duration ∼tens of fs in the near IR (central wavelength ∼ 800 nm). Mathematically, the field is represented by $E(t) = E_0(t)cos(\omega_0 t + \phi)$ where $E_0(t)$, ω_0 and ϕ represent the pulse envelope, carrier frequency, and carrier-envelope phase, respectively. The intensity of the pulses is of the order of 10^{12} W/cm^2, which on focusing by a lens or mirror produces intensities as high as $\sim 10^{14} - 10^{15}$ W/cm^2. At such high intensities, the Coulomb potential of the atoms and molecules is distorted (the Coulomb field strength of hydrogen atoms is $\sim 10^{11}$ V/m). Moreover, as the intensity increases, the energy of the photoelectron traversing in the laser field (called the ponderomotive energy, U_p) increases compared to that of the absorbed photon. Therefore, perturbation theory breaks down in the strong-field regime. The first theoretical approach explaining the strong-field ionization (SFI) of hydrogen atom was given by Keldysh in 1965 [24]. Primarily, SFI was found to occur in two regimes: (i) multiphoton ionization, and (ii) tunneling ionization. The Keldysh parameter or the adiabaticity parameter, given by $\gamma = \sqrt{\frac{I_p}{2U_p}}$, describes the ionization regime as a function of the ionization potential of the atom (I_p), and the ponderomotive energy ($U_p = \frac{E^2}{4\omega^2}$, in atomic units). Here, ω is the carrier frequency, and E is the electric field strength. The two strong-field ionization regimes are discussed as follows:

- **Multiphoton ionization:** this is a low intensity and high-frequency regime, so $\gamma >> 1$. In this regime, the field is not strong enough to distort the Coulomb potential and the atoms are ionized by the absorption of multiple photons, as shown in figure 1.1(b). The ionization probability (w_{MPI}) is related to the laser field strength as [25]

$$w_{MPI} \propto E^{2n}, \tag{1.1}$$

  where n is the number of photons absorbed.

- **Tunneling ionization:** this regime is marked by high intensity and low frequency fields that is, $\gamma \leq 1$. When the field is very strong but also alternating slowly, the electron has sufficient time to tunnel out into the continuum

through the potential barrier formed by the sum of the Coulomb potential and the laser field, as shown in figure 1.1(c). The ionization probability (w_{TI}) of the system in this regime is related to the laser field as [25]

$$w_{TI} \propto \exp\left\{ -\frac{4}{3}\frac{(2I_p^3)^{1/2}}{E} \right\}. \tag{1.2}$$

It must be noted that at extremely high intensities ($\gamma << 1$) the resultant Coulomb potential is distorted to the extent that the maxima of the barrier falls below the energy state in which the electron is located, as seen in figure 1.1(d). This phenomenon is called *over-the-barrier ionization* or *barrier-suppression ionization* and the ejected photoelectron is swiftly removed from the system into the continuum.

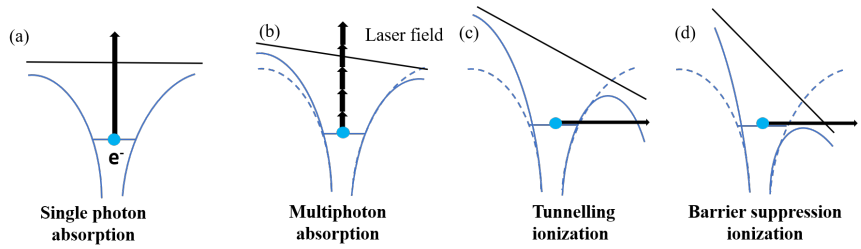

FIGURE 1.1: Schematic diagrams demonstrating the atomic Coulomb potentials in the case of (a) single photon ionization, (b) multiphoton ionization, (c) tunneling ionization, and (d) over-the-barrier ionization.

The photoelectron ejected into the continuum accelerates in the laser field. For a linearly polarized pulse, the laser field oscillates and changes direction every half cycle, thereby reversing the electron trajectory. This may lead to one of the following processes:

- **High-harmonic generation (HHG):** the electron may recombine with the parent ion. This is accompanied by the release of a photon of a higher frequency (photon energy is the sum of the ionization potential and the ponderomotive energy) than that of the driving laser field. This semi-classical three-step model of HHG was presented by Kulander [26] in 1992 and Corkum [27] in 1993. In 1994, the quantum theory of high-harmonic generation was introduced by Lewenstein et al. [28]. High harmonic generation from atoms and molecules

generates single attosecond pulses or attosecond pulse trains in the UV and X-ray regimes [29]. The cut-off energy in HHG is given by $E_{max} = 3.17U_p + I_p$.

- **Non-sequential double ionization (NSDI):** in a multi-electron system, the electron may recollide inelastically with the parent ion, transfer energy to the ionic core, and further ionize the parent ion by releasing a second electron [30]. In this case, there exists a strong momentum correlation between the two ejected photoelectrons [31]. The ejection of the second electron can either be instantaneous (known as electron impact ionization or EII) or delayed (known as recollision excitation with subsequent ionization or RESI) [32, 33]. In the case of RESI, the energy transferred to the second bound electron (e_2) by the recolliding tunnel electron (e_1) is not sufficient to remove it and therefore, transfers e_2 to an excited state. At a later time, e_2 absorbs energy from the laser field and the parent ion becomes doubly ionized.

- **Above Threshold Ionization (ATI):** in the presence of an intense IR field, an atom can absorb more photons than required for it to be ionized. This process called above threshold ionization results in the photoelectron spectra showing multiple peaks. Each peak in the photoelectron spectra is separated by the photon energy ($\hbar\omega$). The higher-order ATI peaks result from the elastic and inelastic scattering of the tunnel electron from the parent ion [34].

Many refinements were subsequently made to the Keldysh theory and various analytical expressions defining the tunneling ionization rate were obtained, by taking into consideration the time-dependence of the laser field [35], the instantaneous phase of the field for few-cycle pulses [36], polarization of the field [37], and the molecular structure [38]. The Keldysh-Faisal-Reiss (KFR) and Ammosov-Delone-Krainov (ADK) theories are the most widely used approaches to obtain the ionization probability of atoms. Most of the theoretical models developed for explaining the strong-field processes are based on approximations like the single active electron (SAE) approximation, the dipole approximation, the strong-field approximation (SFA), and neglects the electron-electron correlations in many-electron systems, the

Stark effect due to the laser field. The quantum-mechanical [28, 39–41] and semiclassical [27, 42] theories agree well with the experimental results in strong-field ionization, above threshold ionization, and high harmonic generation in atoms. However, studying the strong-field ionization of polyatomic molecules is extremely complicated due multiple factors like the larger number of degrees of freedom, the presence of multi-center potentials [43], the non-spherically symmetric charge distribution, the coupling between the rotational, vibrational, and electronic motions. This coupling between the electronic and nuclear motions becomes stronger at the conical intersections which are found in large numbers in polyatomic molecules [44]. In addition, the valence and inner-valence orbitals (HOMO, HOMO-1, HOMO-2, etc.) in the polyatomic molecules are very closely-spaced so, during interaction with the intense field, electrons are lost not only from the HOMO but also HOMO-1 and HOMO-2 orbitals. The symmetry of the molecular orbital from which the electrons are removed as well as the relative orientation of the molecular axis with respect to the polarization direction are found to play a key role in the ionization rate of molecules [45]. It is also known that, the ionization rate of molecules is a function of the internuclear separation, and for intermediate to large separations compared to the equilibrium separation, the ionization rate is greatly enhanced [46, 47]. This process termed charge resonance enhanced ionization (CREI), is ascribed to the coupling of pairs of orbitals by the laser field, leading to charge localization, and therefore, enhanced ionization. Thus, an increase in the size of the molecule results in more complex nuclear and electron dynamics thereby, increasing the computational complexity.

1.2 Photoionization and photodissociation of polyatomic molecules

In this thesis, we shall discuss two important light-induced processes – ionization and dissociation. As discussed in the previous section, the strong-field ionization of molecules takes place either by the absorption of multiple photons or tunneling, depending on the intensity and wavelength of the laser field and the ionization potential of the system. A part of the energy absorbed from the laser field ($n\hbar\omega$),

called the bond dissociation energy (D_o), is utilized in overcoming the potential barriers to undergo dissociation, while the rest (excess energy) is redistributed among the various degrees of freedom of the molecule (translational, electronic, vibrational and rotational). It must be noted that the probability of transition of the molecular wavepacket from an initial to a final state (electronic, vibrational or rotational) is governed by the selection rules that arise from the transition dipole moment and is given by [48]

$$P_{21} = \int \psi_2 \, \mu \, \psi_1 \, d\tau, \tag{1.3}$$

where μ is the transition dipole moment. When the dipole moment is aligned parallel to the polarization direction, the ionization probability is maximum. Using the Born-Oppenheimer approximation, we can separate the nuclear and electronic wavefunctions, then

$$P_{21} = \int \psi'_e(r, R_e) \, \mu_e \, \psi''_e(r, R_e) \, dr \int \psi'_v(R) \, \mu_v \, \psi''_v(R) \, dR, \tag{1.4}$$

where r and R represent the position coordinates of the electrons and nuclei, respectively, ψ' and ψ'' represent the upper and lower states, respectively, and the subscripts e and v stand for the electronic and vibrational degrees of freedom. The rotational degree of freedom is neglected in this equation. The first and second integrals lead to the selection rules for electronic and vibrational transitions, respectively. Further, the selection rule for vibrational transition indicates that there must be significant overlap between the vibrational levels for transition to occur. When this happens, it leads to instantaneous transition between the two vibrational energy states which can be represented by a vertical line in the potential energy diagram (Frank-Condon principle).

Once ionized, the molecular wavepacket undergoes a transition from the ground state of the neutral molecule to either a ground or an excited ionic state. The ionic state may be stable, metastable, or dissociative/repulsive. The ions populating the

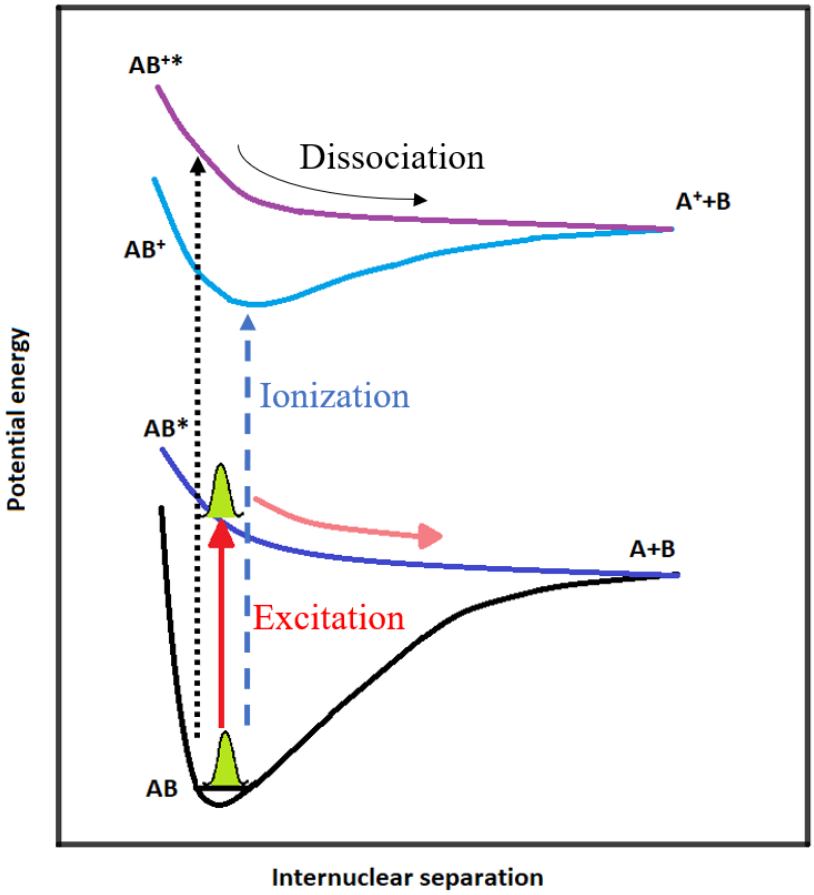

FIGURE 1.2: Potential energy diagram demonstrating the ionization, excitation, and dissociation of a hypothetical molecule AB.

stable states have a long lifetime and do not dissociate much. The metastable states, on the other hand, have lifetime ranging from a few picoseconds to milliseconds. Finally, the molecular ions populating the repulsive PESs are highly unstable and undergo rapid dissociation. In the excited state, the molecular ion undergoes geometrical changes as it tries to gain stability. This leads to various ultrafast processes like rotation [49–51] (on a timescale of hundreds of fs to ps) and vibration [52–54] (like bending, scissoring, symmetric and asymmetric stretching, wagging, and twisting on a timescale of tens of fs), leading to bond-breaking, bond formation, intramolecular migration [55], bond softening [56], and bond hardening [57], prior to molecular fragmentation.

The dissociation of a molecule, therefore, depends on the molecular geometry and the excited PES from which the dissociation occurs. By determining the total kinetic energy of all the fragments in a particular dissociative channel, it is possible

to obtain information about the PES from which the dissociation took place. In addition, the molecular orbital from which the electron(s) was removed and the nature of the excited PES determine the timescale of dissociation, as well as the angular distribution of the fragments. As a result, obtaining the complete kinematic information for each fragmentation pathway can provide compete understanding of the excited-state nuclear dynamics leading to each pathway.

1.3 Controlling reactions

One of the aims of strong-field physics is to understand how to control molecular reactions. Understanding what triggers light-induced reactions, how the absorbed energy is redistributed among the nuclei and electrons, the excited-state state nuclear and electron dynamics, geometrical deformations, leading to the end products, will help us control reactions by controlling the transition states and intermediates. Strong-field ionization of atoms and small molecules usually remove the valence electrons, but in case of polyatomic molecules, electrons may be removed from the inner valence orbitals as well. By ionizing the molecules from the valence or the inner-valence orbitals and controlling the population of the ionic states, it is possible to control the dissociative pathways of the molecule. Several experimental techniques have been developed to control light-induced reactions. Controlling the fragmentation pathway of molecules by the carrier envelope phase (CEP) of intense few-cycle pulses has been demonstrated [58–62]. Impulsively aligning molecules with respect to the laser polarization direction has been shown to provide control over the relative yield of the various fragmentation pathways [63, 64]. On the other hand, using a pair of pulses in the pump-probe technique offers control on the shape of the electric field, and it is possible to control the reaction pathway by changing the delay between the pulse pair [65, 66]. Orthogonal two-color pulses have also been used to control the ultrafast nuclear dynamics by adjusting the phase between the fundamental and second-harmonic fields [67]. In addition, laser parameters like intensity and pulse duration have also been used to control the outcome of fragmentation reactions[68, 69].

1.4 Our Focus

In this thesis, we have focused on the strong-field physics of a few polyatomic molecules like CH_3Cl, CH_3OH, and its deuterated isotopomer CD_3OH. For this purpose, we have performed the strong-field ionization of these molecules induced by intense femtosecond laser pulses in our in-house developed spectrometers. We investigated the formation of H_2^+ and H_3^+ ions by bond-breakup, intramolecular H migration, and bond formation, and the factors affecting them. Further, we selected a few two- and three-body fragmentation pathways of a molecular dication and investigated the excited-state nuclear dynamics in each pathway with the help of the total kinetic energy, momentum distribution, and angular distribution of the fragments. We show that it is possible to control the excited-state dynamics of the dication and hence, the yield of the pathways by using the laser parameters like intensity and pulse duration. In addition, we have investigated the three-body fragmentation dynamics of the dication and obtained the complex momentum sharing between the fragments and the fragmentation mechanisms using Dalitz plot and Newton diagram. We demonstrate the control of light-induced reactions in small polyatomic molecules, which can have important applications in the control of reactions in the field of medicine like radiotherapy in cancer treatment (controlling the damage of ionizing radiation to healthy cells) and enhancing the efficiency of energy harvesting devices.

1.5 Thesis Outline

The thesis is divided into six chapters. The present chapter introduces the concepts of light-matter interaction, strong-field ionization, photodissociation and the control of reactions. In the next chapter (chapter 2), the experimental methodology is discussed. This includes a description of the ultrafast laser system, the spectrometers used, the detectors, data acquisition and data analysis techniques. The experimental results are then discussed in the subsequent chapters. Chapter 3 discusses the results of strong-field ionization of of the polyatomic molecules. Here, we have investigated the control of H_n^+ (n =1-3) formation using laser intensity, pulse duration,

polarization, and wavelength. In chapter 4, four two-body fragmentation pathways of CH_3Cl^{2+} that produce H_n^+ (n =1-3) and HCl^+ as one of the fragments are investigated. Here, we have demonstrated the control of the ultrafast excited-state dynamics of the parent dication and hence, the yield of the four pathways. In chapter 5, we have discussed the complex fragmentation dynamics of CH_3Cl^{2+} for three-body fragmentation pathways, the fragmentation mechanisms, and their control. Finally, the thesis work is summarized along with the future scope in chapter 6.

Chapter 2

Experimental Methodology

The photoionization experiments were performed in our in-house developed Recoil Ion Momentum Spectrometer setup using intense, femtosecond laser pulses from a Ti:sapphire laser (Coherent). Some of the experiments were performed in our home-built Velocity Map Imaging spectrometer. The Recoil Ion Momentum spectrometer (RIMS) setup was developed for performing strong-field ionization experiments and obtaining the the three-dimensional momenta of the fragments detected in coincidence. In this chapter, we discuss the laser system, pulse characterization technique, the spectrometers, and finally the data acquisition and analysis methods.

2.1 Intense ultrashort laser pulses

The Ti:sapphire laser facility in PRL, Ahmedabad produces pulses of duration 29 fs, central wavelength 800 nm, average power 10 W, having linear polarization, and a repetition rate of 1 kHz. A part of this beam (2 W) was used to perform the experiments in the RIMS setup. On focusing the pulses with a lens or a concave mirror, intensities of the order of PW/cm^2 were achieved. Femtosecond lasers are based on the chirped pulse amplification technique which was first developed by Gérard Mourou and Donna Strickland [70], for which they were awarded the Nobel Prize in 2018. This technique successfully generated ultrashort pulses (having tens of fs duration) of petawatt per square centimetre intensities for the first time. Before the development of the CPA technique, the maximum intensity of pulses that could be achieved was of the order of gigawatt per square centimeters. Such intense pulses when propagating through air or a medium, generate plasma due to nonlinear optical processes like self-focusing [71, 72], thereby damaging the medium, as well

as affecting the quality of the beam. The CPA technique, on the other hand, first stretches the ultrashort pulses in time and frequency domain, followed by amplification in a gain medium, and are finally recompressed back, resulting in ultrashort pulses of high (TW/cm^2 to PW/cm^2) intensities. Therefore, the four main components on which the Ti:sapphire laser is based are: (i) a mode-locked oscillator, (ii) a stretcher, (iii) an amplifier, and (iv) a compressor, as shown in figure 2.1. In the following sections, I shall briefly discuss the Ti:sapphire laser in PRL's Femtosecond laser lab. Figure 2.2 shows the femtosecond laser facility at PRL, Ahmedabad. The figure shows the femtosecond oscillator (Vitara), amplifier (Legend Elite Duo), and the CEP stabilization units for the oscillator and the amplifier. In addition, the driving diode (Nd:YLF) lasers for pumping the Ti:sapphire media (Regen and SPA) in the amplifier are present (not shown here).

FIGURE 2.1: Chirped pulse amplification technique in Ti:sapphire lasers to generate intense, ultrashort laser pulses.

2.1.1 Femtosecond oscillator

The mode-locked oscillator generates femtosecond pulses (pulse energy $\sim$ nanojoules, repetition rate $\sim$ 80 MHz, pulse duration $\sim$ 29 fs, average power $\sim$ 0.6W) which act as seed pulses for the amplifier. It has four components: a pump laser (Nd:YLF laser), a lasing medium (Ti:sapphire crystal), a set of mirrors forming the optical cavity, and optical components for dispersion compensation. The gain medium, titanium (Ti^{3+})-doped sapphire, is a widely-used gain medium for solid-state lasers. While sapphire's high thermal conductivity reduces the heating effects, titanium has a broad gain bandwidth which is essential for the generation of ultrashort pulses. These lasers have emission wavelength in the range of 700 nm to 900 nm, with a maximum gain at 800 nm. The Ti:sapphire crystal is pumped by a frequency-doubled Nd-YLF laser (at 532 nm) having an output power of $\sim$ 18W (in PRL's laboratory). A very essential aspect of generating ultrashort pulses is mode-locking.

This involves locking the phase difference between the longitudinal modes oscillating in the optical cavity thereby, attaining a periodic series of pulses of duration $\Delta\tau \approx 1/\Delta\nu$, where $\Delta\nu$ is the width of the gain curve [72], and a repetition rate of $T = 2L/c$, where L is the length of the cavity and c is the velocity of light in vacuum. Of all the possible longitudinal modes, only those modes survive for which the gain is greater than the cavity losses. To ensure a constant phase difference between these oscillating modes, various mode-locking techniques are used. The Ti:sapphire laser oscillator used in our experiments is based on the Kerr lens mode-locking.

Mode-locking

Ultrashort laser pulses having durations of the order of picoseconds to femtoseconds are achieved using the mode-locking technique. Mode-locking can be both active and passive. Active mode-locking techniques rely on some external signals to modulate the light in the laser cavity, like an electro-optic modulator. On the other hand, passive mode-locking techniques use an element placed in the cavity that modulates the light. Passive mode-locking technique is based on the optical Kerr effect, a nonlinear response of some optical media to the intensity of the laser beam passing through it [73]. A combination of a saturable absorber and the amplifying medium placed in the optical cavity together amplify the strongest intensity maxima in the cavity at the expense of the lower intensity maxima. In this way, a periodic series of short and intense laser pulses is generated. In the present Ti:sapphire laser however, the mode-locking does not require any external modulation (active mode-locking) or any saturable absorber (passive mode-locking). In this self-locking technique, the amplifying medium itself is responsible for the narrowing of the pulses by a process where the high intensity maxima suffer less losses in the cavity due to a modification in its transverse structure. This is possible due to the nonlinear properties of the amplifying medium, leading to an intensity-dependent refractive index ($n = n_0 + n_2 I$, where n_2 is the nonlinear coefficient of the refractive index). Since the intensity along the axis is maximum for a Gaussian beam, the beam experiences a stronger refraction along the axis of the beam thereby, forming a convex lens. This intensity-dependent process known as self-focusing causes the stronger intensity maxima to experience stronger focusing and their transverse structures reduce with successive round trips

and experience far less losses than the weak intensity maxima. Finally, a slit placed in the cavity facilitates the self-locking of the modes by enhancing the difference in the cavity losses experienced by the strong and weak intensities.

2.1.2 Pulse Stretcher

The seed pulses from the femtosecond oscillator cannot be sent directly for amplification, since the high laser intensity may damage optical components due to nonlinear effects like self-focusing. To reduce the peak intensity of the pulses, they must be first stretched thereby, increasing the pulse duration by $\sim 10^4$ times [72]. As the pulses are passed through a medium, the different frequency components encounter different delays in time. This phenomenon is termed group velocity dispersion (GVD) and it causes pulse broadening. The pulses are said to be positively-chirped when the red frequency components experience less delay compared to the blue frequency components, thereby giving rise to a pulse whose leading edge consists of the red frequencies, while the trailing edge consists of the blue frequencies. Pulse stretching can be achieved by the use of components like optical fibers, prism pairs, diffraction gratings, to name a few.

2.1.3 Amplifier

As mentioned above, one of the challenges in femtosecond pulse generation is the high peak power that can damage the optics due to nonlinear optical effects. Additionally the generation of femtosecond pulses requires the amplifying medium to have a broad gain bandwidth. These requirements limit the materials that can be used in the femtosecond amplifiers. Ti:sapphire has served as an ideal solid-state amplifying medium having a high damage threshold and broad gain bandwidth. The mode-locked seed pulses from the oscillator, after passing through the pulse stretcher, are sent into the amplifier where they are amplified in two stages using a regenerative amplifier and a single pass amplifier (SPA) [74]. In the regenerative amplification stage, the pulse is trapped in the cavity using a Pockel cell and a broadband polarizer and passed through the gain medium multiple times, until all the energy stored in the medium is extracted. By varying the voltage on the Pockel

cell crystal, it is switched between a quarter ($\lambda/4$) and half ($\lambda/2$) waveplate, thereby switching between the trapping and extraction of the pulses. The single-pass amplifier (SPA), as the name suggests, involves the seed pulse from the oscillator passing once through the Ti:sapphire amplifying medium that is pumped optically or electrically. It must be noted that in the oscillator-amplifier system, the parameters like pulse width, spectral width and beam divergence are determined by the oscillator, while the power and pulse energy depend on the amplifier [75].

2.1.4 Pulse compressor

Finally, after the amplification stage, intense pulses are achieved which however, have a long pulse duration (up to nanoseconds) with a positive chirp (dephasing of the spectral components). To achieve intense ultrashort pulses as short as a few tens of fs duration, the pulses from the amplifier need to be recompressed based on two phenomena – group velocty dispersion (GVD) and self-phase modulation (SPM). SPM broadens the pulses, while GVD is responsible for compensating for the delays introduced to the different spectral components (down-chirp). Similar to pulse stretching, pulse compression can be achieved by prism pairs, grating pairs and optical fibers.

2.2 Pulse characterization: SPIDER

Once the ultrashort pulses were produced, it required the development of techniques to characterize them that is, determine the pulse duration, intensity, and carrier-envelope phase. Initially, autocorrelation techniques were used to measure the intensity of the pulses but the phase information could not be obtained using these methods. Furthermore, all detectors like power meters used to measure the average power have a response time of the order of $\sim$ns, while the ultrashort pulses have a duration of few tens of fs. Therefore, these detectors measure the time-averaged intensity, that is $\int_{-\infty}^{\infty} |E(t)|^2 dt$, where E is the strength of the field. Eventually, techniques like Frequency Resolved Optical Gating (FROG) and Spectral Phase Interferometry for Direct Electric-Field Reconstruction (SPIDER) were developed which made complete pulse characterization possible.

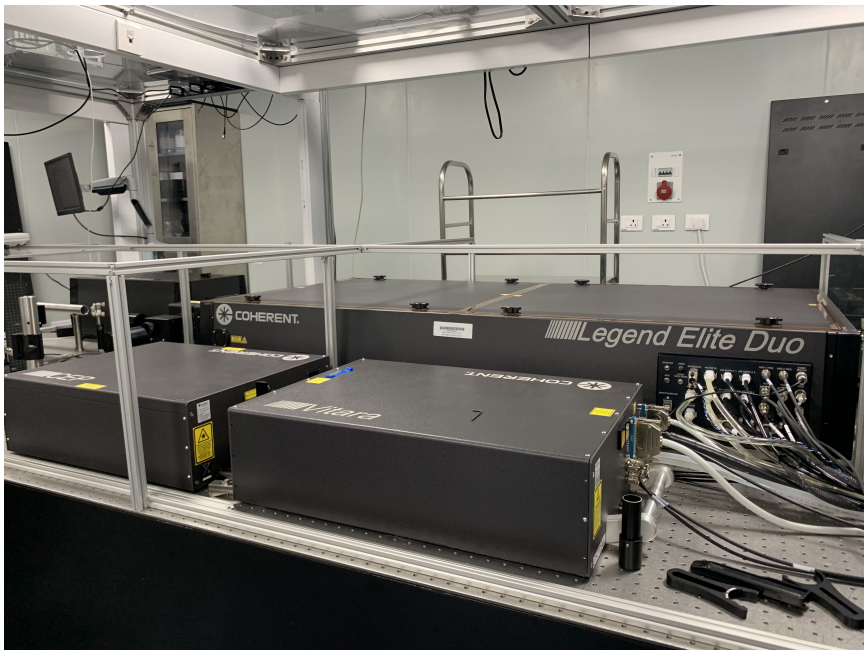

FIGURE 2.2: The femtosecond laser facility in PRL, Ahmedabad. It is a carrier-envelope phase stabilized Ti:sapphire laser (Coherent) producing 29 fs, 800 nm, linearly polarized pulses having intensity of the order of $\sim 10^{12}$ W/cm^2 (average power of 10 W).

In all our experiments, we have used a commercial SPIDER setup (FC Spider, APE), which temporally and spatially characterizes the pulses and has been discussed in detail in ref. [74]. Here, we shall briefly discuss the principle of the SPIDER setup.

The SPIDER technique is based on spectral shearing interferometry to directly reconstruct the electric field in real-time. The spectral intensity is measured using a spectrometer. To obtain the spectral phase, the pulse is split into two. One part of the pulse is passed through a stretcher (dispersive optical element) to stretch it from fs to ps duration, while the other part is further split into two parts by passing it through a mismatched Michelson interferometer. This produces three pulses - a chirped pulse, and a pair of unchirped pulses with a delay τ between them. The chirped pulse is then overlapped with the unchirped pulse pair in a sum-frequency generation (SFG) BBO (Barium β-borate) crystal. This causes the unchirped pulse pair to overlap with different parts of the chirped pulse, resulting in spectral shearing and the upconverted pulse pairs have different central frequencies. These pulse

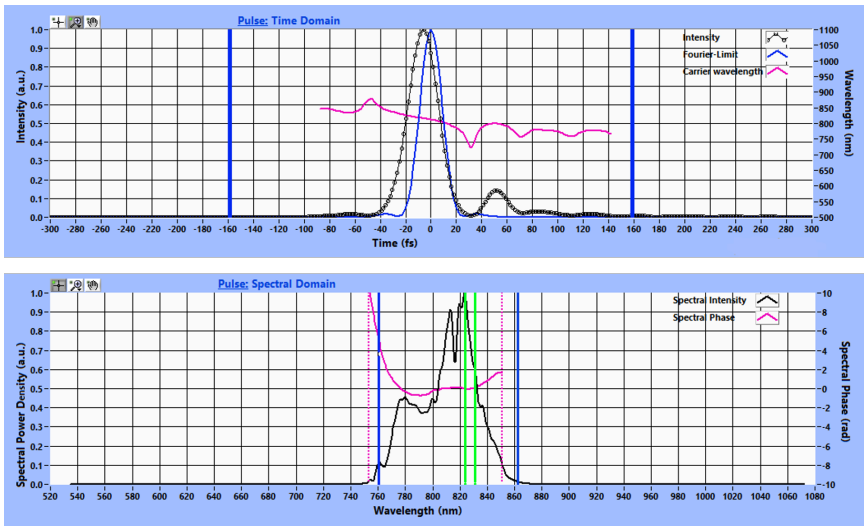

FIGURE 2.3: Pulse characterization of the femtosecond pulses using the SPIDER setup (figure used from ref. [74]).

pairs are then sent to an interferogram to reconstruct the phase information by comparison with a calibrated interferogram. Figure 2.3 shows the reconstructed pulse with the pulse duration and phase information.

2.3 Spectrometers

The strong-field ionization experiments were performed in our in-house developed spectrometers – Recoil Ion Momentum Spectrometer (RIMS) and Velocity Map Imaging (VMI) setups. Since I developed the RIMS setup as a part of my thesis work, I shall discuss the RIMS in detail. In addition, a part of the work was performed in a VMI setup, which is briefly discussed.

2.3.1 Recoil Ion Momentum Spectrometer (RIMS)

The RIMS is a powerful instrument (shown in figure 2.5) that provides complete kinematic information of the fragments formed in each dissociative pathway in coincidence. Using this setup, we can obtain the three-dimensional momentum and kinetic energy information of ions and electrons in coincidence, thereby facilitating the study of the ultrafast nuclear dynamics in the molecular frame. We shall discuss the individual components of the setup in detail below.

RIMS chamber

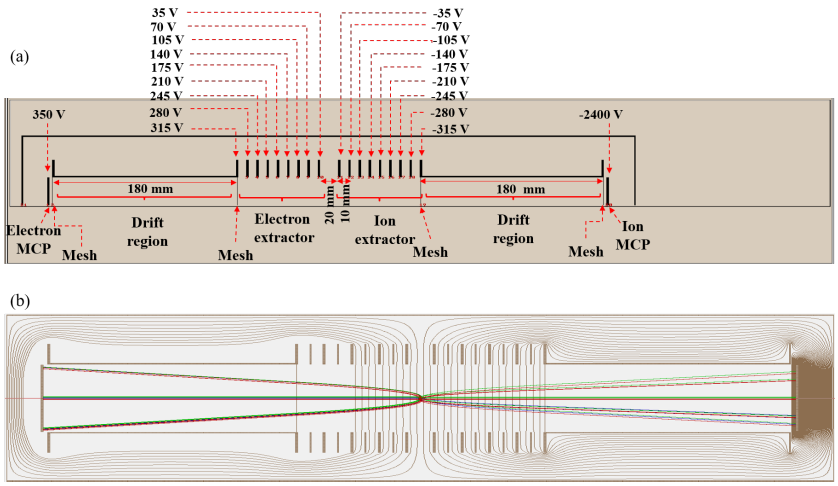

FIGURE 2.4: Charged particle trajectory simulation of the RIMS setup obtained using the SIMION 8.0.4 software. (a) Potentials applied to the individual electrodes and the dimensions of the extraction and drift regions. (b) The equipotential lines (in brown) and the ion and electron trajectories are shown here. In the simulation, the trajectories have been obtained for ions and electrons having kinetic energies 4 eV and 10 eV, respectively. Particles ejected towards and away from the detector at angles 0°, 45°, 90°, 135°, and 180° are considered.

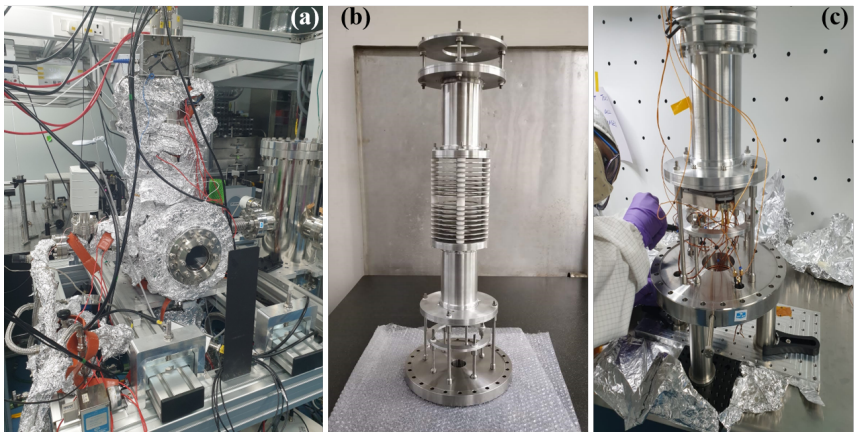

FIGURE 2.5: (a) The Recoil Ion Momentum Spectrometer (RIMS) setup in PRL's femtosecond laser laboratory. (b) RIMS spectrometer assembly. (c) Mounting of the MCP and DLD on the CF200 flange.

The spectrometer was designed based on the charged particle trajectory simulations performed using the SIMION 8.0.4 software. Figure 2.4(a) shows the typical potentials applied to the plates along with the dimensions, while figure 2.4(b) shows the simulated trajectories of the ions and electrons along with the equipotential lines obtained in SIMION for an electric field of 35 V/cm. In the figure, the trajectories are simulated for ions and electrons having kinetic energies 4 eV and 10 eV, respectively.

Particles ejected towards and away from the detector at various angles (0°, 45°, 90°, 135°, and 180°) are considered in the simulation. Based on the results of our simulation, the spectrometer was developed in the PRL workshop and assembled in-house.

The spectrometer, housed inside the RIMS ultrahigh vacuum chamber, is essentially an assembly of electrodes. The chamber is maintained at a pressure of $\sim 10^{-8}$ mbar using a turbo pump (Pfeiffer) and a root pump (Leybold). Two sets of annular rings/electrodes (made of aluminium) are arranged on either side of the ionization region (the region where the laser pulses interact with the molecular beam). The electron and ion sides of the spectrometer have a length of 270 mm each, of which the extraction and drift regions have a length of 90 mm and 180 mm, respectively. The length of the spectrometer affects the energy resolution; the longer the spectrometer, the higher its resolving power. The separation between the rings is 10 mm, while the ionization region has a length of 20 mm. The electrodes/rings have an inner diameter of 80 mm and an outer diameter of 130 mm. Potentials are applied to the electrodes using resistors connected in series and a power supply (NHQ power supply module). A constant electric field of 35 V/cm was maintained in all the experiments.

For the strong-field ionization experiments, the molecular beam was interacted with the laser pulses at right angles (termed 'crossed-beam geometry') at the ionization region, leading to the formation of positively-charged ions and negatively-charged electrons. The uniform electric field in the spectrometer then separates the ions and electrons by directing them to the opposite ends of the chamber. The times-of-flight (TOFs) and (x,y) position information of the ions/electrons are obtained using detectors. An 80 mm diameter microchannel plate detector (MCP, Roentdek) on the ion-side, and a 40 mm diameter MCP detector (Roentdek) on the electron-side provide the TOFs of the ions and electrons, respectively. Further, the position information of the ions is obtained from a position-sensitive delay line detector (DLD, Roentdek). The MCP detector and the position-sensitive DLD are discussed briefly below.

Time and position information

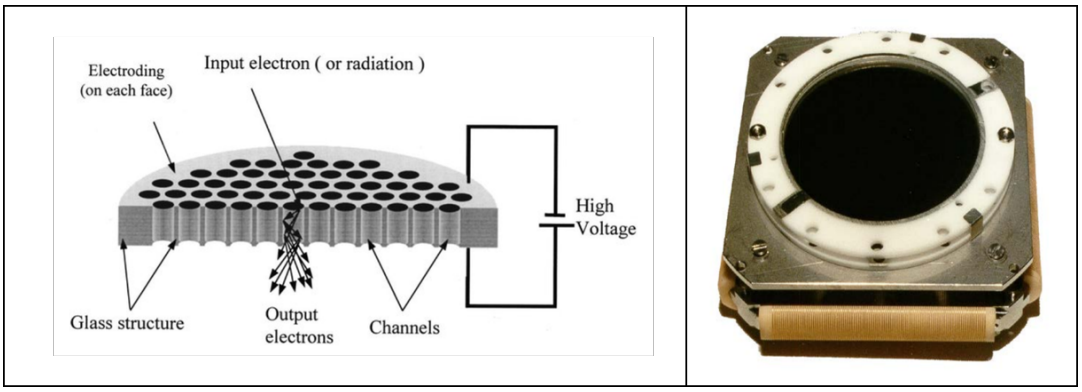

FIGURE 2.6: (left) Transverse view of the MCP detector showing its basic operation [76]. (right) MCP-DLD assembly.

The micro-channel plate (MCP) detector is a device that detects the time of impact (TOF) of particles/photons with very high precision (position resolution$<$ 0.1 mm, time resolution$<$ 0.2 ns), using fast timing amplifiers, discriminators and digitizers. The active diameters of the MCPs on the ion and electron sides are 80 mm and 40 mm, respectively. The detectors are operated under ultrahigh vacuum condition ($\sim 10^{-8}$ mbar) in the RIMS setup. The MCP consists of two plates stacked in chevron configuration, and supported by partly metalized ceramic rings. The MCP is mounted above the delay line detector (DLD) which is an array of two pairs of wires. Five DC voltages are applied to the MCP-DLD under the operating conditions – two high voltages on the MCP front and back contacts, one voltage on the holder supporting the DLD, and two DC voltages for the DLD signal and reference wires. The voltages applied in our setup for ion and electron detection are given in the table below.

TABLE 2.1: Voltages applied to the MCP-DLD on the ion-side and the MCP on the electron-side, respectively.

	Ion detection	Electron detection
MCP front	-2400 V	350 V
MCP back	grounded	2250 V
Holder	100 V	grounded
DLD signal	300 V	–
DLD reference	250 V	–

To understand the operation of the MCP detector in TOF measurement, we have shown the transverse view of the MCP in figure 2.6 (left) and the real image of the

DLD assembly in figure 2.6 (right). These images are taken from the Roentdek manual. Each MCP plate has a thickness of 1.5 mm and is made of a resistive material (glass, resistance $\sim$ 100 MΩ). The microchannels are an array of parallel tubes each having a diameter of 5 to 20 μm. An ion or electron falling on the MCP enters one of these microchannels produces a signal that is too feeble to detect. To overcome this problem, the array of microchannels are manufactured at a very small inclination of about $8^\circ - 13^\circ$ with respect to the normal to the surface of the detector. This ensures that a charged particle entering the channel hits the wall of the channel, resulting in the generation of a cascade of electrons travelling through the channel due to the high voltage difference between the MCP front and back. The two MCPs are stacked in Chevron configuration so that the ion feedback in the opposite direction of the electrons do not result in distorted signals. Therefore, the MCP amplifies the electron/ion/photon signal by producing an electron cloud, leading to a gain of $\sim 10^6$. The signals from the MCP are sent to a constant fraction discriminator (ATR-19, Roentdek), which produces digital (NIM) signals having a precision $<$ 0.2 ns. Finally, these NIM signals are sent to a TDC8HP card for time-to-digital conversion. The TDC8HP card is triggered by the laser sync-out, and for each start signal, the card records the timestamps of all the stop signals (from the ions/electrons impinging on the MCP) in a range (user-defined).

The position-sensitive DLD gives the (x,y) coordinate of each charged particle hitting the MCP. It consists of two sets of bare copper wires wound perpendicular to each another on a square support, as shown in the figure 2.7. The x and y coordinates of a charge cloud falling on the DLD are obtained from the time difference between the signals reaching the two ends of the wires (figure 2.7 (a)), that is

$$x = (t_{X1} - t_{X2}).v_{signal}, \;\; y = (t_{Y1} - t_{Y2}).v_{signal}, \tag{2.1}$$

where v_{signal} is nearly close to the speed of light. This time difference is proportional to the position at which the ion hits. To obtain each position coordinate, a pair of delay lines or wires (called the signal and reference) is used instead of a single wire in order to reduce the pickup/noise. The signal wire is maintained at a more

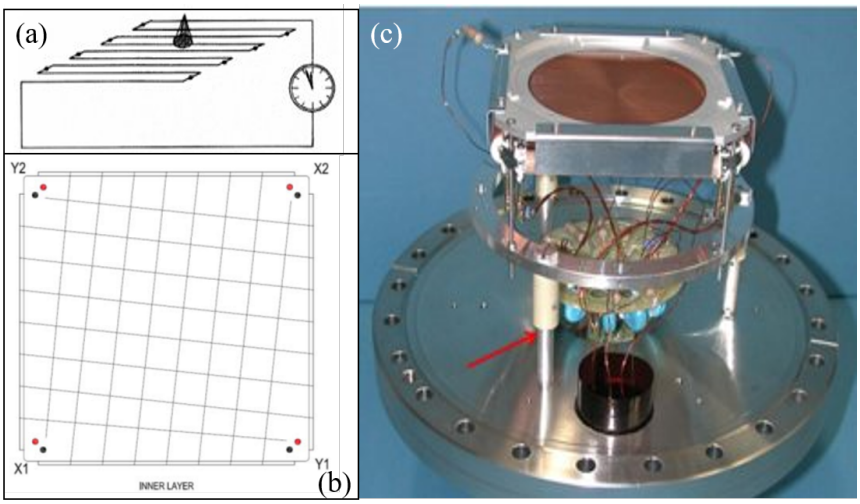

FIGURE 2.7: (a) Principle of operation of the delay line detector. (b) Rear view of the DLD showing the delay line pairs and the four terminals (X_1,X_2,Y_1,Y_2) from which the signals are sent for differential amplification using feedthroughs. (c) Mounting of the DLD on the CF200 flange. Figures (a)-(c) have been used from the Roentdek manual.

positive potential compared to the reference to ensure that the electron charge cloud is picked up by the signal, while the reference monitors the noise. Again the ends of the two pairs of delay lines are connected to the constant fraction discriminator and fast differential amplifier to remove the noise and amplify the signal. The differential signal gives the time difference between the signals reaching the two ends of the wire. It must be noted that the sum of the times taken by the signals to reach the ends of the delay lines, called the time-sum ($t_{X1} + t_{X2}$ and $t_{Y1} + t_{Y2}$), is a constant for a given length of the wire.

Molecular beam

The molecular beam was effused into the RIMS chamber using a needle valve having an orifice of diameter $\sim 250\mu$m. The needle was joined to a $1/4''$ diameter stainless steel pipe. The needle was kept very close ($\sim$ 2 mm) to the ionization region to ensure minimum divergence of the molecular beam. As a result, the laser pulses interact with the gas molecules at the centre of the molecular beam which are colder (have lesser kinetic energy) compared to those away from the axis. During experiments, the RIMS chamber pressure was maintained at a pressure of $\sim 10^{-8}$ mbar, while the gasline pressure was maintained at $\sim 10^{-1}$ mbar pressure. After adding

the liquid sample, the gasline was first evacuated to remove any residual gas, after which the RIMS chamber and the gasline were baked upto $\sim 120°$.

2.3.2 Principle of RIMS

- **TOF measurement:** The RIMS setup identifies various fragments on the basis of the time they take to reach the detector (TOF). The TOF is linearly proportional to the square root of the mass-to-charge ratio (TOF $\propto \sqrt{\frac{m}{q}}$), which means that for particles having the same charge, the lighter particles have a smaller TOF than the heavier ones. The detailed TOF derivation is discussed in ref. [74]. The principle of TOF measurement is illustrated in figure 2.8 and a typical TOF spectrum of a molecule (CH_3Cl) is shown in figure 2.9 (a). It must be noted that the space focusing condition was taken into account while designing the spectrometer, which is briefly discussed below.

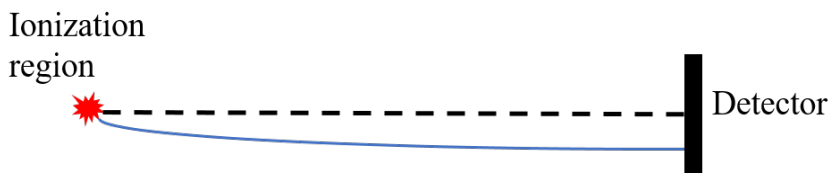

FIGURE 2.8: Principle of time-of-flight measurement in the RIMS setup.

Space focusing condition

Ideally, the TOFs of fragments having identical m/q ratio should be exactly same, given all the fragments are born along an axis in the interaction region. However, there exists a spread in the initial positions and kinetic energies of the fragments. The ions are formed in a spherical region of diameter ≤ 1 mm^3, which is responsible for the spread in their initial positions. In addition, the ions having their initial velocities directed towards the detector will have smaller TOFs compared to the ones with their initial velocities directed away from the detector. As a result, the TOF peaks have a distribution, the full-width half maximum (FWHM) of which should be minimized for better resolution. This is achieved by the space focusing condition. If Δs is the diameter of the interaction (or focal) volume, and s_0 is its center, then the ions

formed at $s_{min} = s_0 - \frac{1}{2}\Delta s$ are overtaken by those formed at $s_{max} = s_0 + \frac{1}{2}\Delta s$, since the ions formed further away from the detector gain more kinetic energy compared to the ones formed closer to the detector. Space focusing condition requires that the ions formed at s_{max} and s_{min} be focused at the detector, to minimise the difference in their TOFs, thereby ensuring an improved resolution. Our RIMS setup was designed according to the Wiley-McLaren condition[77] ($D = 2s$, where D is the length of the drift tube, and s is the length of the extraction region) to achieve the space focusing condition. The mass resolution, given by $16(s/\Delta s)^2$ [77], is 129600 for our RIMS setup. The mass resolution depends on the initial position spread which is minimized by the space focusing condition.

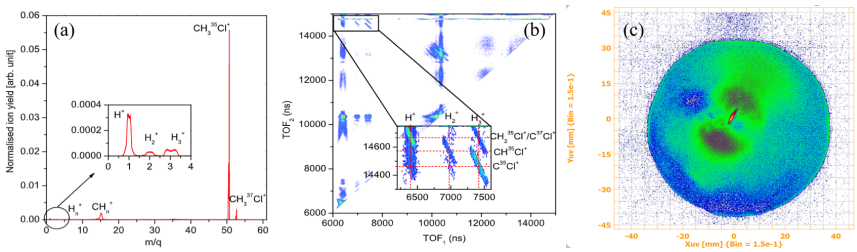

FIGURE 2.9: (a) Time-of-flight spectrum of a molecule (CH_3Cl). (b) Photoion-photoion coincidence map (CH_3Cl) showing the coincidence islands corresponding to the various fragmentation pathways. (c) x-y image of the ions arising from all dissociative pathways.

- **Coincidence detection:** As discussed above, fragments having the same m/q ratio have the same TOF. However, the same ion can arise from multiple dissociative pathways. Let us understand this with an example. The SFI and fragmentation of a polyatomic molecule, CH_3OH, leads to the formation of H^+ from the doubly ionized parent along two possible pathways:

$$CH_3OH^{2+} \longrightarrow H^+ + H_2COH \tag{2.2}$$

$$CH_3OH^{2+} \longrightarrow H^+ + CH_3O. \tag{2.3}$$

Since the H^+ ions formed along the pathways (2.2) and (2.3) are indistinguishable, both the ions have the same TOF. To distinguish between identical fragments arising from different fragmentation pathways, multi-hit coincidence

detection is performed. In this technique, the fragments formed in each fragmentation event are ordered according to their m/q or TOF and numbered as hit 1, hit 2, hit 3, etc. This is possible by the TDC8HP data acquisition card which acquires data in list-mode, as explained using the table below. The laser sync-out, having a repetition rate of 1 kHZ, serves as the trigger for the TDC8HP. Each TTL-pulse from the laser serves as the start signal for the TDC8HP, marking an ionization event (time $t = 0$). The fragments hitting the detector are the stop signals for the TDC8HP and the TOF and (x,y) information of each of the fragments/hits are recorded with respect to the start time and stored in the list-mode file. It must be noted that, the photoion-photoion coincidence is achieved under single collision condition. This means that a single laser pulse must interact with a single molecule to avoid false coincidences. This is achieved by maintaining an event rate $\sim 200 - 250$ Hz, that is one ionization event in every four laser shots (laser repetition rate is 1 kHz), by controlling the laser power, the gas pressure and the focal volume.

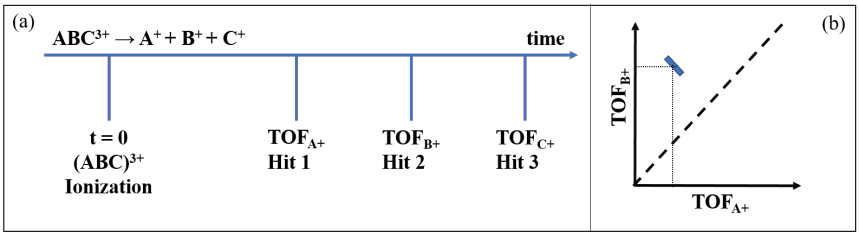

FIGURE 2.10: (a) Principle of the multi-hit TOF coincidence detection technique. (b) Photoion-photoion coincidence plot showing a coincidence island corresponding to a fragmentation pathway.

The principle of the coincidence detection technique is shown in figure 2.10. To identify the two-body fragmentation pathways, the TOF coincidence maps are obtained by plotting the TOFs of the hit 1 and hit 2 fragments, as shown in the figure. Since $\mathrm{TOF}_{\mathrm{hit1}}$ is smaller than $\mathrm{TOF}_{\mathrm{hit2}}$, all dissociation events must lie above the 45° dashed line shown in figure 2.10 (b). Anti-correlated fragments arising from the same parent molecule by two-body breakup will form an island (blue box) inclined at $-45°$, indicating their back-to-back ejection with identical momenta. In case of three- or multi-body fragmentation,

the dissociation is complex and TOF coincidence plots must be obtained between the successive hits (that is, TOF_{hit1} vs TOF_{hit2}, TOF_{hit2} vs TOF_{hit3}, and so on). The shape of the coincidence islands contain information about the fragmentation dynamics [78]. A photoion-photoion coincidence plot of CH_3Cl is shown in figure 2.9 (b).

TABLE 2.2: Data acquisition in list-mode by the TDC8HP.

Event number	Hit 1	Hit 2	Hit 3	...
1	$(TOF,x,y)_{1,1}$	$(TOF,x,y)_{1,2}$	$(TOF,x,y)_{1,3}$	...
2	$(TOF,x,y)_{2,1}$	$(TOF,x,y)_{2,2}$	$(TOF,x,y)_{2,3}$	...
...	...	...	...	...
1000	$(TOF,x,y)_{1000,1}$	$(TOF,x,y)_{1000,2}$	$(TOF,x,y)_{1000,3}$	...
1001	$(TOF,x,y)_{1001,1}$	$(TOF,x,y)_{1001,2}$	$(TOF,x,y)_{1001,3}$	...
1002	$(TOF,x,y)_{1002,1}$	$(TOF,x,y)_{1002,2}$	$(TOF,x,y)_{1002,3}$	...
...	...	...	...	...

- **Momentum imaging:** Once the TOF and (x,y) coordinates (an X-Y image of the ions formed by the photodissociation of CH_3Cl ions is shown in figure 2.9 (c)) of each fragment in a dissociation pathway are recorded, a fragmentation pathway is selected from the TOF coincidence map by applying conditions on the TOFs of the fragments. Next, using the TOF and position coordinates of each fragment in the island, the three-dimensional momentum information can be obtained using the formulae:

$$p_x = \frac{m.x}{TOF}, \quad p_y = \frac{m.y}{TOF}, \quad p_z = q.E.(TOF - t_0), \tag{2.4}$$

where p_x, p_y, p_z are the momentum components of each fragment, m and q are the mass and charge of the fragment, E is the electric field, and t_0 is the TOF of the fragments ejected with zero kinetic energy. Here, p_z is the longitudinal component ($p_{||}$) of the fragment momentum, while $\sqrt{p_x^2 + p_y^2}$ is the transverse component ($p_\perp$) of momentum.

From the 3D momentum information, we obtain the kinetic energy of the individual fragments in a pathway by

$$E_{hit1} = \frac{p_x^2 + p_y^2 + p_z^2}{2.m}. \tag{2.5}$$

Similarly, the kinetic energies of all fragments can be obtained from their corresponding momentum information. Finally, the sum of the kinetic energies of the individual fragments in the pathway, termed the total kinetic energy release (KER) distribution is obtained by

$$(KER = E_{hit1} + E_{hit2} + E_{hit3} + ...). \tag{2.6}$$

Additionally, the angular distribution (θ) of each fragment is obtained using the relation

$$\theta = cos^{-1}\left(\frac{p_y}{p_\perp}\right), \tag{2.7}$$

where θ is the angle between the fragment momentum vector and the polarization direction. In our studies, the polarization was kept parallel to the plane of the detector, therefore, the longitudinal momentum component (p_z) was not considered in the momentum vector while calculating the angular distribution of the fragments.

2.3.3 Data acquisition and data analysis

Data acquisition is performed by the TDC8HP card to which we send six timing (NIM) signals. First, the TDC8HP is triggered by the laser sync-out which is sent to channel 8 of the card. Next, the NIM of the MCP signal is sent to channel 7 of the card which gives the TOF information. Finally, four NIM signals (corresponding to X1, X2, Y1, Y2) from the DLD are sent to channels 1 to 4 of the card for position information. The data acquisition rate of TDC8HP is 1 kHZ, which is identical to the laser repetition rate. To reduce the false coincidences, single collision condition was maintained throughout the measurements. This low event rate is obtained by controlling the laser power, gas pressure, and the focal volume. The COmputer Based Online offline Listmode Dataanalyzer or COBOLD PC software (which is a C++ program) was used for both data acquisition (DAQ) and data analysis (DAN). For offline data analysis, the COBOLD PC program was used to analyze the data stored in the list-mode files (.lmf).

2.4 Velocity Map Imaging Mass Spectrometer (VMI-MS)

The strong-field ionization experiment discussed in chapter 3 was performed in our in-house developed thick-lens Velocity Map Imaging (VMI) mass spectrometer [79], which is discussed in detail in ref. [74]. Here, we shall only briefly discuss the VMI spectrometer. The VMI-MS can be operated in two modes – (i) the TOF mode, in which a uniform electric field is applied, and (ii) the lensing mode, in which a non-uniform field is applied to form an electrostatic lens and focus the charged particles on to the detector. In the experiments discussed in this thesis, the VMI was operated in the TOF mode only, so we shall not discuss the lensing (imaging) mode. The setup consists of a VMI chamber and a supersonic jet chamber. The VMI chamber is maintained at ultrahigh vacuum $\sim 10^{-8}$ mbar, while the supersonic jet chamber is maintained at a pressure of $\sim 10^{-5}$ mbar during operating conditions.

The VMI chamber houses the spectrometer assembly, consisting of eleven electrodes. The first electrode is a circular plate, called the repeller, followed by nine electrodes/annular rings (extractors), and finally, a drift tube. The interaction of the molecular beam with the laser pulses takes place at right angles between the repeller and the first extraction plates. In the TOF mode, a uniform electric field of 100 V/cm is maintained. An MCP (40 mm, Roentdek) is placed at the end of the drift tube for recording the TOF information of the ions/electrons, followed by a phosphor screen for recording the 2D ion/electron images. In the experiment discussed in this thesis, the VMI was operated in the TOF mode only to obtain the ion TOFs. The TOF measurement technique using the MCP has been discussed in detail in the previous section.

The supersonic jet chamber is connected to the VMI chamber via a manual gate valve on one end. On the other end, the chamber is connected to an Amsterdam Cantilever Piezo Valve (ACPV2 200μm diameter nozzle) and a skimmer of orifice diameter $\sim$ 900μm. The pulsed molecular beam (repetition rate of 1 kHz) produced by the valve enters the chamber after supersonic expansion, leading to the cooling of the gas to temperatures $<$ 1 K. Performing experiments with cold gas helps to

reduce the initial energy distribution of the molecules, thereby improving the mass resolution of the spectrometer.

The strong-field ionization of the molecules produces positively-charged ions and negatively-charged electrons. In the VMI-MS, either the ions or the electrons can be detected at a time. The data acquisition and analysis are performed using the TDC8HP card and the COBOLD PC software, the details of which have already been discussed in the previous section. In the next few chapters, we shall discuss the experimental results.

Chapter 3

Strong-field ionization of polyatomic molecules: formation of H_n^+ (n = 1-3) ions

In this chapter, we have investigated the SFI of polyatomic molecules. First, we have experimentally obtained the single ionization rate of a molecule (CH_3Cl) as a function of laser intensity and further, fitted it with the results obtained using MO-ADK model. Next, we have obtained the yield of H_n^+ (n = 1-3) ions from all possible dissociation pathways of the ionized parent molecules and investigated the control of the H_n^+ yield using the laser parameters like intensity, chirp, wavelength, and polarization.

Hydrocarbons have been used as a prototype for studying geometrical deformation and structural changes in molecules for several decades [55, 80–86]. Such changes in molecules in their excited and ionized states give rise to processes like bond-breaking[87, 88], intramolecular migration of moieties[89–91], isomerization[55, 92], and bond association[93, 94], prior to the dissociation or Coulomb explosion of the molecular ion. Intramolecular proton migration and bond formation phenomena have been a topic of interest to researchers for a long time due to their importance in many physical[95], chemical[96], and biological[89] processes. The dissociation of hydrocarbons initiated by ionizing sources like electrons[97, 98], ions[99–101], or laser pulses[85, 96], and the detection of H_2^+ and H_3^+ ions have confirmed the fact that bond-breaking, intramolecular migration, and bond association occur before

the fragmentation of unstable molecular ions.

The formation of H_2^+ and H_3^+ ions during the photodissociation of polyatomic molecules is ubiquitous and of much importance [84, 102]. Both singly [97, 103] and doubly ionized methanol [84, 85, 94, 104, 105] have been shown to exhibit intramolecular H migration, and H_n^+ (n =2,3) formation. Some of the possible pathways leading to H_2^+, H_3^+ formation from singly and doubly ionized methanol are:

$$CH_3OH^+ \Longrightarrow HCHO + H_2^+ \tag{3.1}$$

$$CH_3OH^+ \Longrightarrow HCO + H_3^+ \tag{3.2}$$

$$CH_3OH^{2+} \Longrightarrow HCOH^+ + H_2^+ \tag{3.3}$$

$$CH_3OH^{2+} \Longrightarrow CH_2O^+ + H_2^+ \tag{3.4}$$

$$CH_3OH^{2+} \Longrightarrow COH^+ + H_3^+ \tag{3.5}$$

$$CH_3OH^{2+} \Longrightarrow H_2CO^+ + H_2^+ \tag{3.6}$$

$$CH_3OH^{2+} \Longrightarrow HCO^+ + H_3^+ \tag{3.7}$$

$$CH_3OH^{2+} \Longrightarrow H + H_2^+ + COH^+ \tag{3.8}$$

$$CH_3OH^{2+} \Longrightarrow H + H_3^+ + CO^+ \tag{3.9}$$

While eqns. 3.1-3.7 are two-body fragmentation channels, eqns. 3.8 and 3.9 are three-body breakup channels. Ekanayake et al. showed that the H_3^+ formation from doubly ionized CH_3OH can proceed in two ways and they also obtained the relative yield of these two pathways [85]. By performing time-resolved ionization of CH_3OH, its isotopomers, ethylene glycol, and acetone, and detecting the photoions in each dissociation pathway in coincidence, they exhibited that the first step is the formation of a neutral H_2 molecule, which roams in the vicinity of the $CHOH^+$ ion. In the second step, the neutral H_2 either extracts a proton from the C or the O atom. Using ab-initio molecular dynamics (AIMD) simulations, it was shown that the timescale of H_3^+ formation is $\sim$ 100 fs, which has also been reported in the refs. [106, 107]. They further determined that the relative yield of H_3^+ from the two pathways (the first pathway represents H_3^+ formation by the association of three H atoms attached to C, while the second pathway represents H_3^+ formation by the association

of two H atoms attached to C and one attached to O) is 10 : 1. H_3^+ formation by H_2 roaming mechanism using AIMD simulations has also been reported in other studies [83, 85, 108–112]. On the other hand, H_2^+ is formed by a long-range electron transfer from the neutral H_2 to the parent dication by a process known as "inverse harpooning" [108]. Ando et al. used a 6 fs pulse pair with a delay ranging from -2 fs to 500 fs to investigate the CH_3OH^+ vibrational wavepacket by projecting it onto the dication PES and measuring the H_3^+ yield as function of the pump-probe delay [111]. The ion yield oscillations have a period of $\sim$ 38 fs, which was ascribed to the vibrational frequency of the CO bond stretching mode of the CH_3OH^+ ground state.

In order to confirm that H_2^+ and H_3^+ are formed both along migration and non-migration pathways, the photodissociation of deuterated isotopomer of CH_3OH is performed [85, 111]. In our study we used the isotopomer CD_3OH to confirm intramolecular H migration during the photodissociation of methanol. The two-body dissociation channels of doubly ionised CD_3OH yielding H_nD_m (n =0-1, m =0-3) as one of the dissociation products include:

$$CD_3OH^{2+} \Longrightarrow CD_3O^+ + H^+ \tag{3.10}$$

$$CD_3OH^{2+} \Longrightarrow D_2CO^+ + DH^+ \tag{3.11}$$

$$CD_3OH^{2+} \Longrightarrow CDOH^+ + D_2^+ \tag{3.12}$$

$$CD_3OH^{2+} \Longrightarrow DCO^+ + D_2H^+ \tag{3.13}$$

$$CD_3OH^{2+} \Longrightarrow COH^+ + D_3^+ \tag{3.14}$$

The fragments DH^+ and D_2H^+ can only be formed by the migration and bond association processes before dissociation of the parent ion, which confirms intramolecular H-migration in methanol. While these migration products were observed in refs. [84, 85, 111], De et al. reported H_3^+ formation by bond formation between the H atoms in the methyl group only, and did not observe any H migration between the methyl and hydroxyl groups during the dissociation of CH_3OH^{2+} induced by collision with Ar^{8+} ions [113].

Further, we have investigated the SFI and H_n^+ formation from CH_3Cl. The dissociation of CH_3Cl ions has been studied extensively using ion bombardment [114, 115], synchrotron radiation [116–119], and femtosecond lasers [120–122]. H_n^+ (n =2,3) and HCl^+ formation during the photodissociation of CH_3Cl is of particular interest since they require the breakup of bonds, intramolecular proton migration, and association. In this chapter, we shall focus on the control of H_n^+ yield from ionized CH_3OH, CD_3OH and CH_3Cl molecules. Various laser parameters like intensity (1.5 W/cm^2 - 12.5 W/cm^2), chirp (0 fs^2 and 5330 fs^2), wavelength (800 nm and 1300 nm), and polarization (linear and circular) were found to serve as a control for hydrogen migration and the yield of H_n^+ (n=1-3) ions in this study.

3.1 Experimental methodology

Photoionization experiments of CH_3OH and CD_3OH were performed using 800 nm, 29 fs, 1 kHz, 1.5 mJ laser pulses in the VMI-MS. At the same time, laser pulses of 6 mJ energy were used to pump an optical parametric amplifier (OPA) which allows wavelength tunability from 1300 nm to 1600 nm for signal, and 1661 nm to 2185 nm for idler beams. Of these, we used the 1300 nm pulses from the OPA to perform wavelength-dependent studies on CH_3OH. The description of the VMI-MS is given in the previous chapter. The pulses were focused at the ionization region using a 2-inch concave mirror of focal length $= -10$ cm. Methanol (CH_3OH) and methanol-D3 (CD_3OH) samples, having a purity of 99.8% from Sigma Aldrich were used without any further purification. Helium was used as a carrier gas. The cold molecular beam was first introduced into the gas chamber using an Amsterdam Cantilever Piezo Valve (ACPV2, 200 μm diameter nozzle) and a skimmer having an orifice of 900 μm. The piezo valve opening time was set to 40 μs during measurements. The gas-line pressure was kept at 4 bars while, the pressure in the VMI chamber was 2×10^{-7} mbar in the presence of molecular beam and 6 x 10^{-9} mbar without the molecular beam.

The photoionization experiment of CH_3Cl was performed in the RIMS setup. A 2-inch concave mirror (effective focal length = -10 cm, Newport) mounted inside the RIMS chamber was used to focus the pulses on the molecular beam at the ionization region. The description of the RIMS setup is given in chapter 2. CH_3Cl (Sigma Aldrich, purity of $\geq$ 99.5%) in gas-phase was effused into the RIMS chamber using a needle having an orifice diameter of 250 μm. The RIMS chamber pressure was maintained at $\sim 9 \times 10^{-8}$ Torr at room temperature during operating conditions.

In all the experiments, the femtosecond pulse characterization was performed using the commercial SPIDER setup from APE Germany (model: FC-SPIDER), as discussed in the previous chapter. The measured pulse duration of the fundamental 800 nm pulses was 29 fs. Further, we used SF11 windows of different thicknesses to stretch the laser pulses to different durations and study its influence on the H_n^+

yield. Characterization of the stretched pulses after passing through the SF11 windows was also performed by SPIDER. The pulse duration in each case has been summarized in columns 1 and 2 of table 3.3. The beam diameters at the focus for the 800 and 1300 nm beams were measured to be 38 μm and 42 μm, respectively, using the Beamage-4M, Gentec-EO. The intensity of the beam was estimated using the average power, pulse duration, and spot size. During the experiments, the event rate was maintained around 200-250 Hz, which is essential for avoiding false coincidences and space charge effect. The schematic diagrams of the VMI setup is shown in figure 3.1, while that in the RIMS setup is shown in figure 3.2.

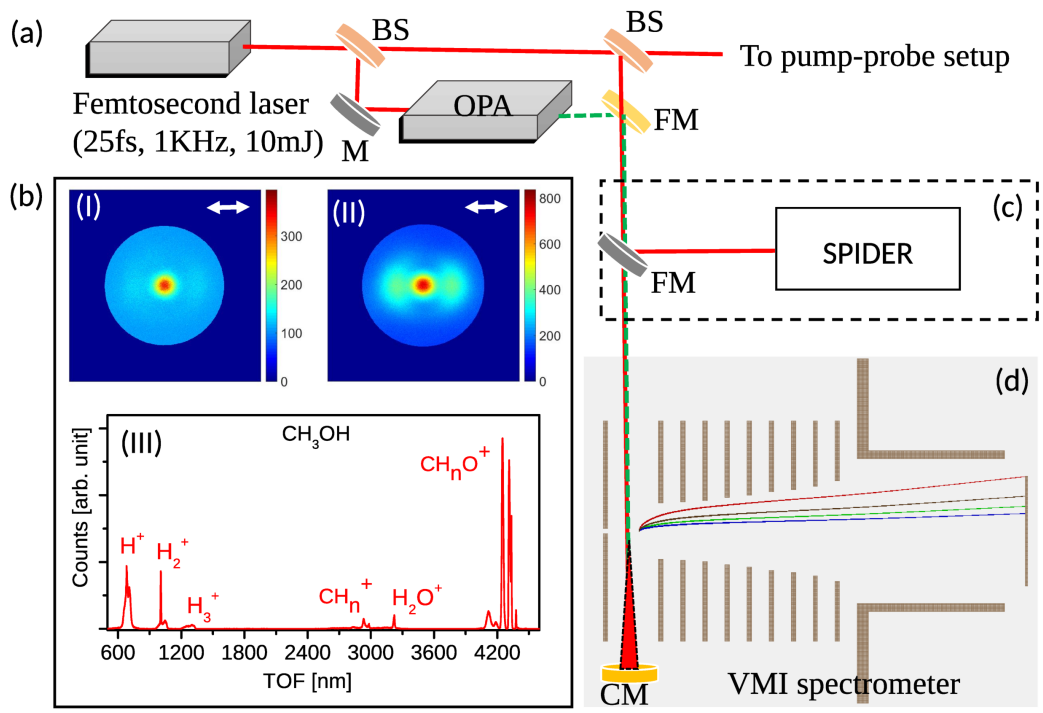

FIGURE 3.1: (a) Schematic diagram of the experimental setup. This setup has been used for photo-ionization experiments with femtosecond laser's 800 nm and OPA's 1300 nm pulses. (b) (I) and (II) show the H_n^+ (n= 1 - 3) ions VMI images for 800 nm, 29 fs and 195 fs pulses, respectively, (III) shows the time-of-flight (TOF) mass spectrum recorded for methanol, (c) pulse characterization using SPIDER, and (d) multi-plate velocity map imaging spectrometer. The VMI images are shown here to demonstrate the working of the VMI in the imaging mode. (BS = beam splitter, OPA = optical parametric amplifier, FM = flip mirror, CM = concave mirror, M = mirror)

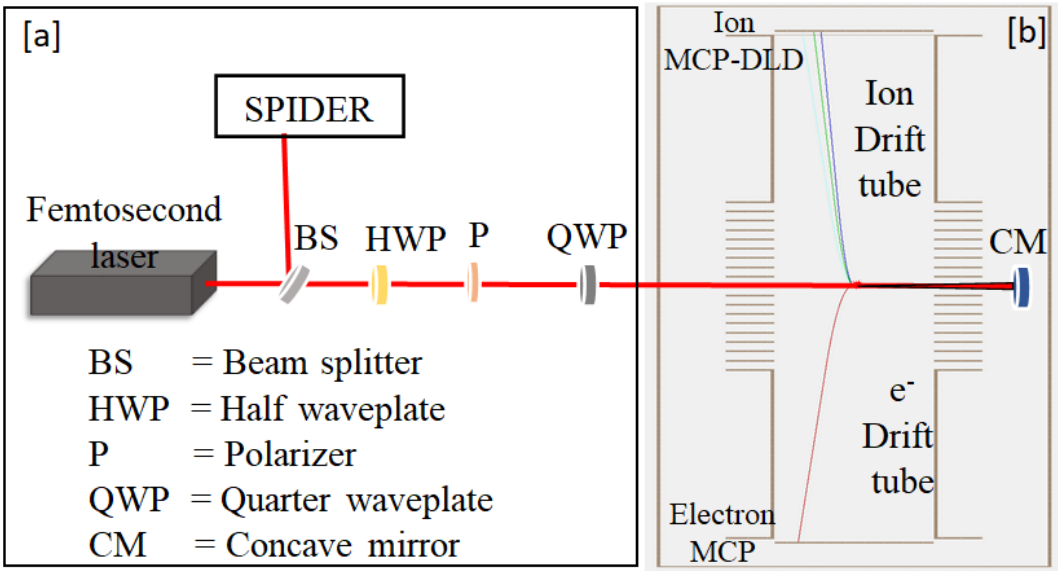

FIGURE 3.2: Schematic diagram of the experimental setup and the femtosecond pulse characterization (SPIDER) unit.

3.2 Theoretical Methodology

The theoretical ionization rate of CH_3Cl^+ was obtained using the molecular Ammosov-Delone-Krainov (MO-ADK) theory and compared with experimental results. A detail of this theory is given in [35, 38]. Here, we briefly introduce the essential equations used for getting the theoretical ionization rate. Assuming the molecular axis to be aligned parallel to the external field, the rate of tunnelling ionization for a molecule can be expressed as [35, 38, 123]:

$$\omega_{MO-ADK}(F,0) = \frac{B^2(m)}{2^{|m|}|m|!}\frac{1}{\kappa^{\frac{2Z_c}{\kappa-1}}}\left(\frac{2\kappa^3}{F}\right)^{\frac{2Z_c}{\kappa-|m|-1}} \times \exp\left(\frac{-2\kappa^3}{3F}\right) \tag{3.15}$$

where,

$$B(m) = \sum_l C_l Q(l,m), \tag{3.16}$$

F is the laser field strength, l is the azimuthal quantum number, m is magnetic quantum number along the molecular axis, Z_c is the effective Coulomb charge, and

$\kappa = \sqrt{I_p}$ where I_p denotes the ionization potential for the given valence orbital. C_l is the structure co-efficient for the valence orbital whose values are tabulated in Table 3.1 [124].

For an arbitrary alignment **R** of the molecular axis with respect to the laser field, B(m) can be expressed as:

$$B(m') = \sum_l C_l D^l_{m',m}(\mathbf{R}) Q(l,m) \tag{3.17}$$

where, $D^l_{m',m}(\mathbf{R})$ is the rotation matrix, and **R** represents the Euler angles between the molecular axis and the laser field direction. Therefore, the ionization rate in a static field is given by [35, 38, 123]:

$$\omega_{MO-ADK}(F,\mathbf{R}) = \sum_{m'} \frac{B^2(m')}{2^{|m'|}|m'|!} \frac{1}{\kappa^{\frac{2Z_c}{\kappa-1}}} \left(\frac{2\kappa^3}{F}\right)^{\frac{2Z_c}{\kappa-|m'|-1}} \times \exp\left(\frac{-2\kappa^3}{3F}\right) \tag{3.18}$$

In a pulsed laser field, the electric field has the form of:

$$F(\mathbf{t},r,z) = F_0 \exp\left(-2ln2\,t^2/\tau^2\right) \exp\left(-2ln2\,r^2/W(z)^2\right) \tag{3.19}$$

where, F_0 is the laser field peak strength and τ is the FWHM of the pulse. W(z) is given by $w_0\sqrt{(}1+z^2/z_R^2)$, where w_0 is the beam spot size and z_R is the Rayleigh range, is given by $\pi w_0^2/\lambda$. λ is laser wavelength. Ionisation rate is given by the following equation:

$$P(F,\mathbf{R}) = 1 - \exp\int w(F,\mathbf{R})dt \tag{3.20}$$

Theoretical ionization rate is obtained using the in-house developed program in MATLAB. The laser electric field strength was calculated from the experimental intensities value varying from 1.4×10^{13} to 24.2×10^{13} W/cm^2. The focal volume averaging was taken into account by integrating over the spatial components (i.e.,

TABLE 3.1: C_{lm} structure coefficients for HOMO orbital of CH_3Cl used in theoretical model from Ref.[124] is given below.

Molecule	I_p(eV)	$C_{1\pm1}$	$C_{2\pm1}$	$C_{2\pm2}$
CH_3Cl (HOMO1)	11.3	0.58i	1.72i	0.21
		$C_{3\pm1}$	$C_{3\pm2}$	$C_{4\pm1}$
		-0.36i	-0.27	0.54i
		$C_{4\pm2}$	$C_{5\pm1}$	$C_{5\pm2}$
		0.24	-0.13i	0.17
		$C_{6\pm1}$	$C_{6\pm2}$	
		0.06i	0.09	

integrating over r and z). The r was integrated from -45μm to 45 μm, and z was integrated over 0 to z_R. The measured w_0 was 19 μm. The Rayleigh range for this case was calculated to be 1.42 mm. The ionization rate was calculated using eqn. 3.20 integrating over 't' from -29 fs to 29 fs. The obtained MO-ADK curve is discussed in the results section.

3.3 Results and discussion

Firstly, we have investigated the effect of laser intensity on the strong-field single ionization rate of CH_3Cl by varying the intensity from 1.6×10^{13} W/cm^2 to 2.4×10^{14} W/cm^2, while keeping all other parameters constant. Figure 3.3 shows the experimental (blue) intensity-dependent yield of CH_3Cl cations compared with the ionization rate predicted by the MO-ADK theory (red). It can be seen from the figure that as the intensity is increased from 1.6×10^{13} W/cm^2 to 8×10^{13} W/cm^2, the yield of CH_3Cl cations increases monotonically. At these moderate intensities, ionization of the molecule takes place in the MPI regime (Keldysh parameter $\gamma > 1$) [24] by the absorption of multiple photons. In this regime, the rate of single ionization of CH_3Cl is higher than that of double or triple ionization. As the intensity is increased, the single ionization rate increases monotonically and then saturates at intensities beyond 1.2×10^{14} W/cm^2 (in agreement with Grugan et al. [122]). This saturation intensity I_{sat}, which can be attributed to the depletion of ground states at high intensities [125], depends on the ionization potential (I_p) of the molecule. For the photoionization of CH_3Cl ($I_p = 11.28$ eV), saturation in the ionization rate occurs at intensities above 1.2×10^{14} W/cm^2, which lie in the tunneling regime ($\gamma < 1$). Although the single ionization rate saturates in this regime, the tunnel electron recollision produces highly charged states (2+, 3+, 4+, etc.) of CH_3Cl. The ionization rate predicted by the MO-ADK theory (red curve) scaled with a factor of 0.12 agrees well with the experimental result at high intensities (above 1×10^{14} W/cm^2), but shows some deviation at low intensities (MPI regime). Since the MO-ADK theory gives us the tunnelling ionization rate, the theory breaks down in the low-intensity multiphoton absorption regime, which explains the deviation. Tong et al.[38] have reported a similar discrepancy between the ionization rates of SO molecule obtained experimentally and using MO-ADK theory at low intensities.

Next, we focus on the influence of various laser parameters on the formation of H_n^+ (n =1-3) ions along all possible dissociative channels of the ionized (1+, 2+, 3+, ...) molecules.

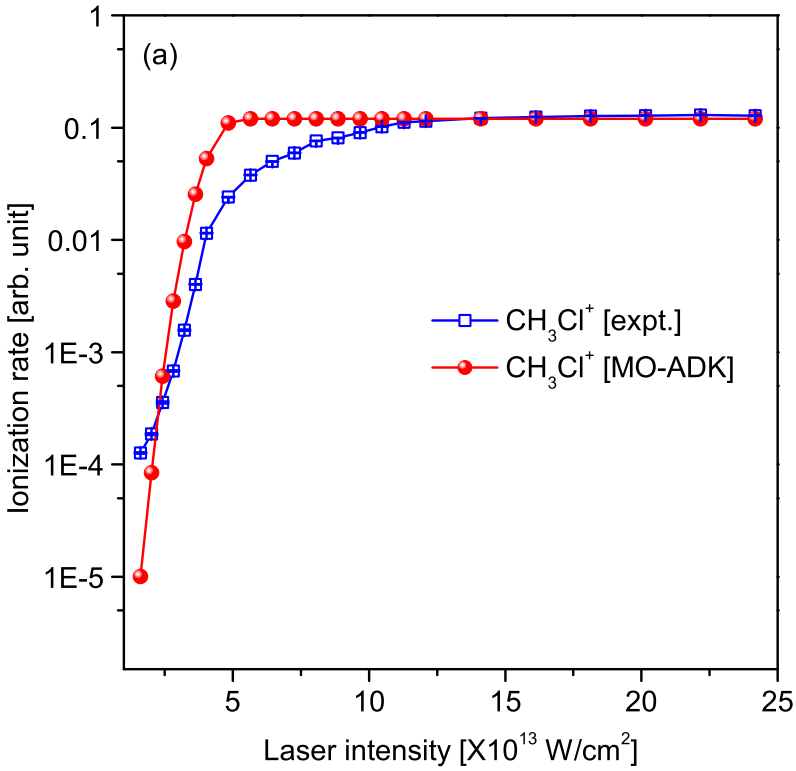

FIGURE 3.3: Intensity-dependent yield of CH_3Cl cations obtained experimentally (red) and using the MO-ADK model (blue). In the experimental curve, the maximum error is 2%. The ions yield was normalized by the total counts of all ions in each TOF spectrum.

3.3.1 H_n^+ (n=1-3) ions formation: intensity dependence

We first investigate the effect of laser intensity on the yield of H^+, H_2^+, and H_3^+ ions during the fragmentation of ionized CH_3OH. Figures 3.4 (a)-(c) compare the TOF spectra recorded for the photoionization of CH_3OH molecules with 800 nm, 29 fs, and linearly polarized (parallel to the plane of the MCP-phosphor detector) pulses of intensities (a) 1.5×10^{13} W/cm^2, (b) 3.9×10^{13} W/cm^2, and (c) 5.7×10^{13} W/cm^2, respectively. It is evident that in the first case (a), the TOF spectrum is dominated by the singly ionized CH_3OH peak, and the yield of fragments is nearly negligible. On increasing the intensity, the singly ionized parent yield decreases gradually until it is completely suppressed at the highest intensity (c), with a simultaneous enhancement in the fragment yield. At the intermediate intensity (b), H_n^+ (n =1-3) and CH_nO^+ (n =0-4) yields are nearly comparable, while at the maximum intensity (c) the TOF spectrum is dominated by the H_n^+ yield.

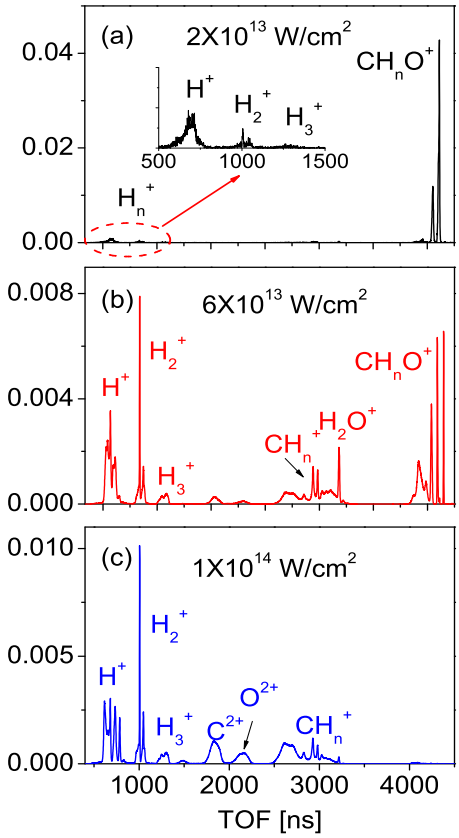

FIGURE 3.4: Time-of-flight spectrum of CH_3OH recorded at three different laser intensities, for 29 fs, 800 nm, and linearly polarized (parallel to the plane of the MCP-phosphor detector) light pulses. Laser intensities in the three cases were (a) 2×10^{13} W/cm^2, (b) 6×10^{13} W/cm^2, and (c) 1×10^{14} W/cm^2. The y-axis represents the normalized counts. Normalization was done by the total counts ((a) 5.8×10^4, (b) 1.1×10^6, and (c) 1.3×10^6) recorded in each spectrum. The yields of CH_nO^+ (n=0,4) are very low and are only visible in the logarithmic scale.

As already discussed in chapter 1, the ionization rate of a molecule (or atom) is a function of the laser field strength, frequency, and I_p. For CH_3OH (I_p = 10.829 eV), the Keldysh parameter $\gamma > 1$ at the intensity 2×10^{13} W/cm^2 (figure 3.4 (a)), which indicates that MPI is the dominant ionization mechanism here. CH_3OH is singly ionized by the absorption of multiple photons from the field, and the single electron is removed primarily from the HOMO orbital. The resulting CH_3OH^+ ion is produced in the ground state which is highly stable and hence, does not fragment much. This explains the high yield of the CH_3OH cations, with a very small yield of dissociation fragments.

As the intensity increases and approaches the limit $\gamma \approx 1$ (figure 3.4 (b)), tunneling ionization comes into play, in addition to MPI. In this intermediate regime, the ionization of molecules increases, producing doubly-charged ions. The CH_3OH^{2+} ions are primarily unstable indicated by a negligible yield of the dications. Therefore, in this regime fragmentation of CH_3OH^{2+} results in an increased yield of fragments, as seen in the figure. As a result, the H_n^+ yield is now comparable to that of the CH_3OH^+ ions.

For intensities $\sim 10^{14}$ W/cm^2 (figure 3.4 (c)), the ionization of CH_3OH takes place purely by tunneling ($\gamma < 1$), and ionization process dominates over dissociation. Furthermore, the ionization rate as a function of the internuclear separation has been studied in diatomic molecules H_2^+ [46], I_2 [126], HeH^{2+} [127], which revealed that at high intensities $\sim 10^{14}$ W/cm^2, the ionization rate is greatly enhanced as the internuclear separations reach values larger than that at equilibrium. This process known as charge-resonance-enhanced ionization (CREI) [46, 128, 129] was first discovered theoretically in H_2^+ by Bandrauk et al [46]. CREI was ascribed to (i) the presence of charge resonant (CR) states in molecules which are coupled by the laser field leading to population transfer to the higher charge state, and (ii) the sum of the coulomb fields of the constituent atoms and the laser field alters at intermediate internuclear separations, thus causing the upper field-induced state to ionize [46]. CREI has applications in increasing the molecular high-harmonic generation (MHHG) bandwidth and increase the harmonic cut-off [130–133].

Therefore, in this high-intensity regime, it is expected that multiply-charged CH_3OH molecules are produced mainly by CREI. First the molecules are stripped of one or two electrons by the field. On reaching a repulsive state, the internuclear separation starts increasing along one of the bonds and the ion starts to dissociate, until a critical internuclear separation (R_c) is reached. At this point, the ionization rate is greatly enhanced leading to the absorption of more photons and multiple electrons are removed thereby, producing highly charged states (+4, +5, etc). These multiply-charged states are highly unstable and they dissociate rapidly. This is confirmed by the large yield of smaller fragments like H_n^+ and doubly charged fragments like C^{2+} and O^{2+}, while the larger ions like CH_nO^+ (n =0-4) are totally suppressed (figure 3.4 (c)).

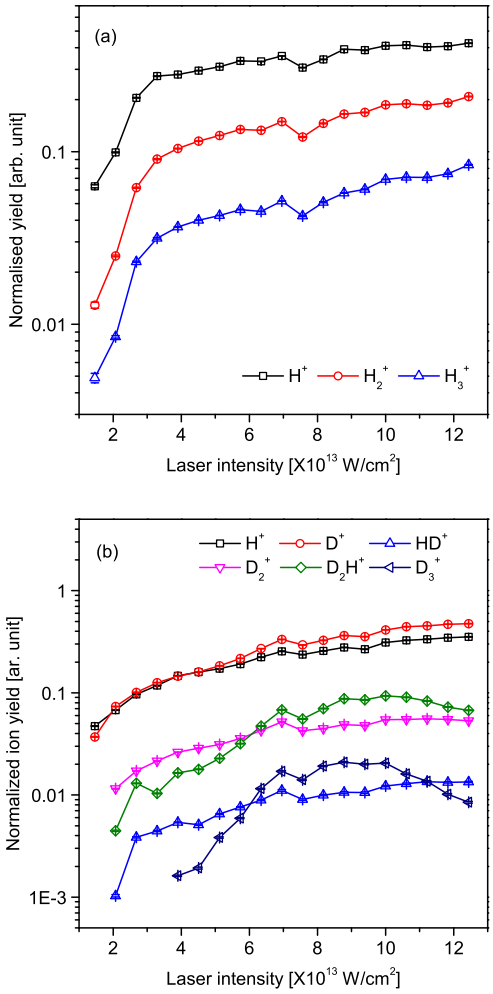

FIGURE 3.5: (a) Normalised H_n^+ (n=1-3) ion yield as a function of laser intensity for CH_3OH (maximum error is 7%). (b) Normalised yield of H^+, D^+, HD^+, D_2^+, D_2H^+, and D_3^+ as a function of laser intensity for the photodissociation of CD_3OH by linearly polarized pulses (maximum error is 3%). The laser parameters such as pulse duration (29 fs), wavelength (800 nm), and VMI spectrometer voltages were kept constant during the measurements. Normalisation in all the cases has been done by the total ions yield.

We next show the intensity-dependent yield of the H_n^+ (n =1-3) ions resulting from the photodissociation of ionized (1+, 2+, 3+,...) CH_3OH, as shown in figure 3.5 (a). The x-axis shows the laser intensity ranging from 1.5×10^{13} W/cm^2 to 1.2×10^{14} W/cm^2, while the y-axis shows the H_n^+ ion yield (calculated by integrating the counts under the TOF peaks of the H_n^+ ions) normalised by the total ion yield recorded in each TOF spectrum at each intensity. As seen in the figure, the H_n^+ yield

is low at low intensities. As discussed before, in the low-intensity MPI regime, single ionization of the parent molecule is dominant and the resulting CH_3OH^+ ions are highly stable in nature. Only a very few ions populate the excited states of the CH_3OH cation or are doubly ionized by absorbing excess number of photons. These ions are unstable and undergo fragmentation. This explains the low yield of the H_n^+ ions in the low-intensity regime. On increasing the intensity to very high values, more molecules are doubly, triply or multiply ionized due to tunnel electron recollision with the ionic core or due to CREI. As a result, the rate of fragmentation increases, thereby increasing the H_n^+ yield along various dissociative pathways.

To verify whether the H_2^+, H_3^+ formation takes place by the migration pathway (intramolecular H migration from C to O) in addition to the non-migration pathway, we studied the photodissociation of deuterated isotopomer of methanol (CD_3OH) and obtained the intensity-dependent (intensities ranging from 1.5×10^{13} W/cm^2 to 1.2×10^{14} W/cm^2) yield of H^+, D^+, HD^+, D_2^+, D_2H^+, and D_3^+ ions, as shown in figure 3.5 (b). Firstly, the formation of DH^+ and D_2H^+ ions is possible only by intramolecular H migration thereby, confirming that H_2^+ and H_3^+ ions are not only formed by bond formation between the H atoms in the methyl group, but also by H (or H_2) migration between C and O atoms followed by bond formation. While the yield of H^+, D^+, HD^+, and D_2^+ ions have an increasing trend similar to that seen in CH_3OH (figure 3.5 (a)), the yield of D_2H^+ and D_3^+ initially show an increasing trend, and then decreases at very high intensities (beyond 10^{14} W/cm^2). This observation may be attributed to the fact that the precursor states which contribute to the formation of D_2H^+ and D_3^+ ions have long dissociation times, due to which the ion undergoes further (enhanced) ionization to higher charge states before it can dissociate.

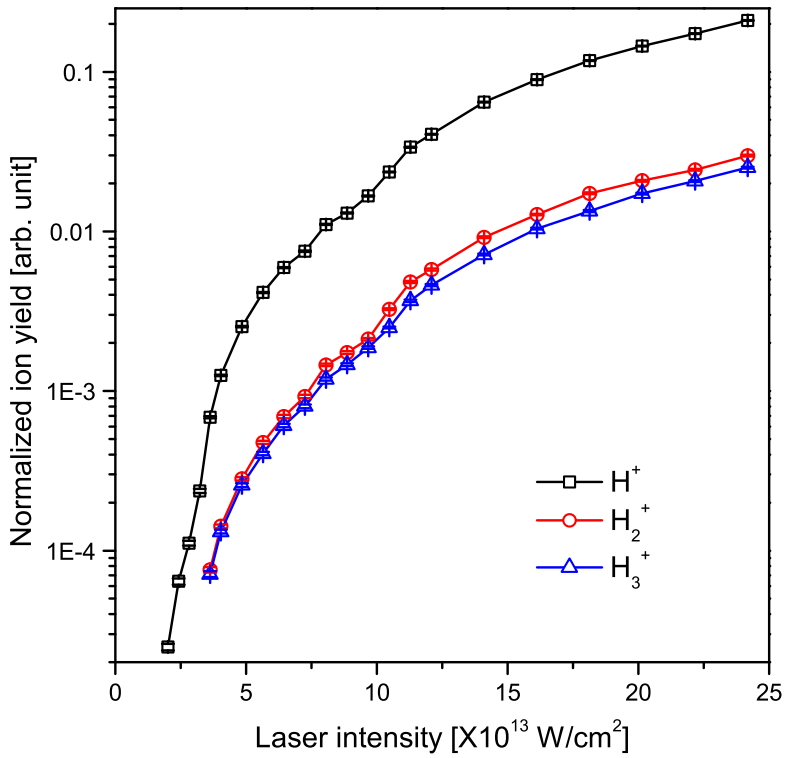

FIGURE 3.6: Intensity-dependent yield of H_n^+ (n =1-3) ions (maximum error is 5% for H^+, and 4% for H_2^+ and H_3^+) from the photoionization of CH_3Cl obtained with 29 fs, 800 nm, and linearly polarized pulses. The ions yield were normalized by the total counts of all ions in each TOF spectrum.

Figure 3.6 shows the intensity-dependent yield of H_n^+ ions formed by the photodissociation of CH_3Cl induced by 29 fs, 800 nm, linearly polarized pulses, for intensities ranging from 2×10^{13} to 2.5×10^{14} W/cm^2. The plot shows a similar trend as seen in CH_3OH and CD_3OH, which can be explained as above. Hence, these results suggest that the laser intensity affects the SFI (single, double or multiple) of the molecules, the subsequent ultrafast excited-state dynamics of the parent ion and its dissociation along pathways forming H_n^+ (n =1-3) ions as one of the fragments.

3.3.2 H_n^+ (n=1-3) formation: pulse duration dependence

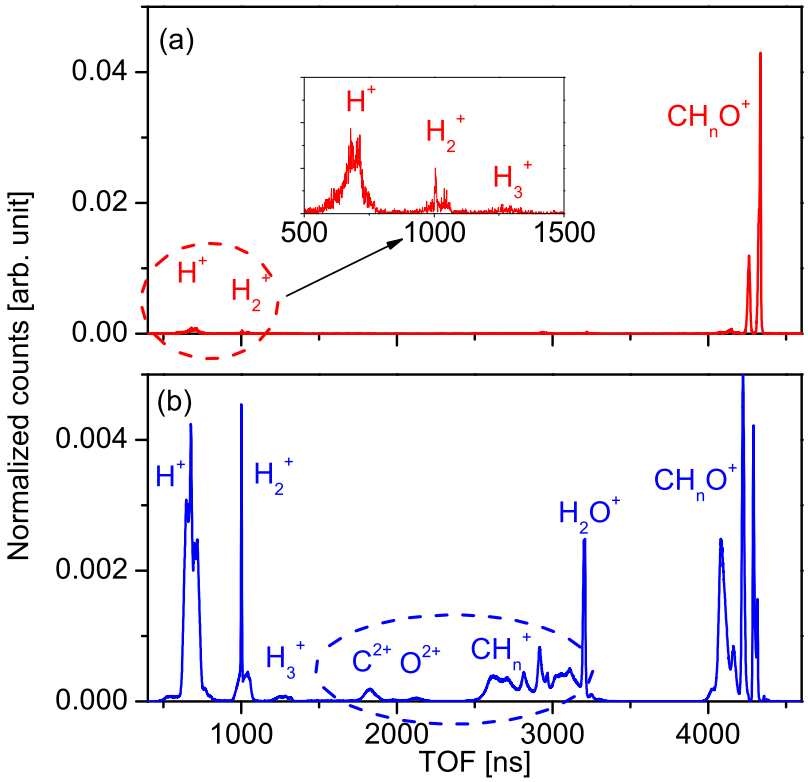

FIGURE 3.7: Time-of-flight spectrum of CH_3OH obtained for 800 nm, linearly polarized light having intensity 1.46×10^{13} W/cm^2, and pulse duration (a) 29 fs, and (b) 230 fs (GDD = 2390 fs^2). The y-axis represents the normalized counts. Normalization is done by the total counts ((a) 5.8×10^4, and (b) 3.4×10^5) recorded in each spectrum.

Next, we examined the effect of chirped pulses on the photodissociation of polyatomic molecules leading to the formation of H_n^+ ions. As mentioned in chapter 2, we passed the beam through SF11 plates of different thicknesses to stretch the pulses, which also introduced a chirp. Due to the chirp, the red frequency components travel faster and are present in the leading edge of the pulse, while the blue components are present in the trailing edge. Since SF11 plates produce positively-chirped pulses only, we did not study the negative chirp-dependence on the fragmentation of the molecular ions. To estimate the amount of chirp, we have calculated the group delay dispersion (GDD) for SF11 of different thicknesses which are displayed in Table 3.2.

TABLE 3.2: Group delay dispersion (GDD) and stretching of the laser pulses for different thicknesses of SF11.

Thickness of SF11 (mm)	GDD (fs^2)	P. D. (fs)
0	0	29
5	600	64
10	1650	160
15	2390	230
20	3120	300
25	4380	420
30	5330	510

Figure 3.7 shows the TOF spectra of CH_3OH obtained using 800 nm, linearly polarized pulses with pulse duration (a) 29 fs, and (b) 230 fs (GDD = 2390 fs^2). As evident from this figure, the yield of H_n^+ (n=1-3) ions is nearly negligible in the case of 29 fs pulses and the TOF spectrum is dominated by the CH_3OH^+ ions. On the other hand, photoionization by chirped pulses (230 fs, 2390 fs^2) results in a higher rate of fragmentation compared to the ionization of the parent molecules, thereby producing a high yield of H_n^+ ions, as seen in figure 3.7 (b).

The strong-field ionization of atoms [134–136] and polyatomic molecules [137–139] has been found to be strongly affected by chirp, and its control using shaped pulses has been demonstrated in earlier experiments. It was shown that both positively- and negatively-chirped pulses produce a higher yield of fragments compared to parent ions, due to enhanced ionization of the molecules [140, 141]. In addition, the laser pulse duration affects the ultrafast excited-state dynamics of the parent ion and its subsequent fragmentation [69, 138, 142, 143]. For pulses with durations $\sim$ 100 fs or more, ionization and the subsequent nuclear dynamics occur in the presence of the field. This leads to a more significant stretching of the bond lengths, affecting the molecular restructuring and fragmentation dynamics. Enhanced ionization of polyatomic molecules at long internuclear distances has been attributed to an energy upshift of the inner-valence shells leading to larger coupling of multiple orbitals [142, 144, 145].

Therefore, it is expected that the photoionization of CH_3OH with chirped pulses will lead to enhanced ionization of the molecule. These multiply-charged ions are highly unstable and fragment easily, producing H_n^+ ions as one of the fragments.

The C^{2+} and O^{2+} ions observed in the TOF spectrum (figure 3.7 (b)) confirms that these ions must have been formed due to the fragmentation of multiply-charged molecules. We have also obtained the chirp-dependent yield of H^+, D^+, HD^+, D_2^+, D_2H^+, and D_3^+ ions resulting from the photodissociation of CD_3OH. Table 3.3 shows the normalized yield of the above-mentioned ions for pulse durations ranging from 29 fs to 300 fs (corresponding GDD values are mentioned in the table), at a fixed intensity of 1.46×10^{13} W/cm^2. The yield of all the fragments have an increasing trend with increasing chirp, indicating that they are formed by the fragmentation of multiply-charged CD_3OH ions.

TABLE 3.3: Yield of H^+, D^+, HD^+, D_2^+, D_2H^+, and D_3^+ ions (in %) from CD_3OH as a function of pulse duration. 'd' stands for the thickness of the SF11 window in mm, while 'τ' represents the pulse duration in fs. The intensity was maintained at 1.46×10^{13} W/cm^2 for all the cases.

d (mm)	τ (fs)	GDD (fs^2)	H^+	D^+	HD^+	D_2^+	D_2H^+	D_3^+
0 (unchirped)	29	0	4.7	3.7	0.1	0.5	0.2	0.1
5	64	600	8.4	7.7	0.1	1.3	1.3	0.9
10	160	1650	10.4	10.8	0.3	1.8	1.4	1.0
15	230	2390	14.9	20.1	0.5	2.4	3.0	2.4
20	300	3120	17.7	27.7	0.7	2.9	4.8	4.3

Similarly, we have investigated the chirp-dependent SFI of CH_3Cl and the yield of H_n^+ ions induced by 800 nm, linearly polarized pulses of durations ranging from 29 fs to 510 fs (GDD = 5330 fs^2), at a constant intensity of 4.2×10^{13} W/cm^2. Figure 3.8 shows the TOF spectrum of CH_3Cl recorded using (a) 29 fs and (b) 510 fs (GDD = 5330 fs^2) pulses. The effect of chirped pulses on the photodissociation of CH_3Cl is similar to that we observed in the case of CH_3OH and the results are already discussed above.

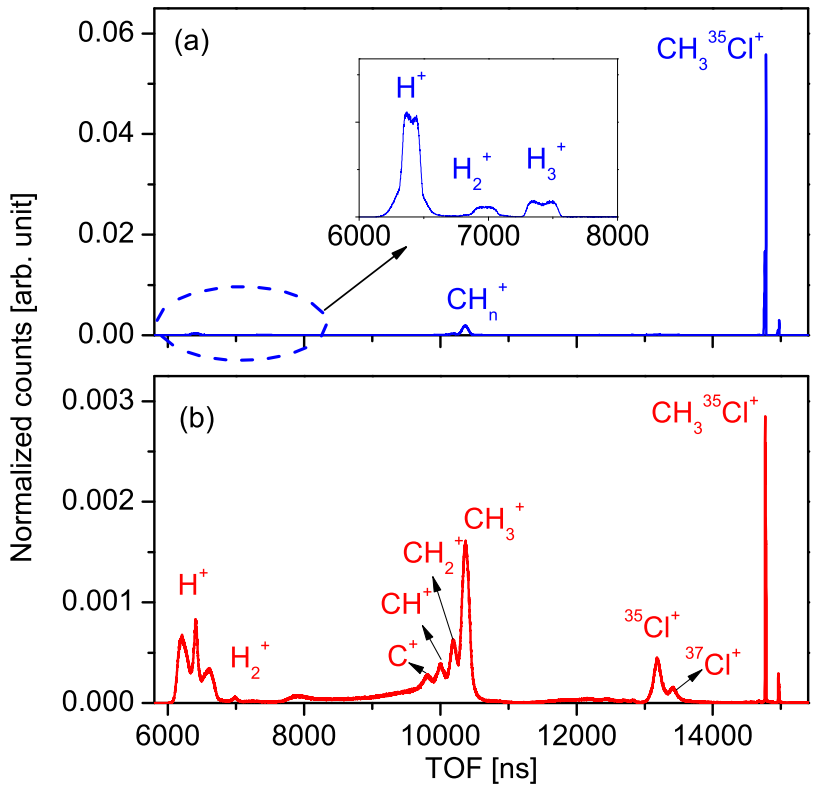

FIGURE 3.8: Time-of-flight spectrum of CH_3Cl obtained for 800 nm, linearly polarized light having intensity 4.2×10^{13} W/cm^2, and pulse duration (a) 29 fs , and (b) 510 fs (GDD = 5330 fs^2). The y-axis represents the normalized counts. Normalization is done by the total counts ((a) 1.2×10^7, and (b) 2.8×10^6) recorded in each spectrum.

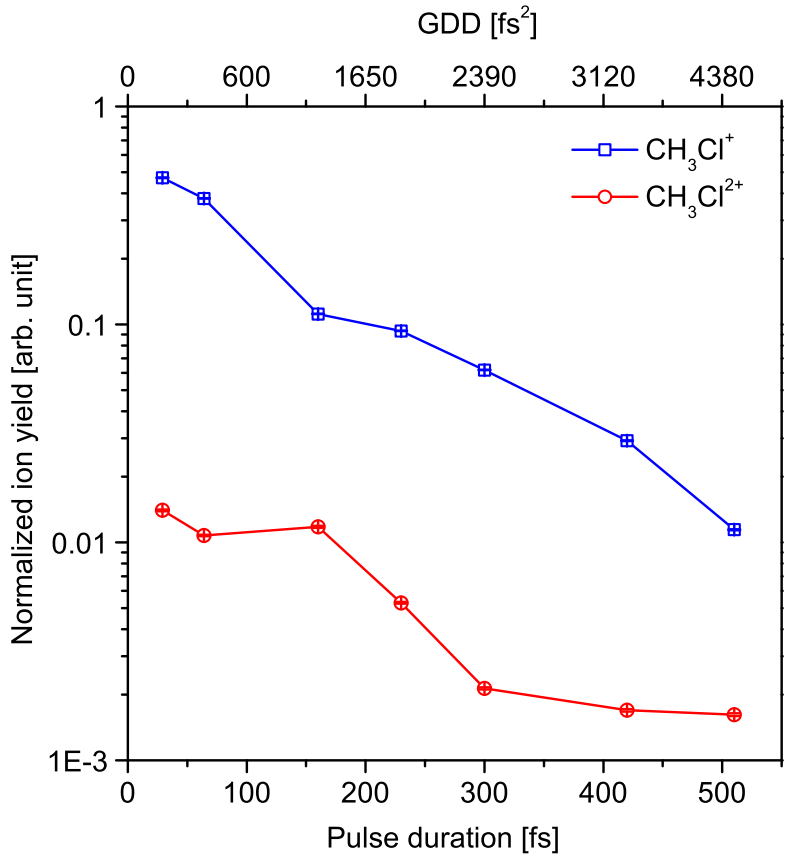

FIGURE 3.9: Pulse duration and chirp-dependent yield of CH_3Cl cations and dications (maximum errors are 0.1% for $CH_3^{35}Cl^+$ and 0.01% for $CH_3^{35}Cl^{2+}$). The other laser parameters like intensity (4.2×10^{13} W/cm^2), wavelength (800 nm), and polarization (linear) of the pulses were maintained constant throughout the measurements. The ions yield were normalized by the total ion yield in each TOF spectrum.

Next, we have obtained the normalized yield of CH_3Cl cations and dications as a function of chirp in figure 3.9. The yields of both the cations and dications show a decreasing trend with increasing chirp (and pulse duration). CH_3Cl is primarily singly-ionized for the unchirped pules (similar to CH_3OH) since the yield of CH_3Cl^+ is an order of magnitude higher than that of CH_3Cl^{2+} (evident from the figure). On chirping the pulses, the CH_3Cl^+ yield drops due to an enhanced ionization of the molecules, while the yield of multiply-charged CH_3Cl (+2, +3, etc.) is enhanced. However, a majority of the CH_3Cl^{2+} ions populate the dissociative states, leading to higher fragmentation, which explains the decreased CH_3Cl^{2+} yield.

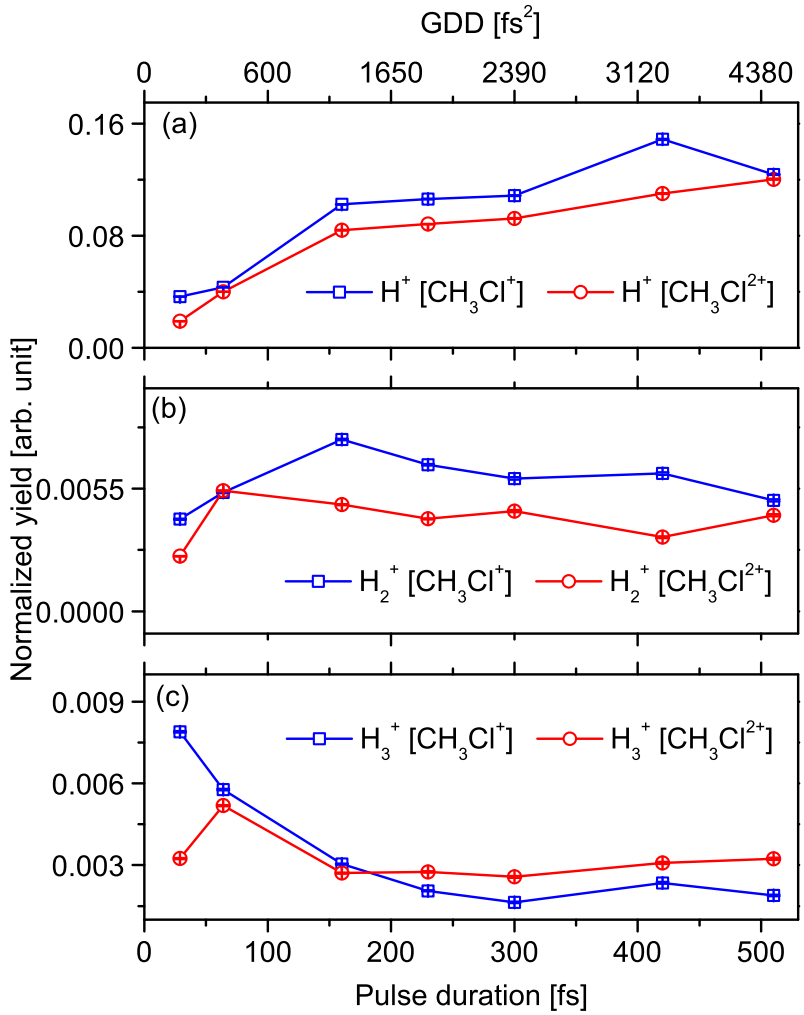

FIGURE 3.10: Normalized (a) H^+, (b) H_2^+, and (c) H_3^+ yield as a function of pulse duration and chirp. The other laser parameters like intensity (4.2×10^{13} W/cm^2), wavelength (800 nm), and polarization (linear) of the pulses were maintained constant throughout the measurements. Normalization was done by the total ion yield in each TOF spectrum. The total H_n^+ yield is shown in blue, while the H_n^+ ions contributed by CH_3Cl cations and dications are shown in black and red, respectively. The maximum error in all the cases is less than 1%.

The pulse duration-dependent normalized yield of (a) H^+, (b) H_2^+, and (c) H_3^+ ions formed by the photodissociation of CH_3Cl is shown in figure 3.12. The blue and red curves in each case represent the H_n^+ ions produced by the fragmentation of CH_3Cl cations and dications, respectively. As evident from the figures, while the H^+ yield has an increasing trend as a function of chirp and pulse duration, the H_2^+ and H_3^+ ions yield show a decreasing trend. Duflot et al. showed that H^+ is formed from the dissociation of the most stable isomer H_2CClH^{2+} (the $^1A'$ state of this isomer

lies 34.83 kcal/mol below the $^1A'$ state of CH_3Cl^{2+}) [146]. This means that the H^+-forming pathways are energetically favoured compared to the H_2^+ and H_3^+ forming pathways. Our study shows that photoionizing CH_3Cl by chirped pulses further favours the H^+-forming pathways compared to the H_2^+ and H_3^+ forming pathways for larger positive chirp. The two stable isomers of the CH_3Cl dication are shown in figure 3.11.

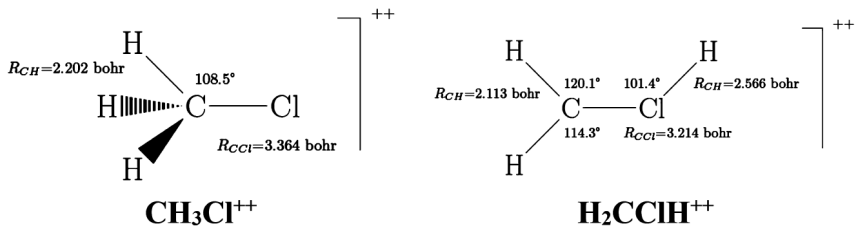

FIGURE 3.11: Stable isomers of CH_3Cl^{2+}.

3.3.3 H_n^+ (n=1-3) formation: wavelength dependence

The next parameter that we used to control the SFI and formation of H_n^+ ions is the laser wavelength. Figure 3.12 compares the TOF spectra of CH_3OH obtained with 29 fs, linearly polarized pulses of intensity 4.5×10^{13} W/cm^2 having wavelengths – (a) 800 nm, and (b) 1300 nm (generated from the OPA unit). As evident from the figure, the 800 nm pulses produced a high yield of fragments like H_n^+, CH_n^+, CH_nO^+, and doubly-charged ions like C^{2+} and O^{2+}. In contrast, the 1300 nm pulses of the same intensity and pulse duration are capable of primarily singly ionizing the molecules, therefore, the H_n^+ yield is low.

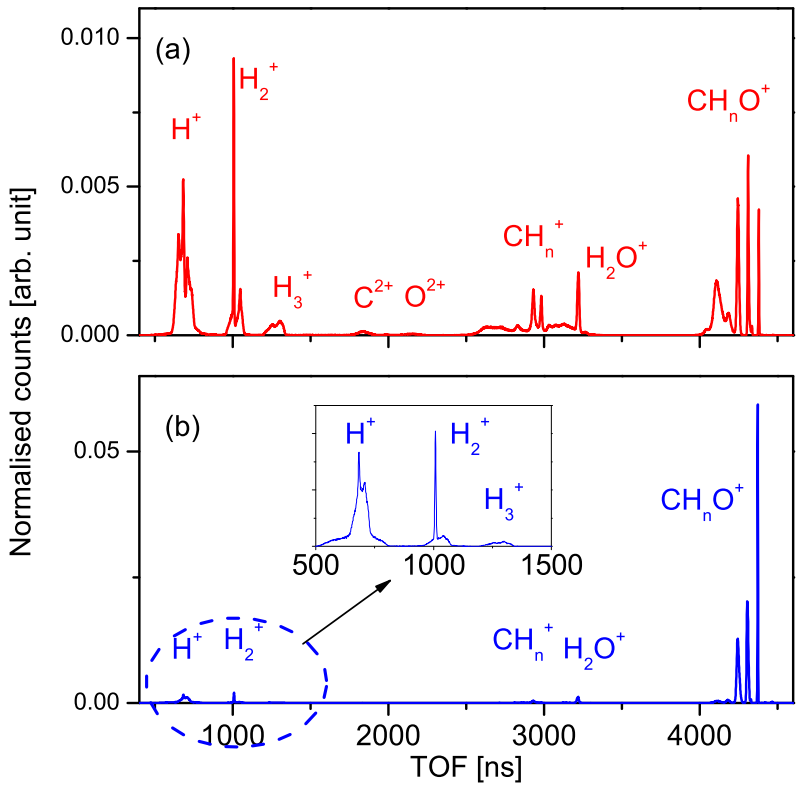

FIGURE 3.12: TOF spectrum of CH_3OH obtained for 29 fs, linearly polarized pulses of intensity 4.5×10^{13} W/cm^2, and wavelength (a) 800 nm, and (b) 1300 nm. The y-axis represents the normalized counts. Normalization is done by the total counts ((a) 2.2×10^6, and (b) 2.5×10^6) recorded in each spectrum.

Now it is known that, wavelength affects the strong-field ionization of molecules, as shown in the Keldysh theory. For the intensities used in our experiment, the SFI of CH_3OH takes place in the MPI regime for 800 nm pulses ($\gamma = 1.4$) and in the tunneling regime in the case of 1300 nm pulses ($\gamma = 0.8$). Ionization of CH_3OH by tunneling of an electron and its subsequent rescattering from the ion core is more efficient in low-frequency fields due to its quasi-static nature, which however, comes at the cost of low rescattering cross-sections. This is because at long wavelengths (more pronounced in mid-IR fields), the tunnel electron travels in the laser field for longer durations, leading to larger kinetic energy of the electrons but a simultaneous longitudinal and transverse spreading of the electron wavepacket. This process of quantum diffusion results in the ratio of rescattered to direct electrons to scale as λ^{-4} [147]. Colosimo et al. studied the SFI of Ar induced by pulses of wavelengths

800 nm, 1300 nm, 2000 nm, and 3600 nm [148]. Their findings reveal that the photoelectron energy distribution for 1300 nm pulses decays rapidly upto $2U_p$ energies, followed by a plateau region upto $10U_p$. Unlike the photolectron energy distribution for 800 nm pulses, the electrons emitted for 1300 nm pulses do not exhibit the ATI structure, and the counts are greatly reduced as well. Therefore, SFI experiments with long wavelength pulses suffers from very long acquisition times (time required to achieve standard signal-to-noise ratio). Therefore, such reduced recollision probability of the tunnel electron explains the lower yield of H_n^+ ions and other fragments on ionizing CH_3OH with 1300 nm pulses.

3.3.4 H_n^+ (n=1-3) formation: polarization dependence

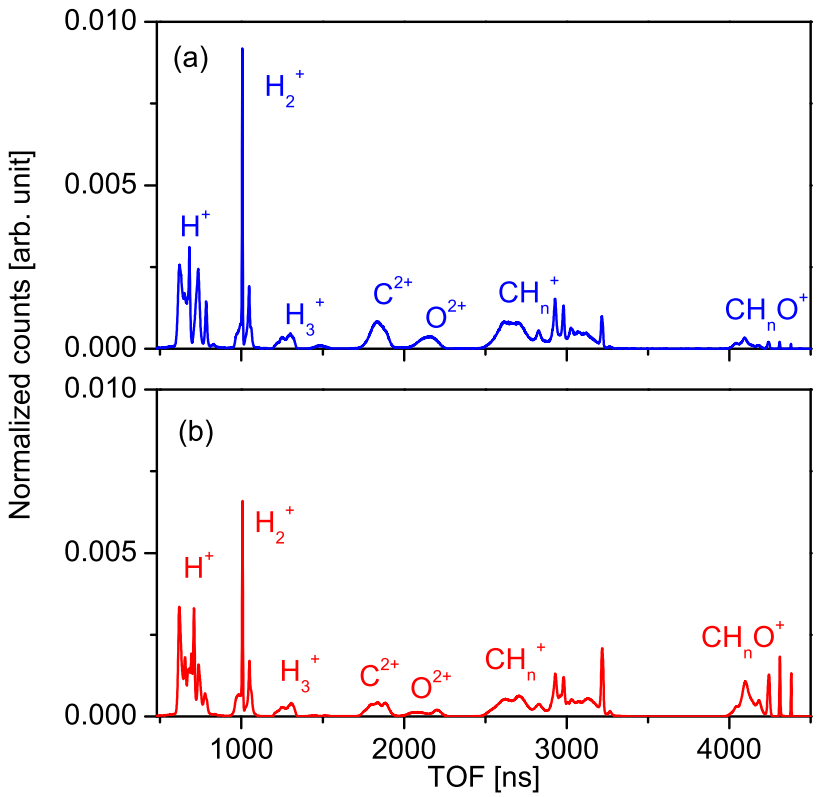

FIGURE 3.13: Linear and circularly polarized light-induced time of flight mass spectrum of CH_3OH. The parameters like wavelength (800 nm), pulse duration (29 fs), and intensity (8.7×10^{13} W/cm^2) were kept identical for both (a) linearly polarised, and (b) circularly polarized cases. The y-axis represents the normalised ion counts. Normalization is done by the total counts ((a) 2.9×10^6, and (b) 1.3×10^7) recorded in each spectrum. In both (a) and (b), n = 0-3 in CH_n^+ and n = 0-4 in CH_nO^+.

Finally, we examined the effect of polarization on the photodissociation and the yield of H_n^+ (n=1-3) ions. Figures 3.13 (a) and (b) compare the TOF spectra obtained for linearly and circularly polarised pulses, respectively. The intensity (8.7×10^{13} W/cm^2) used in both the cases show that CH_3OH is ionized primarily by tunneling ($\gamma \approx 1$). It should be noted that the intensity was same in both the cases, which means that the magnitude of the electric field strength in the circular polarization (CP) case was half the value in the linear (LP) case. As seen in the figure, there is very subtle difference in the two spectra. CH_3OH^+ yield is extremely small in the case of LP pulses and the TOF spectrum is dominated by $H_n^+$and other fragments (like H_n^+, CH_n^+, C^{2+}, O^{2+}). In the CP case however, there is a substantial yield of the heavier CH_nO^+ (n =0-4) ions, and the fragments have a slightly lower yield compared to the LP case.

As mentioned above, the intensity at which the polarization-dependent study is performed is close to the tunneling regime, so tunnel electron recollision-induced processes come into play. It is known that in the case of linear polarization, the tunnel electron reverses its trajectory as the laser field direction changes, and it may recollide with the parent ion (three-step model). Circular polarization is expected to cause the tunnel electron to spiral away from the parent ion, thereby, reducing the recollision cross-section and the yield of fragment ions. This has been confirmed by many experiments[104, 149, 150]. Therefore, the smaller fragmentation rate of CH_3OH in the CP case may be attributed to the suppression of tunnel ionization in the CP case.

3.4 Conclusion

To summarize, we have investigated the SFI of a few polyatomic molecules and the control of H_n^+ yield using the laser parameters. Firstly, we experimentally obtained the single ionization rate of a molecule (CH_3Cl) and fitted it with the MO-ADK model. Next, we used intensity, chirp, wavelength, and pulse duration to demonstrate the control of H_n^+ yield. In the next chapter, we shall investigate the ultrafast nuclear and electron dynamics responsible for this control.

Chapter 4

Fragmentation of CH_3Cl^{2+}: two-body dissociation of CH_3Cl^{2+}

In the previous chapter, we discussed the effects of various laser parameters on the SFI of polyatomic molecules, their subsequent fragmentation, and the yield of H_n^+ ions. In this chapter, we delve a little deeper into the fragmentation of an ionized molecule. Here, we shall discuss four two-body fragmentation pathways of doubly-ionized methyl chloride (CH_3Cl^{2+}) that produce H_n^+ (n =1-3) and HCl^+ as one of the fragments. Methyl chloride is a polar molecule having C_{3v} symmetry and its electronic configuration can be written as [118]

$$(1a_1)^2(2a_1)^2(3a_1)^2(4a_1)^2(1e)^4(5a_1)^2(6a_1)^2(2e)^4(7a_1)^2(3e)^4(8a_1)^0. \tag{4.1}$$

The first five atom-like orbitals are the inner-shell orbitals having $1s$, $2s$ or $2p$ characteristics and they are localized on the C and Cl atoms. The $5a_1$ and $6a_1$ are the inner-valence orbitals, while the $2e$, $7a_1$, and $3e$ are the outer-valence orbitals. The $8a_1$ orbital is the lowest unoccupied molecular orbital (LUMO).

Duflot et al. studied the various two- and three-body dissociation channels of CH_3Cl dication using the complete active space self-consistent field (CASSCF) method [151]. A similar study was performed experimentally by Ruhl et al. [152] on the cleavage of the CH_3Cl dication by the PEPIPICO method. In ref. [153], H_3^+ formation from CH_3Cl dication was proposed by three C-H bond breakups followed by the three H atoms coming close to each other and forming H_3^+ ions, in contrast to

the roaming mechanism of H_3^+ formation proposed by Ekanayake et al. [85]. The mechanism by which the stable HCl^+ ion is formed in CH_3Cl following Auger decay has also been studied [154]. Additionally, two-color asymmetric fields have been used to study the angle and momentum resolved ionization and Coulomb explosion of CH_3Cl [155]. In this study, the head-to-tail ionization asymmetry in the ejection of CH_3^+ and X^+ from methyl halide dications (CH_3X^{2+}, X = F, Cl, Br, I) was investigated experimentally by controlling the phase between the fundamental and second-harmonic fields. Theoretically, the emission asymmetries were ascribed to the asymmetry of the highest occupied molecular orbital (HOMO) of the CH_3X neutral molecule or the excited states from which ionization takes place, along with a contribution from the Stark effect, using the weak field asymptotic theory (WFAT). Further, Ma et al. used 800 nm and 400 nm pulses of duration 50 fs to study the ultrafast H migration and Coulomb explosion (CE) in CH_3Cl along various two-body breakup channels of the parent dication and trication [121].

In this chapter, we have investigated the effect of intensity and pulse duration on the single and double ionization of CH_3Cl. To understand how these parameters influence the fragmentation of CH_3Cl^{2+} and the formation of H_n^+ (n=1-3) and HCl^+ ions, photoion-photoion coincidence is performed. This has further helped us understand the contribution of the CH_3Cl cations and dications in producing these fragments. We have also identified four two-body breakup channels of CH_3Cl^{2+} as follows: $H^+ + CH_2Cl^+$, $H_2^+ + CHCl^+$, $H_3^+ + CCl^+$, and $CH_2^+ + HCl^+$. The yield, kinetic energy releases, and two-dimensional coincidence momentum distribution of the fragments (H_n^+ and HCl^+) have been measured as a function of pulse duration. Further, the anisotropy $< \cos^2\theta >$ in the angular distribution of H_n^+ and HCl^+ ions has been obtained, which helped us to understand the lifetime of the precursor. Our study suggests that it is possible to control the ultrafast dynamics of the parent dication in the excited potential energy surfaces and hence, the outcome of its dissociation by using laser intensity and pulse duration. The SFI experiment of CH_3Cl was performed in the RIMS setup and the setup has been discussed in chapters 2 and 3.

4.1 Results and Discussion

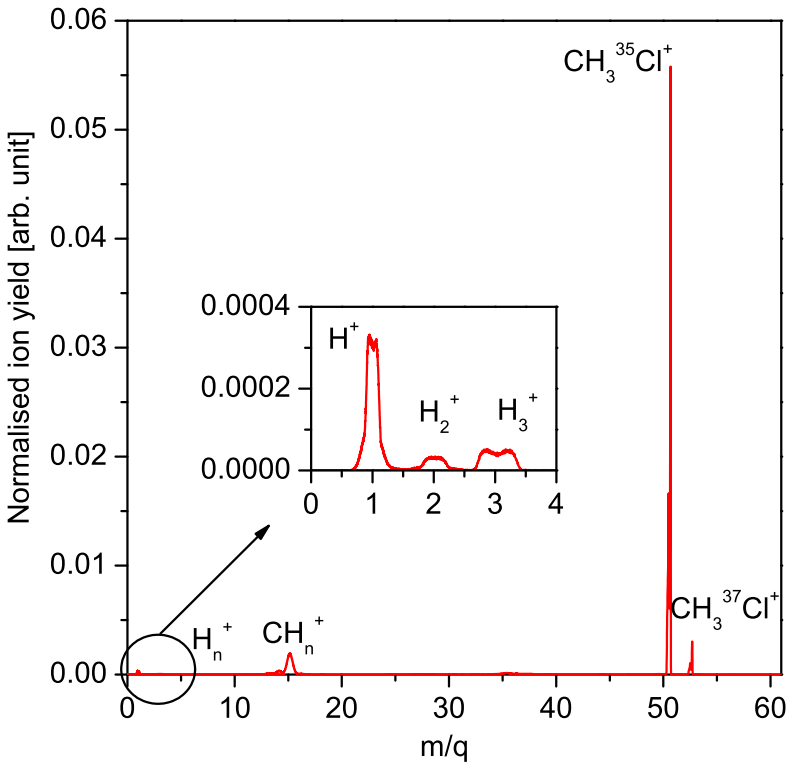

FIGURE 4.1: Normalized TOF spectrum of CH_3Cl recorded for 29 fs, 800 nm, linearly polarized pulses having an intensity of 4.2×10^{13} W/cm^2. Normalization has been performed with respect to the total counts in the spectrum.

The TOF spectrum of CH_3Cl recorded using 29 fs, 800 nm, linearly polarized pulses having an intensity of 4.2×10^{13} W/cm^2 is shown in figure 4.1. The yield of CH_3Cl^+ ions is maximum, which indicates that for the moderately intense pulses (10^{13} W/cm^2) used here, the single ionization of CH_3Cl is predominant. In addition, there is a small yield of smaller fragments like H_n^+ (n = 1-3, shown in the inset) and CH_n^+ (n =0-3) for the given laser parameters. These fragments are formed from the dissociation of both CH_3Cl^+ and CH_3Cl^{2+} ions. Among the H_n^+ ions, H^+ has the highest yield (the ratio of H^+ yield with respect to the CH_3Cl yield is 11%), which is expected due to the ease of C-H bond breakup. H_2^+ (1%) and H_3^+ (2%) formation has a lower cross-section as they require bond association and, therefore, have a comparatively much lower yield. It is also interesting to note that despite H_3^+ formation being a complex process requiring bond association between three H atoms, its yield is slightly higher than H_2^+. This observation is in contrast to previous studies

on H_n^+ formation from other hydrocarbons [97, 156]. Duflot et al. reported that H_3^+ formation is energetically easier (potential barrier is lower) compared to H_2^+ in the two-body breakup of CH_3Cl^{2+}. In fact, the potential energy of the final state ($H_3^+ + CCl^+$) is lower than the energy required for the double ionization of CH_3Cl. Duflot et al. also suggested that the second ionization occurs from the Rydberg states of CH_3Cl^+, resulting in the lower potential energy barrier for the $H_3^+ + CCl^+$ pathway, and hence, the H_3^+ yield is higher than that of H_2^+.

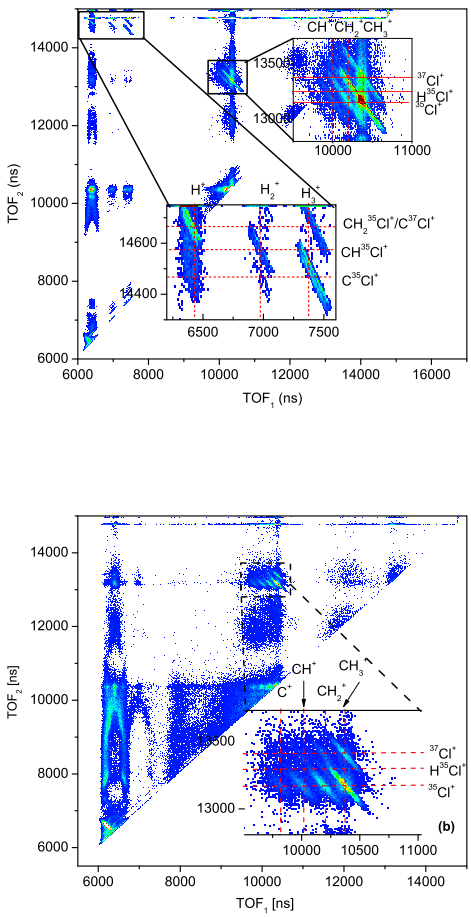

FIGURE 4.2: Photoion-photoion coincidence plots of CH_3Cl recorded for 800 nm, linearly polarized pulses of intensity 4.2×10^{13} W/cm^2, and durations (a) 29 fs and (b) 510 fs (GDD = 5330 fs^2). The dissociation pathways (4.2)-(4.5) are shown in expanded form in both (a) and (b). However, as seen in (b), the pathways (4.2)-(4.4) are completely suppressed, while the yield of pathway (4.5) is enhanced for 510 fs pulses.

To ascertain the different fragmentation pathways of CH_3Cl^{2+} contributing to

the formation of H_n^+ ions, we have obtained the photoion-photoion coincidence (PIPICO) of CH_3Cl for 29 fs, 800 nm pulses at an intensity of $I = 4.2 \times 10^{13}$ W/cm^2 in figure 4.2 (a). Various islands corresponding to the two- and three-body dissociation channels can be seen in the figure. The two-body fragmentation of CH_3Cl^{2+} results in the two fragments having anti-correlated momenta, and are characterized by islands having a slope of -1 (due to momentum conservation) [78]. Here, we have investigated the effects of intensity and pulse duration variations on the following two-body breakup channels of CH_3Cl^{2+}:

$$CH_3^{35}Cl^{2+} \Longrightarrow H^+ + CH_2^{35}Cl^+ \tag{4.2}$$

$$CH_3^{35}Cl^{2+} \Longrightarrow H_2^+ + CH^{35}Cl^+ \tag{4.3}$$

$$CH_3^{35}Cl^{2+} \Longrightarrow H_3^+ + C^{35}Cl^+ \tag{4.4}$$

$$CH_3^{35}Cl^{2+} \Longrightarrow CH_2^+ + H^{35}Cl^+ \tag{4.5}$$

While the equations (4.2)-(4.4) show the H_n^+-forming pathways, equation (4.5) corresponds to the $H^{35}Cl^+$ formation pathway. HCl^+ is formed by the intramolecular hydrogen migration from C to Cl atoms, followed by H-Cl bond formation before the C-H bond breakup occurs (shown in the inset of figure 4.2 (a). From here on, we shall refer to $H^{35}Cl^+$ ion as HCl^+. The islands corresponding to all the four pathways in the PIPICO have a slope of -1, thereby, confirming the two-body breakup of CH_3Cl^{2+}. Figure 4.2 (b) shows the PIPICO obtained for 510 fs pulses of intensity I. We shall discuss the effects of pulse stretching on the two-body fragmentation of CH_3Cl^{2+} later.

We now use the photoion-photoion coincidence to determine the contribution of CH_3Cl cations (red) and dications (blue) in the normalized H_n^+ yield as a bar plot in figure 4.3. The y-axis represents the normalized yield of H_n^+ ions and the x-axis represents the ions. As seen in the figure, CH_3Cl dications have a higher contribution in the H_n^+ yield ($\sim$ 2 times for H^+ and H_2^+, and 1.4 times for H_3^+ ions) than the cations. As previously mentioned, the PESs predominantly populated by the CH_3Cl^+ ions are stable and have a long lifetime, so they do not fragment much and have very

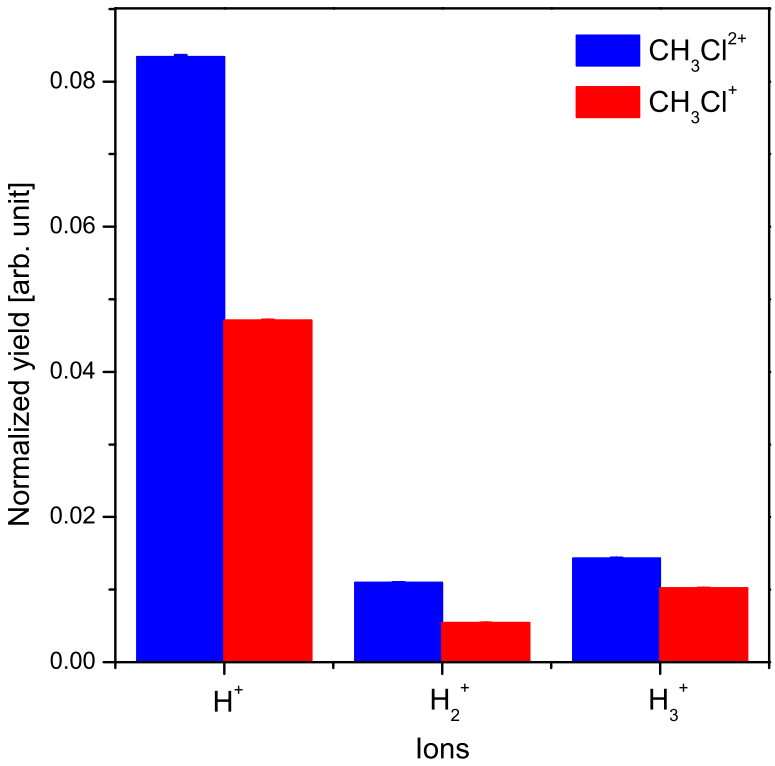

FIGURE 4.3: Comparative yield of H_n^+ (n =1-3) ions CH_3Cl mono- and dication. The yield of the H_n^+ ions has been normalized with respect to the total ion yield in each case.

little contribution to H_n^+ formation. On the other hand, the CH_3Cl^{2+} ions are unstable (confirmed by the very low yield of CH_3Cl dications experimentally) because the populated dication states are primarily repulsive, and they undergo fragmentation. Therefore, the parent dications have a higher contribution in the H_n^+ yield.

Finally, to examine the effect of laser intensity on the yield of the dissociative pathways (4.2)-(4.5) and investigate if intensity can serve as a parameter to control the dissociation of CH_3Cl, we have obtained the yield of the channels as a function of intensity in figure 4.4. The x-axis represents the four fragmentation pathways, while the y-axis represents the normalized yield of the pathways. The yields for three values of intensity are considered - 4.3×10^{13} W/cm^2 (black), 6.6×10^{13} W/cm^2 (red), and 8.5×10^{13} W/cm^2 (blue) - and shown as a bar plot. It is evident from the figure that as the intensity is doubled, all four pathways are suppressed (the reduction in H^+ yield is 5 times, 3 times for H_2^+, 4 times for H_3^+, and 2 times for HCl^+). The

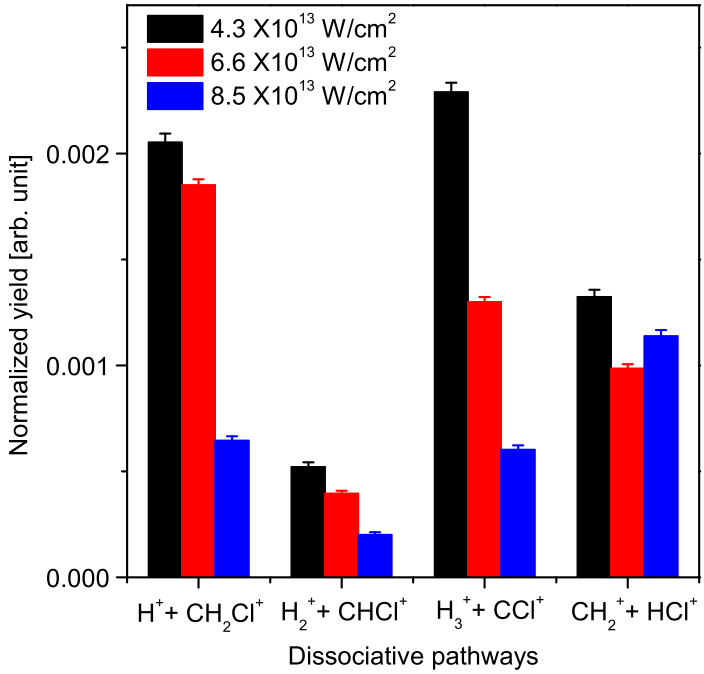

FIGURE 4.4: Normalized yield of the dissociation pathways (4.2)-(4.5) for the intensities 4.3×10^{13} W/cm^2, 6.6×10^{13} W/cm^2, and 8.5×10^{13} W/cm^2. The other laser parameters like pulse duration (29 fs), polarization (linear), and wavelength (800 nm) were maintained constant in all three cases. The % yield represents the ratio of the number of counts in a particular pathway and the total number of coincidence events.

three intensity values chosen in this experiment are in the MPI regime, so the double ionization of CH_3Cl takes place essentially by multiphoton absorption in all the cases. At high intensities, the rate of ionization of molecules is higher than that of dissociation [46]. It is known that the ionization rate of molecules depends on the internuclear separation [46, 47], and at separations much larger than the equilibrium separation, the ionization rate has been found to be enhanced by a few times. This phenomenon, known as charge resonance-enhanced ionization (CREI), is attributed to the coupling of pairs of electronic states by the laser field, leading to charge localization and enhanced ionization. As the laser intensity is increased to 8.5×10^{13} W/cm^2, the dication evolving on the excited PES undergoes further ionization at a critical internuclear separation (R_c) before the dication can dissociate, thereby producing triply ionized molecules. As a result, the yield of the dissociation pathways decreases with increasing intensity. This observation suggests that varying the intensity leads to changes in the excited state dynamics of the parent ion, which in

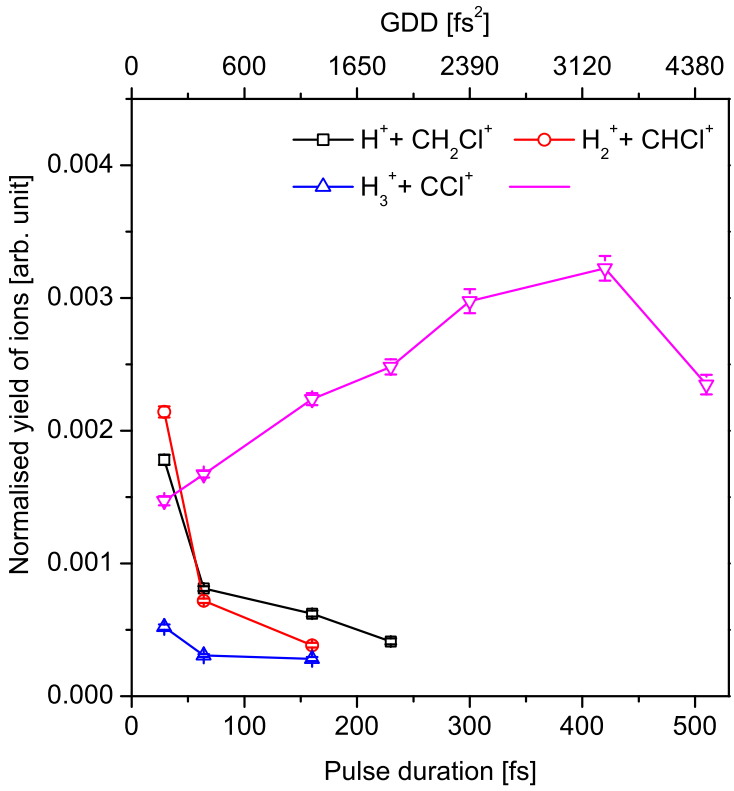

FIGURE 4.5: Normalized yield of the dissociation channels (4.2)-(4.5) as a function of pulse duration and chirp. The other laser parameters like intensity (4.2×10^{13} W/cm^2), wavelength (800 nm), and polarization (linear) of the pulses were maintained constant throughout the measurements. The maximum errors are 6%, 5%, 5%, and 3% for channels (7), (8), (9), and (10), respectively.

turn, affects the yield of the pathways.

Next, we studied the effect of chirp on the two-body fragmentation of CH_3Cl^{2+}. Some of the chirp-dependent results have already been discussed in the previous chapter. Now, we shall investigate the ultrafast excited-state dynamics of the CH_3Cl dication leading to the four pathways and their control. Firstly, the variation in the yield of the dissociation pathways (4.2)-(4.5) is shown in Figure 4.5. Pathways (4.2)-(4.4), which involve H_n^+ (n=1-3) formation, have a decreasing trend in their yield as the pulses are stretched and chirped. These pathways are almost completely suppressed for pulses beyond 160 fs, and their yields are negligible. In contrast, pathway (4.5) shows an enhancement in the fragments' yield for stretched and positively

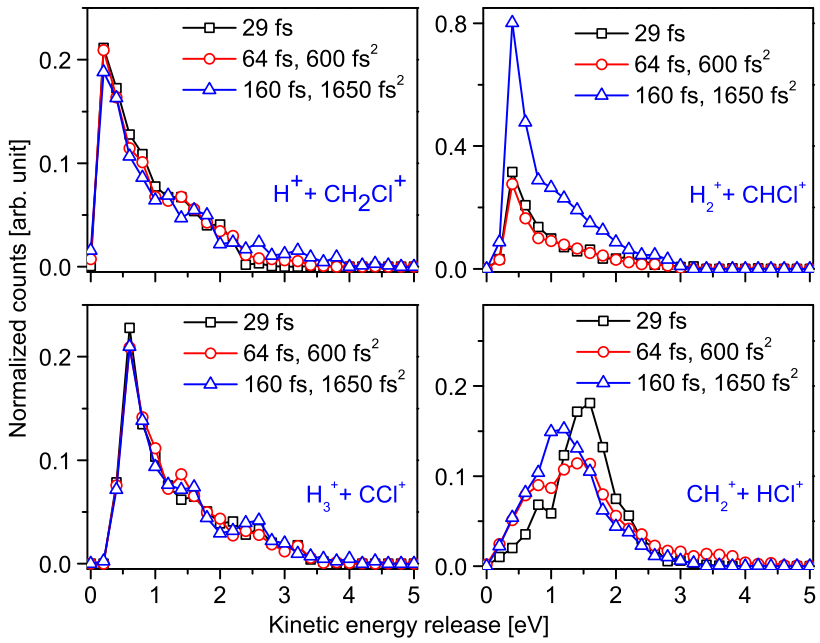

FIGURE 4.6: Kinetic energy releases of the dissociation channels (4.2)-(4.5) for various pulse durations and chirp. The other laser parameters like intensity (4.2×10^{13} W/cm^2), wavelength (800 nm), and polarization (linear) of the pulses were maintained constant throughout the measurements.

chirped pulses. This is an isomerization pathway involving an intramolecular migration of the H atom to the Cl atom, H-Cl bond formation, and finally, C-Cl bond breakup. To explain the observed trends in the overall yields of the four pathways, we have tried to understand the excited state dynamics of CH_3Cl^{2+} by determining the kinetic energies, two-dimensional momenta, and angular distributions of the fragments in each pathway.

Firstly, we discuss the kinetic energy release (KER) distributions of the pathways. The kinetic energy of fragments has information about the potential energy surface on which the molecular wavepacket evolution took place, the molecular geometry, and the charge distribution on the ions just before it underwent dissociation. Figure 4.6 shows the KER (sum of kinetic energies of the fragments in a particular channel) distributions for the channels (4.2)-(4.5) for varying chirps and pulse durations. The KER distributions for pathways (4.2)-(4.5) peak at 0.2 eV, 0.4 eV, and 0.6 eV, respectively. The peaks and FWHM of the KER distributions for pathways (4.2)-(4.4) do not

show any change as the pulses are chirped. However, the KER peak for the pathway 4.5 shows a shift to lower energy values (from 1.6 eV to 1 eV) as the pulses are chirped. This is accompanied by a decrease in the FWHM of the KER distribution. Earlier studies have shown that a shift in the KER of a dissociation pathway with increasing pulse duration is due to the parent ion dissociating from a Coulombic (or repulsive) PES, where the bond length maps onto the total KER [47, 93]. Therefore, for pathway (4.5), the dication must dissociate from a repulsive PES and therefore, has a rapid dissociation time. On the contrary, the pathways (4.2)-(4.4) originate from non-Coulombic (metastable) weakly attractive PESs having a lifetime of the order of the rotational period of the dication, due to which their KER distributions do not show a shift to lower energies with pulse stretching, that is, the bond length does not map onto the KER in this case. At the same time, the FWHM of the KER distributions for all the pathways is broad. However, the FWHM of the KER distribution for the $CH_2^+ + HCl^+$ pathway is reduced with increasing chirp. A broad KER distribution suggests the contribution of multiple excited electronic states [157] in a dissociation pathway. Therefore, some of the electronic states participating in the case of unchirped pulses are suppressed with an increased positive chirp. The KER distribution of the four pathways as a function of intensity ($I = 4.3 \times 10^{13}$ W/cm^2 and $2I = 8.5 \times 10^{13}$ W/cm^2) are not shown here. For the H_n^+ forming pathways ((4.2)-(4.4)), the KER peaks showed no variation as a function of intensity. However, there was a shift in the KER peak observed in the HCl^+ forming pathway (4.5) from 1.6 eV to 1.4 eV as the intensity was increased from I to $2I$. The KER values reported by Ma et al. for the same pathways are significantly higher than that observed here [121]. It must be noted that the intensities used in our experiment is $\sim 10^{13}$ W/cm^2, which is an order of magnitude less than that used by Ma et al. [121]. A previous study on the ultrafast dynamics of H_2^+ ions by He et al. reported a shift in the KER distribution of the Coulomb explosion channel to higher energies as the intensity was increased from 7.7×10^{13} W/cm^2 to 2.5×10^{14} W/cm^2 [158]. Therefore, the discrepancy in the KER values may be attributed to the low intensity used in our study.

Further, we have plotted the two-dimensional coincidence momentum images of H_n^+ (n=1-3) and HCl^+ ions (figure 4.7). The polarization direction is parallel to the

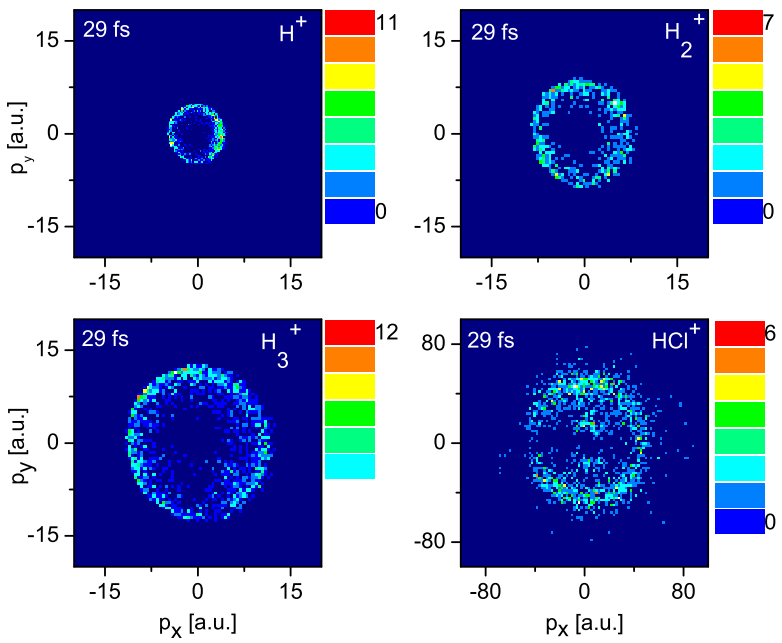

FIGURE 4.7: Two-dimensional coincidence momentum images of H^+, H_2^+, H_3^+, and HCl^+ ions produced by the two-body breakup of CH_3Cl^{2+} along the pathways (4.2)-(4.5)obtained with 29 fs, 800 nm, linearly polarized pulses of intensity 4.2×10^{13} W/cm^2.

p_y axis. As seen in the figure, the momentum of H^+ is the least (5 a.u.), followed by H_2^+ (9 a.u.) and H_3^+ (14 a.u.) ions. The distribution of HCl^+ has a lower momentum component (14 a.u.) and a higher momentum component (27 a.u.). The two components indicate the involvement of two excited states (PESs) in the HCl^+ formation. The momentum distributions of the H_n^+ ions are nearly isotropic, while that of HCl^+ is anisotropic. To quantify the anisotropy in the ejection direction of the fragments, we have obtained their angular distribution. It is known that the ionization rate of a molecule depends on the relative orientation of the molecular axis with respect to the laser polarization direction, and it maps the shape of the molecular orbital from which ionization takes place [159, 160]. Since the molecular orbitals of polyatomic molecules are very closely spaced, the interaction of the molecules with intense fs pulses removes electrons not only from the HOMO but also the HOMO-1, and the HOMO-2 orbitals (the inner-valence orbitals) [161–163]. Therefore, the angular distribution of the ejected fragments also depends on whether the molecule was ionized from the valence or inner-valence orbitals. In addition, the lifetime of the precursor

ion affects the extent of anisotropy in the ejection direction of the fragments [68, 120, 164, 165].

The angular distributions of the pathways (4.2)-(4.5) are shown in figure 4.8. Here, θ is the angle between the laser polarization direction and the momentum vector of the fragment. I_1 and I_2 stand for the intensities 4.3×10^{13} W/cm^2 and 8.5×10^{13} W/cm^2, respectively. The experimentally obtained distributions were then fitted with the equation:

$$I(\theta) = 1 + \Sigma_i a_i \mathbf{P}_i (\cos(\theta)) \quad (i = 2, 4, 6) \tag{4.6}$$

where a_i represents the expansion coefficients, $\mathbf{P}_i(\cos(\theta))$ are the Legendre polynomials, and $I(\theta)$ represents the angular distribution. The expansion coefficients a_i for the various pathways are summarized in Table 4.1 for varying pulse durations and intensities. For the H_n^+ forming pathways, the angular distribution plots show that these ions are ejected in all directions (also at 90° with respect to the polarization direction) with respect to the polarization direction. The Legendre coefficients a_2 for the H_n^+ ions are ≤ 0, indicating their nearly uniform angular distributions, including at 90° with respect to the polarization direction. As discussed earlier, in the case of dissociation along the H_n^+ forming pathways, the CH_3Cl dication dissociates from non-Coulombic PESs and, therefore, has a long dissociation time. The rotation of the precursor with respect to the polarization direction destroys the anisotropy in the ejection directions of the fragments, and we observe a nearly uniform angular distribution.

On the other hand, the HCl^+ fragments are distributed primarily close to 0° and 180°. The HCl^+ ions are formed from repulsive PESs and have a fast dissociation time, so the anisotropy in their ejection direction is not destroyed by the rotation of the molecule [120, 164]. On using chirped pulses, the angular distribution of the H_n^+ ions remains nearly unchanged, while that of the HCl^+ ions becomes more anisotropic. For stretched pulses, electrons are removed not only from the HOMO, but also from the HOMO-1 and HOMO-2 orbitals [47, 68, 142], due to the coupling of

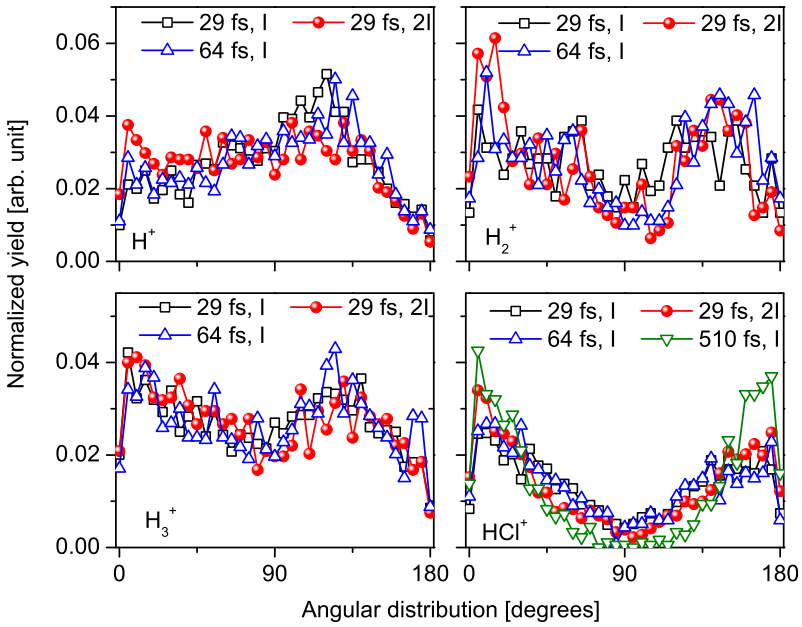

FIGURE 4.8: Angular distributions of H_n^+ and HCl^+ ejected during the two-body breakup of CH_3Cl^{2+} along the pathways (4.2)-(4.5) as a function of intensity (I and $2I$, at a constant pulse duration 29 fs) and pulse duration (at a constant intensity I). Here, θ is the angle between the polarization direction and the momentum vector of the fragment.

electronic states by the laser field at large internuclear distances. Thus, the increased anisotropy in the HCl^+ ejection direction is due to (i) the symmetry of the inner valence orbitals from which ionization takes place, and (ii) the rapid dissociation of the dication from the excited PESs thereby, preserving the anisotropy. On the contrary, the slow dissociation of the dication along the H_n^+ forming pathways is responsible for the isotropic distribution of the fragments even for chirped pulses. At this point, we can explain the results of figure 4.5. Due to the long dissociation time of CH_3Cl^{2+} along the H_n^+ forming pathways, we expect that the dication absorbs more energy from the field (which is still present in the case of stretched pulses) and is further excited or ionized. Thus, the yields of the pathways (4.2)-(4.5) are suppressed on stretching the pulses. On the other hand, $CCl^+ + HCl^+$ pathway is favoured over the H_2^+ and H_3^+ forming pathways because its precursor (H_2CClH^{2+}) is highly stable. The increased yield of the HCl^+ pathway with increased chirp can be attributed to the dication populating the PESs that dissociate along this pathway. The angular distribution of the H_n^+ ions for the pathways (4.2)-(4.4) reported by Ma et al. [121] differ from our findings. The H_n^+ and HCl^+ ions have an anisotropic angular

TABLE 4.1: Coefficients of Legendre polynomial a_i ($i = 2, 4, 6$) for the angular distributions of the fragments formed the two-body breakup of CH_3Cl^{2+} ion. I and $2I$ stand for the intensities 4.3×10^{13} W/cm^2 and 8.5×10^{13} W/cm^2, respectively, and P.D. represents pulse duration.

Dissociation pathways	P. D. (fs)	I (W/cm^2)	a_2	a_4	a_6
$H^+ + CH_2Cl^+$	29	I	-0.4	-0.2	0.1
	64	I	-0.2	-0.2	0
	29	$2I$	-0.2	-0.2	0
$H_2^+ + CHCl^+$	29	I	0.2	-0.5	0.2
	64	I	0.7	-0.6	0
	29	$2I$	0.7	-0.5	0
$H_3^+ + CCl^+$	29	I	0	-0.2	0
	64	I	0	-0.2	0.1
	29	$2I$	0.1	-0.2	0
$CH_2^+ + HCl^+$	29	I	1.0	-0.1	-0.2
	64	I	1.2	-0.2	-0.1
	160	I	2.3	0.6	-0.1
	230	I	2.4	0.8	-0.2
	300	I	2.4	0.9	-0.4
	420	I	2.4	1.0	0.0
	510	I	2.8	1.0	-0.5
	29	$2I$	1.5	0.2	-0.1

distribution in their study, suggesting that the CH_3Cl^{2+} ions populate high energy repulsive PESs. This observation may be due to the high intensity (10^{14} W/cm^2) used by Ma et al. On increasing the intensity from I to $2I$ while keeping all other laser parameters constant, we do not observe very significant changes in the angular distributions of the H_n^+ fragments. On the other hand, the HCl^+ fragments show a slightly increased anisotropy at the intensity $2I$. Therefore, the intensity and pulse duration control the excited dynamics of the parent dication and the orbitals contributing to the double ionization, which in turn, control the outcome of dissociation and the overall yield.

4.2 Conclusion

In conclusion, we have demonstrated the effects of laser intensity and pulse duration on the strong-field ionization and two-body fragmentation pathways of CH_3Cl^{2+} that involve intramolecular H migration and bond formation. Increasing the intensity from $I = 4.3 \times 10^{13}$ W/cm^2 to $I = 8.5 \times 10^{13}$ W/cm^2 suppressed the yields of the four pathways, which was attributed to an increased ionization of the parent dication compared to dissociation. On the other hand, chirping the pulses from 0 fs^2 (29

fs) to 533 fs^2 (510 fs) enhanced the HCl^+-forming pathway, while suppressing the H_n^+ forming pathways. The KER distributions, two-dimensional coincidence momentum distribution and angular distributions of the H_n^+ and HCl^+ ions revealed that the H_n^+ ions are formed by the dissociation of CH_3Cl^{2+} from non-Coulombic metastable PESs, so their bond lengths do not map onto the KER. These pathways have a long dissociation time (of the order of ps) and the anisotropy in their ejection direction is destroyed by the rotation of the dication. Conversely, the HCl^+ forming pathways arise from the dissociation of CH_3Cl^{2+} from Coulombic (repulsive) PESs, due to which their KER distribution shows a shift to lower energies with increased pulse stretching. Since this pathway has a rapid dissociation time, the HCl^+ ions have an anisotropic distribution. Hence, we demonstrated the control of the ultrafast fragmentation dynamics of CH_3Cl^{2+} and the resulting dissociation pathways using laser intensity, pulse duration, and chirp.

Chapter 5

Three-body fragmentation of CH_3Cl: investigating the fragmentation dynamics of CH_3Cl^{2+}

In this chapter, we discuss the three-body fragmentation of the CH_3Cl dication. The three-body fragmentation of linear, triatomic inorgranic molecules like CO_2 [166, 167], SO_2 [168], N_2O [169, 170], CS_2 [171, 172], and OCS [173, 174] has been investigated extensively. The various concerted and sequential fragmentation pathways of the multiply-charged ions have been disentangled. However, it was only recently that the three-body fragmentation of multiply-charged hydrocarbons like ethylene [175], acetylene [176–178], methanol [179], ethanol [96], benzene [180], 1,3-butadiene [181] and allene [182] was explored. Three-body fragmentation can take place either by the simultaneous bond-breaking and ejection of three fragments in a single step (concerted) or in two steps (sequential). Interestingly, a non-trivial three-body fragmentation pathway in addition to the traditional concerted and sequential mechanisms in SO_2 [168], C_2H_2 [177, 183] and 1,3-butadiene [184] was reported. Using the pump-probe technique, Burger et al established that one of the three-body fragmentation pathways of $C_2H_2^{3+}$ involved the ultrafast proton migration and isomerization from acetylene to vinylidene configuration (with a time constant of 54 fs), followed by three-body breakup along the $CC^+ + H^+ + H^+$ pathway [177].

The kinetic energy release (KER, sum of the kinetic energies of the fragments released in the pathway) of a dissociation pathway obtained using the RIMS setup helps us to study the ultrafast excited-state dynamics of the precursor and its subsequent dissociation. With the help of momentum maps and Dalitz plots, multiple studies have been reported on the three-body fragmentation of polyatomic molecules. Since the ultimate aim of studying strong-field interactions is to control reactions, it is interesting to study how these fragmentation dynamics can be controlled by various laser parameters [183, 185–187]. For instance, it was shown that the laser polarization affects the bending of CS_2 molecule before the Coulomb explosion, during the three-body fragmentation of charge states higher than 4+ [186]. On the other hand, high intensities ($> 10^{14}$ W/cm^2) and large pulse durations lead to larger stretching of bonds towards a critical internuclear distance (R_c) resulting in efficient coupling between the molecular orbitals and an enhanced ionization [46, 47, 144], known as charge resonance enhanced ionization (CREI). Recently, the control of fragmentation dynamics in the three-body breakup of OCS by using pulses of durations ranging from 7 fs to 200 fs was demonstrated [185]. With increasing pulse duration, the concerted fragmentation pathways revealed increasing geometrical deformation of the precursor (OCS^{3+} and OCS^{4+}). On the other hand, the sequential pathways were suppressed initially, but for very long pulses, these processes reappear again.

Previously, the strong-field ionization and fragmentation of CH_3Cl along various dissociative pathways have been studied extensively both theoretically [151, 153] and experimentally [114–118, 121, 122, 152, 154, 155, 188–190]. Duflot et al. theoretically investigated the various two- and three-body dissociation pathways using the complete active space self-consistent field (CASSCF) method [151]. Ruhl et al. used the photoelectron-photoion-photoion triple coincidence method to identify the various two- and three-body fragmentation pathways of the CH_3Cl dication, and found evidence of bond rearrangement processes before dissociation. In our study, we have identified the various two- and three-body dissociation pathways of CH_3Cl^{2+} using photoion-photoion coincidence. Here, we have focused on two

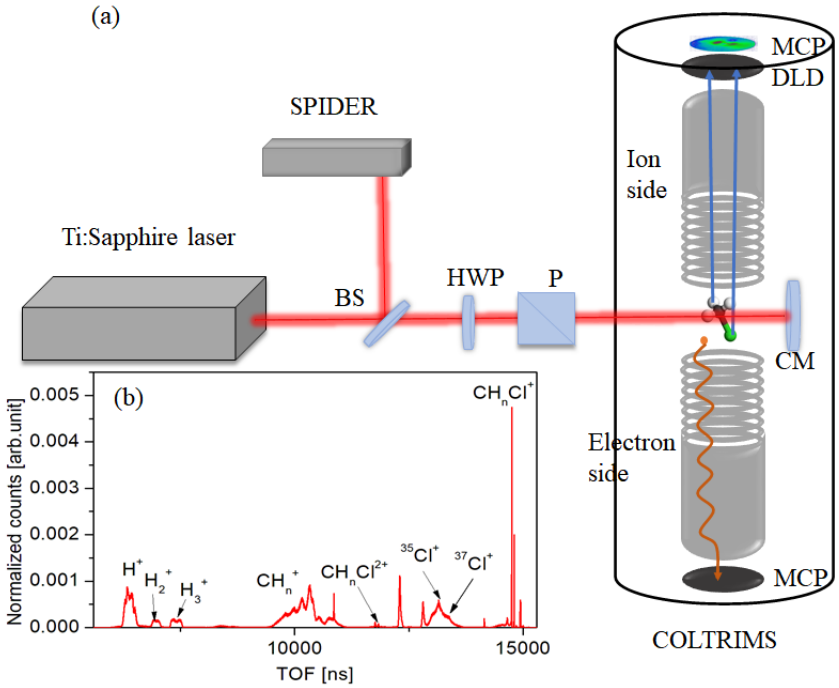

FIGURE 5.1: Schematic diagram of the experimental setup (BS = beam splitter, HWP = half waveplate, P = polarizer, MCP = microchannel plate detector, DLD = delay line detector, CM = concave mirror).

three-body dissociation pathways:

$$CH_3Cl^{2+} \longrightarrow CH^+ + Cl^+, \tag{5.1}$$

$$CH_3Cl^{2+} \longrightarrow H^+ + CH_2^+. \tag{5.2}$$

Using Dalitz plots and Newton diagrams, we have investigated the fragmentation mechanism of CH_3Cl^{2+} along the pathways (5.1) and (5.2). Due to the overlap of the concerted and sequential mechanisms in the plots, we further used the native frame method to distinguish between the different fragmentation mechanisms [191]. In addition, we have demonstrated the effect of pulse chirp on the ultrafast excited state dynamics of the parent dication and hence, the fragmentation mechanism. The SFI experiment of CH_3Cl was performed in the RIMS setup, and the setup has been discussed in chapters 2 and 3. The schematic diagram in figure 5.1 shows the experimental setup that is, the optical setup guiding the laser pulses to the RIMS setup.

5.1 Results and Discussion

5.1.1 Pathway 1: CH_2^+ + Cl^+

The $CH_2^+ + Cl^+$ pathway can be seen in the inset of figure 4.2 (a). Two of the fragments, CH_2^+ and Cl^+, are detected in coincidence, while the third fragment (H) is undetected. It must be noted that the H may either be neutral or charged but undetected. In fact, we observed some multi-coincidence signal corresponding to the $H^+ + CH_2^+ + Cl^+$ pathway using triple coincidence [192], and its KER is expected to be large (due to the Coulomb explosion of the trication) [193]. The momentum of the third fragment (H or H^+) was determined on the basis of the principle of conservation of momentum.

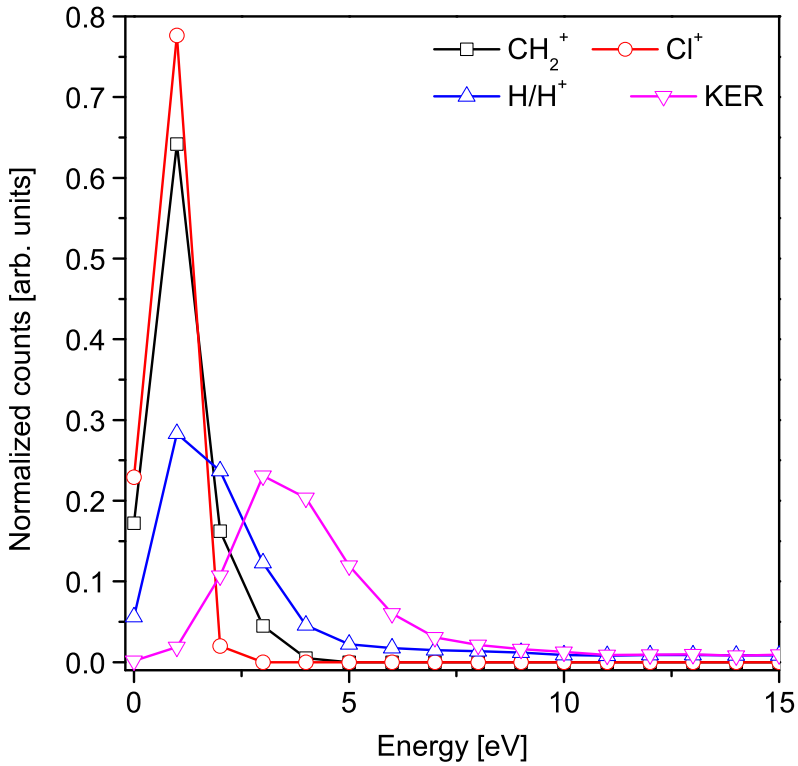

FIGURE 5.2: Kinetic energy distributions of CH_2^+, Cl^+ and H/H^+ for the $CH_2^+ + Cl^+$ pathway are shown in black, red, and blue, respectively. The total KER distribution is shown in pink.

Firstly, we have obtained the kinetic energy distributions of the individual fragments and the total KER, as shown in figure 5.2. As discussed in chapter 4, the KER provides information about the PES from which fragmentation of the molecular ion

occurred, the molecular geometry just before fragmentation, and the momentum sharing between the fragments. The energy distributions of CH_2^+ and Cl^+ range from 0 to 4 and 3 eV, respectively. Interestingly, H/H^+ shows a broad energy distribution – while the majority of the H/H^+ fragments have energy ranging from 0 to 4 eV with a peak at 1 eV, a very small fraction of the fragments carry a large kinetic energy up to 15 eV. It must be noted that the slope of the island corresponding to this pathway is -1 (as shown in the PIPICO map in figure 4.2), indicating that CH_2^+ and Cl^+ are mainly ejected back-to-back with equal momenta in the centre-of-mass frame, while the lightest fragment H is nearly at rest and carries negligible momentum. These are the low KER events producing a neutral H with very small energy. On the other hand, the small fraction of very high KER events can be ascribed to the Coulomb explosion of the parent trication (where H^+ is undetected), as mentioned above. In this case, H^+ being the lightest, carries maximum energy during the explosion.

Next, to understand the fragmentation mechanism for the three-body breakup events, we have obtained the Dalitz plot which is an extremely useful tool in reconstructing the complete kinematic information of three-body dissociation pathways [174, 180, 182, 193]. It is a momentum correlation map representing the distribution of the dissociation process in the final state in terms of the arrangement of the final momentum vectors [194]. The scale of the Dalitz plot is normalized by energy, and momentum conservation confines all the dissociation events in a circle of radius 1/3. Therefore, the plot reveals the final state geometries of the precursor during its three-body dissociation, in a two-dimensional phase space. In the Dalitz plot, the y-axis represents the fraction of energy carried by H, while the x-axis corresponds to the difference in the fraction of energy carried by CH_2^+ and Cl^+ ions. The centre represents the origin of the Cartesian coordinate system, while the axes x_D and y_D are given by:

$$x_D = (p^2_{CH_2^+} - p^2_{Cl^+})/\sqrt{3}\sum p_i^2, \;\; y_D = p_H^2/\sum p_i^2 - 1/3, \tag{5.3}$$

where $i = 1, 2, 3$ represent the fragments CH_2^+, Cl^+, and H, respectively and

p_i represents the momentum of each fragment in the center-of-mass frame of the molecule [182]. Usually, the coordinates x_D and y_D represent the relationship between the kinetic energy of the ith fragment in the centre-of-mass frame normalized by the total kinetic energy release, to the final arrangement of the momentum vectors. Here, the Dalitz coordinates x_D, and y_D are a function of p_i^2 due to the negligible mass of H compared to CH_2^+ and Cl^+, similar to reference [182].

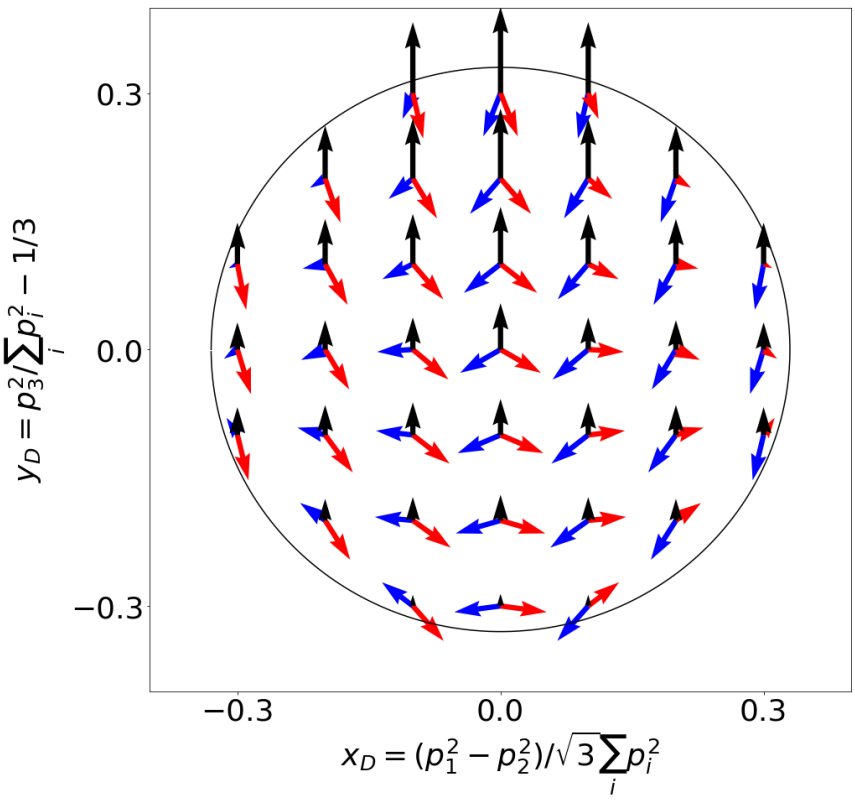

FIGURE 5.3: Calculated Dalitz plot for the $CH_2^+ + Cl^+$ pathway. The black, blue and red arrows indicate the momentum vectors of H, CH_2^+ and Cl^+, respectively.

Figure 5.3 shows the calculated Dalitz plot for the $CH_2^+ + Cl^+$ pathway, where the black, blue, and red arrows indicate the momentum vectors of H, CH_2^+, and Cl^+, respectively. Comparing the calculated and experimental Dalitz plots, we have tried to explain the fragmentation mechanism and the final state geometry of the molecular ion at the time of dissociation. Figure 5.4 shows the Dalitz plot for the $CH_2^+ + Cl^+$ pathway obtained using 29 fs, 800 nm pulses of intensity 4.3×10^{13} W/cm^2. As seen in the plot, the majority of the events appear centered at (−0.14,−0.29), while some events appear in the second quadrant of the plot. Using filters on the total

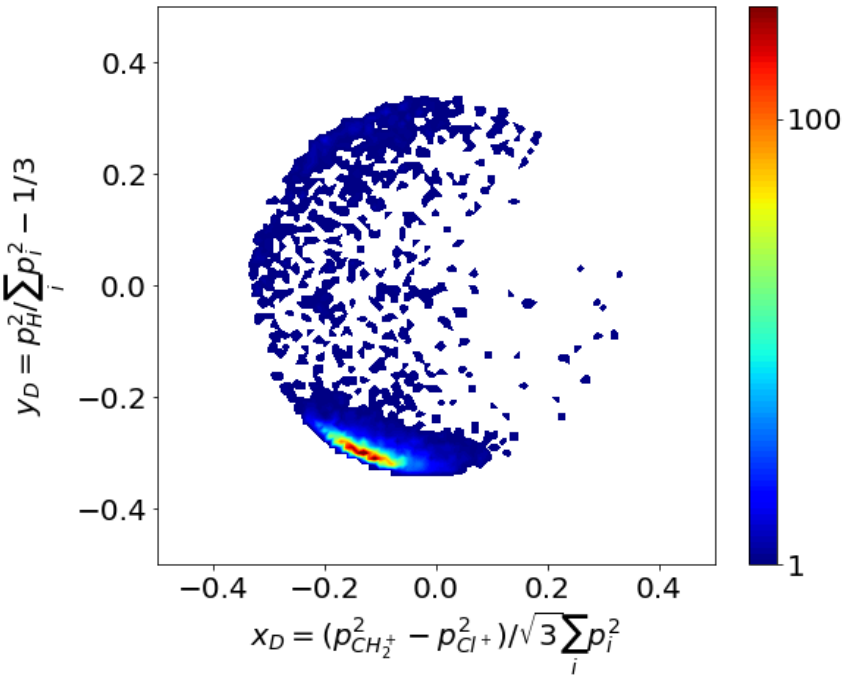

FIGURE 5.4: Dalitz plot for the $CH_2^+ + Cl^+$ pathway obtained for 29 fs pulses of intensity $I = 4.3 \times 10^{13}$ W/cm^2, wavelength 800 nm, and linear polarization.

KER, we have shown the same Dalitz plot separately for KERs below and above 7 eV separately in figures 5.5a and 5.5b, respectively. As seen in figure 5.5a for the low KER events, H carries nearly zero momentum, while the momenta of CH_2^+ and Cl^+ are nearly equal in magnitude. These events mainly correspond to the asynchronous concerted dissociation (asymmetric stretching of the bonds) of the parent ion; that is, there is geometrical deformation in the parent molecule before dissociation. This can also be confirmed from the calculated Dalitz plot in figure 5.3. Some events also arise from the synchronous concerted dissociation. On the other hand, the events with KER $>$ 7 eV appear in the upper left region of the Dalitz plot (figure 5.5b). In this case, H/H^+ is ejected with very high energy and can, therefore, be attributed to the three-body Coulomb explosion of CH_3Cl^{3+}, as discussed above.

Now, the three-body breakup of CH_3Cl^{2+} can be either concerted or sequential. In the concerted fragmentation mechanism, the Coulomb explosion of the precursor leads to the ejection of the fragments in a single step,

$$CH_3Cl^{2+} \longrightarrow CH_2^+ + Cl^+ + H, \tag{5.4}$$

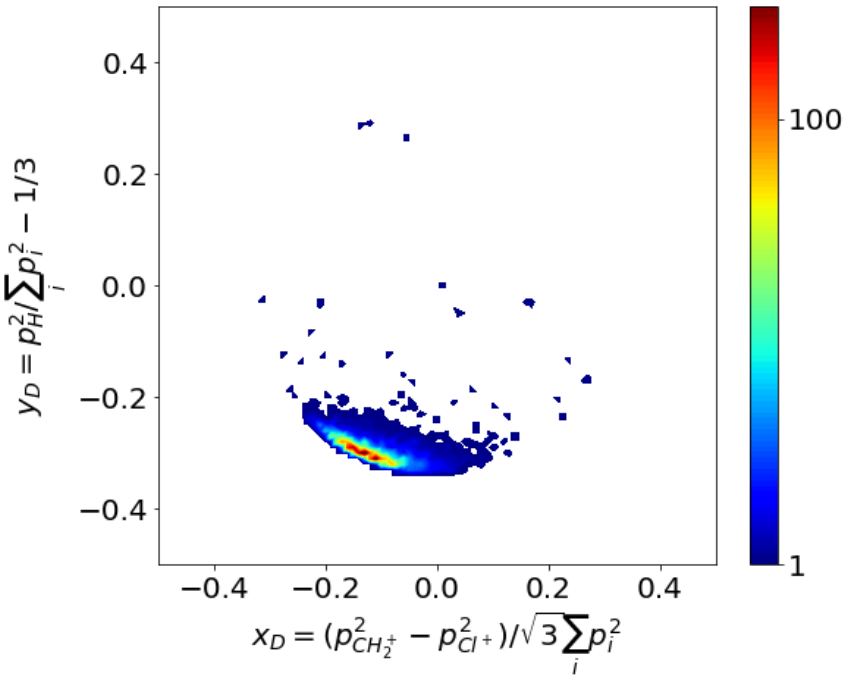

(A) KER < 7 eV

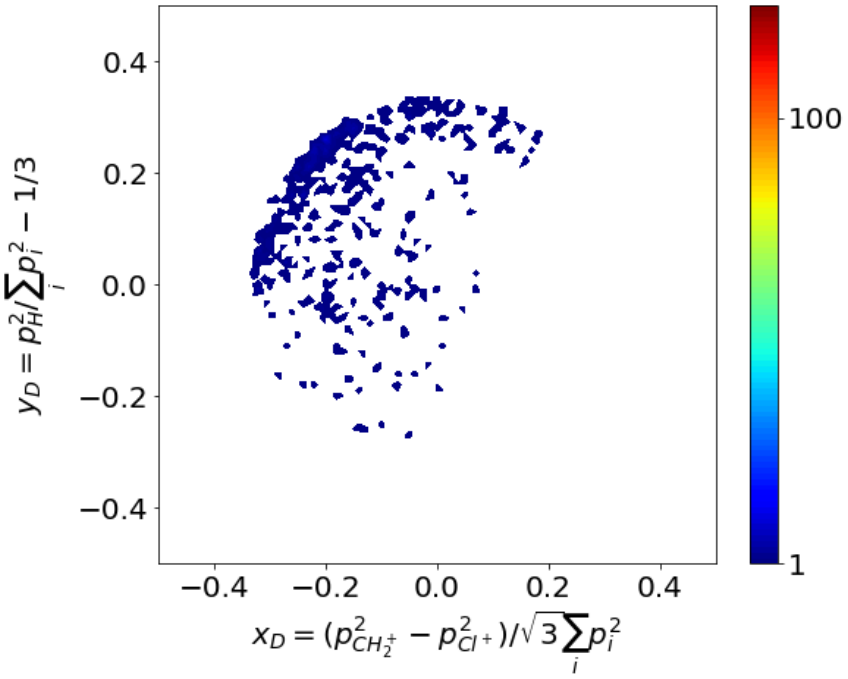

(B) KER > 7 eV

FIGURE 5.5: Dalitz plot for the $CH_2^+ + Cl^+$ pathway shown in figure 5.4 using filters on the KER.

while the sequential three-body fragmentation may proceed along one of the three pathways:

$$CH_3Cl^{2+} \longrightarrow CH_3^+ + Cl^+ \longrightarrow CH_2^+ + Cl^+ + H \tag{5.5}$$

$$CH_3Cl^{2+} \longrightarrow CH_2Cl^{2+} + H \longrightarrow CH_2^+ + Cl^+ + H \tag{5.6}$$

$$CH_3Cl^{2+} \longrightarrow CH_2^+ + HCl^+ \longrightarrow CH_2^+ + Cl^+ + H. \tag{5.7}$$

Pathway (5.5) proceeds with the C-Cl bond breakup leading to the ejection of Cl^+ and an intermediate CH_3^+ in the first step. In the second step, the CH_3^+ intermediate dissociates into CH_2^+ and a neutral H. In pathway (5.6), the neutral H is released in the first step of fragmentation, followed by the separation of CH_2^+ and Cl^+ in the second step. This process is referred to as deferred charged separation [195, 196]. Pathway (5.7) is slightly different from the previous two. It involves an intramolecular H migration and the formation of the stable H_2CClH^{2+} isomer before the C-Cl bond breaks into CH_2^+ and an intermediate HCl^+ ion. In the next step, HCl^+ dissociates into a neutral H and a Cl^+ ion. Duflot et al. theoretically obtained the potential energy diagrams for the various two- and three-body dissociation pathways of CH_3Cl^{2+} [151]. In this study, the deferred charge separation along the pathway (5.6) was reported to be difficult to observe experimentally due to the presence of two large barriers, which was also confirmed in a previous experimental study by Ruhl et al. [152]. We shall now investigate the fragmentation mechanism for the $CH_2^+ + Cl^+$ pathway.

Duflot et al. [151] demonstrated the three-body breakup of CH_3Cl^{2+} along the $CH_2^+ + Cl^+ + H$ pathway sequentially using energy diagrams. From this study it was clear that the sequential mechanism involving a CH_3^+ or HCl^+ intermediate involves large potential energy barriers which reduces the probability of the dissociation of the dication along these pathways. On the other hand, the sequential pathway involving a CH_2Cl^{2+} intermediate has much lower barriers, making this more probable.

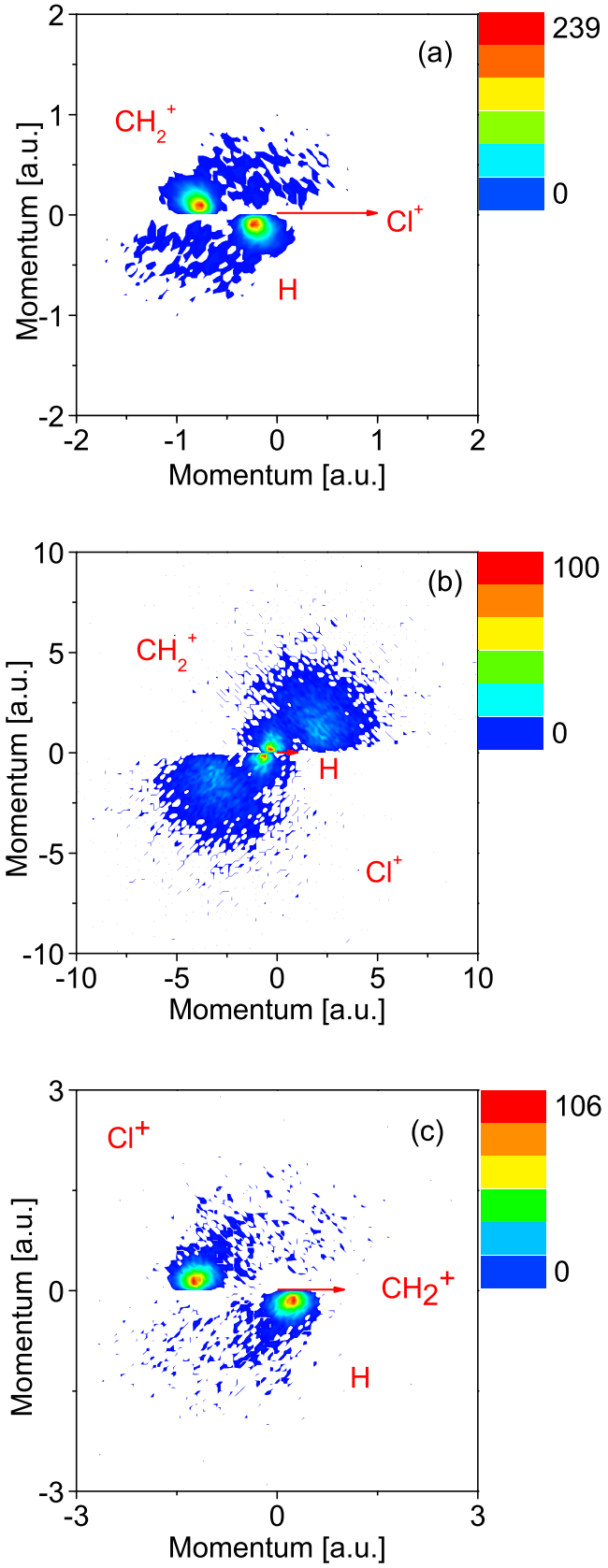

FIGURE 5.6: Newton diagrams showing the momentum correlations between the fragments with respect to (a) Cl^+ (b) H, and (c) CH_2^+, obtained for 29 fs, 800 nm pulses of intensity 4.3×10^{13} W/cm^2. (int = intermediate)

To confirm the fragmentation mechanism, we have obtained the Newton diagrams. The Newton diagram is a momentum correlation map in which the normalized momentum of one of the fragments is taken as the reference, and the momenta of the other two fragments normalized by that of the reference are plotted above and below the x-axis, respectively. The Newton diagrams for the $CH_2^+ + Cl^+$ pathway with respect to Cl^+, H and CH_2^+ are shown in figures 5.6 (a)-(c). A semicircular pattern in the Newton diagram indicates sequential fragmentation where the intermediate has a long lifetime during which it undergoes rotation before dissociating.

It must be noted that for multiply-ionized polyatomic molecules like CH_3Cl, the three-body fragmentation of the molecular ion is expected to take place along various dissociation pathways. Therefore, we have obtained the Newton diagrams with respect to the normalized momentum of H, CH_2^+ and Cl^+ to investigate the possible fragmentation mechanisms. With respect to the momentum of Cl^+, figure 5.6 (a) shows dense regions above and below the x-axis suggesting that these events arise from the concerted mechanism. For these events, H carries very little momentum (position of the dense region in the Newton diagram is close to zero momentum), while CH_2^+ and Cl^+ are ejected with nearly equal and substantial momenta in opposite directions. In addition, some events having higher momenta form a distribution, indicating an overlap between mostly concerted and very few sequential processes.

Next, figure 5.6 (b) shows the momentum correlation with respect to H, where we observe two dense regions above and below the x-axis. Both the regions correspond to the concerted mechanism. The region having smaller momentum may be attributed to the double-ionization events, while the events having higher momenta may be attributed to the high KER Coulomb explosion in the triple-ionization events. Additionally, some sparse events can be seen forming a semicircular pattern which can be attributed to the sequential fragmentation involving a CH_2Cl^{2+} intermediate.

Lastly, figure 5.6 (c) shows the momentum correlation with respect to CH_2^+. Again, most events arise from the concerted mechanism. H carries nearly zero momentum for these events. In addition, a very few events show a semicircular pattern,

originating from a sequential mechanism. Therefore, in the dissociation pathway $CH_2^+ + Cl^+$, concerted mechanism (5.4) is dominant, although some sequential processes along pathways (5.5)-(5.7) take place as well.

Since the three-body dissociation along the $CH_2^+ + Cl^+$ pathway is complicated and simultaneously involves concerted and sequential mechanisms, the Dalitz plot and Newton diagram have overlapping regions indicating both the processes. Hence, the Dalitz plot and Newton diagram are not always sufficient to distinguish between them. Therefore, we have used the native frame method developed by Rajput et al. [191] to distinguish between concerted and sequential mechanisms. In this method, we assume all dissociation processes to be sequential with a metastable intermediate, having a long lifetime (of the order of ps). Therefore, for the pathway $ABC^{3+} \longrightarrow A^+ + BC^{2+} \longrightarrow A^+ + B^+ + C^+$, we obtain the plot between $KER_{BC^{2+}}$ and $\gamma_{BC^{2+}}$ [197], where $KER_{BC^{2+}}$ is the KER of the intermediate (BC^{2+}) and $\gamma_{BC^{2+}}$ is the angle between the fragmentation axis of the first step in the center-of-mass (COM) frame of ABC^{3+} and the fragmentation axis of the second step in the COM frame of BC^{2+}. Now, $\gamma_{BC^{2+}}$ is given by

$$\gamma_{BC^{2+}} = \cos^{-1}\left(\frac{\Delta\vec{p}_{1st}.\Delta\vec{p}_{2nd}}{|\Delta\vec{p}_{1st}||\Delta\vec{p}_{2nd}|}\right), \tag{5.8}$$

where, $\Delta\vec{p}_{1st}$ is the difference between the momentum vectors of A^+ and BC^{2+} in the COM frame of ABC^{3+}, and $\Delta\vec{p}_{2nd}$ is the difference between the momentum vectors of B^+ and C^+ in the COM frame of BC^{2+}, that is

$$\Delta\vec{p}_{1st} = \vec{p}_A - (\vec{p}_B + \vec{p}_C), \tag{5.9}$$

$$\Delta\vec{p}_{2nd} = \left(\vec{p}_B + \frac{m_B}{m_{BC}}.\vec{p}_A\right) - \left(\vec{p}_C + \frac{m_C}{m_{BC}}.\vec{p}_A\right). \tag{5.10}$$

As the sequential mechanism can proceed along either of the pathways (5.5)-(5.7), we have obtained the $KER_{BC^{2+}}$ vs $\gamma_{BC^{2+}}$ plots for each of the processes (shown in figures 5.8a-5.8c). A uniform distribution of the events along γ from 0° to 180° indicates a sequential mechanism due to the rotation of the metastable intermediate

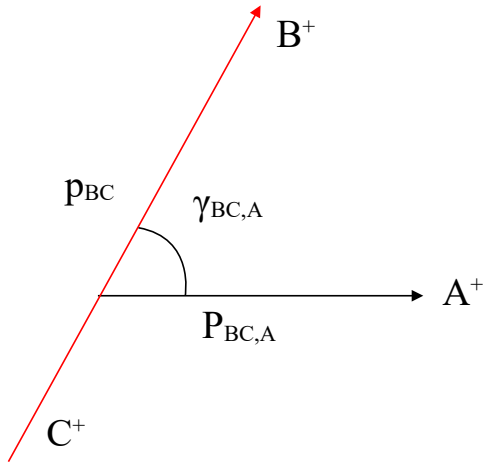

FIGURE 5.7: Relative momenta of the three-body dissociation $ABC^{3+} \longrightarrow A^{+} + BC^{2+} \longrightarrow A^{+} + B^{+} + C^{+}$. The black and red arrows indicate the momenta of the first and second steps, while $\gamma_{BC,A}$ represents the angle between them.

ion, otherwise, the dissociation is concerted.

Considering the three-body breakup along the sequential pathway (5.5) with a CH_3^+ intermediate, figure 5.8a shows that the majority of the events are concentrated in the dense region ranging from 0° to 100° and centered at $\sim$ 35° which indicate a concerted mechanism. Very few events appear forming a band distribution along $\gamma_{CH_3^+,Cl^+}$ indicating a sequential mechanism as well. We also note that the high-energy events have a concerted mechanism.

Next, considering the sequential fragmentation along pathway (5.6) with a CH_2Cl^{2+} intermediate, a uniform band distribution centred at $KER_{CH_2Cl^+} = 0.3$ eV (figure 5.8b) is observed along the entire range of $\gamma_{CH_2Cl^{2+}}$. These events arise from the sequential mechanism with a CH_2Cl^{2+}. In addition, we observe another dense region in figure 5.8b centered at 0.3 eV which arises from the concerted mechanism. The yield of the sequential pathway (5.6) can be obtained from the counts in the entire range of $\gamma_{CH_3^+,Cl^+}$ [197]. Then, the yield of the concerted mechanism (5.4) can be obtained from the counts in the dense region extending from $\gamma_{CH_3^+,Cl^+} = 0°$ to 100°. Therefore, the branching ratios of the sequential and concerted pathways, in this case, are determined to be 25% and 75%, respectively.

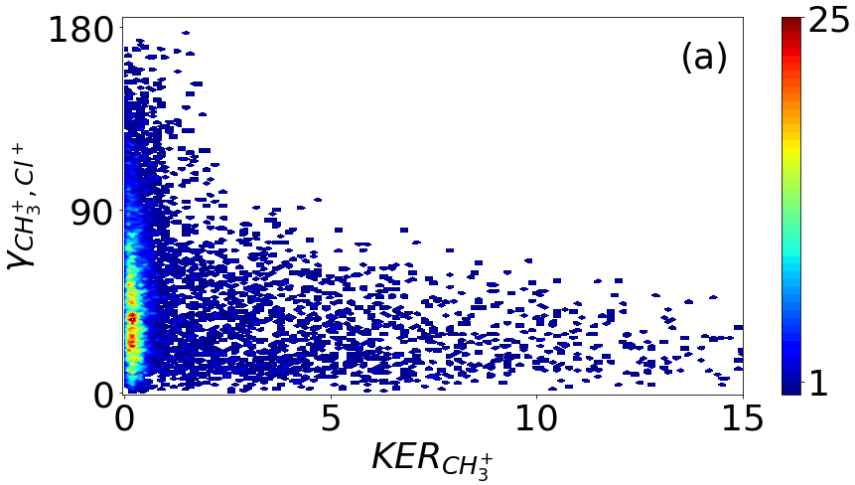

(A) CH_3^+ intermediate

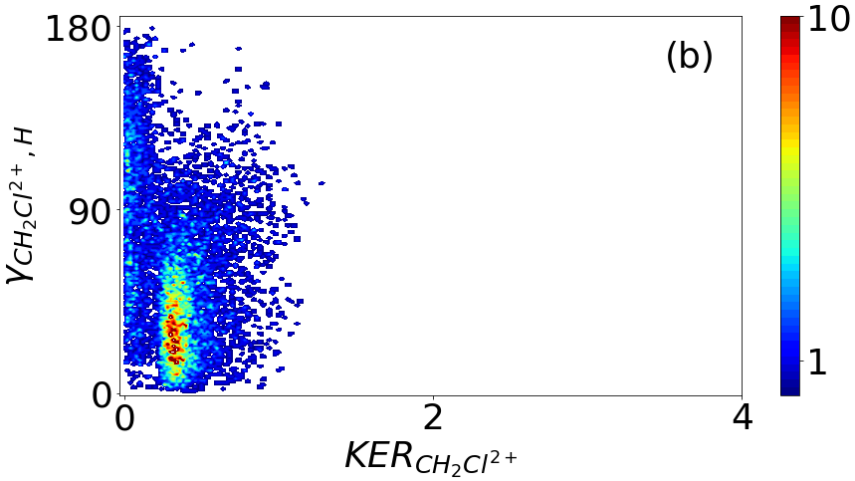

(B) CH_2Cl^{2+} intermediate

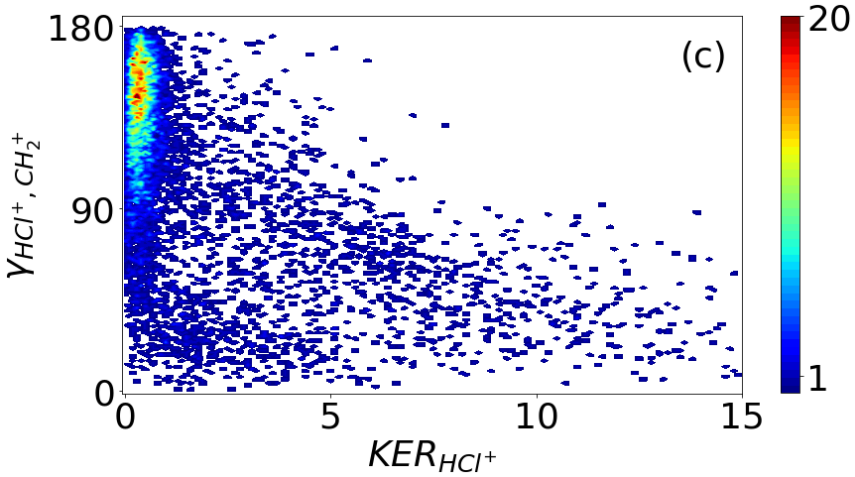

(C) HCl^+ intermediate

FIGURE 5.8: Density plot as a function of KER_{int} and γ_{int} for the sequential fragmentation via (a) $CH_3^+ + Cl^+$, (b) CH_2Cl^+, and (c) $CH_2^+ + Cl^+$ pathways, obtained for 29 fs, 800 nm pulses of intensity 4.3×10^{13} W/cm^2. (int = intermediate)

Finally, considering the three-body breakup along pathway 5.7 with an HCl^+ intermediate, the density plot in figure (5.8c) suggests that the dissociation is mainly concerted. Only a very few events form a uniform band distribution along γ_{HCl^+,CH_2^+} indicating that the sequential mechanism involving an HCl^+ intermediate is scarcely present. Thus, we conclude that for the $CH_2^+ + Cl^+$ pathway, the fragmentation proceeds primarily concertedly (5.5) along with some sequential processes. In addition, we observe a clear distribution of events along γ for the CH_2Cl^{2+} intermediate in figure 5.8b, which is very sparse in the other two cases. Therefore, our results confirm that this sequential pathway is more probable compared to the other two due to the low potential barriers involved, as also shown in ref. [151].

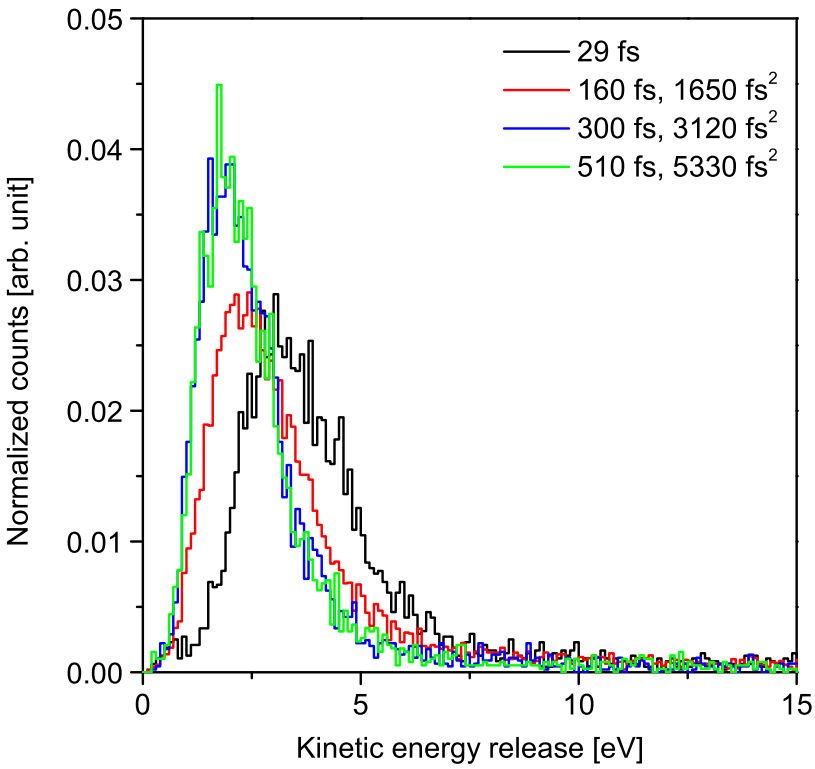

FIGURE 5.9: Kinetic energy release distribution (KERD) for the pathway $CH_3Cl^{2+} \longrightarrow CH_2^+ + Cl^+ + H$ for pulse durations ranging from 29 fs to 510 fs at the fixed intensity $I = 4.3 \times 10^{13}$ W/cm^2. The other laser parameters (wavelength = 800 nm, intensity = 4.3×10^{13} W/cm^2, polarization = linear) are constant in all the cases.

Next, to investigate the effect of chirped pulses on the fragmentation mechanism along the CH_2^+ + Cl^+ pathway, we performed the strong-field ionization of CH_3Cl

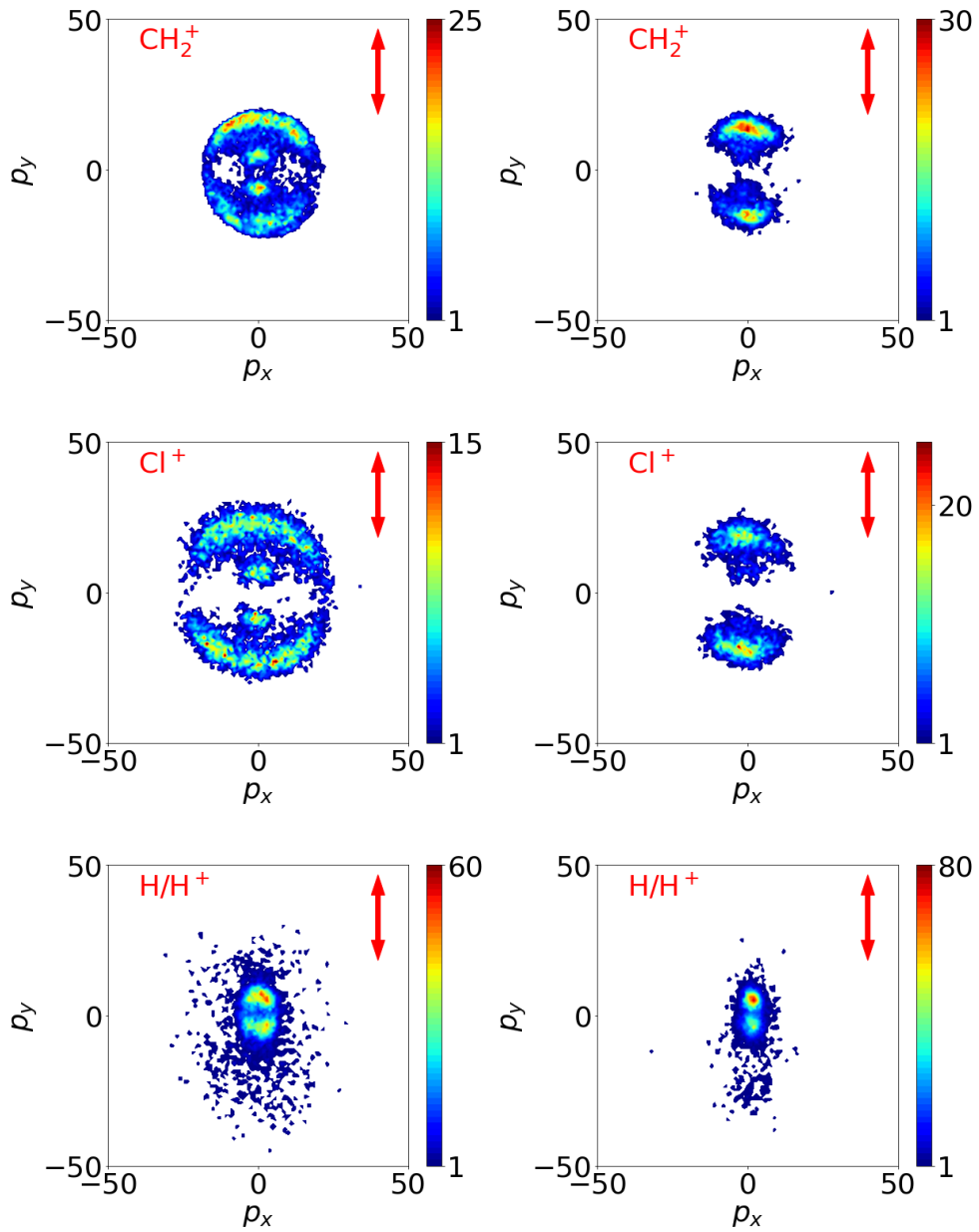

FIGURE 5.10: Two-dimensional coincidence momentum images of CH_2^+, Cl^+ and H/H^+ fragments. The left panel shows the images obtained for 29 fs (unchirped) pulses while that on the right was obtained for 510 fs (chirp = 5330 fs^2) pulses. The other laser parameters like wavelength (800 nm) and intensity (4.3×10^{13} W/cm^2) were maintained constant in both cases. The laser polarization direction is indicated by the red arrow.

with increasingly chirped pulses of constant intensity (as discussed in chapter 4). The total KER distribution of the pathway for pulses of various chirps is shown in figure 5.9. The KER peak shifts from 3.1 eV for unchirped pulses to 1.8 eV for 510 fs (chirp = 5330 fs^2) pulses. A shift in the KER peak to lower energy values is attributed to the dissociation of the parent ion from repulsive PESs [47], as discussed in chapter 4. On using chirped pulses for ionizing CH_3Cl, more energy is transferred to the molecule thereby, causing its rapid explosion and a smaller dissociation time. We compared the two-dimensional coincidence momentum images of the CH_2^+, Cl^+ and H fragments obtained for unchirped and chirped (510 fs, 5330 fs^2) pulses in figure 5.10. The images in the left panel were obtained for unchirped (29 fs) pulses, while those on the right were obtained for chirped (510 fs, 5330 fs^2) pulses. We clearly observe an enhanced anisotropy in the fragment ejection direction when using chirped pulses for ionizing CH_3Cl. This observation can be ascribed to a rapid dissociation of the precursor associated with its evolution on a Coulombic PES.

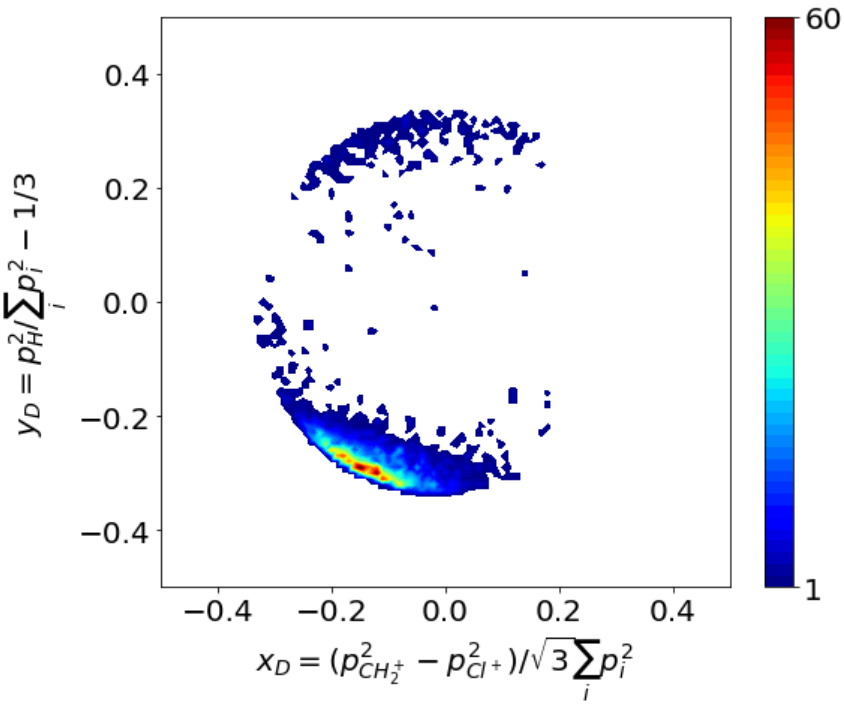

FIGURE 5.11: Dalitz plot for the $CH_2^+ + Cl^+$ pathway obtained for 510 fs (5330 fs^2) pulses of intensity $I = 4.3 \times 10^{13}$ W/cm^2, wavelength 800 nm, and linear polarization.

The Dalitz plot obtained for a case of ionization of CH_3Cl by chirped pulses (510

fs, 5330 fs^2) is shown in figure 5.11. On comparison with the plot obtained for the unchirped pulses (figure 5.4), it is observed that the events are mainly concentrated in the lower left corner of the plot, with very few events in the other regions, in the case of chirped pulses. This indicates that the dissociation pathways having low KER are now dominant along with reduced high KER events, which is also confirmed by a shift in the KER peak to a lower energy value (figure 5.9). As dissociation is taking place rapidly from a highly repulsive PES in the case of chirped pulses, the bonds stretch to a large extent, leading to the ejection of the fragments with lower KERs.

The Newton diagrams shown in figures 5.12 (a)-(c) represent the momentum correlations with respect to Cl^+, H, and CH_2^+, respectively. Comparing with the Newton diagrams obtained previously for the unchirped pulses (5.6), we observe that the few events showing a sequential mechanism are now suppressed, and dissociation is primarily concerted. Therefore, chirping the pulses affects the PESs populated by the parent ion, the subsequent excited-state dynamics, and hence, the fragmentation mechanism.

Using the native frame method, we tried to distinguish between the concerted and sequential mechanisms in figure (5.13a)-(5.13c). In the case of the CH_3^+ intermediate, the plot (5.13a) shows a dense region for $\gamma_{CH_3^+,Cl^+}$ ranging from 0° to 90°. We do not observe a uniform band distribution up to 180°, which suggests that for this pathway, dissociation is primarily concerted. Similarly, for the HCl^+ intermediate again, the density plot (5.13c) indicates a concerted mechanism of breakup and a complete absence of the sequential pathway 5.7. However, for the CH_2Cl^+ intermediate, we observe some events forming a uniform band distribution along $\gamma_{CH_3^+,Cl^+}$ along with a dense region (from 0° to 80°) thereby, suggesting an overlap between concerted and sequential (5.6) mechanisms with a branching ratio of 21% and 79%, respectively. We, therefore, see that there is a slight reduction in the number of events having a sequential mechanism, and concerted is still the dominant process.

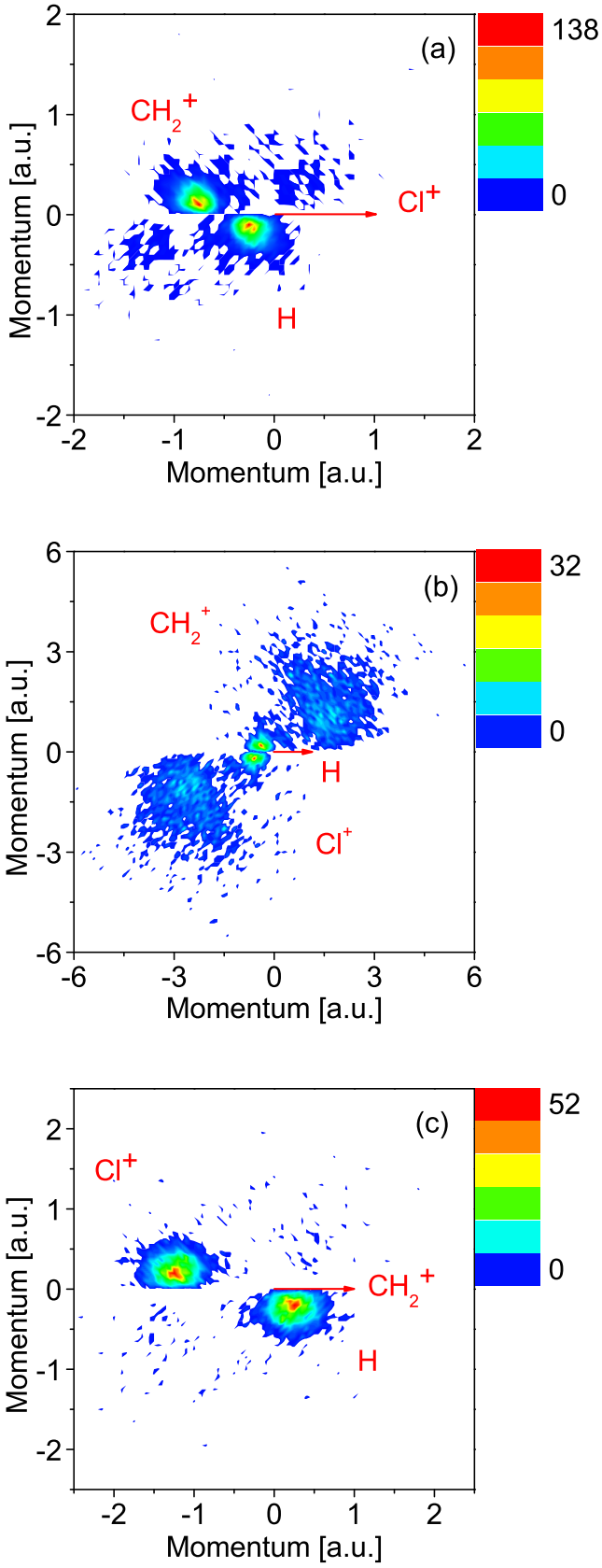

FIGURE 5.12: Newton diagrams showing the momentum correlations between the fragments with respect to (a) Cl^+ (b) H, and (c) CH_2^+, obtained for 510 fs (5330 fs^2), 800 nm pulses of intensity 4.3×10^{13} W/cm^2. (int = intermediate)

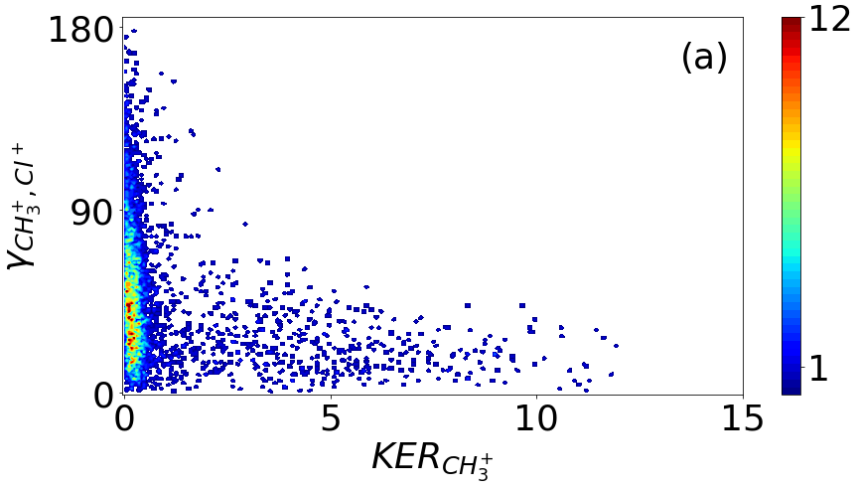

(A) CH_3^+ intermediate

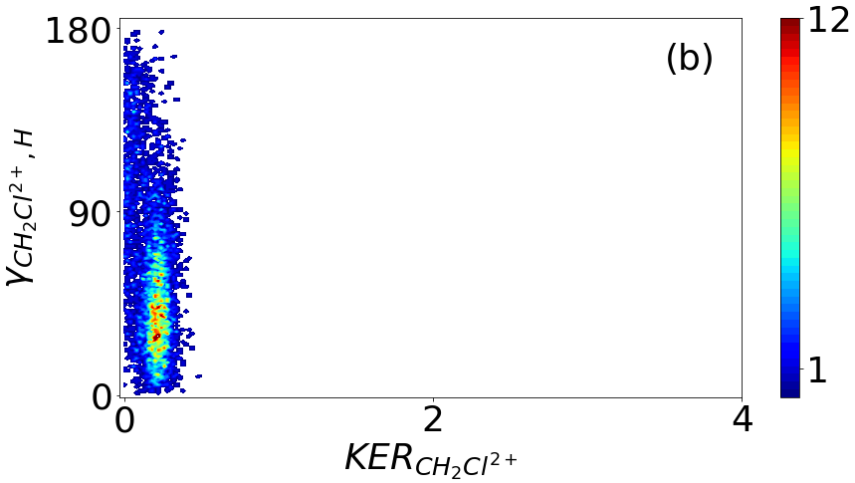

(B) CH_2Cl^{2+} intermediate

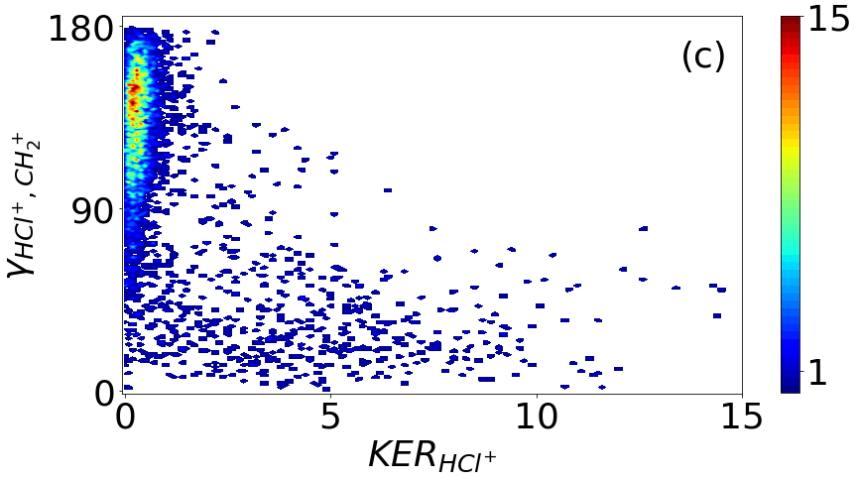

(C) HCl^+ intermediate

FIGURE 5.13: Density plot as a function of KER_{int} and γ_{int} for the sequential fragmentation via (a) $CH_3^+ + Cl^+$, (b) CH_2Cl^+, and (c) $CH_2^+ + Cl^+$ pathways, obtained for 510 fs (5330 fs^2), 800 nm pulses of intensity 4.3×10^{13} W/cm^2. (int = intermediate)

5.1.2 Pathway 2: $H^+ + CH_2^+$

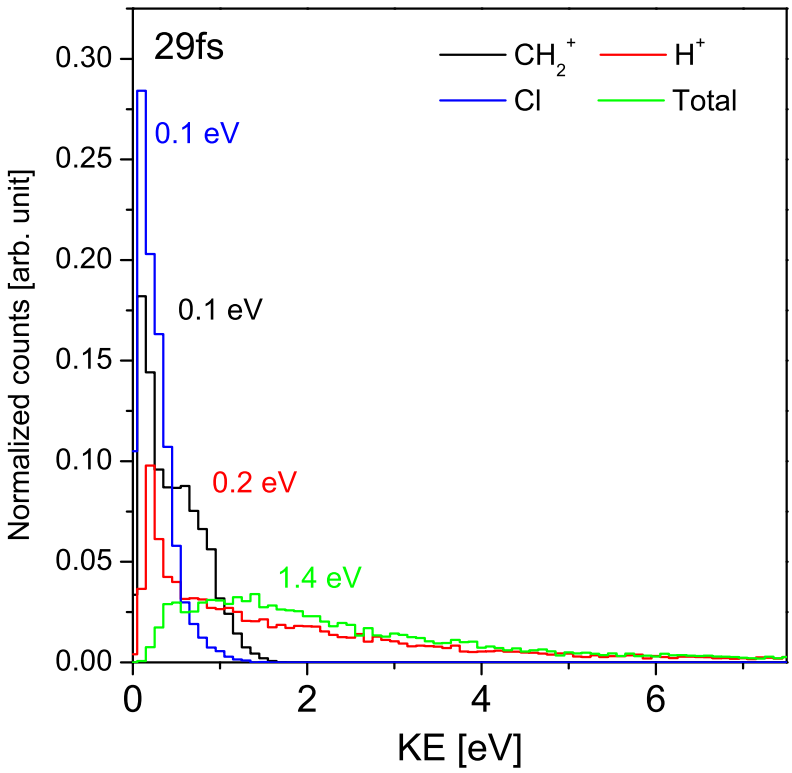

FIGURE 5.14: Kinetic energy distribution for the fragmentation channel $CH_3Cl^{2+} \longrightarrow H^+ + CH_2^+ + Cl$ for 29 fs pulses of intensity $I = 4.3 \times 10^{13}$ W/cm^2, wavelength 800 nm, and linear polarization.

For this three-body breakup channel (figure 4.2), it is difficult to predict the fragmentation mechanism directly from the slope of the island due to its broad distribution. Therefore, we must rely on the Dalitz plot and native frame method to explain the fragmentation dynamics. Firstly, figure 5.14 shows the kinetic energy distributions of the fragments and the total KER. H^+ being the lightest of the three fragments, carries the maximum kinetic energy and hence, shows a broad kinetic energy distribution ranging from 0 to 7 eV, with a peak at 0.2 eV. The heavier fragments, CH_2^+ and Cl, move much more slowly, and their kinetic energy distributions peak at 0.1 eV.

To understand the fragmentation mechanism for this pathway, we have again obtained the Dalitz plot, as shown in figure 5.15. Most of the dissociation events in the plot are centered at (0,-0.3). This region corresponds to H^+ being ejected with

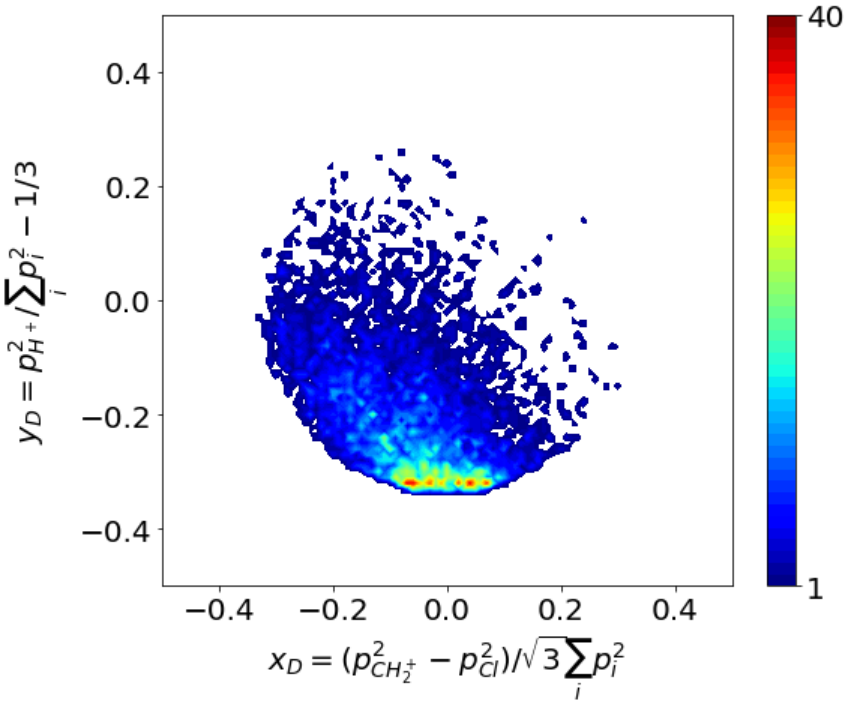

FIGURE 5.15: Dalitz plot for the $H^+ + CH_2^+$ pathway obtained for 29 fs pulses of intensity $I = 4.3 \times 10^{13}$ W/cm^2, wavelength 800 nm, and linear polarization.

very little momentum (nearly at rest), while CH_2^+ and Cl are ejected back-to-back with equal momentum. In addition, some events appear obliquely just above the dense region, which corresponds to an overlap between an asynchronous concerted dissociation (asymmetric stretching of the bonds before dissociation) and a sequential mechanism. The possible pathways leading to the formation of H^+, CH_2^+, and Cl fragments are:

$$CH_3Cl^{2+} \longrightarrow H^+ + CH_2^+ + Cl \tag{5.11}$$

$$CH_3Cl^{2+} \longrightarrow H^+ + CH_2Cl^+ \longrightarrow H^+ + CH_2^+ + Cl \tag{5.12}$$

$$CH_3Cl^{2+} \longrightarrow CH_2^+ + HCl^+ \longrightarrow H^+ + CH_2^+ + Cl \tag{5.13}$$

$$CH_3Cl^{2+} \longrightarrow CH_3^{2+} + Cl \longrightarrow H^+ + CH_2^+ + Cl. \tag{5.14}$$

Equation (5.11) represents the concerted breakup of the molecular ion, while equations (5.12)-(5.14) are the sequential pathways.

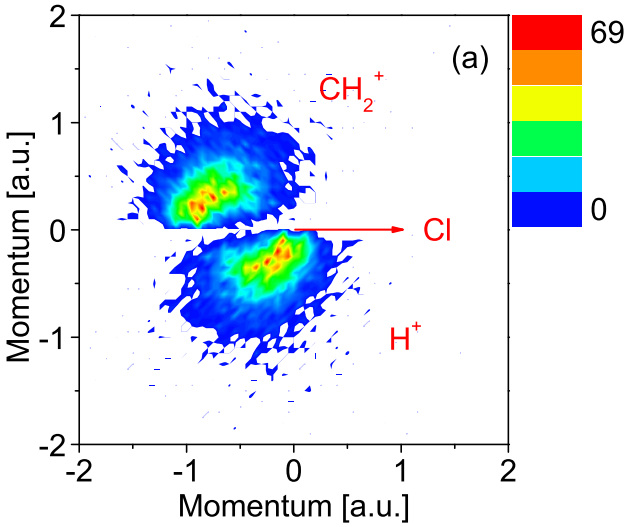

(A) CH_3^+ intermediate

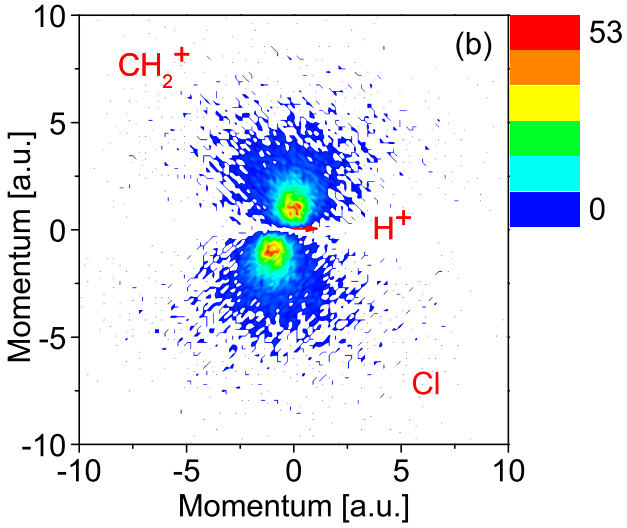

(B) CH_2Cl^{2+} intermediate

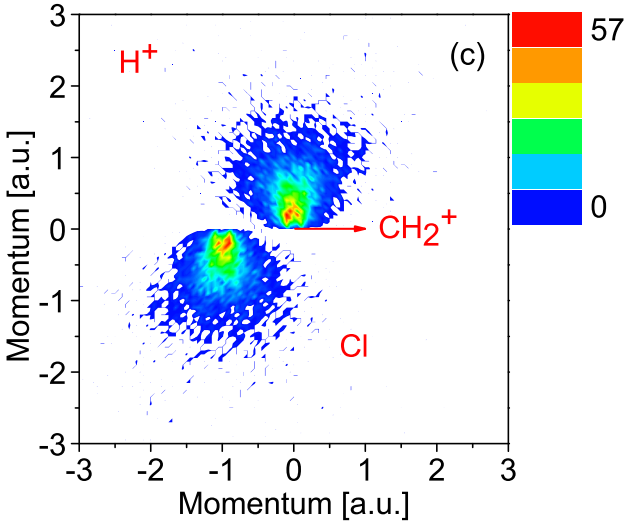

(C) HCl^+ intermediate

FIGURE 5.16: Newton diagrams showing the momentum correlations between the fragments with respect to (a) Cl^+ (b) H, and (c) CH_2^+, obtained for 29 fs, 800 nm pulses of intensity 4.3×10^{13} W/cm^2. (int = intermediate)

Figure 5.16 shows the Newton diagrams, where the momentum correlation between the fragments with respect to the momentum of (a) Cl^+, (b) H, and (c) CH_2^+ have been determined. The plots in figure 5.16 (b) and (c) show two dense regions above and below the x-axis, suggesting that the dissociation is primarily concerted. However, we observe a semicircular distribution in figure 5.16 (a), which indicates the sequential pathways (5.12). In fact, the Dalitz plot in figure 5.15 shows an oblique strip. Comparison with the calculated Dalitz plot in figure 5.3 suggests that in this region, the momentum vector of Cl shows no change (as it is released in the first step), while the momentum vectors of H^+ and CH_2^+ show change both in magnitude and the angle between them, suggesting the sequential mechanism with a CH_3^{2+} intermediate.

We again use the native frame method to further distinguish between the fragmentation mechanisms. The density plots of KER_{int} and γ_{int} for the CH_3^{2+}, CH_2Cl^+ and HCl^+ intermediates are shown in figures 5.17 (a)-(c), respectively. Again, we consider all fragmentation mechanisms to be sequential with a long-lived intermediate and perform the calculations in two steps in the COMs of the parent and the intermediate ions. For each of the pathways (5.12)-(5.14), shown in figures 5.17 (a)-(c), we observe an overlap of the sequential mechanism (uniform band distribution along the entire range of $\gamma_{CH_3^{2+},Cl}$) and the concerted pathway, although the concerted mechanism is the dominant dissociation pathway. In fact, it is difficult to separate the concerted and sequential pathways due to the overlapping of the two regions.

Finally, we investigate the effect of pulse chirp on the fragmentation mechanism along this three-body breakup pathway. Figure 5.18 shows the effect of pulse stretching on the KER distribution for the H^+ + CH_2^+ + Cl pathway. The KER peak shifts from 1.4 eV to 0.9 eV, that is, to lower energy values, as the ionizing pulses are increasingly positively chirped. This indicates the dissociation of the parent ion from repulsive PESs where the increased stretching of the bonds is mapped onto the KER [47]. In addition, we observe that the kinetic energy distribution of H^+ ranges to higher values (40 eV) for highly chirped (5330 fs^2) pulses compared to the unchirped

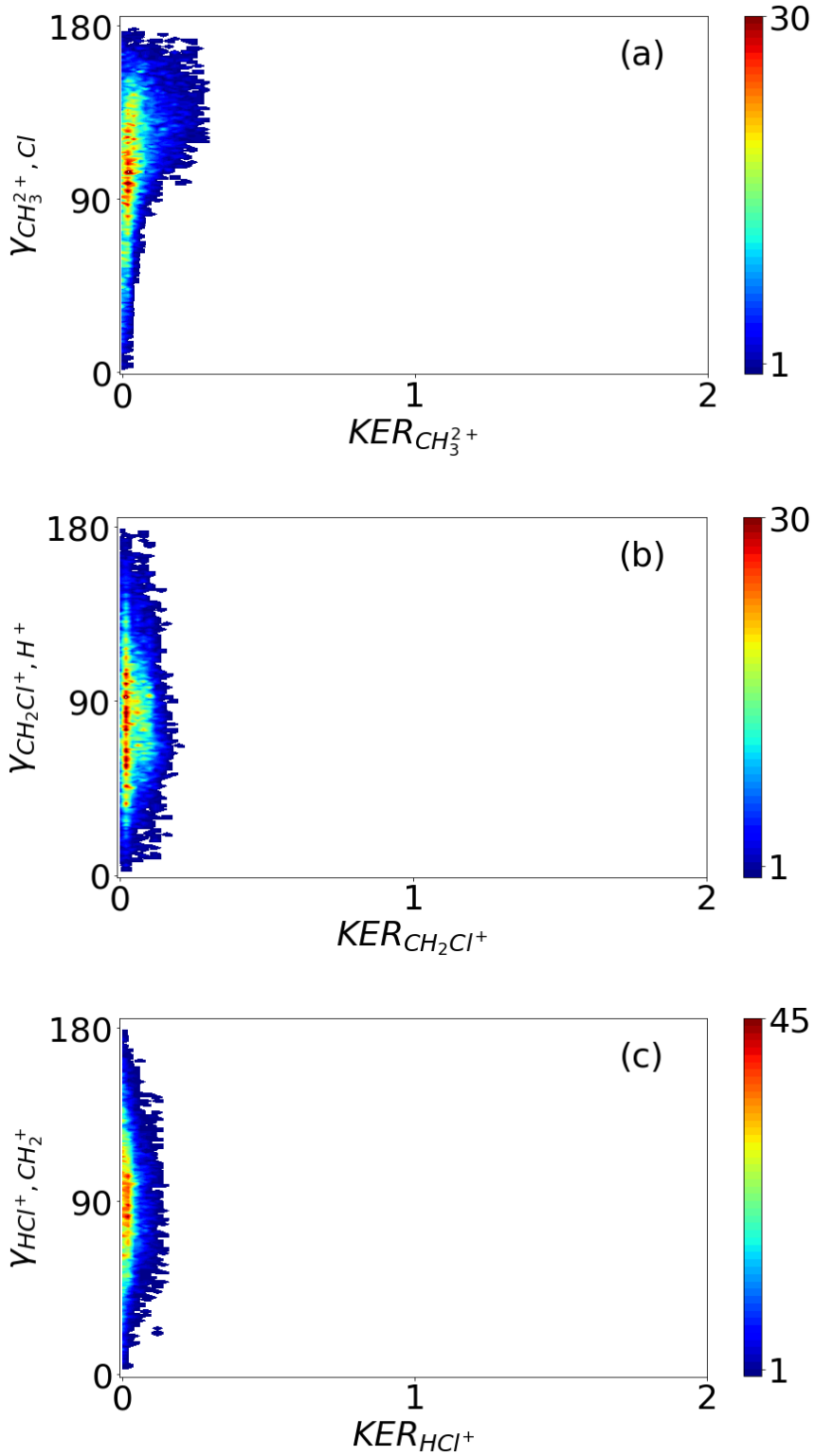

FIGURE 5.17: Density plot as a function of KER_{int} and γ_{int} for the sequential fragmentation via (a) $CH_3^+ + Cl^+$, (b) CH_2Cl^+, and (c) $CH_2^+ + Cl^+$ pathways, obtained for 29 fs, 800 nm pulses of intensity 4.3×10^{13} W/cm^2. (int = intermediate)

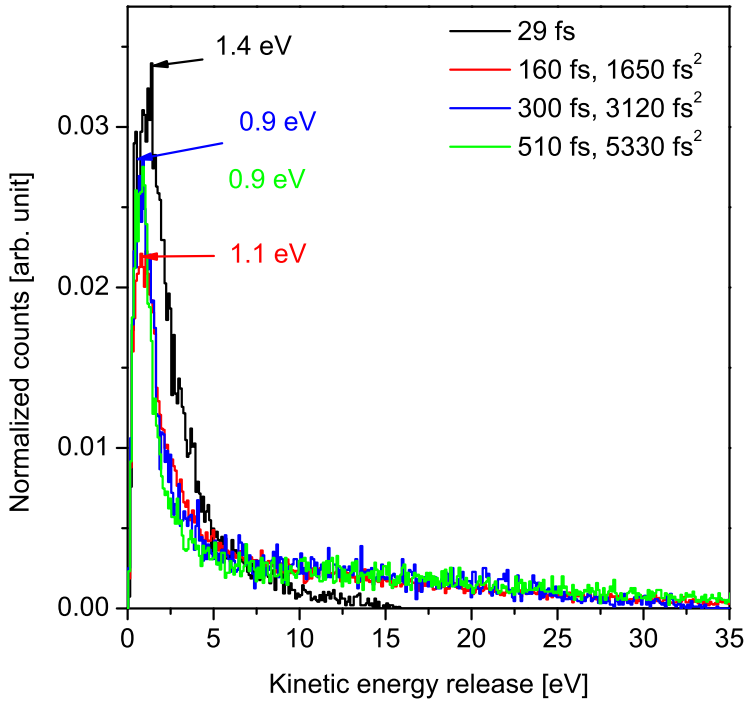

FIGURE 5.18: Kinetic energy release of the fragmentation channel $CH_3Cl^{2+} \longrightarrow H^+ + CH_2^+ + Cl$ for pulse durations ranging from 29 fs to 510 fs (GDD = 5330 fs^2) at the fixed intensity $I = 4.3 \times 10^{13}$ W/cm^2. The other laser parameters (wavelength = 800 nm, polarization = linear) are constant in all the cases.

pulses (12 eV). As a result, the KER tail is found to extend to much higher values (> 30 eV) for pulses having a duration of 160 fs and above. This observation may be attributed to the contamination from the three-body dissociation of CH_3Cl^{3+}, where the Coulomb explosion of the trication leads to the ejection of H^+ with very high kinetic energy.

Next, we have obtained the Dalitz plot, shown in figure 5.18. A small dense region is observed, centered at (-0.02,0.29) corresponding to the ejection of CH_2^+ and Cl with equal momenta in opposite directions, leaving H^+ nearly at rest. In addition, a significant number of events is observed in a broad oblique strip in the Dalitz plot. This region corresponds to an overlap between the sequential and concerted fragmentation pathways.

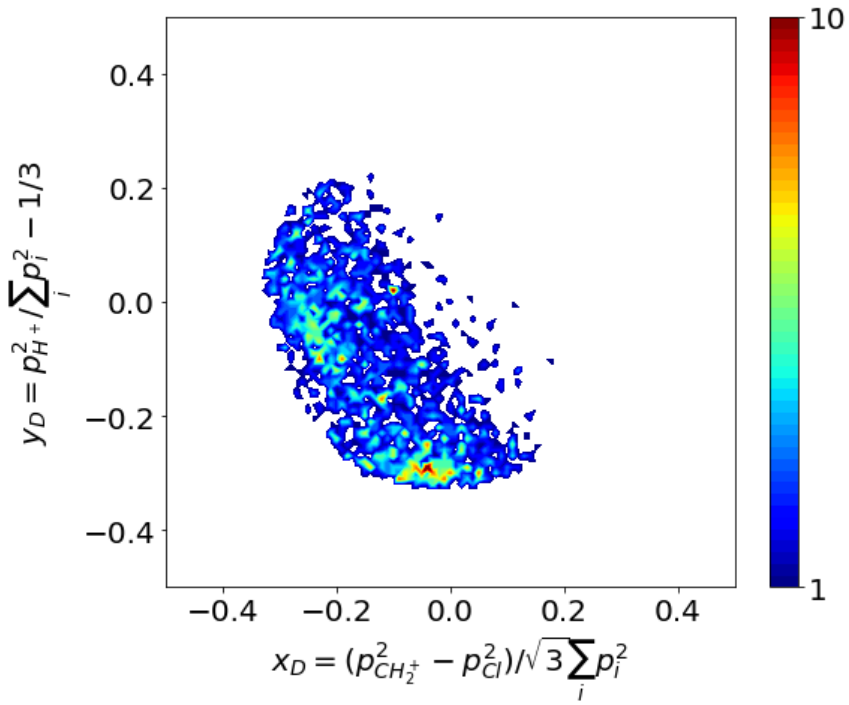

FIGURE 5.19: Dalitz plot for the $H^+ + CH_2^+$ pathway obtained for 510 fs (5330 fs^2) pulses of intensity $I = 4.3 \times 10^{13}$ W/cm^2, wavelength 800 nm, and linear polarization.

The Newton diagrams for chirped pulses are shown in figures 5.20 (a)-(c). For the momentum correlation map with respect to Cl, we observe a nearly semicircular pattern suggesting a sequential mechanism with a CH_3^{2+} intermediate. For the other two diagrams, concerted mechanism appears dominant, while the sequential mechanism (observed for a few events for unchirped pulses in figure 5.16) is less.

We confirm the fragmentation mechanism further by obtaining the density plots obtained using the native frame method as shown in figures (5.21a)-(5.21c). For the CH_3^{2+} intermediate pathway, a band-like distribution is observed, suggesting some sequential processes, along with events arising from concerted dissociation. For the CH_2Cl^+ and HCl^+ intermediate pathways, the events take place mainly by concerted mechanism, and we observe that the sequential mechanism is nearly suppressed. Therefore, introducing a positive chirp to the pulses leads to the dissociation of the parent ion along the $H^+ + CH_2^+$ pathway in a concerted manner with a near suppression of the sequential mechanism.

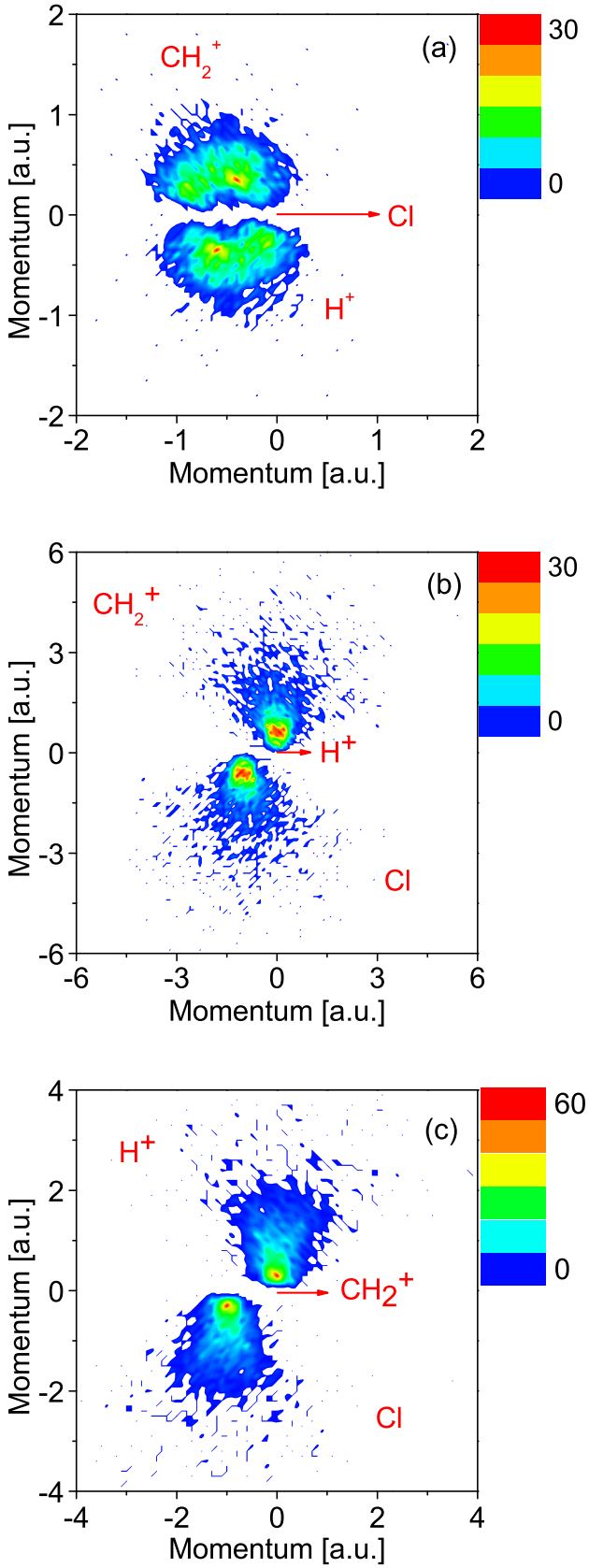

FIGURE 5.20: Newton diagrams showing the momentum correlations between the fragments with respect to (a) Cl^+ (b) H, and (c) CH_2^+, obtained for 510 fs, 800 nm pulses of intensity 4.3×10^{13} W/cm^2. (int = intermediate)

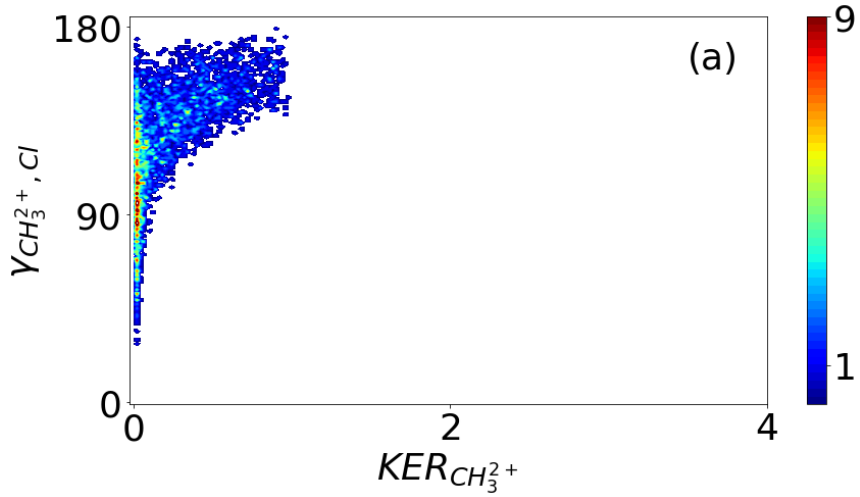

(A) CH_3^+ intermediate

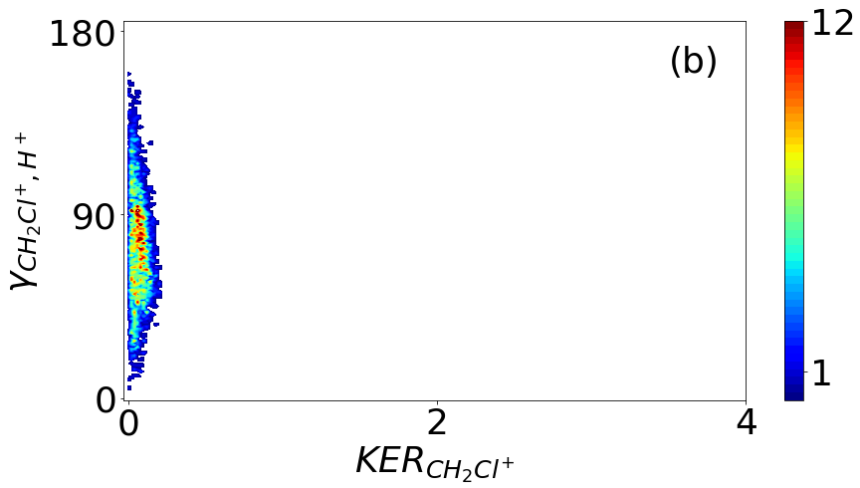

(B) CH_2Cl^{2+} intermediate

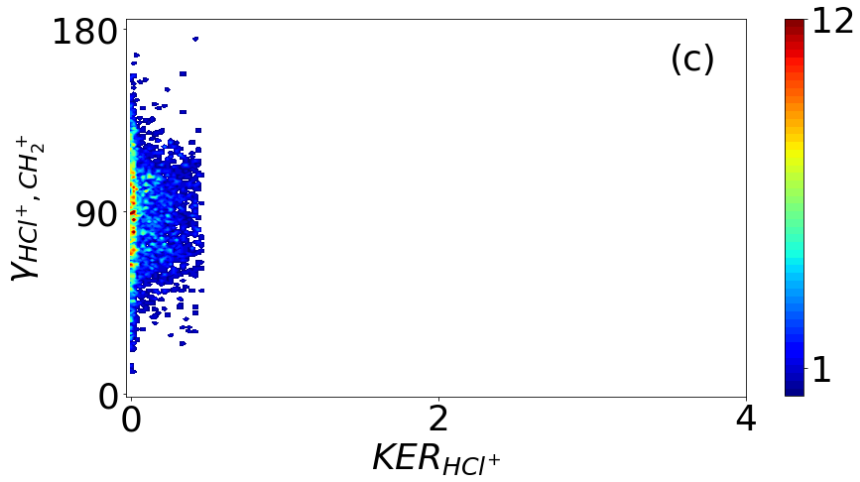

(C) HCl^+ intermediate

FIGURE 5.21: Density plot as a function of KER_{int} and γ_{int} for the sequential fragmentation via (a) $CH_3^+ + Cl^+$, (b) CH_2Cl^+, and (c) $CH_2^+ + Cl^+$ pathways, obtained for 510 fs (5330 fs^2), 800 nm pulses of intensity 4.3×10^{13} W/cm^2. (int = intermediate)

5.2 Conclusion

In conclusion, in this chapter, we have investigated the complex three-body fragmentation dynamics of CH_3Cl^{2+} for the CH_2^+ + Cl^+ and H^+ + CH_2^+ pathways. Using Dalitz plots, Newton diagrams, and the native frame method, we identified the concerted and sequential fragmentation mechanisms. For both pathways, dissociation occurs primarily by the concerted mechanism – the Coulomb explosion of the parent ion. In addition, some of the events were found to occur sequentially by forming a CH_3^+, CH_2Cl^{2+}, and HCl^+ intermediate. The CH_2^++ Cl^+ pathway had some contribution from the H^++ CH_2^++ Cl^+ pathway in which the H^+ is undetected. This three-body fragmentation pathway occurs by the Coulomb explosion (concerted) of the trication and leads to the ejection of H^+ with very high kinetic energy. Positively chirping and stretching the pulses influence the excited-state dynamics of the parent ion and hence, the fragmentation mechanism. For the CH_2^+ + Cl^+ pathway, the sequential pathways were nearly suppressed, and the concerted mechanism is dominant. We also observed that the dissociation takes place faster for chirped pulses which were confirmed by an enhanced anisotropy in the two-dimensional momentum distribution of the fragments. For the H^++ CH_2^+ pathway, the dissociation primarily takes place by the concerted mechanism and some sequential process. On ionization with chirped pulses, we observe the ejection of fragments with very high KER. This observation was attributed to the contamination from the H^++ CH_2^++ Cl^+ pathway. In addition, the sequential mechanism with a CH_3^{2+} intermediate was found to be enhanced for chirped pulses, while the sequential fragmentation along the other two pathways is nearly suppressed for chirped pulses and concerted processes dominate. Therefore, we demonstrate the control of the fragmentation mechanism of the parent ion by using chirped pulses for the strong-field ionization of CH_3Cl.

Chapter 6

Summary and Future Scope

In conclusion, controlling the bond breakup, intramolecular H migration and bond formation involved in H_n^+ (and HCl^+) formation during the photodissociation of ionized polyatomic molecules (CH_3OH, CD_3OH and CH_3Cl) were investigated in this thesis work. The findings have strengthened our understanding of controlling molecular reactions.

Firstly, we obtained the experimental single ionization rate of a molecule (CH_3Cl) as a function of laser intensity (ranging from 10^{13} W/cm^2 to 10^{14} W/cm^2) and fitted the result with the MO-ADK model. While the theoretical and experimental results agree well at intensities greater than 1.2×10^{14} W/cm^2, there is a discrepancy in the low-intensity regime. The MO-ADK models the tunneling regime of molecules therefore, the ionization rates in the MPI regime show some deviation. Next, to demonstrate the control of H_n^+ (n =1-3) yield arising from all possible dissociative channels of the ionized parent molecules, we varied the intensity (from MPI to tunneling regime), chirp (unchirped and positive-chirp), wavelength (800 nm and 1300 nm) and polarization (linear and circular). The results indicated that varying one of the laser parameters while keeping the others constant, influences the ionization and fragmentation rates of the parent molecule, resulting in a change in the H_n^+ yield. At low intensities (MPI regime), the H_n^+ ions are formed by the dissociation of mainly singly and some doubly-ionized parent molecules. The cations primarily populate the ground states and are highly stable. Therefore, very few cations which populate the excited electronic states and the dications dissociate in this regime, leading to the low H_n^+ yield. However, the H_n^+ yield increases with intensity. This was attributed to

the dissociation of the multiply-charged (2+, 3+, 4+, etc.) parent molecules formed at very high intensities by tunnel electron recollision with the ionic core and charge resonance enhanced ionization. Chirp was found to again strongly influence the H_n^+ yield. While unchirped (29 fs) pulses primarily produced parent cations which do not fragment much, chirped pulses lead to enhanced ionization and an increased rate of fragmentation. Therefore, the H_n^+ yield was higher for photoionization of the molecules with chirped pulses. However, in the case of CH_3Cl, the trend was reversed; the H_2^+ and H_3^+ yields were found to decrease with increasing positive chirp. This may be attributed to the increased potential barriers needed to be overcome in this case. Our wavelength-dependent study showed that the H_n^+ yield was lower in the case of 1300 nm pulses than the 800 nm pulses. There is a trade-off between the energy gained by the tunneling electron in the laser field and its recollision probability. We concluded that in the case of 1300 nm pulses, the recollision probability of the tunneling electron with the ionic core is less than in the case of 800 nm pulses. Hence, the fragmentation rate of the molecules and the H_n^+ yield are less for 1300 nm pulses. Finally, linearly polarized pulses produced a slightly higher H_n^+ yield than circularly polarized pulses. The tunneling electron recollision-induced double ionization of molecules is suppressed by the CP pulses, which is responsible for the lower yield of the H_n^+ ions. These results indicate that the laser parameters control the fragmentation of molecular ions and H_n^+ yield.

To further understand the control of the excited-state dynamics of the parent ion leading H_n^+ formation, we identified a few two-body fragmentation pathways of CH_3Cl dication that produce H_n^+ and HCl^+ as one of the fragments using PIPICO. Increasing the intensity from $I = 4.3 \times 10^{13}$ W/cm^2 to $I = 8.5 \times 10^{13}$ W/cm^2 suppressed the yields of all the pathways, which was attributed to an increased ionization of the parent dication compared to dissociation. On the other hand, stretching the pulses (introducing a positive chirp) from 29 fs to 510 fs enhanced the HCl^+ forming pathway, while suppressing the H_n^+ forming pathways. The KER distributions, two-dimensional coincidence momentum distribution and angular distributions of the H_n^+ and HCl^+ ions revealed that the H_n^+ ions are formed by the dissociation of CH_3Cl^{2+} from non-Coulombic metastable PESs, so their bond lengths do

not map onto the KER. These pathways have a long dissociation time (of the order of ps), and the anisotropy in their ejection direction is destroyed by the rotation of the dication. Conversely, the HCl^+ forming pathways arise from the dissociation of CH_3Cl^{2+} from Coulombic (repulsive) PESs, due to which their KER distribution shows a shift to lower energies with increased pulse stretching. Since this pathway has a rapid dissociation time, the HCl^+ ions have an anisotropic distribution. Therefore, we demonstrated the control of the ultrafast fragmentation dynamics of CH_3Cl^{2+} and the resulting dissociation pathways using laser intensity, and chirp.

In the final work, we have investigated the complex three-body fragmentation dynamics of the molecular ion for the CH_2^+ + Cl^+ and H^+ + CH_2^+ pathways. Using Dalitz plots and the native method we have identified the concerted and sequential fragmentation mechanisms. Our study suggests that the dications dissociate primarily by the concerted mechanism and some sequential processes with a CH_2Cl^{2+} intermediate. In these cases, H is nearly at rest and is ejected with very little kinetic energy, while CH_2^+ and Cl^+ are ejected back-to-back with nearly equal momentum. In addition, some events corresponding to the H^++ CH_2^++ Cl^+ pathway with an undetected H^+ are observed which are ejected with very high kinetic energy due to the Coulomb explosion of the trication. Chirping the pulses leads to the near suppression of the sequential mechanism, while the concerted mechanism is dominant. For the H^+ + CH_2^+ pathway again, dissociation occurs primarily by the concerted mechanism along with some sequential events with CH_3^{2+}, CH_2Cl^+ and HCl^+ intermediates. However, the overlapping of the concerted and sequential mechanisms makes it difficult to distinguish between them. On using chirped pulses, the sequential mechanism is suppressed, and the concerted process dominates. Therefore, we demonstrate the control of the fragmentation mechanism of the molecular ion by using chirped pulses.

Based on our current findings on the ultrafast excited-state dynamics and the two- and three-body fragmentation of polyatomic molecules from the present thesis work, we intend to study the following in future:

1. Investigate the effect of molecular geometry on the bond breakup, intramolecular H migration and bond formation in polyatomic molecules. For this purpose, we have performed the photoionization of geometrical isomers with a double bond – *cis*- and *trans*-1,2-dichloroethylene. The inherent differences in the molecular geometry are expected to affect the bond rearrangement processes for the various two- and three-body dissociative pathways. Isomers are of huge significance in many biological processes [198, 199]. The difference in the geometry of the isomers results in significant differences in their physical and chemical properties. Hence, identifying the isomers based on their excited-state dynamics using the coincidence momentum imaging (CMI) technique as demonstrated in the present thesis, can be useful.

2. Using pump-probe technique to investigate the time-resolved excited-state molecular dynamics like intramolecular H migration in polyatomic molecules. To study the nuclear dynamics in the ionic state of the molecule, the pump pulse will initially ionize the parent. The probe pulse is sent after various time delays to probe the evolving wavepacket in the PES. Time-resolved studies will enable us to form a better understanding of the bond rearrangements in the excited state of molecules.

3. The same pump-probe technique can be used to study the ultrafast excited-state dynamics of molecules by impulsively aligning them. In this thesis work, the molecules were randomly aligned in space in all the experiments. This means that the kinematic information obtained for the molecules is averaged for various alignments. However, if first align the molecules along the laser polarization direction by a pump pulse, and then probe the excited-state nuclear dynamics, then the information will give us the angle-dependent ionization and fragmentation of the molecules [200, 201], and also control the fragmentation [63].

4. Control of the excited-state nuclear dynamics and fragmentation of polyatomic molecules using a two-color field. All the experiments in this thesis used a single laser field for photoionization. However, using a two-color field, that is 800 nm and 400 nm (ω-2ω) pulses, have been shown to control the ionization

rate [202], and the fragment ejection direction by varying the phase ϕ between the ω and 2ω fields [203].

5. We shall also extend these studies to investigate the excited-state dynamics in aromatic hydrocarbons like benzene. Aromatic hydrocarbons are ubiquitous, from biomolecules to the interstellar medium. Understanding the time-resolved excited-state dynamics of aromatic hydrocarbons and controlling the dynamics and the various dissociative pathways can have useful implications in medicine.

6. Finally, we are developing a high-harmonic generation (HHG) facility in our lab, which can produce attosecond x-ray single pulses and pulse trains. Combining the HHG and the RIMS setups, we shall perform XUV-IR pump-probe studies. In these studies, we can study the core-hole dynamics in molecules by first removing a core electron from the molecule using an x-ray pump pulse. The subsequent dynamics in the ion can be probed using an IR probe pulse.

Bibliography

[1] Z. Chang. *Fundamentals of Attosecond Optics*. CRC Press, 2016. ISBN: 9781420089387. DOI: https://doi.org/10.1201/b10402. URL: https://books.google.co.in/books?id=J5HLBQAAQBAJ.

[2] H. Kandori, Y. Shichida, and T. Yoshizawa. "Photoisomerization in Rhodopsin". In: *Biochemistry (Moscow)* 66.11 (2001), pp. 1197–1209. ISSN: 1608-3040. DOI: 10.1023/A:1013123016803. URL: https://doi.org/10.1023/A:1013123016803.

[3] Samer Gozem et al. "Theory and simulation of the ultrafast double-bond isomerization of biological chromophores". In: *Chemical reviews* 117.22 (2017), pp. 13502–13565. DOI: 10.1021/acs.chemrev.7b00177. URL: https://doi.org/10.1021/acs.chemrev.7b00177.

[4] Thomas Renger, Volkhard May, and Oliver Kühn. "Ultrafast excitation energy transfer dynamics in photosynthetic pigment–protein complexes". In: *Physics Reports* 343.3 (2001), pp. 137 –254. ISSN: 0370-1573. DOI: https://doi.org/10.1016/S0370-1573(00)00078-8. URL: http://www.sciencedirect.com/science/article/pii/S0370157300000788.

[5] Pablo López-Tarifa et al. "Ultrafast nonadiabatic fragmentation dynamics of biomolecules". In: *Journal of Physics: Conference Series* 488.1 (2014), p. 012037. DOI: 10.1088/1742-6596/488/1/012037. URL: https://doi.org/10.1088%2F1742-6596%2F488%2F1%2F012037.

[6] Dongping Zhong. "Electron transfer mechanisms of DNA repair by photolyase". In: *Annual review of physical chemistry* 66 (2015), pp. 691–715. DOI: 0.1146/annurev-physchem-040513-103631.

[7] H Knudsen et al. "Ionization of atomic hydrogen by 30–1000 keV antiprotons". In: *Physical review letters* 74.23 (1995), p. 4627. DOI: 10.1103/PhysRevLett.74.4627.

[8] DSF Crothers and JF McCann. "Ionisation of atoms by ion impact". In: *Journal of Physics B: Atomic and Molecular Physics (1968-1987)* 16.17 (1983), p. 3229. DOI: 10.1088/0022-3700/16/17/015. URL: https://doi.org/10.1088/0022-3700/16/17/015.

[9] Raimonds K Peterkop. "Theory of ionization of atoms by electron impact". In: (1977). DOI: 10.1063/1.2165617. URL: https://aip.scitation.org/doi/abs/10.1063/1.2165617.

[10] R Ehlich, M Westerburg, and EEB Campbell. "Fragmentation of fullerenes in collisions with atomic and molecular targets". In: *The Journal of chemical physics* 104.5 (1996), pp. 1900–1911. DOI: 10.1063/1.470946. URL: https://doi.org/10.1063/1.470946.

[11] Vidhya Krishnamurthi, I Ben-Itzhak, and KD Carnes. "Projectile charge dependence of ionization and fragmentation of CO in fast collisions". In: *Journal of Physics B: Atomic, Molecular and Optical Physics* 29.2 (1996), p. 287. DOI: 10.1088/0953-4075/29/2/016. URL: https://doi.org/10.1088/0953-4075/29/2/016.

[12] I Ben-Itzhak, SG Ginther, and KD Carnes. "Multiple-electron removal and molecular fragmentation of CO by fast F^{4+} impact". In: *Physical Review A* 47.4 (1993), p. 2827. DOI: 10.1103/PhysRevA.47.2827.

[13] M Tarisien et al. "Ion-induced molecular fragmentation: beyond the Coulomb explosion picture". In: *Journal of Physics B: Atomic, Molecular and Optical Physics* 33.1 (2000), p. L11. DOI: 10.1088/0953-4075/33/1/102. URL: https://doi.org/10.1088/0953-4075/33/1/102.

[14] Udo Werner et al. "3D imaging of the collision-induced Coulomb fragmentation of water molecules". In: *Physical review letters* 74.11 (1995), p. 1962. DOI: 10.1103/PhysRevLett.74.1962. URL: https://link.aps.org/doi/10.1103/PhysRevLett.74.1962.

[15] I Ben-Itzhak, SG Ginther, and KD Carnes. "Coincidence time-of-flight studies of molecular fragmentation". In: *Nuclear Instruments and Methods in Physics Research Section B: Beam Interactions with Materials and Atoms* 66.4 (1992), pp. 401–

414. DOI: https://doi.org/10.1016/0168-583X(92)95411-J. URL: https://www.sciencedirect.com/science/article/pii/0168583X9295411J.

[16] TS Luk et al. "Collision-free multiple photon ionization of atoms and molecules at 193 nm". In: *Physical Review A* 32.1 (1985), p. 214. DOI: 10.1103/PhysRevA.32.214. URL: https://link.aps.org/doi/10.1103/PhysRevA.32.214.

[17] Eefei Chen, Robert A Goldbeck, and David S Kliger. "Nanosecond time-resolved spectroscopy of biomolecular processes". In: *Annual review of biophysics and biomolecular structure* 26.1 (1997), pp. 327–355. DOI: 10.1146/annurev.biophys.26.1.327.

[18] Takayoshi Kobayashi et al. "Picosecond and nanosecond laser photolyses of p-(dimethylamino) phenyl azide in solution". In: *The Journal of Physical Chemistry* 89.5 (1985), pp. 776–779. DOI: 10.1021/j100251a013. URL: https://doi.org/10.1021/j100251a013.

[19] Ahmed H Zewail. "Femtochemistry: Atomic-scale dynamics of the chemical bond". In: *The Journal of Physical Chemistry A* 104.24 (2000), pp. 5660–5694. DOI: 10.1021/jp001460h. URL: https://doi.org/10.1021/jp001460h.

[20] Hideki Hashimoto, Mitsuru Sugisaki, and Masayuki Yoshizawa. "Ultrafast time-resolved vibrational spectroscopies of carotenoids in photosynthesis". In: *Biochimica et Biophysica Acta (BBA) - Bioenergetics* 1847.1 (2015). Vibrational spectroscopies and bioenergetic systems, pp. 69–78. ISSN: 0005-2728. DOI: https://doi.org/10.1016/j.bbabio.2014.09.001. URL: https://www.sciencedirect.com/science/article/pii/S0005272814005830.

[21] Zahra Omidvar, Ahmad Asoodeh, and Jamshidkhan Chamani. "Studies on the Antagonistic Behavior Between Cyclophosphamide Hydrochloride and Aspirin with Human Serum Albumin: Time-Resolved Fluorescence Spectroscopy and Isothermal Titration Calorimetry". In: *Journal of Solution Chemistry* 42.5 (2013), pp. 1005–1017. ISSN: 1572-8927. DOI: 10.1007/s10953-013-0009-7. URL: https://doi.org/10.1007/s10953-013-0009-7.

[22] Martina Samiotaki et al. "Seven-Color Time-Resolved Fluorescence Hybridization Analysis of Human Papilloma Virus Types". In: *Analytical Biochemistry* 253.2 (1997), pp. 156–161. ISSN: 0003-2697. DOI: https://doi.org/10.1006/

abio.1997.2387. URL: https://www.sciencedirect.com/science/article/pii/S0003269797923873.

[23] C. S. Ponseca Jr. and V. Sundström. "Revealing the ultrafast charge carrier dynamics in organo metal halide perovskite solar cell materials using time resolved THz spectroscopy". In: *Nanoscale* 8 (12 2016), pp. 6249–6257. DOI: 10.1039/C5NR08622A. URL: http://dx.doi.org/10.1039/C5NR08622A.

[24] L V Keldysh. "Ionization in the field of a strong electromagnetic wave". In: *Zh. Eksperim. i Teor. Fiz.* Vol: 47 (Nov. 1964), pp. 1307–1314. DOI: 10.1134/S1063776116030043. URL: https://doi.org/10.1134/S1063776116030043.

[25] M V Fedorov. "L. V. Keldysh's "Ionization in the Field of a Strong Electromagnetic Wave" and modern physics of atomic interaction with a strong laser field". In: *Journal of Experimental and Theoretical Physics* 122.3 (Mar. 2016), pp. 449–455.

[26] Jeffrey L Krause, Kenneth J Schafer, and Kenneth C Kulander. "High-order harmonic generation from atoms and ions in the high intensity regime". In: *Physical Review Letters* 68.24 (1992), p. 3535. DOI: 10.1103/PhysRevLett.68.3535. URL: https://link.aps.org/doi/10.1103/PhysRevLett.68.3535.

[27] Paul B Corkum. "Plasma perspective on strong field multiphoton ionization". In: *Physical review letters* 71.13 (1993), p. 1994. DOI: 10.1103/PhysRevLett.71.1994. URL: https://link.aps.org/doi/10.1103/PhysRevLett.71.1994.

[28] Maciej Lewenstein et al. "Theory of high-harmonic generation by low-frequency laser fields". In: *Physical Review A* 49.3 (1994), p. 2117. DOI: 10.1103/PhysRevA.49.2117. URL: https://link.aps.org/doi/10.1103/PhysRevA.49.2117.

[29] Jie Li et al. "Attosecond science based on high harmonic generation from gases and solids". In: *Nature Communications* 11.1 (2020), pp. 1–13. DOI: 10.1038/s41467-020-16480-6. URL: https://doi.org/10.1038/s41467-020-16480-6.

[30] Samuel Micheau et al. "Quantitative rescattering theory for nonsequential double ionization of atoms by intense laser pulses". In: *Physical Review A* 79.1

(2009), p. 013417. DOI: 10.1088/1674-1056/ab54b3. URL: https://doi.org/10.1088/1674-1056/ab54b3.

[31] Th Weber et al. "Correlated electron emission in multiphoton double ionization". In: *Nature* 405.6787 (2000), pp. 658–661. DOI: 10.1038/35015033. URL: https://doi.org/10.1038/35015033.

[32] Xiaolei Hao et al. "Recollision of excited electron in below-threshold nonsequential double ionization". In: *Communications Physics* 5.1 (2022), pp. 1–7. DOI: 10.1038/s42005-022-00809-2. URL: https://doi.org/10.1038/s42005-022-00809-2.

[33] T Shaaran, MT Nygren, and C Figueira de Morisson Faria. "Laser-induced nonsequential double ionization at and above the recollision-excitation-tunneling threshold". In: *Physical Review A* 81.6 (2010), p. 063413. DOI: 10.1103/PhysRevA.81.063413. URL: https://link.aps.org/doi/10.1103/PhysRevA.81.063413.

[34] HG Muller. "Numerical simulation of high-order above-threshold-ionization enhancement in argon". In: *Physical Review A* 60.2 (1999), p. 1341. DOI: 10.1103/PhysRevA.60.1341. URL: https://link.aps.org/doi/10.1103/PhysRevA.60.1341.

[35] Maxim V. Ammosov, Nikolai B. Delone, and Vladimir P. Krainov. "Tunnel Ionization Of Complex Atoms And Atomic Ions In Electromagnetic Field". In: *High Intensity Laser Processes SPIE Proceedings* (1986). DOI: 10.1117/12.938695.

[36] Gennady L Yudin and Misha Yu Ivanov. "Nonadiabatic tunnel ionization: Looking inside a laser cycle". In: *Physical Review A* 64.1 (2001), p. 013409. DOI: 10.1103/PhysRevA.64.013409. URL: https://link.aps.org/doi/10.1103/PhysRevA.64.013409.

[37] NB Delone and Vladimir P Krainov. "Energy and angular electron spectra for the tunnel ionization of atoms by strong low-frequency radiation". In: *JOSA B* 8.6 (1991), pp. 1207–1211. DOI: 10.1364/JOSAB.8.001207. URL: http://opg.optica.org/josab/abstract.cfm?URI=josab-8-6-1207.

[38] Xiao-Min Tong, ZX Zhao, and Chii-Dong Lin. "Theory of molecular tunneling ionization". In: *Physical Review A* 66.3 (2002), p. 033402. DOI: 10.1103/PhysRevA.66.033402. URL: https://link.aps.org/doi/10.1103/PhysRevA.66.033402.

[39] KJ Schafer et al. "Above threshold ionization beyond the high harmonic cutoff". In: *Physical review letters* 70.11 (1993), p. 1599. DOI: 10.1103/PhysRevLett.70.1599. URL: https://link.aps.org/doi/10.1103/PhysRevLett.70.1599.

[40] Anne L'Huillier et al. "High-order harmonic-generation cutoff". In: *Physical Review A* 48.5 (1993), R3433. DOI: 10.1103/physreva.48.r3433.

[41] W Becker, A Lohr, and M Kleber. "Effects of rescattering on above-threshold ionization". In: *Journal of Physics B: Atomic, Molecular and Optical Physics* 27.14 (1994), p. L325. DOI: 10.1103/PhysRevA.52.4043. URL: https://link.aps.org/doi/10.1103/PhysRevA.52.4043.

[42] Barry Walker et al. "Elastic rescattering in the strong field tunneling limit". In: *Physical review letters* 77.25 (1996), p. 5031. DOI: 10.1103/PhysRevLett.77.5031. URL: https://link.aps.org/doi/10.1103/PhysRevLett.77.5031.

[43] Merrick J DeWitt and Robert J Levis. "Concerning the ionization of large polyatomic molecules with intense ultrafast lasers". In: *The Journal of chemical physics* 110.23 (1999), pp. 11368–11375. DOI: 10.1063/1.479077. URL: https://doi.org/10.1063/1.479077.

[44] Markus Kowalewski et al. "Catching conical intersections in the act: Monitoring transient electronic coherences by attosecond stimulated X-ray Raman signals". In: *Physical review letters* 115.19 (2015), p. 193003. DOI: 10.1103/PhysRevLett.115.193003. URL: https://link.aps.org/doi/10.1103/PhysRevLett.115.193003.

[45] TK Kjeldsen et al. "Role of symmetry in strong-field ionization of molecules". In: *Physical Review A* 68.6 (2003), p. 063407. DOI: 10.1103/PhysRevA.68.063407. URL: https://link.aps.org/doi/10.1103/PhysRevA.68.063407.

[46] Tao Zuo and André D Bandrauk. "Charge-resonance-enhanced ionization of diatomic molecular ions by intense lasers". In: *Physical Review A* 52.4 (1995), R2511.

[47] Irina Bocharova et al. "Charge Resonance Enhanced Ionization of CO_2 Probed by Laser Coulomb Explosion Imaging". In: *Physical Review Letters* 107.6 (2011), p. 063201. DOI: 10.1103/PhysRevLett.107.063201.

[48] E. Teller. "The Crossing of Potential Surfaces." In: *The Journal of Physical Chemistry* 41.1 (1937), pp. 109–116. DOI: 10.1021/j150379a010. URL: https://doi.org/10.1021/j150379a010.

[49] Sizuo Luo et al. "Identifying the Multielectron Effect on Chemical Bond Rearrangement of CH_3Cl Molecules in Strong Laser Fields". In: *The Journal of Physical Chemistry A* 122.43 (2018), pp. 8427–8432. ISSN: 1089-5639. DOI: 10.1021/acs.jpca.8b06415. URL: https://doi.org/10.1021/acs.jpca.8b06415.

[50] Sizuo Luo et al. "Multiorbital effects in strong-field ionization and dissociation of aligned polar molecules CH_3I and CH_3Br, journal=Physical Review A, year=2017, month=Dec, day=19, publisher=American Physical Society, volume=96, number=6, pages=063415, doi=10.1103/PhysRevA.96.063415, url=https://link.aps.org/do in: ().

[51] Sizuo Luo et al. "Nonadiabatic laser-induced orientation and alignment of rotational-state-selected CH_3Br molecules". In: *Physical Review A* 91.5 (2015), p. 053408. DOI: 10.1103/PhysRevA.91.053408. URL: https://link.aps.org/doi/10.1103/PhysRevA.91.053408.

[52] F. P. Sturm et al. "Mapping and controlling ultrafast dynamics of highly excited H_2 molecules by VUV-IR pump-probe schemes". In: *Physical Review A* 95.1 (2017), p. 012501. DOI: 10.1103/PhysRevA.95.012501. URL: https://link.aps.org/doi/10.1103/PhysRevA.95.012501.

[53] F. P. Sturm et al. "Time resolved 3D momentum imaging of ultrafast dynamics by coherent VUV-XUV radiation". In: *Review of Scientific Instruments* 87.6 (2016), p. 063110. DOI: 10.1063/1.4953441. URL: https://doi.org/10.1063/1.4953441.

[54] A R Bainbridge et al. "VUV excitation of a vibrational wavepacket in D_2 measured through strong-field dissociative ionization". In: *New Journal of Physics* 17.10 (2015), p. 103013. DOI: 10.1088/1367-2630/17/10/103013. URL: https://doi.org/10.1088%2F1367-2630%2F17%2F10%2F103013.

[55] Matteo McDonnell et al. "Ultrafast Laser-Induced Isomerization Dynamics in Acetonitrile". In: *The Journal of Physical Chemistry Letters* 11.16 (2020), pp. 6724–6729. DOI: 10.1021/acs.jpclett.0c01344. URL: https://doi.org/10.1021/acs.jpclett.0c01344.

[56] Phil H Bucksbaum et al. "Softening of the H_2^+ molecular bond in intense laser fields". In: *Physical review letters* 64.16 (1990), p. 1883. DOI: 10.1103/physrevlett.64.1883. URL: https://doi.org/10.1103/PhysRevLett.64.1883.

[57] Guanhua Yao and Shih-I Chu. "Laser-induced molecular stabilization and trapping and chemical bond hardening in intense laser fields". In: *Chemical physics letters* 197.4-5 (1992), pp. 413–418. DOI: https://doi.org/10.1016/0009-2614(92)85793-A. URL: https://www.sciencedirect.com/science/article/pii/000926149285793A.

[58] Xinhua Xie et al. "Attosecond-recollision-controlled selective fragmentation of polyatomic molecules". In: *Physical review letters* 109.24 (2012), p. 243001. DOI: 10.1103/PhysRevLett.109.243001. URL: https://link.aps.org/doi/10.1103/PhysRevLett.109.243001.

[59] Yunquan Liu et al. "Selective steering of molecular multiple dissociative channels with strong few-cycle laser pulses". In: *Physical review letters* 106.7 (2011), p. 073004. DOI: 10.1103/PhysRevLett.106.073004. URL: https://link.aps.org/doi/10.1103/PhysRevLett.106.073004.

[60] KJ Betsch et al. "Controlled directional ion emission from several fragmentation channels of CO driven by a few-cycle laser field". In: *Physical Review A* 86.6 (2012), p. 063403. DOI: 10.1103/PhysRevA.86.063403. URL: https://link.aps.org/doi/10.1103/PhysRevA.86.063403.

[61] Hui Li et al. "Carrier-envelope phase dependence of the directional fragmentation and hydrogen migration in toluene in few-cycle laser fields". In: *Structural Dynamics* 3.4 (2016), p. 043206. DOI: 10.1063/1.4941601. URL: https://doi.org/10.1063/1.4941601.

[62] Matthias F Kling et al. "(Sub-) femtosecond control of molecular reactions via tailoring the electric field of light". In: *Physical Chemistry Chemical Physics* 15.24 (2013), pp. 9448–9467. DOI: 10.1039/C3CP50591J. URL: http://dx.doi.org/10.1039/C3CP50591J.

[63] Xinhua Xie et al. "Selective control over fragmentation reactions in polyatomic molecules using impulsive laser alignment". In: *Physical review letters* 112.16 (2014), p. 163003. DOI: 10.1103/PhysRevLett.112.163003. URL: https://link.aps.org/doi/10.1103/PhysRevLett.112.163003.

[64] Katharina Doblhoff-Dier, Markus Kitzler, and Stefanie Gräfe. "Theoretical investigation of alignment-dependent intense-field fragmentation of acetylene". In: *Physical Review A* 94.1 (2016), p. 013405. DOI: 10.1103/PhysRevA.94.013405. URL: https://link.aps.org/doi/10.1103/PhysRevA.94.013405.

[65] Th Ergler et al. "Time-resolved imaging and manipulation of H_2 fragmentation in intense laser fields". In: *Physical review letters* 95.9 (2005), p. 093001. DOI: 10.1103/PhysRevLett.95.093001. URL: https://link.aps.org/doi/10.1103/PhysRevLett.95.093001.

[66] P Tzallas et al. "Extreme-ultraviolet pump–probe studies of one-femtosecond-scale electron dynamics". In: *Nature Physics* 7.10 (2011), pp. 781–784. DOI: 10.1038/nphys2033. URL: https://doi.org/10.1038/nphys2033.

[67] Qiying Song et al. "Double ionization of nitrogen molecules in orthogonal two-color femtosecond laser fields". In: *Journal of Physics B: Atomic, Molecular and Optical Physics* 51.7 (2018), p. 074002. DOI: 10.1088/1361-6455/aab198. URL: https://doi.org/10.1088/1361-6455/aab198.

[68] Xinhua Xie et al. "Electronic predetermination of ethylene fragmentation dynamics". In: *Physical Review X* 4.2 (2014), p. 021005. DOI: 10.1103/PhysRevX.4.021005. URL: https://link.aps.org/doi/10.1103/PhysRevX.4.021005.

[69] Xinhua Xie et al. "Duration of an intense laser pulse can determine the breakage of multiple chemical bonds". In: *Scientific reports* 5.1 (2015), pp. 1–11. DOI: 10.1038/srep12877. URL: https://doi.org/10.1038/srep12877.

[70] Donna Strickland and Gerard Mourou. "Compression of amplified chirped optical pulses". In: *Optics communications* 55.6 (1985), pp. 447–449. DOI: https://doi.org/10.1016/0030-4018(85)90120-8. URL: https://www.sciencedirect.com/science/article/pii/0030401885901208.

[71] E Cumberbatch. "Self-focusing in non-linear optics". In: *IMA Journal of Applied Mathematics* 6.3 (1970), pp. 250–262. DOI: 10.1093/imamat/6.3.250.

[72] Claude Rulliere et al. *Femtosecond laser pulses*. Springer, 2005.

[73] A. Ducasse, C. Rullière, and B. Couillaud. "Methods for the Generation of Ultrashort Laser Pulses: Mode-Locking". In: *Femtosecond Laser Pulses: Principles and Experiments*. Ed. by Claude Rullière. New York, NY: Springer New York, 2005, pp. 57–87. ISBN: 978-0-387-26674-9. DOI: 10.1007/0-387-26674-7_3. URL: https://doi.org/10.1007/0-387-26674-7_3.

[74] P Madhusudhan et al. "Modern experimental techniques in ultrafast atomic and molecular physics". In: *Modern Techniques of Spectroscopy*. Springer, 2021, pp. 257–285. DOI: 10.1007/978-981-33-6084-6_10. URL: https://doi.org/10.1007/978-981-33-6084-6_10.

[75] Walter Koechner. "Laser Amplifier". In: *Solid-State Laser Engineering*. New York, NY: Springer New York, 2006, pp. 156–209. ISBN: 978-0-387-29338-7. DOI: 10.1007/0-387-29338-8_5. URL: https://doi.org/10.1007/0-387-29338-8_5.

[76] Whikun Yi et al. "Characteristic features of new electron-multiplying channels in a field emission display". In: *Journal of Vacuum Science & Technology B: Microelectronics and Nanometer Structures Processing, Measurement, and Phenomena* 19.6 (2001), pp. 2247–2251. DOI: 10.1116/1.1420206. URL: https://avs.scitation.org/doi/abs/10.1116/1.1420206.

[77] W. C. Wiley and I. H. McLaren. "Time-of-Flight Mass Spectrometer with Improved Resolution". In: *Review of Scientific Instruments* 26.12 (1955), pp. 1150–1157. DOI: 10.1063/1.1715212. URL: https://doi.org/10.1063/1.1715212.

[78] JHD Eland. "Dynamics of fragmentation reactions from peak shapes in multiparticle coincidence experiments". In: *Laser Chemistry* 11.3-4 (1991), pp. 259–263.

[79] André T. J. B. Eppink and David H. Parker. "Velocity map imaging of ions and electrons using electrostatic lenses: Application in photoelectron and photofragment ion imaging of molecular oxygen". In: *Review of Scientific Instruments* 68.9 (1997), pp. 3477–3484. DOI: 10.1063/1.1148310. URL: https://doi.org/10.1063/1.1148310.

[80] Shuai Li et al. "Control of electron recollision and molecular nonsequential double ionization". In: *Communications Physics* 3.1 (2020), p. 35. ISSN: 2399-3650. DOI: 10.1038/s42005-020-0297-3. URL: https://doi.org/10.1038/s42005-020-0297-3.

[81] Ester Livshits et al. "Time-resolving the ultrafast H2 roaming chemistry and H_3^+ formation using extreme-ultraviolet pulses". In: *Communications Chemistry* 3.1 (2020), p. 49. ISSN: 2399-3669. DOI: 10.1038/s42004-020-0294-1. URL: https://doi.org/10.1038/s42004-020-0294-1.

[82] Felix Schell et al. "Sequential and direct ionic excitation in the strong-field ionization of 1-butene molecules". In: *Phys. Chem. Chem. Phys.* 20 (21 2018), pp. 14708–14717. DOI: 10.1039/C7CP08195B. URL: http://dx.doi.org/10.1039/C7CP08195B.

[83] Nagitha Ekanayake et al. "Substituent effects on H_3^+ formation via H_2 roaming mechanisms from organic molecules under strong-field photodissociation". In: *The Journal of Chemical Physics* 149.24 (2018), p. 244310. DOI: 10.1063/1.5065387. URL: https://doi.org/10.1063/1.5065387.

[84] Nagitha Ekanayake et al. "H_2 roaming chemistry and the formation of H_3^+ from organic molecules in strong laser fields". In: *Nature Communications* 9.1 (2018), p. 5186. ISSN: 2041-1723. DOI: 10.1038/s41467-018-07577-0. URL: https://doi.org/10.1038/s41467-018-07577-0.

[85] Nagitha Ekanayake et al. "Mechanisms and time-resolved dynamics for trihydrogen cation (H_3^+) formation from organic molecules in strong laser fields". In: *Scientific Reports* 7.1 (2017), p. 4703. ISSN: 2045-2322. DOI: 10.1038/s41598-017-04666-w. URL: https://doi.org/10.1038/s41598-017-04666-w.

[86] Akiyoshi Hishikawa, Hirokazu Hasegawa, and Kaoru Yamanouchi. "Hydrogen migration in acetonitrile in intense laser fields in competition with two-body Coulomb explosion". In: *Journal of Electron Spectroscopy and Related Phenomena* 141.2 (2004). Frontiers of Coincidence Experiments, pp. 195 –200. ISSN: 0368-2048. DOI: https://doi.org/10.1016/j.elspec.2004.06.009. URL: http://www.sciencedirect.com/science/article/pii/S0368204804003378.

[87] P Farmanara, V Stert, and W Radloff. "Ultrafast internal conversion and fragmentation in electronically excited C_2H_4 and C_2H_3Cl molecules". In: *Chemical Physics Letters* 288.2 (1998), pp. 518 –522. ISSN: 0009-2614. DOI: https://doi.org/10.1016/S0009-2614(98)00312-1. URL: http://www.sciencedirect.com/science/article/pii/S0009261498003121.

[88] P. López-Tarifa et al. "Ultrafast Nonadiabatic Fragmentation Dynamics of Doubly Charged Uracil in a Gas Phase". In: *Phys. Rev. Lett.* 107 (2 2011), p. 023202. DOI: 10.1103/PhysRevLett.107.023202. URL: https://link.aps.org/doi/10.1103/PhysRevLett.107.023202.

[89] M. C. Castrovilli et al. "Ultrafast Hydrogen Migration in Photoionized Glycine". In: *The Journal of Physical Chemistry Letters* 9.20 (2018), pp. 6012–6016. DOI: 10.1021/acs.jpclett.8b02089. URL: https://doi.org/10.1021/acs.jpclett.8b02089.

[90] Huailiang Xu et al. "Communication: Two stages of ultrafast hydrogen migration in methanol driven by intense laser fields". In: *The Journal of Chemical Physics* 133.7 (2010), p. 071103. DOI: 10.1063/1.3473931. URL: https://doi.org/10.1063/1.3473931.

[91] Tomoya Okino et al. "Ultrafast hydrogen scrambling in methylacetylene and methyl-d_3-acetylene ions induced by intense laser fields". In: *Phys. Chem. Chem. Phys.* 14 (30 2012), pp. 10640–10646. DOI: 10.1039/C2CP40849J. URL: http://dx.doi.org/10.1039/C2CP40849J.

[92] Chelsea E. Liekhus-Schmaltz et al. "Ultrafast isomerization initiated by X-ray core ionization". In: *Nature Communications* 6.1 (2015), p. 8199. ISSN: 2041-1723. DOI: 10.1038/ncomms9199. URL: https://doi.org/10.1038/ncomms9199.

[93] Huailiang Xu, Tomoya Okino, and Kaoru Yamanouchi. "Ultrafast hydrogen migration in allene in intense laser fields: Evidence of two-body Coulomb explosion". In: *Chemical Physics Letters* 469.4-6 (2009), pp. 255–260. DOI: https://doi.org/10.1016/j.cplett.2008.12.097. URL: https://www.sciencedirect.com/science/article/pii/S0009261409000049.

[94] Kennosuke Hoshina et al. "Efficient ejection of H_3^+ from hydrocarbon molecules induced by ultrashort intense laser fields". In: *The Journal of Chemical Physics* 129.10 (2008), p. 104302. DOI: 10.1063/1.2973588. URL: https://doi.org/10.1063/1.2973588.

[95] Tomasz J. Wasowicz and Bogusław Pranszke. "Observation of the hydrogen migration in the cation-induced fragmentation of the pyridine molecules". In: *The Journal of Physical Chemistry A* 120.7 (2016), pp. 964–971. ISSN: 1089-5639. DOI: 10.1021/acs.jpca.5b11298. URL: https://doi.org/10.1021/acs.jpca.5b11298.

[96] Nora G. Kling et al. "Time-resolved molecular dynamics of single and double hydrogen migration in ethanol". In: *Nature Communications* 10.1 (2019), p. 2813. ISSN: 2041-1723. DOI: 10.1038/s41467-019-10571-9. URL: https://doi.org/10.1038/s41467-019-10571-9.

[97] R.K. Kushawaha and B. Bapat. "Fragmentation dynamics of the methanol dication". In: *Chemical Physics Letters* 463.1 (2008), pp. 42 –46. ISSN: 0009-2614. DOI: https://doi.org/10.1016/j.cplett.2008.08.019. URL: http://www.sciencedirect.com/science/article/pii/S0009261408010981.

[98] M. D. Burrows et al. "Studies of H^+, H_2^+, and H_3^+ dissociative ionization fragments from methane, ethane, methanol, ethanol, and some deuterated methanols using electron-impact excitation and a time-of-flight method incorporating mass analysis". In: *The Journal of Chemical Physics* 71.12 (1979), pp. 4931–4940. DOI: 10.1063/1.438306. URL: https://aip.scitation.org/doi/abs/10.1063/1.438306.

[99] Y. Zhang et al. "Formation of H_3^+ from hydrocarbon dications induced by collisions with charged particles". In: *Phys. Rev. A* 100 (5 2019), p. 052706. DOI: 10.1103/PhysRevA.100.052706. URL: https://link.aps.org/doi/10.1103/PhysRevA.100.052706.

[100] Y. Zhang et al. "Proton migration in hydrocarbons induced by slow highly charged ion impact". In: *The Journal of Chemical Physics* 150.20 (2019), p. 204303. DOI: 10.1063/1.5088690. URL: https://doi.org/10.1063/1.5088690.

[101] Y. Zhang et al. "Three-body fragmentation of methane dications produced by slow Ar^{8+}-ion impact". In: *Phys. Rev. A* 97 (2 2018), p. 022703. DOI: 10.1103/PhysRevA.97.022703. URL: https://link.aps.org/doi/10.1103/PhysRevA.97.022703.

[102] Manish Garg, Ashwani K Tiwari, and Deepak Mathur. "Quantum dynamics of proton migration in H_2O dications: H_2^+ formation on ultrafast timescales". In: *The Journal of chemical physics* 136.2 (2012), p. 024320. DOI: 10.1063/1.3676086. URL: https://doi.org/10.1063/1.3676086.

[103] Hua Wu et al. "Theoretical and experimental studies on hydrogen migration in dissociative ionization of the methanol monocation to molecular ions H_3^+ and H_2O^+". In: *RSC Adv.* 9 (29 2019), pp. 16683–16689. DOI: 10.1039/C9RA02003A. URL: http://dx.doi.org/10.1039/C9RA02003A.

[104] Matthew J. Michie et al. "Quantum coherent control of H_3^+ formation in strong fields". In: *The Journal of Chemical Physics* 150.4 (2019), p. 044303. DOI: 10.1063/1.5070067. URL: https://doi.org/10.1063/1.5070067.

[105] Yusuke Furukawa et al. "Ejection of triatomic hydrogen molecular ion from methanol in intense laser fields". In: *Chemical Physics Letters* 414.1 (2005), pp. 117 –121. ISSN: 0009-2614. DOI: https://doi.org/10.1016/j.cplett.2005.07.108. URL: http://www.sciencedirect.com/science/article/pii/S0009261405011218.

[106] Sylvain Maclot et al. "Dynamics of glycine dications in the gas phase: ultrafast intramolecular hydrogen migration versus Coulomb repulsion". In: *The Journal of Physical Chemistry Letters* 4.22 (2013), pp. 3903–3909. DOI: 10.1021/jz4020234. URL: https://doi.org/10.1021/jz4020234.

[107] MC Castrovilli et al. "Ultrafast hydrogen migration in photoionized glycine". In: *The journal of physical chemistry letters* 9.20 (2018), pp. 6012–6016. DOI: 10.1021/acs.jpclett.8b02089. URL: https://doi.org/10.1021/acs.jpclett.8b02089.

[108] Ester Livshits et al. "Time-resolving the ultrafast H_2 roaming chemistry and H_3^+ formation using extreme-ultraviolet pulses". In: *Communications Chemistry* 3.1 (2020), pp. 1–6. DOI: 10.1038/s42004-020-0294-1. URL: https://doi.org/10.1038/s42004-020-0294-1.

[109] Krishnendu Gope et al. "Absence of triplets in single-photon double ionization of methanol". In: *The Journal of Physical Chemistry Letters* 11.19 (2020), pp. 8108–8113. DOI: 10.1021/acs.jpclett.0c02445. URL: https://doi.org/10.1021/acs.jpclett.0c02445.

[110] Enliang Wang et al. "Ultrafast proton transfer dynamics on the repulsive potential of the ethanol dication: roaming-mediated isomerization versus coulomb explosion". In: *The Journal of Physical Chemistry A* 124.14 (2020), pp. 2785–2791. DOI: 10.1021/acs.jpca.0c02074. URL: https://doi.org/10.1021/acs.jpca.0c02074.

[111] Toshiaki Ando et al. "Coherent vibrations in methanol cation probed by periodic H_3^+ ejection after double ionization". In: *Communications Chemistry* 1.1 (2018), pp. 1–7. DOI: 10.1038/s42004-017-0006-7. URL: https://doi.org/10.1038/s42004-017-0006-7.

[112] Fukiko Ota et al. "Imaging intramolecular hydrogen migration with time-and momentum-resolved photoelectron diffraction". In: *Physical Chemistry Chemical Physics* 23.36 (2021), pp. 20174–20182. DOI: 10.1039/D1CP02055B. URL: http://dx.doi.org/10.1039/D1CP02055B.

[113] Sankar De et al. "Formation of H_3^+ due to intramolecular bond rearrangement in doubly charged methanol". In: *Physical review letters* 97.21 (2006), p. 213201. DOI: 10.1103/PhysRevLett.97.213201.

[114] MN Monce et al. "Dissociation of CH_3Cl by 1 MeV H^+, He^+, and O^+". In: *The Journal of Chemical Physics* 74.5 (1981), pp. 2860–2865. DOI: 10.1063/1.441458. URL: https://doi.org/10.1063/1.441458.

[115] MN Monce et al. "Coincidence detection of dissociative fragments from CH_3Cl". In: *The Journal of Chemical Physics* 78.1 (1983), pp. 597–598. DOI: 10.1063/1.444490. URL: https://doi.org/10.1063/1.444490.

[116] R Bohinc et al. "Dissociation of chloromethanes upon resonant σ^* excitation studied by x-ray scattering". In: *The Journal of chemical physics* 139.13 (2013), p. 134302. DOI: 10.1063/1.4822326. URL: https://doi.org/10.1063/1.4822326.

[117] Catalin Miron et al. "Multipathway dissociation dynamics of core-excited methyl chloride probed by high resolution electron spectroscopy and Auger-electron–ion coincidences". In: *The Journal of chemical physics* 128.15 (2008), p. 154314. DOI: 10.1063/1.2900645. URL: https://doi.org/10.1063/1.2900645.

[118] L El Khoury et al. "Resonant inelastic x-ray scattering of methyl chloride at the chlorine K edge". In: *The Journal of chemical physics* 136.2 (2012), p. 024319. DOI: 10.1063/1.3675685. URL: https://doi.org/10.1063/1.3675685.

[119] Denis Ceolin et al. "Fragmentation of methyl chloride studied by partial positive and negative ion-yield spectroscopy". In: *The Journal of chemical physics* 126.8 (2007), p. 084309. DOI: 10.1063/1.2464093. URL: https://doi.org/10.1063/1.2464093.

[120] Shengzhi Sun et al. "Ejection of triatomic molecular ion H_3^+ from methyl chloride in an intense femtosecond laser field". In: *Chemical Physics Letters* 581 (2013), pp. 16–20. DOI: https://doi.org/10.1016/j.cplett.2013.06.068. URL: https://www.sciencedirect.com/science/article/pii/S0009261413008609.

[121] Pan Ma et al. "Ultrafast proton migration and Coulomb explosion of methyl chloride in intense laser fields". In: *The Journal of chemical physics* 146.24 (2017), p. 244305. DOI: 10.1063/1.4989565. URL: https://doi.org/10.1063/1.4989565.

[122] P D Grugan et al. "Molecular ionization of chloromethane in strong fields: nearest neighbor gateway to highly charged ions". In: *Journal of Physics B:*

Atomic, Molecular and Optical Physics 51.16 (2018), p. 165601. DOI: 10.1088/1361-6455/aacf82. URL: https://doi.org/10.1088/1361-6455/aacf82.

[123] C. D. Lin et al. *Attosecond and Strong-Field Physics: Principles and Applications*. Cambridge University Press, 2018. DOI: 10.1017/9781108181839.

[124] Song-Feng Zhao et al. "Effect of orbital symmetry on the orientation dependence of strong field tunnelling ionization of nonlinear polyatomic molecules". In: *Journal of Physics B: Atomic, Molecular and Optical Physics* 44.3 (2011), p. 035601. DOI: 10.1088/0953-4075/44/3/035601. URL: https://doi.org/10.1088/0953-4075/44/3/035601.

[125] Benjamin Wolter et al. "Strong-field physics with mid-IR fields". In: *Physical Review X* 5.2 (2015), p. 021034. DOI: 10.1103/PhysRevX.5.021034. URL: https://link.aps.org/doi/10.1103/PhysRevX.5.021034.

[126] Hui Chen et al. "Angle-resolved and internuclear-separation-resolved measurements of the ionization rate of the B state of I_2 by strong laser fields". In: *Physical Review A* 84.4 (2011), p. 043427. DOI: 10.1103/PhysRevA.84.043427. URL: https://link.aps.org/doi/10.1103/PhysRevA.84.043427.

[127] G Lagmago Kamta and AD Bandrauk. "Phase dependence of enhanced ionization in asymmetric molecules". In: *Physical review letters* 94.20 (2005), p. 203003. DOI: 10.1103/PhysRevLett.94.203003. URL: https://link.aps.org/doi/10.1103/PhysRevLett.94.203003.

[128] Tamar Seideman, M Yu Ivanov, and Paul B Corkum. "Role of electron localization in intense-field molecular ionization". In: *Physical review letters* 75.15 (1995), p. 2819. DOI: 10.1103/PhysRevLett.75.2819. URL: https://link.aps.org/doi/10.1103/PhysRevLett.75.2819.

[129] C Cornaggia. "Electronic dynamics of charge resonance enhanced ionization probed by laser-induced alignment in C_2H_2". In: *Journal of Physics B: Atomic, Molecular and Optical Physics* 49.19 (2016), 19LT01. DOI: 10.1088/0953-4075/49/19/19lt01. URL: https://doi.org/10.1088/0953-4075/49/19/19lt01.

[130] André D Bandrauk et al. "Effect of nuclear motion on molecular high-order harmonics and on generation of attosecond pulses in intense laser pulses".

In: *Physical review letters* 101.15 (2008), p. 153901. DOI: 10.1103/PhysRevLett.101.153901. URL: https://link.aps.org/doi/10.1103/PhysRevLett.101.153901.

[131] M Yu Emelin, M Yu Ryabikin, and AM Sergeev. "Monitoring long-term evolution of molecular vibrational wave packet using high-order harmonic generation". In: *New Journal of Physics* 10.2 (2008), p. 025026. DOI: 10.1088/1367-2630/10/2/025026. URL: https://doi.org/10.1088/1367-2630/10/2/025026.

[132] M Lara-Astiaso et al. "Enhancing high-order harmonic generation in light molecules by using chirped pulses". In: *Physical Review Letters* 117.9 (2016), p. 093003. DOI: 10.1103/PhysRevLett.117.093003. URL: https://link.aps.org/doi/10.1103/PhysRevLett.117.093003.

[133] Baoning Wang et al. "Resonance enhanced high-order harmonic generation in H_2^+ by two sequential laser pulses". In: *Optics Express* 25.15 (2017), pp. 17777–17787. DOI: 10.1364/OE.25.017777. URL: http://opg.optica.org/oe/abstract.cfm?URI=oe-25-15-17777.

[134] M Krug et al. "Coherent strong-field control of multiple states by a single chirped femtosecond laser pulse". In: *New Journal of Physics* 11.10 (2009), p. 105051. DOI: 10.1088/1367-2630/11/10/105051. URL: https://doi.org/10.1088/1367-2630/11/10/105051.

[135] M Wollenhaupt et al. "Quantum control by selective population of dressed states using intense chirped femtosecond laser pulses". In: *Applied Physics B* 82.2 (2006), pp. 183–188. DOI: 10.1007/s00340-005-2066-0. URL: https://doi.org/10.1007/s00340-005-2066-0.

[136] Barry D Bruner et al. "Strong-field spatiotemporal ultrafast coherent control in three-level atoms". In: *Physical Review A* 81.6 (2010), p. 063410. DOI: 10.1103/PhysRevA.81.063410. URL: https://link.aps.org/doi/10.1103/PhysRevA.81.063410.

[137] Arno Vredenborg et al. "The reaction microscope: imaging and pulse shaping control in photodynamics". In: *ChemPhysChem* 12.8 (2011), pp. 1459–1473. DOI: 10.1002/cphc.201100107.

[138] Tapas Goswami et al. "Control of laser induced molecular fragmentation of n-propyl benzene using chirped femtosecond laser pulses". In: *Chemical physics* 360.1-3 (2009), pp. 47–52. DOI: 10.1016/j.chemphys.2009.04.009.

[139] Tiana Townsend et al. "Controlling H_3^+ Formation From Ethane Using Shaped Ultrafast Laser Pulses". In: *Frontiers in Physics* 9 (2021). DOI: 10.3389/fphy.2021.691727. URL: https://www.frontiersin.org/articles/10.3389/fphy.2021.691727.

[140] Vadim V. Lozovoy et al. "Control of molecular fragmentation using shaped femtosecond pulses". In: *The Journal of Physical Chemistry A* 112.17 (May 2008), pp. 3789–3812. DOI: 10.1021/jp071691p. URL: https://doi.org/10.1021/jp071691p.

[141] Ryuji Itakura et al. "Dissociative ionization of ethanol in chirped intense laser fields". In: *The Journal of chemical physics* 119.8 (2003), pp. 4179–4186. DOI: 10.1063/1.1592504. URL: https://doi.org/10.1063/1.1592504.

[142] Arnab Sen et al. "Dissociation dynamics of multiply charged CH_3I in moderately intense laser fields". In: *Phys. Rev. A* 103 (4 2021), p. 043107. DOI: 10.1103/PhysRevA.103.043107. URL: https://link.aps.org/doi/10.1103/PhysRevA.103.043107.

[143] X. Li et al. "Pulse Energy and Pulse Duration Effects in the Ionization and Fragmentation of Iodomethane by Ultraintense Hard X Rays". In: *Phys. Rev. Lett.* 127 (9 2021), p. 093202. DOI: 10.1103/PhysRevLett.127.093202. URL: https://link.aps.org/doi/10.1103/PhysRevLett.127.093202.

[144] Sonia Erattupuzha et al. "Enhanced ionisation of polyatomic molecules in intense laser pulses is due to energy upshift and field coupling of multiple orbitals". In: *Journal of Physics B: Atomic, Molecular and Optical Physics* 50.12 (2017), p. 125601. DOI: 10.1088/1361-6455/aa7098. URL: https://doi.org/10.1088/1361-6455/aa7098.

[145] Erik Lötstedt, Tsuyoshi Kato, and Kaoru Yamanouchi. "Intramolecular electron dynamics in the ionization of acetylene by an intense laser pulse". In: *The Journal of chemical physics* 138.10 (2013), p. 104304. DOI: 10.1063/1.4794130. URL: https://doi.org/10.1063/1.4794130.

[146] D Duflot, J-M Robbe, and J-P Flament. "Stability of the CH_3Cl dication". In: *The Journal of chemical physics* 103.24 (1995), pp. 10571–10579. DOI: 10.1063/1.469841. URL: https://doi.org/10.1063/1.469841.

[147] J Tate et al. "Scaling of wave-packet dynamics in an intense midinfrared field". In: *Physical Review Letters* 98.1 (2007), p. 013901. DOI: 10.1103/PhysRevLett.98.013901. URL: https://link.aps.org/doi/10.1103/PhysRevLett.98.013901.

[148] P Colosimo et al. "Scaling strong-field interactions towards the classical limit". In: *Nature Physics* 4.5 (2008), pp. 386–389. DOI: 10.1038/nphys914. URL: https://doi.org/10.1038/nphys914.

[149] B. Walker et al. "Double ionization in the perturbative and tunneling regimes". In: *Phys. Rev. A* 48 (2 1993), R894–R897. DOI: 10.1103/PhysRevA.48.R894. URL: https://link.aps.org/doi/10.1103/PhysRevA.48.R894.

[150] P. Dietrich et al. "High-harmonic generation and correlated two-electron multiphoton ionization with elliptically polarized light". In: *Phys. Rev. A* 50 (5 1994), R3585–R3588. DOI: 10.1103/PhysRevA.50.R3585. URL: https://link.aps.org/doi/10.1103/PhysRevA.50.R3585.

[151] Denis Duflot, Jean-Michel Robbe, and Jean-Pierre Flament. "Ab initio study of the chloromethane dication fragmentation". In: *International journal of mass spectrometry and ion processes* 171.1-3 (1997), pp. 215–230. DOI: https://doi.org/10.1016/S0168-1176(97)00123-7. URL: https://www.sciencedirect.com/science/article/pii/S0168117697001237.

[152] E Ruhl et al. "Charge separation mass spectrometry: Part 2. Methyl compounds". In: *International journal of mass spectrometry and ion processes* 97.2 (1990), pp. 175–201. DOI: https://doi.org/10.1016/0168-1176(90)85058-A. URL: https://www.sciencedirect.com/science/article/pii/016811769085058A.

[153] Jerome Palaudoux and Majdi Hochlaf. "Formation of H_3^+ through chloromethane dication fragmentation". In: *ACS Earth and Space Chemistry* 3.6 (2019), pp. 980–985. DOI: 10.1021/acsearthspacechem.9b00045. URL: https://doi.org/10.1021/acsearthspacechem.9b00045.

[154] E Kokkonen et al. "Formation of stable HCl^+ following resonant Auger decay in CH_3Cl". In: *Physical Review A* 94.3 (2016), p. 033409. DOI: 10.1103/PhysRevA.94.033409. URL: https://link.aps.org/doi/10.1103/PhysRevA.94.033409.

[155] Samuel G Walt et al. "Role of multi-electron effects in the asymmetry of strong-field ionization and fragmentation of polar molecules: the methyl halide series". In: *The Journal of Physical Chemistry A* 119.49 (2015), pp. 11772–11782. DOI: 10.1021/acs.jpca.5b07331. URL: https://doi.org/10.1021/acs.jpca.5b07331.

[156] Y Malakar et al. "Time-resolved imaging of bound and dissociating nuclear wave packets in strong-field ionized iodomethane". In: *Physical Chemistry Chemical Physics* 21.26 (2019), pp. 14090–14102. DOI: 10.1039/C8CP07032F. URL: http://dx.doi.org/10.1039/C8CP07032F.

[157] Stefano Falcinelli et al. "Angular distribution of ion products in the double photoionization of propylene oxide". In: *Frontiers in chemistry* 7 (2019), p. 621. DOI: 10.3389/fchem.2019.00621. URL: https://www.frontiersin.org/articles/10.3389/fchem.2019.00621.

[158] Haixiang He et al. "Theoretical investigation of the origin of the multipeak structure of kinetic-energy-release spectra from charge-resonance-enhanced ionization of H 2+ in intense laser fields". In: *Physical Review A* 84.3 (2011), p. 033418. DOI: 10.1103/PhysRevA.84.033418. URL: https://link.aps.org/doi/10.1103/PhysRevA.84.033418.

[159] Domagoj Pavičić et al. "Direct measurement of the angular dependence of ionization for N_2, O_2, and CO_2 in intense laser fields". In: *Physical review letters* 98.24 (2007), p. 243001. DOI: 10.1103/PhysRevLett.98.243001. URL: https://link.aps.org/doi/10.1103/PhysRevLett.98.243001.

[160] Song-Feng Zhao et al. "Effect of orbital symmetry on the orientation dependence of strong field tunnelling ionization of nonlinear polyatomic molecules". In: *Journal of Physics B: Atomic, Molecular and Optical Physics* 44.3 (2011), p. 035601. DOI: 10.1088/0953-4075/44/3/035601. URL: https://doi.org/10.1088/0953-4075/44/3/035601.

[161] Brian K McFarland et al. "High harmonic generation from multiple orbitals in N_2". In: *Science* 322.5905 (2008), pp. 1232–1235. DOI: 10.1126/science.1162780.

[162] P Von den Hoff et al. "Effects of multi orbital contributions in the angular-dependent ionization of molecules in intense few-cycle laser pulses". In: *Applied Physics B* 98.4 (2010), pp. 659–666. DOI: 10.1007/s00340-009-3860-x. URL: https://doi.org/10.1007/s00340-009-3860-x.

[163] Hiroshi Akagi, Tomohito Otobe, and Ryuji Itakura. "Deformation of an inner valence molecular orbital in ethanol by an intense laser field". In: *Science Advances* 5.5 (2019), eaaw1885. DOI: 10.1126/sciadv.aaw1885. URL: https://www.science.org/doi/abs/10.1126/sciadv.aaw1885.

[164] Tomoya Okino et al. "Coincidence momentum imaging of ultrafast hydrogen migration in methanol and its isotopomers in intense laser fields". In: *Chemical physics letters* 423.1-3 (2006), pp. 220–224. DOI: https://doi.org/10.1016/j.cplett.2006.03.068. URL: https://www.sciencedirect.com/science/article/pii/S0009261406004131.

[165] Tomoya Okino et al. "Ultrafast hydrogen scrambling in methylacetylene and methyl-d 3-acetylene ions induced by intense laser fields". In: *Physical Chemistry Chemical Physics* 14.30 (2012), pp. 10640–10646. DOI: 10.1039/C2CP40849J. URL: http://dx.doi.org/10.1039/C2CP40849J.

[166] N Neumann et al. "Fragmentation dynamics of CO_2^{3+} investigated by multiple electron capture in collisions with slow highly charged ions". In: *Physical review letters* 104.10 (2010), p. 103201. DOI: 10.1103/PhysRevLett.104.103201. URL: https://link.aps.org/doi/10.1103/PhysRevLett.104.103201.

[167] Enliang Wang et al. "Pathways for nonsequential and sequential fragmentation of $CO_2$3+ investigated by electron collision". In: *Physical Review A* 91.5 (2015), p. 052711. DOI: 10.1103/PhysRevA.91.052711. URL: https://link.aps.org/doi/10.1103/PhysRevA.91.052711.

[168] Kang Lin et al. "Femtosecond Resolving Photodissociation Dynamics of the SO_2 Molecule". In: *The Journal of Physical Chemistry Letters* 11.8 (2020), pp. 3129–3135. DOI: 10.1021/acs.jpclett.0c00599. URL: https://doi.org/10.1021/acs.jpclett.0c00599.

[169] Arnab Khan, Lokesh C Tribedi, and Deepankar Misra. "Three-body fragmentation of multiply charged nitrous oxide induced by Ar^{8+}- and Xe^{15+}-ion impact". In: *Physical Review A* 96.1 (2017), p. 012703. DOI: 10.1103/PhysRevA.96.012703. URL: https://link.aps.org/doi/10.1103/PhysRevA.96.012703.

[170] Arnab Khan and Deepankar Misra. "Decay dynamics of N_2O under the impact of fast electrons". In: *Journal of Physics B: Atomic, Molecular and Optical Physics* 49.5 (2016), p. 055201. DOI: 10.1088/0953-4075/49/5/055201. URL: https://doi.org/10.1088/0953-4075/49/5/055201.

[171] R Guillemin et al. "Selecting core-hole localization or delocalization in CS_2 by photofragmentation dynamics". In: *Nature communications* 6.1 (2015), pp. 1–6. DOI: 10.1038/ncomms7166. URL: https://doi.org/10.1038/ncomms7166.

[172] Enliang Wang et al. "Fragmentation dynamics of CS_2 in collisions with 1.0 keV electrons". In: *The Journal of Chemical Physics* 149.20 (2018), p. 204301. DOI: 10.1063/1.5059347. URL: https://doi.org/10.1063/1.5059347.

[173] Ali Ramadhan et al. "Ultrafast molecular dynamics of dissociative ionization in OCS probed by soft x-ray synchrotron radiation". In: *Journal of Physics B: Atomic, Molecular and Optical Physics* 49.21 (2016), p. 215602. DOI: 10.1088/0953-4075/49/21/215602. URL: https://doi.org/10.1088/0953-4075/49/21/215602.

[174] Bo Wang et al. "Dissociative ionization of OCS induced by highly charged ion impact". In: *Physical Review A* 103.4 (2021), p. 042810. DOI: 10.1103/PhysRevA.103.042810. URL: https://link.aps.org/doi/10.1103/PhysRevA.103.042810.

[175] Baihui Ren et al. "Three-body fragmentation mechanism of $C_2H_4^{3+}$ produced by 18- keV/u Ne^{8+} impact". In: *Physical Review A* 104.2 (2021), p. 022811. DOI:

10.1103/PhysRevA.104.022811. URL: https://link.aps.org/doi/10.1103/PhysRevA.104.022811.

[176] T Jiang et al. "Three-fragment dissociation of $C_2H_2^{2+}$ and $C_2H_2^{3+}$ produced by slow-Ar^{8+}-ion impact". In: *Physical Review A* 100.2 (2019), p. 022705. DOI: 10.1103/PhysRevA.100.022705. URL: https://link.aps.org/doi/10.1103/PhysRevA.100.022705.

[177] Christian Burger et al. "Visualization of bond rearrangements in acetylene using near single-cycle laser pulses". In: *Faraday Discussions* 194 (2016), pp. 495–508. DOI: 10.1039/C6FD00082G. URL: http://dx.doi.org/10.1039/C6FD00082G.

[178] S Xu et al. "Dynamics of $C_2H_2^{3+} \longrightarrow H^+ + H^+ + C_2^+$ investigated by 50-keV/u Ne^{8+} impact". In: *Physical Review A* 97.6 (2018), p. 062701.

[179] Itamar Luzon et al. "Making sense of Coulomb explosion imaging". In: *The Journal of Physical Chemistry Letters* 10.6 (2019), pp. 1361–1367. DOI: 10.1021/acs.jpclett.9b00576. URL: https://doi.org/10.1021/acs.jpclett.9b00576.

[180] Jiaqi Zhou et al. "Ultrafast ring-opening fragmentation dynamics of $C_6H_6^{3+}$ induced by electron-impact ionization". In: *Physical Review A* 104.3 (2021), p. 032807. DOI: 10.1103/PhysRevA.104.032807. URL: https://link.aps.org/doi/10.1103/PhysRevA.104.032807.

[181] Li Zhang et al. "Path-selective investigation of intense laser-pulse-induced fragmentation dynamics in triply charged 1,3-butadiene". In: *Journal of Physics B: Atomic, Molecular and Optical Physics* 45.8 (2012), p. 085603. DOI: 10.1088/0953-4075/45/8/085603. URL: https://doi.org/10.1088/0953-4075/45/8/085603.

[182] Chao Ma et al. "Three-body fragmentation dynamics of $CH_2CCH_2^{3+}$ investigated by 50-keV/u Ne^{8+} impact". In: *Physical Review A* 101.5 (2020), p. 052701. DOI: 10.1103/PhysRevA.101.052701. URL: https://link.aps.org/doi/10.1103/PhysRevA.101.052701.

[183] Akiyoshi Hishikawa et al. "Acetylene-vinylidene isomerization in ultrashort intense laser fields studied by triple ion-coincidence momentum imaging". In: *The Journal of chemical physics* 128.8 (2008), p. 084302. DOI: 10.1063/1.2828557. URL: https://doi.org/10.1063/1.2828557.

[184] Huailiang Xu et al. "Two-proton migration in 1,3-butadiene in intense laser fields". In: *Physical Chemistry Chemical Physics* 12.40 (2010), pp. 12939–12942. DOI: 10.1039/C0CP00628A. URL: http://dx.doi.org/10.1039/C0CP00628A.

[185] Benji Wales et al. "Coulomb imaging of the concerted and stepwise break up processes of OCS ions in intense femtosecond laser radiation". In: *Journal of Electron Spectroscopy and Related Phenomena* 195 (2014), pp. 332–336.

[186] Pan Ma et al. "Comparison study for multiple ionization of carbonyl sulfide by linearly and circularly polarized intense femtosecond laser fields using Coulomb explosion imaging". In: *Journal of Physics B: Atomic, Molecular and Optical Physics* 51.9 (2018), p. 094002. DOI: 10.1088/1361-6455/aab5aa. URL: https://doi.org/10.1088/1361-6455/aab5aa.

[187] Chien-Ming Tseng et al. "Coincidence momentum imaging of four-and three-body Coulomb explosion of formaldehyde in ultrashort intense laser fields". In: *Journal of Electron Spectroscopy and Related Phenomena* 228 (2018), pp. 25–30. DOI: https://doi.org/10.1016/j.elspec.2018.07.001. URL: https://www.sciencedirect.com/science/article/pii/S0368204818301129.

[188] Robert C Rhew, Benjamin R Miller, and Ray F Weiss. "Natural methyl bromide and methyl chloride emissions from coastal salt marshes". In: *Nature* 403.6767 (2000), pp. 292–295. DOI: 10.1038/35002043. URL: https://doi.org/10.1038/35002043.

[189] Yoko Yokouchi et al. "Strong emission of methyl chloride from tropical plants". In: *Nature* 416.6877 (2002), pp. 163–165. DOI: 10.1038/416163a. URL: https://doi.org/10.1038/416163a.

[190] Shanlan Li et al. "Emission estimates of methyl chloride from industrial sources in China based on high frequency atmospheric observations". In: *Journal of Atmospheric Chemistry* 74.2 (2017), pp. 227–243. DOI: 10.1007/s10874-016-9354-4. URL: https://doi.org/10.1007/s10874-016-9354-4.

[191] Jyoti Rajput et al. "Native frames: Disentangling sequential from concerted three-body fragmentation". In: *Physical Review Letters* 120.10 (2018), p. 103001. DOI: 10.1103/PhysRevLett.120.103001. URL: https://link.aps.org/doi/10.1103/PhysRevLett.120.103001.

[192] Jiaqi Zhou et al. "Triple ionization and fragmentation of benzene trimers following ultrafast intermolecular Coulombic decay". In: *Nature Communications* 13.1 (2022), p. 5335. ISSN: 2041-1723. DOI: 10.1038/s41467-022-33032-2. URL: https://doi.org/10.1038/s41467-022-33032-2.

[193] Noelle Walsh et al. "Molecular dynamics of NH_3 induced by core-electron excitation". In: *Physical Chemistry Chemical Physics* 17.29 (2015), pp. 18944–18952. DOI: 10.1039/C5CP02959G. URL: http://dx.doi.org/10.1039/C5CP02959G.

[194] Ulrich Galster et al. "Experimental and quantum-chemical studies on the three-particle fragmentation of neutral triatomic hydrogen". In: *Physical Review A* 72.6 (2005), p. 062506. DOI: 10.1103/PhysRevA.72.062506. URL: https://link.aps.org/doi/10.1103/PhysRevA.72.062506.

[195] Long Wei et al. "Dissociation of NH_3^{2+} induced by collision of 300 eV electrons with NH_3". In: *The European Physical Journal D* 74.6 (2020), pp. 1–7. DOI: 10.1140/epjd/e2020-10094-7. URL: https://doi.org/10.1140/epjd/e2020-10094-7.

[196] ZD Pešić et al. "Three-body fragmentation of CO_2^{2+} upon K-shell photoionization". In: *Physical Review A* 78.5 (2008), p. 051401. DOI: 10.1103/PhysRevA.78.051401. URL: https://link.aps.org/doi/10.1103/PhysRevA.78.051401.

[197] Hang Yuan et al. "Three-body fragmentation dynamics of CH_3CCH^{3+} investigated by 50-keV/u Ne^{8+} impact: Comparison with its isomer ion $CH_2CCH_2{}^{3+}$". In: *Phys. Rev. A* 105 (2 2022), p. 022814. DOI: 10.1103/PhysRevA.105.022814. URL: https://link.aps.org/doi/10.1103/PhysRevA.105.022814.

[198] Christophe Dugave and Luc Demange. "CisTrans Isomerization of Organic Molecules and Biomolecules: Implications and Applications". In: *Chemical*

Reviews 103.7 (2003), pp. 2475–2532. ISSN: 0009-2665. DOI: 10.1021/cr0104375. URL: https://doi.org/10.1021/cr0104375.

[199] Amy H. Andreotti. "Native State Proline Isomerization: An Intrinsic Molecular Switch". In: *Biochemistry* 42.32 (2003), pp. 9515–9524. ISSN: 0006-2960. DOI: 10.1021/bi0350710. URL: https://doi.org/10.1021/bi0350710.

[200] Huynh Van Sa Lam et al. "Angle-dependent strong-field ionization and fragmentation of carbon dioxide measured using rotational wave packets". In: *Phys. Rev. A* 102 (4 2020), p. 043119. DOI: 10.1103/PhysRevA.102.043119. URL: https://link.aps.org/doi/10.1103/PhysRevA.102.043119.

[201] S. De et al. "Field-Free Orientation of CO Molecules by Femtosecond Two-Color Laser Fields". In: *Phys. Rev. Lett.* 103 (15 2009), p. 153002. DOI: 10.1103/PhysRevLett.103.153002. URL: https://link.aps.org/doi/10.1103/PhysRevLett.103.153002.

[202] H. Li et al. "Orientation dependence of the ionization of CO and NO in an intense femtosecond two-color laser field". In: *Phys. Rev. A* 84 (4 2011), p. 043429. DOI: 10.1103/PhysRevA.84.043429. URL: https://link.aps.org/doi/10.1103/PhysRevA.84.043429.

[203] K. J. Betsch, D. W. Pinkham, and R. R. Jones. "Directional Emission of Multiply Charged Ions During Dissociative Ionization in Asymmetric Two-Color Laser Fields". In: *Phys. Rev. Lett.* 105 (22 2010), p. 223002. DOI: 10.1103/PhysRevLett.105.223002. URL: https://link.aps.org/doi/10.1103/PhysRevLett.105.223002.

Faraday Discussions

Cite this: DOI: 10.1039/d0fd00129e

ROYAL SOCIETY OF CHEMISTRY

PAPER

View Article Online
View Journal

Strong-field ionization of polyatomic molecules: ultrafast H atom migration and bond formation in the photodissociation of CH_3OH†

Rituparna Das,[ab] Deepak K. Pandey,[c] Vinitha Nimma,[a] Madhusudhan P.,[ab] Pranav Bhardwaj,[ab] Pooja Chandravanshi,[a] Muhammed Shameem K. M.,[a] Dheeraj K. Singh[c] and Rajesh K. Kushawaha *[a]

Received 1st December 2020, Accepted 5th January 2021

DOI: 10.1039/d0fd00129e

Strong-field ionization induces various complex phenomena like bond breaking, intramolecular hydrogen migration, and bond association in polyatomic molecules. The H-atom migration and bond formation in CH_3OH induced by intense femtosecond laser pulses are investigated using a Velocity Map Imaging (VMI) spectrometer. Various laser parameters like intensity (1.5×10^{13} W cm^{-2}–12.5×10^{13} W cm^{-2}), pulse duration (29 fs and 195 fs), wavelength (800 nm and 1300 nm), and polarization (linear and circular) can serve as a quantum control for hydrogen migration and the yield of H_n^+ ($n = 1$–3) ions which have been observed in this study. Further, in order to understand the ejection mechanism of the hydrogen molecular ions H_2^+ and H_3^+ from singly-ionized CH_3OH, quantum chemical calculations were employed. The dissociation processes of CH_3OH^+ occurring by four dissociative channels to form $CHO^+ + H_3$, $H_3^+ + CHO$, $CH_2^+ + H_2O$, and $H_2O^+ + CH_2$ are studied. Using the combined approach of experiments and theory, we have successfully explained the mechanism of intramolecular hydrogen migration and predicted the dissociative channels of singly-ionized CH_3OH.

Light-induced chemical and biological processes, like the *cis–trans* isomerization in rhodopsin responsible for vision,[1] the absorption of sunlight by photoactive pigments and the subsequent transfer of energy to the reaction center in photosynthesis,[2] the interaction of short-wavelength radiation with human skin

[a]*Physical Research Laboratory, Ahmedabad, India. E-mail: kushawaha@prl.res.in; Fax: +91-79-2631-4900; Tel: +91-79-2631-4560*

[b]*Indian Institute of Technology, Gandhinagar, Gujarat 382355, India*

[c]*Department of Physics, Institute of Infrastructure Technology Research and Management, Ahmedabad, 380026, India*

† Electronic supplementary information (ESI) available. See DOI: 10.1039/d0fd00129e

resulting in skin damage,[3] and so on, occur on a timescale of a few tens of femtoseconds to a few nanoseconds. The advent of intense ultrashort lasers has made it possible to study such ultrafast processes in real-time. In molecules, the nuclear dynamics occur on femtosecond to picosecond timescales while electron dynamics take place in the attosecond domain. Under perturbation by intense ultrashort laser pulses, the transfer of energy to molecules initiates dynamical processes such as excitation,[4] ionization,[5–7] molecular vibrations,[8–10] and rotations.[11–13]

Hydrocarbons have been used as a prototype for studying geometrical deformation and structural changes in molecules for several years now.[4,14–20] Such changes in molecules in their excited and ionized states give rise to processes like bond-breaking,[21,22] intramolecular migration of moieties,[23–25] isomerization,[15,26] and bond association,[27,28] prior to the dissociation or Coulomb explosion of the molecular ion. Intramolecular proton migration and bond formation phenomena have been a topic of interest to researchers for a long time due to their importance in many physical,[29] chemical,[30] and biological[23] processes.

Photodissociation of hydrocarbons initiated by any ionizing source like electrons,[31,32] ions,[33–35] or laser pulses,[19,30] and the detection of H_2^+ and H_3^+ ions have confirmed the fact that bond-breaking, intramolecular migration, and bond association occur before the fragmentation of unstable molecular ions. Both singly[31,36] and doubly ionized methanol[18,19,28,37,38] have been shown to exhibit intramolecular migration, and H_2^+ and H_3^+ formation. For example, two possible channels for two-body dissociation in singly ionised CH_3OH are:

$$CH_3OH^+ \rightarrow CH_3O + H^+ \tag{1}$$

$$CH_3OH^+ \rightarrow HCO + H_3^+ \tag{2}$$

Similarly, the two- and three-body fragmentation channels for doubly ionised methanol include:

$$CH_3OH^{2+} \rightarrow HCOH^+ + H_2^+ \tag{3}$$

$$CH_3OH^{2+} \rightarrow COH^+ + H_3^+ \tag{4}$$

$$CH_3OH^{2+} \rightarrow H_2CO^+ + H_2^+ \tag{5}$$

$$CH_3OH^{2+} \rightarrow HCO^+ + H_3^+ \tag{6}$$

$$CH_3OH^{2+} \rightarrow H + H_2^+ + COH^+ \tag{7}$$

Pathways (3) and (4) only involve bond formation while (5) and (6) involve H-migration and bond formation. Pathway (7) demonstrates three-body fragmentation. In order to confirm intramolecular hydrogen migration and bond association in CH_3OH (channels (5) and (6)), photodissociation of the deuterated isotopomer of CH_3OH can be studied as well. The dissociation channels for doubly ionised CD_3OH include:

$$CD_3OH^{2+} \rightarrow D_2CO^+ + DH^+ \tag{8}$$

$$CD_3OH^{2+} \rightarrow DCO^+ + D_2H^+ \quad (9)$$

$$CD_3OH^{2+} \rightarrow D + D_2^+ + COH^+ \quad (10)$$

DH^+ and D_2H^+ can only be formed by the migration and bond association processes before dissociation of the parent ion, which confirms intramolecular H-migration in methanol.

H_2^+ and H_3^+ formation from both singly[36] and doubly ionized[16] CH_3OH has been found to be a two-step process. The first step is the ionization of CH_3OH and the formation of a neutral H_2 molecule which roams on the potential energy surface (PES) of the parent ion. In the second step, the roaming H_2 molecule extracts a proton from the parent ion (and forms H_3^+), before the molecular ion undergoes Coulomb explosion.[16–18] There can also be a long-range electron transfer from the neutral H_2 to $HCOH^+$ (inverse harpooning), in which case a H_2^+ ion is formed.[16] Similarly, the formation of triatomic ions like D_2H^+ and D_3^+ from CD_3OH has been shown to proceed *via* the generation of a neutral, long-lived D_2 moiety.[39] The timescale of intramolecular hydrogen migration and formation of H_2^+ and H_3^+ has been reported to be of the order of tens of fs to a few hundred fs,[19,40] and is still a matter of further investigation.

Single and double ionization of molecules has received attention from researchers for a long time.[5,41,42] Strong-field double ionization of molecules can be further classified as (a) sequential (SDI), and (b) non-sequential (NSDI). In SDI, two electrons are emitted independently from the molecule, while NSDI occurs due to electron–electron correlation and is characterized by the ejection of an electron by tunneling, followed by its inelastic recollision with the parent ion and the removal of a second electron.[43,44] Alternatively, the recolliding tunnel electron may excite the molecular ion which then undergoes further ionization by the laser field. This process is referred to as recollision excitation with subsequent ionization (RESI).[45] Strong-field ionization of a molecule is followed by the evolution of the molecular wave packet, a change in its geometry, and finally dissociation. Laser parameters like intensity, pulse duration, wavelength, and polarization affect the strong-field ionization and fragmentation processes of molecules and hence, the yield of various fragment ions. In this work, we have experimentally investigated the photodissociation of CH_3OH and the yield of H_n^+ ($n = 1$–3) ions under the influence of these parameters, which can serve as a quantum control for the dissociation pathways of methanol. Hydrogen migration and association across the chemical group (methyl or hydroxyl) have been confirmed by studying the photodissociation of CD_3OH. We have also performed quantum chemical calculations to understand the intramolecular hydrogen migration and predict the dissociation channels of singly ionized methanol.

1 Experimental methodology

Photoionization experiments were performed using 800 nm, 29 fs, 1 kHz, and 10 mJ laser pulses and an in-house developed Velocity Map Imaging Spectrometer (VMIS). Laser pulses of 6 mJ energy were used to pump an optical parametric amplifier (OPA) which allows wavelength tunability from 1300 nm to 1600 nm for signals, and 1661 nm to 2185 nm for idler beams, while 1.5 mJ was used directly for performing photodissociation experiments in the VMI.

Table 1 Yield of H^+, D^+, HD^+, D_2^+, D_2H^+, and D_3^+ ions (in %) from CD_3OH as a function of pulse duration. '*d*' stands for the thickness of the SF11 window in mm, while 'τ' represents the pulse duration in fs. The intensity was maintained at 1.46×10^{13} W cm^{-2} for all cases

d (mm)	τ (fs)	H^+	D^+	HD^+	D_2^+	D_2H^+	D_3^+
0 (unchirped)	29	4.7	3.7	0.1	0.5	0.2	0.1
5	39	8.4	7.7	0.1	1.3	1.3	0.9
10	85	10.4	10.8	0.3	1.8	1.4	1.0
15	195	14.9	20.1	0.5	2.4	3.0	2.4
20	290	17.7	27.7	0.7	2.9	4.8	4.3

The femtosecond pulse characterization was performed using the Spectral Phase Interferometry for Direct Electric-field Reconstruction (SPIDER) technique. A commercial SPIDER setup from APE Germany (model: FC-SPIDER) was used for characterizing the laser pulses. The measured pulse duration of the fundamental 800 nm pulses was 29 fs. We used SF11 windows of different thicknesses to stretch the laser pulses for studying the effect of pulse duration on the formation of H_n^+ ($n = 1$–3) ions. Characterization of the stretched pulses after passing through the SF11 windows was also performed by SPIDER. The pulse duration characterization for each case is summarized in columns 1 and 2 of Table 1.

In the photoionization experiment, the laser beam was focused on the ionization region of the VMIS using a 2 inch silver concave mirror with an effective focal length (EFL) of −20 cm (Newport). The cold molecular beam was generated using an Amsterdam Cantilever Piezo Valve (ACPV2, 200 μm diameter nozzle) and a skimmer with an orifice size of 900 μm. The piezo valve opening time was set to 40 μs during measurements.

The methanol (CH_3OH) and methanol-D3 (CD_3OH) samples with purity of 99.8% from Sigma Aldrich were used without any further purification. Helium was used as a carrier gas. The gas-line pressure was kept at 4 bar, while the pressure in the VMIS chamber was 2×10^{-7} mbar in the presence of the molecular beam and 6×10^{-9} mbar without the molecular beam.

The VMIS is a multi-plate VMI similar to the thick-lens (11-plates) mass spectrometer.[46] We kept two focusing plates for adjusting the dispersion and improving the energy resolution in this design. This spectrometer can record the time-of-flight (TOF) mass spectrum of ions in the TOF mode and the VMI image of electrons/ions in the VMI lensing mode. The simulations of ion and electron trajectories were performed in SIMION 8.0 prior to the fabrication of this spectrometer. The ion time-of-flight calibration was performed using nitrogen, argon, and xenon gases.

An NHQ power supply module was used to apply voltages to the microchannel plate (MCP) detector and also to all the electrodes of the VMI spectrometer. The repeller, extractor, and focusing plates are independently connected to the power supply. Resistors connected in series between the remaining plates distribute the voltage to these plates.

A TDC8HP card from RoentDek was used for recording the TOF spectrum. The MCP raw signal was sent to an ATR-19 (pre-amplification and Constant Fraction Discriminator (CFD)) and the Nuclear Instrumentation Modules (NIM) signal from the ATR-19 was given to the TDC8HP card. The laser sync out was used as the

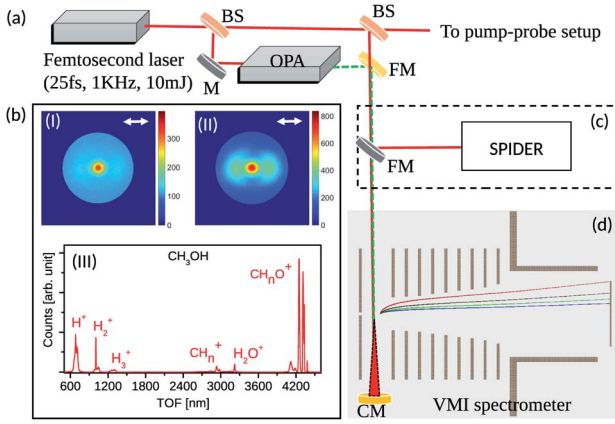

Fig. 1 (a) Schematic diagram of the experimental setup. This setup was used for photoionization experiments with 800 nm femtosecond laser and 1300 nm OPA pulses. (b) (I) and (II) show the H_n^+ (n = 1, 2, 3) ion VMI images for 800 nm, 29 fs and 195 fs pulses, respectively, (III) shows the time-of-flight (TOF) mass spectrum recorded for methanol, (c) pulse characterization using SPIDER, and (d) multi-plate velocity map imaging spectrometer. The VMI images are shown here to demonstrate the working of the VMI in the imaging mode. (BS = beam splitter, OPA = optical parametric amplifier, FM = flip mirror, CM = concave mirror, M = mirror).

trigger. The Cobold PC software was used for TOF data acquisition. Data analysis was performed using the Cobold PC and OriginPro 8.5 software.

A schematic diagram of the experimental setup is shown in Fig. 1.

2 Computational methodology

Density functional theory (DFT) calculations were performed using the Gaussian 16 suite of software[47] to gain in-depth insight into the possible mechanism of the hydrogen migration and dissociation processes in CH_3OH^+ to form various fragments (H_3^+, H_2O^+, CHO, CH_2^+). The initial input geometries of CH_3OH and all the molecular fragments (CH_2, CH_2^+, CHO, CHO^+, H_2O, H_2O^+, H_3, H_3^+), various transition states (TSs), and intermediate complexes of singly ionized CH_3OH^+ were prepared using GaussView 6 software.[48] In order to fully optimize the geometries of different monomers of CH_3OH^+, transition states (TSs), and various fragmented products at the PES, the meta-generalized gradient approximation based Minnesota functional M06-2X and the 6-311++G(d,p) basis set were utilized.[49,50] Four different pathways through which CH_3OH^+ can be dissociated were computed on the CH_3OH^+ ground doublet PES. Furthermore, at the same level of theory, M06-2X/6-311++G(d,p), vibrational frequencies were calculated to obtain the zero-point energies and to verify that the computed structures were either TSs or minima. Using a number of imaginary frequencies, the local minima, and TSs were identified (zero and one, respectively). All the identified TSs have only one imaginary frequency, and the computed intrinsic reaction coordinate (IRC) results suggest that the corresponding vibration path links the reactant and the product accurately. CYLview20 software was used to visualize the final optimized geometries of all the calculated structures.[51]

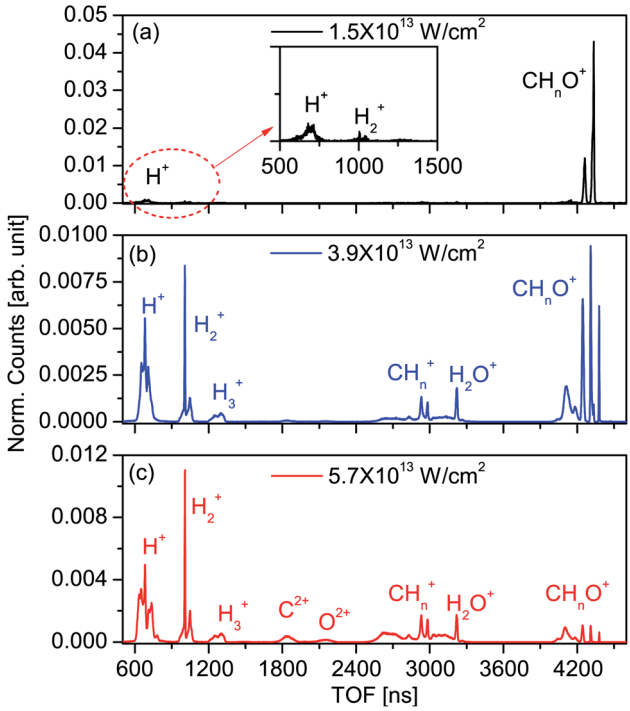

Fig. 2 Time-of-flight spectra of CH_3OH recorded at three different laser intensities, for 29 fs, 800 nm, and linearly polarized (parallel to the plane of the MCP-phosphor detector) light pulses. Laser intensities in the three cases were (a) 1.5×10^{13} W cm^{-2}, (b) 3.9×10^{13} W cm^{-2}, and (c) 5.7×10^{13} W cm^{-2}. The *y*-axes represent the normalized counts. Normalization was done to the total counts ((a) 5.8×10^4, (b) 1.1×10^6, and (c) 1.3×10^6) recorded in each spectrum. In (a) CH_nO^+ ($n = 1$–3) are visible. The yields of CH_nO^+ ($n = 0$, 4) are very low and are only visible on the logarithmic scale. In (b) $n = 0$–3 in CH_n^+, while $n = 0$–4 in CH_nO^+. Similarly $n = 0$–3 in CH_n^+ and $n = 0$–4 in CH_nO^+ in (c).

3 Results and discussion

3.1 H_n^+ ($n = 1$–3) ion formation: intensity dependence

Firstly, we studied the effect of laser intensity on fragmentation and the yield of H^+, H_2^+, and H_3^+ ions during the photodissociation of CH_3OH. Fig. 2 shows the TOF spectra of CH_3OH molecules generated by interaction with 800 nm, 29 fs, and linearly polarized (parallel to the plane of the MCP-phosphor detector) laser pulses. These spectra were recorded at three different laser intensities – 0.015 PW cm^{-2}, 0.039 PW cm^{-2}, and 0.057 PW cm^{-2}.

At low laser intensity, single ionization of CH_3OH occurs by a multiphoton ionization (MPI) process (Keldysh parameter $\gamma > 1$).[52] Single ionization mostly transfers the CH_3OH molecule from the ground state to metastable states with longer lifetimes due to which the yield of heavier fragments like CH_3O^+ and CH_2O^+ is higher in Fig. 2(a). Few of the parent ions, which are in unstable repulsive states, fragment into the H_n^+ ($n = 1$–3), CH_n^+ ($n = 0$–3), OH^+, and H_2O^+ ions. We observe that the yields of CO^+, COH^+, and CH_3OH^+ are very low and visible only on the logarithmic scale. It is most likely that the unstable repulsive

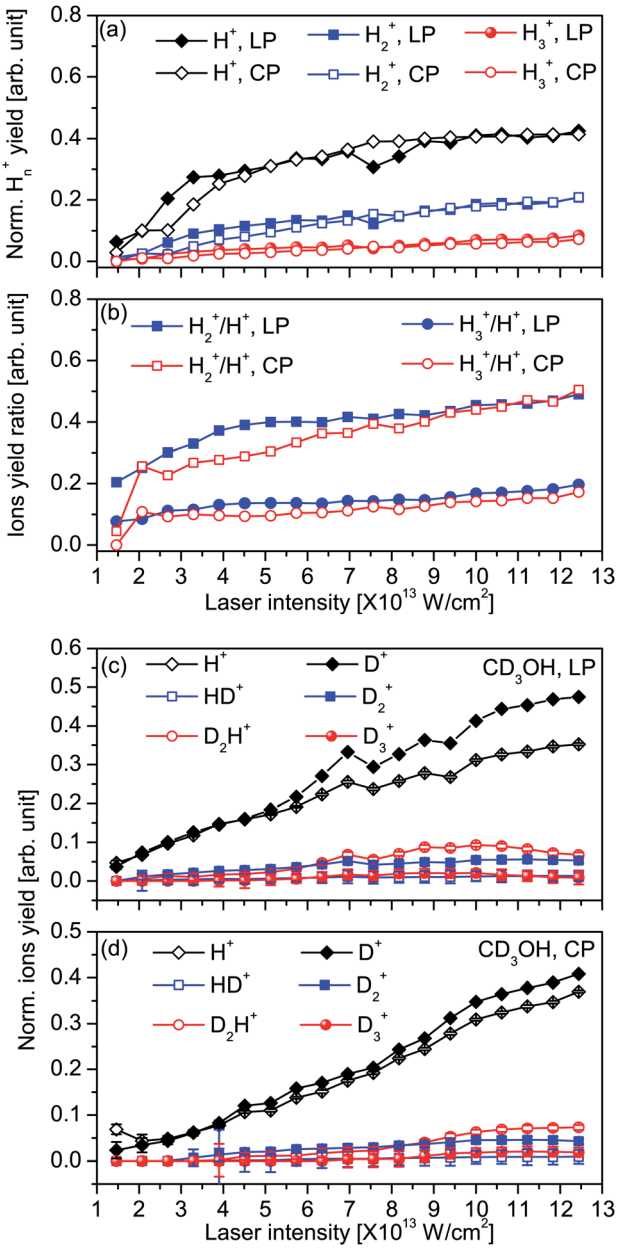

Fig. 3 (a) Normalised H_n^+ ($n = 1$–3) ion yield as a function of laser intensity for CH_3OH (maximum error is 7%). (b) Ratio of bond formation to bond breaking in CH_3OH as a function of laser intensity (maximum error is 6%). Solid symbols stand for linear polarization while hollow symbols stand for circular polarization in both (a) and (b). (c) Normalised yield of H^+, D^+, HD^+, D_2^+, D_2H^+, and D_3^+ as a function of laser intensity for the photodissociation of CD_3OH by linearly polarized pulses (maximum error is 3%). (d) Same as (c) but with circularly polarized pulses (maximum error is 7%). The laser parameters such as pulse duration (29 fs) and wavelength (800 nm), and the VMI spectrometer voltages were kept constant during the measurements. Normalisation in all cases has been done to the total ion yield.

states of the CH_3OH^+ ion are populated at this intensity, leading to its fragmentation. As the laser intensity increases, multiple repulsive states are populated, producing more fragment ions through various dissociation channels. Thus, it enhances the yield of smaller fragments like H_n^+ and CH_n^+, as shown in Fig. 2(b). At high laser intensity (Keldysh parameter $\gamma < 1$), the molecule's Coulomb potential gets distorted. Tunnel ionization and electron recollision-based processes start playing a role in further excitation or ionization of the already ionized molecules. The formation of C^{2+} and O^{2+} ions in the TOF mass spectrum (Fig. 2(c)) is evidence of multiple ionization (double, triple, or even quadruple ionization) of the precursor molecules.

The effect of laser intensity and polarization on the yield of H^+, H_2^+, and H_3^+ ions is shown in Fig. 3(a) and (b). As indicated by Fig. 3(a), the integrated H_n^+ ion yield normalized to the total counts (all ions) initially increases with laser intensity and then saturates for higher intensities. As already discussed above, single ionization by MPI is more common at low intensities, resulting in fewer molecules reaching dissociative excited states. This is why the H_n^+ yield is smaller at low intensities. At high intensities, in addition to the larger number of populated dissociative states of CH_3OH^+, new dissociative channels are created due to the complex phenomena of tunneling and recollision, which transfer the parent molecule to the unstable CH_3OH^{2+} state. A neutral H_2 molecule formed in the vicinity of the ion then roams on the PES and either extracts a proton or donates an electron (and forms H_3^+ or H_2^+, respectively) before the Coulomb explosion of the parent ion.[16]

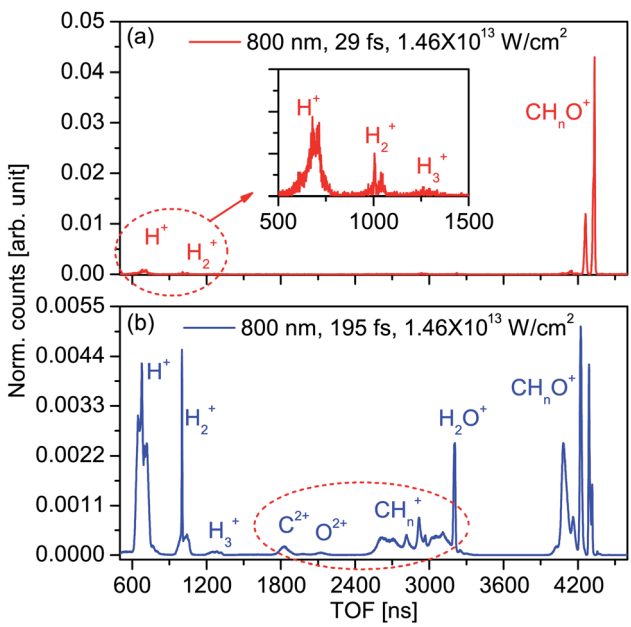

Fig. 4 Time-of-flight spectra of CH_3OH obtained with 800 nm, linearly polarized light with intensity 1.46×10^{13} W cm^{-2}, and pulse duration (a) 29 fs, and (b) 195 fs. The y-axes represent the normalized counts. Normalization is done to the total counts ((a) 5.8×10^4, and (b) 3.4×10^5) recorded in each spectrum. In (a), $n = 1$–3 in CH_nO^+. Similarly $n = 0$–3 in CH_n^+ and $n = 0$–3 in CH_nO^+ in (b).

It is expected that at such high intensities, bond formation should decrease and bond breaking should increase. It is, however, interesting to note that the yield of H_2^+ and H_3^+ ions is not much affected and remains nearly constant at high intensities but the yield of CH_nO^+ ($n = 0$–4) ions is found to decrease at high intensities due to C–H and O–H bond breaking. Fig. 3(a) and (b) clearly show that the yields of H_2^+ and H_3^+ are constant or have little variation over a range of laser intensities, but CH_nO^+ ($n = 0$–4) yields are reduced drastically as clearly visible in Fig. 2(c).

To confirm the intramolecular migration of hydrogen in CH_3OH, we used the deuterated isotopomer of methanol (CD_3OH) and recorded the intensity and polarization dependence of the yield of H^+, D^+, HD^+, D_2^+, D_2H^+, and D_3^+ ions as a function of laser intensity as shown in Fig. 3(c) and (d). The plots show similar trends to CH_3OH and, therefore, confirm that similar processes are involved in the ionization and fragmentation of both parent molecules. These results conform to those obtained in previous studies[17,53] on strong-field photodissociation of hydrocarbons.

3.2 H_n^+ ($n = 1$–3) formation: pulse duration dependence

Next, we examined the effect of laser pulse duration on the photodissociation of CH_3OH and the yield of H_n^+ ions. Fig. 4 shows the TOF spectra of CH_3OH obtained using 800 nm, linearly polarized pulses with pulse duration (a) 29 fs, and

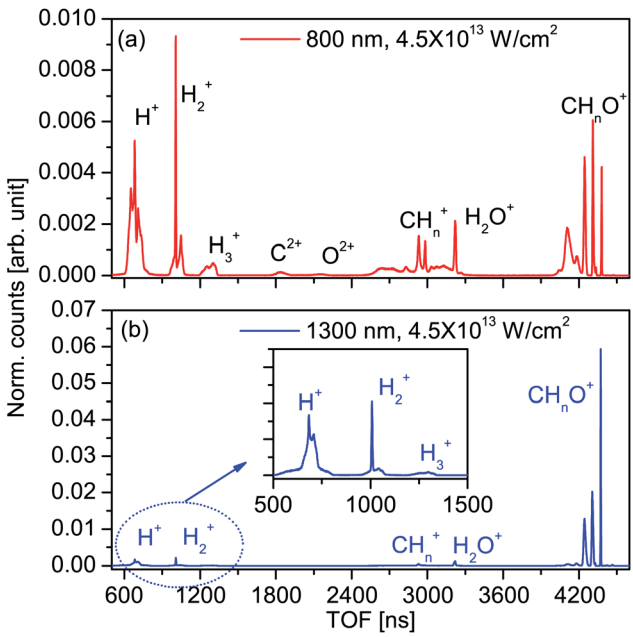

Fig. 5 Time-of-flight spectra of CH_3OH recorded at two different wavelengths: (a) 800 nm, and (b) 1300 nm. We kept the laser parameters such as pulse duration (fundamental 800 nm, 29 fs), intensity (4.5×10^{13} W cm^{-2}), and polarization (linear) constant during the measurements. In these measurements, the laser light polarization was parallel to the plane of the MCP-phosphor detector. The y-axes represent normalized counts. Normalization is done to the total counts ((a) 2.2×10^6, and (b) 2.4×10^6) recorded in each spectrum. In (a), $n = 0$–3 in CH_n^+ and $n = 0$–4 in CH_nO^+. Similarly $n = 2$ in CH_n^+ and $n = 0$–4 in CH_nO^+ in (b).

(b) 195 fs. As evident from this figure, the yield of H_n^+ ($n = 1$–3) ions is minimal in Fig. 4(a), and the CH_n^+ ($n = 0$–3) ions are almost non-existent. On the other hand, photodissociation by stretched pulses results in higher fragmentation of the parent ions, and therefore, a high yield of smaller fragment ions like H_n^+ ($n = 1$–3), CH_n^+ ($n = 0$–3), C^{2+}, and O^{2+} ions is observed. This phenomenon of enhanced fragmentation for ionization with pulses of longer duration has been previously observed in multiple studies.[54–57] In the study on ethanol by Hosaka *et al.*[57] the kinetic energies carried by the photoelectrons resulting from different ionization channels were studied using pulses of different chirps. It was observed that for pulses with longer durations, more fragmentation and electronic excitation occurred. This feature was attributed to the fact that the vibrational wavepacket can evolve on the ground state of the $C_2H_5OH^+$ PES for the longer pulse duration case. This also leads to non-adiabatic couplings with other electronic states.[58]

Therefore, we can also infer that even in our experiments, longer pulses (195 fs) facilitate the evolution of the wavepacket in the ionized PES for a longer time as compared to the 29 fs pulses. This results in increased internal energy of the excited state (in this case CH_3OH^+) just before dissociation, in the case of stretched pulses.[57] This results in higher fragmentation of methanol and a high yield of H_n^+ ions in the case of ionization with 195 fs pulses.

We also studied the dependence of the yield of different fragments like H^+, D^+, HD^+, D_2^+, D_2H^+, and D_3^+ ions (formed by the photodissociation of CD_3OH) on pulse duration. For that, we used SF11 windows of thicknesses 5 mm, 10 mm, 15 mm, and 20 mm. Table 1 shows the % yield of the ions for pulses of different durations. As discussed above, the results are similar to what has been observed in the case of CH_3OH.

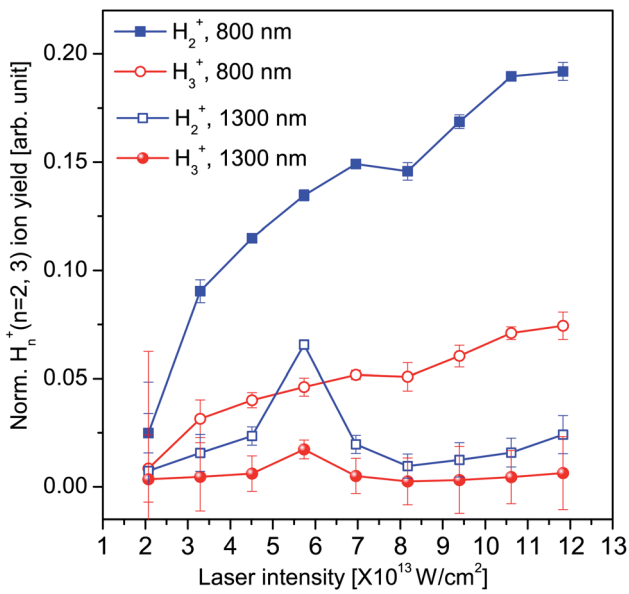

Fig. 6 Normalised H_n^+ ($n = 1$–3) ion yields as a function of laser intensity recorded using 800 nm and 1300 nm pulses. The parameters like pulse duration (29 fs), polarization (parallel to detector plane), and VMI spectrometer voltages were identical for both cases. The maximum error is 7%. Normalization was done to the total ion yield.

3.3 H_n^+ (n = 1–3) formation: wavelength dependence

The next parameter to be studied was the wavelength dependence of H_n^+ (n = 1–3) yield. Fig. 5 compares the TOF spectra of CH_3OH for wavelengths 800 nm and 1300 nm (generated from the OPA unit). As evident from the figure, the degree of fragmentation and the yield of ions are smaller in the case of strong-field ionization by 1300 nm light, while they are much higher for 800 nm light. In a previous study on strong-field ionization of the decatetraene (DT) molecule using 40 fs pulses of intensities $\sim 10^{13}$ W cm^{-2} and $\sim 10^{14}$ W cm^{-2} for wavelengths of 800 nm and 1450 nm respectively,[59] similar results were obtained. Similarly, the non-sequential double ionization yield of Mg decreased as the wavelength was increased from 800 nm to 2000 nm.[60]

At high intensities, ionization of molecules occurs mainly by tunneling. The recollision of the tunnel electron and subsequent ionization of the parent ion (three-step model) are strongly affected by the laser wavelength. For longer wavelengths, the travel time of the electron, and hence the spreading of the electron wavepacket are greater. As reported by Kang *et al.*[60] the energy distribution of the recolliding electron was found to be broader with peaks at energies far above 10 eV in the case of long wavelengths. At the same time, the density of the returning tunnel electron was found to decrease with increasing wavelength. This explains why the degree of fragmentation and the ion yield are lower for pulses of longer wavelength.

Fig. 6 compares the yield of H_n^+ (n = 2, 3) ions as a function of laser intensity for 800 nm and 1300 nm pulses. In the intensity range shown in the figure, the

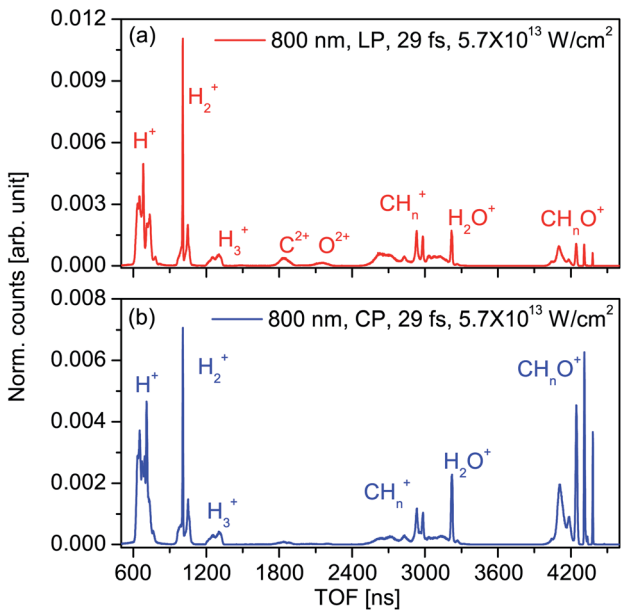

Fig. 7 Linear and circularly polarized light-induced time-of-flight mass spectra of CH_3OH. The parameters like wavelength (800 nm), pulse duration (29 fs), and intensity (5.7 $\times$ 10^{13} W cm^{-2}) were kept identical for both (a) linearly polarised, and (b) circularly polarized cases. The y-axes represent the normalised ion counts. Normalization is done to the total counts ((a) 1.3 $\times$ 10^6, and (b) 2.0 $\times$ 10^6) recorded in each spectrum. In both (a) and (b), n = 0–3 in CH_n^+ and n = 0–4 in CH_nO^+.

H_n^+ ($n = 1$–3) yield has an increasing trend for 800 nm, while it has a decreasing trend at 1300 nm. In fact at 1300 nm, the yield initially increases, reaches a maximum and then decreases. As discussed before, the yield of H_n^+ ions is expected to be lower for 1300 nm pulses. However, it is not clear why the peak in the yield of both H_2^+ and H_3^+ appears at the intensity of 5.7×10^{13} W cm^{-2} for 1300 nm pulses. This trend is under investigation with other wavelengths to understand the phenomena involved.

3.4 H_n^+ ($n = 1$–3) formation: polarization dependence

Finally, we examined the effect of polarization on the photodissociation of CH_3OH and the yield of H_n^+ ($n = 1$–3) ions. Fig. 7(a) and (b) show the TOF spectra obtained for 800 nm, linearly and circularly polarised pulses, respectively. Similarly, Fig. 8(a) and (b) show the TOF spectra obtained for 1300 nm, linearly and circularly polarized pulses, respectively. The 1300 nm pulses are generated by pumping the OPA with 800 nm, 29 fs pulses, and then further stretched by passing through an SF11 window of thickness 15 mm. The details of pulse duration as a function of the window's thickness are provided in Table 1. It is evident from the figures that the degree of fragmentation and the yield of H_n^+ ions are higher for linearly polarized pulses in comparison with circularly polarized pulses.

At high laser intensities, tunnel ionization and tunnel electron recollision-induced processes come into play, as discussed before. Polarization of light pulses can serve as a control in photoionization experiments, but its effect on the

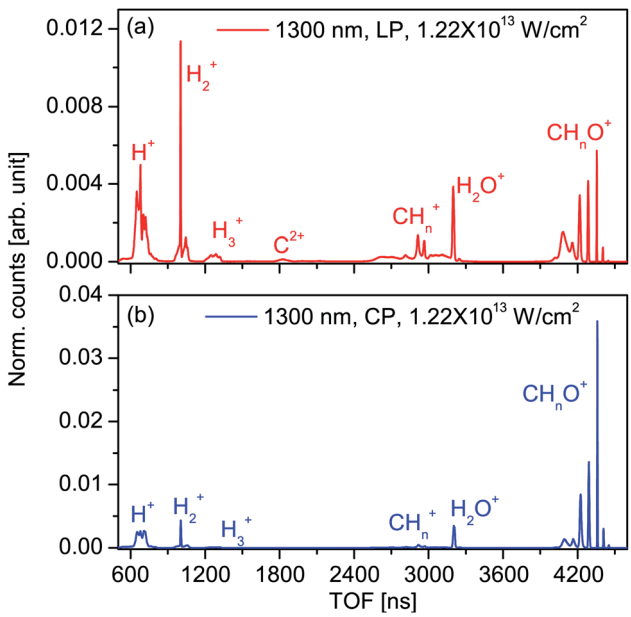

Fig. 8 Linear and circularly polarized light-induced time-of-flight mass spectra of CH_3OH. The parameters like wavelength (1300 nm), pulse duration (195 fs), and intensity (1.22×10^{13} W cm^{-2}) were kept identical for both (a) linearly polarised, and (b) circularly polarized cases. The y-axes represent the normalised ion counts. Normalization is done to the total counts ((a) 9.5×10^6, and (b) 2.4×10^6) recorded in each spectrum. In both (a) and (b), $n = 0$–3 in CH_n^+ and $n = 0$–4 in CH_nO^+.

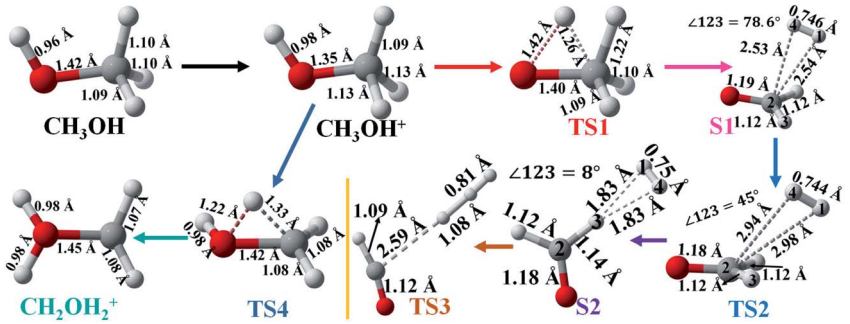

Fig. 9 DFT calculated structures and selected geometric parameters of CH_3OH, CH_3OH^+, $CH_2OH_2^+$, TS1, S1, TS2, S2, TS3, and TS4 optimized at the M06-2X/6-311++G(d,p) level of theory. Bond lengths are in Å and angles are in degrees.

ionization processes is not clearly understood. It is known that in the case of linear polarization, the tunnel electron reverses its trajectory as the laser field direction changes, and recollides with the parent ion (three-step model). Circular polarization is expected to cause the tunnel electron to spiral away from the parent ion, thereby reducing the recollision cross-section and the yield of fragment ions. This has been confirmed by many experiments.[37,61,62] However, it has also been observed in multiple studies that circular polarization significantly enhances double ionization.[63,64]

In our study, we observe that the degree of fragmentation and the yield of ions like H_n^+ and CH_n^+ are slightly higher for linearly polarized light as compared to circularly polarized light. Therefore, the effect of polarization on fragmentation and H_n^+ formation needs to be investigated further.

4 Quantum chemical calculations: dissociation channels of CH_3OH^+

Further, DFT calculations were performed to understand the fragmentation process of CH_3OH^+ and the yield of fragment ions. In order to obtain better precision, the M06-2X functional was utilized as this functional offers high-quality kinetic data for radical–molecule reactions compared to the well-established and accepted B3LYP functional.[65,66] Some of the singly ionized CH_3OH molecules are in meta-stable states (Fig. 2, 4, and 5), so we initially optimized the geometry of CH_3OH and CH_3OH^+ on their singlet and doublet PES, respectively. The local minima, transition states (TSs) and intermediate complexes of CH_3OH^+ involved in the dissociation reaction process are located at the M06-2X/6-311++G(d,p) level of theory, and their structures are presented in Fig. 9. Then the entire reaction routes from the stable geometry of CH_3OH^+ to H_3^+ + CHO and CH_2 + H_2O^+ are computed on the ground state doublet PES of CH_3OH^+ at the same level of theory and the potential energy surface profile is displayed in Fig. 10. The fully relaxed ground state geometries of all the calculated molecular ions, methanol in both the ground and singly ionized states (CH_3OH and CH_3OH^+), the TSs (TS1, TS2, TS3, and TS4) and the intermediate complexes (S1, and S2) along with their optimized energies and zero-

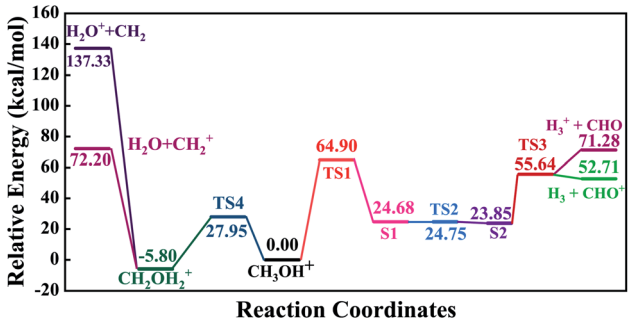

Fig. 10 The potential energy profile for the dissociation of CH_3OH^+ into H_3^+, CHO^+, CH_2^+ and H_2O^+ at the M06-2X/6-311++G(d,p) level of theory. The energies in the figure are relative to the total energy of CH_3OH^+.

point-corrected energies are shown in Fig. S1 in the ESI.† In the first step of the dissociation of CH_3OH^+ to H_3^+, the hydrogen atom in the –OH group shifts towards the carbon atom of the methyl group to create the first transition state TS1 (see Fig. 9). The generation of TS1 is endothermic by approximately 64.90 kcal mol^{-1}. TS1 has an imaginary frequency corresponding to the hydrogen atom situated between the oxygen and carbon atoms and the O–H bond length is elongated by about 0.44 Å (Fig. 9). After crossing TS1, the system reaches the intermediate S1, followed by asynchronous movement of this hydrogen atom. The energy barrier between CH_3OH^+ and S1 is 24.68 kcal mol^{-1}. In this process, the O–H bond completely dissociates, and this hydrogen atom forms a new bond with another hydrogen atom, which separates from the methyl group. In this way, a neutral H_2 moiety is formed that tends to isolate from the rest of the molecule, with distances of 2.53 and 2.54 Å between the carbon atom and the hydrogen atoms H1 and H4, respectively. In this geometrical structure of S1, the angle between the C2 carbon atom and the hydrogen atoms (H1 and H3) is found to be 78° which is further reduced to 45° as the H_2 moiety shifts more towards the H3 atom, leading to the formation of TS2. Here, it can be noticed that the energy difference between TS2 and S1 is negligible (0.08 kcal mol^{-1}). Further, the H_2 moiety continues to move towards the H3 atom to form the second intermediate S2 and the angle ∠123 decreases to 8°. Again, there is a very marginal energy difference between TS2 and S2 of approximately 0.90 kcal mol^{-1}. It can be summarized here that the difference in energy between S1, TS2 and S2 is negligible, suggesting that S1 is stuck in a very shallow quasi-bound well of the PES and can create a barrier free reaction process. Finally, with an activation barrier of 55.64 kcal mol^{-1}, S2 overcomes the third transition state (TS3) to generate H_3^+ and CHO. In this reaction pathway ($CH_3OH^+ \rightarrow H_3^+$), the total sum of the atomic charges on the H1 and H4 atoms remains very close to zero in S1, TS2 and S2. This shows that the neutral H_2 formed from CH_3OH^+ plays a key role in the migration of the H atom prior to the formation of H_3^+ and this is in excellent concurrence with the findings of Nakai *et al.* and Ekanayake *et al.*[18,19,39] Our calculations for this investigated path imitate the experimental findings exactly. This dissociation channel produces H_3^+ ions because of the population of several repulsive states with an increase in laser intensity as observed in Fig. 2 and 3.

Further, to understand the enhancement of the yield of other smaller fragments such as CH_2^+ with the increase in laser intensity, other dissociation channels are also investigated. In another dissociation channel ($CH_3OH^+ \rightarrow CH_2 + H_2O^+$), the migration of hydrogen takes place inside CH_3OH^+ and a hydrogen atom transfers from the methyl group to the –OH group *via* transition state TS4, leading to the formation of $CH_2OH_2^+$. This process overcomes an energy barrier of 27.95 kcal mol^{-1} and then $CH_2OH_2^+$ dissociates into CH_2 and H_2O^+. The calculated energy gap between $CH_2OH_2^+$ and CH_3OH^+ is comparable and close to that observed by the Radom and Wu groups.[36,67–69] Our IRC calculations further confirm that TS1, TS2, TS3 and TS4 are the correct TSs that accurately link the reactant and the product. We have observed H_2O^+ formation in the experiments as well, and the peak corresponding to H_2O^+ is marked in Fig. 2, 4, 5, 7, and 8. We are, however, only focusing on H_n^+ ($n = 1$–3) formation in this study, and therefore we have not discussed H_2O^+ formation in the experimental section.

We have further estimated and calculated two more dissociation channels as the positive charge can be assigned to either part of $CH_2 + H_2O^+$ and $H_3^+ + CHO$ as shown in Fig. 10. On the basis of the comparison of the different dissociation channels, it seems that the dissociation of CH_3OH^+ to $CH_2^+ + H_2O$ and $H_3 + CHO^+$ is preferred. Here, DFT calculations using the M06-2X functional seem to be very helpful in providing invaluable insight into the dissociation processes in CH_3OH^+ and further offering guidance to explain the experimentally observed results even without the excited state calculations.

5 Conclusions

To summarize, we have studied the strong-field ionization of CH_3OH molecules and experimentally investigated the formation of H_2^+ and H_3^+ ions from ionized CH_3OH. The impact of different laser parameters like intensity, pulse duration, wavelength, and polarization on fragmentation and the yield of H_n^+ ($n = 1$–3) ions have been discussed. Our key results can be summarized as follows:

• Low-intensity pulses resulted in a higher yield of heavier fragments like CH_nO^+ ($n = 0$–4) in the TOF spectra. At high intensities, CH_3OH is ionized to multiply-charged states which are highly repulsive and dissociate into smaller fragments like H_n^+ ($n = 1$–3), CH_n^+ ($n = 0$–3), C^{2+}, and O^{2+}.

• Stretched pulses (195 fs) were found to cause enhanced fragmentation and resulted in a higher yield of small fragment ions, compared to shorter pulses (29 fs). Similarly, in CD_3OH, the yield of H^+, D^+, DH^+, D_2^+, D_2H^+, and D_3^+ ions was enhanced as the pulse duration was increased from 29 fs to 290 fs.

• Photodissociation of CH_3OH by shorter wavelength pulses (800 nm) resulted in enhanced fragmentation in comparison to longer wavelength pulses (1300 nm).

• Linear polarization caused more fragmentation and higher ion yield from CH_3OH, as compared to circularly polarized pulses. This was observed for both 800 nm and 1300 nm pulses.

• In the photoionization of CD_3OH, we have observed that the D_nH^+ ($n = 1, 2$) ion yield as a function of laser intensity follows a similar trend to the D_n^+ ($n = 2, 3$) ion yield.

• Quantum chemical calculations were performed to predict the dissociation channels of singly ionized CH_3OH and understand the mechanism of

intramolecular hydrogen migration. Our calculation results show that the neutral H_2 formed from CH_3OH^+ plays an essential role in forming H_3^+ ions.

We conclude that the laser parameters (intensities, pulse widths, wavelengths, and polarization) can directly serve as a control for the dissociation of methanol and the yield of H_n^+ ($n = 1$–3) ions.

Conflicts of interest

There are no conflicts to declare.

Acknowledgements

We thank and acknowledge PRL's support of the research activities of the Femtosecond Laser Lab, AMOPH division. We also thank the PRL workshop for their support and fabrication of the VMI spectrometers. D. K. S. acknowledges financial support from SERB-DST ECR Project ECR/2016/001289. D. K. P. acknowledges DST, India for providing financial support under the INSPIRE Fellowship no. IF170625.

Notes and references

1 H. Kandori, Y. Shichida and T. Yoshizawa, *Biochemistry*, 2001, **66**, 1197–1209.
2 T. Renger, V. May and O. Kühn, *Phys. Rep.*, 2001, **343**, 137–254.
3 P. López-Tarifa, D. Grzegorz, D. G. Piekarski, E. Rossich, M.-A. H. du Penhoat, R. Vuilleumier, M.-P. Gaigeot, I. Tavernelli, M.-F. Politis, Y. Wang, S. Díaz-Tendero, F. Martín and M. Alcamí, *J. Phys.: Conf. Ser.*, 2014, **488**, 012037.
4 F. Schell, A. E. Boguslavskiy, C. P. Schulz, S. Patchkovskii, M. J. J. Vrakking, A. Stolow and J. Mikosch, *Phys. Chem. Chem. Phys.*, 2018, **20**, 14708–14717.
5 C. Guo, M. Li, J. P. Nibarger and G. N. Gibson, *Phys. Rev. A: At., Mol., Opt. Phys.*, 1998, **58**, R4271–R4274.
6 J. P. Farrell, S. Petretti, J. Förster, B. K. McFarland, L. S. Spector, Y. V. Vanne, P. Decleva, P. H. Bucksbaum, A. Saenz and M. Gühr, *Phys. Rev. Lett.*, 2011, **107**, 083001.
7 C. A. Mancuso, D. D. Hickstein, P. Grychtol, R. Knut, O. Kfir, X.-M. Tong, F. Dollar, D. Zusin, M. Gopalakrishnan, C. Gentry, E. Turgut, J. L. Ellis, M.-C. Chen, A. Fleischer, O. Cohen, H. C. Kapteyn and M. M. Murnane, *Phys. Rev. A: At., Mol., Opt. Phys.*, 2015, **91**, 031402.
8 F. P. Sturm, X. M. Tong, A. Palacios, T. W. Wright, I. Zalyubovskaya, D. Ray, N. Shivaram, F. Martín, A. Belkacem, P. Ranitovic and T. Weber, *Phys. Rev. A*, 2017, **95**, 012501.
9 F. P. Sturm, T. W. Wright, D. Ray, I. Zalyubovskaya, N. Shivaram, D. S. Slaughter, P. Ranitovic, A. Belkacem and T. Weber, *Rev. Sci. Instrum.*, 2016, **87**, 063110.
10 A. R. Bainbridge, J. Harrington, A. Kirrander, C. Cacho, E. Springate, W. A. Bryan and R. S. Minns, *New J. Phys.*, 2015, **17**, 103013.
11 S. Luo, S. Zhou, W. Hu, J. Yu, X. Li, P. Ma, L. He, C. Wang, F. Guo, Y. Yang and D. Ding, *J. Phys. Chem. A*, 2018, **122**, 8427–8432.
12 S. Luo, S. Zhou, W. Hu, X. Li, P. Ma, J. Yu, R. Zhu, C. Wang, F. Liu, B. Yan, A. Liu, Y. Yang, F. Guo and D. Ding, *Phys. Rev. A*, 2017, **96**, 063415.

13 S. Luo, R. Zhu, L. He, W. Hu, X. Li, P. Ma, C. Wang, F. Liu, W. G. Roeterdink, S. Stolte and D. Ding, *Phys. Rev. A: At., Mol., Opt. Phys.*, 2015, **91**, 053408.
14 S. Li, D. Sierra-Costa, M. J. Michie, I. Ben-Itzhak and M. Dantus, *Commun. Phys.*, 2020, **3**, 35.
15 M. McDonnell, A. C. LaForge, J. Reino-González, M. Disla, N. G. Kling, D. Mishra, R. Obaid, M. Sundberg, V. Svoboda, S. Díaz-Tendero, F. Martín and N. Berrah, *J. Phys. Chem. Lett.*, 2020, **11**, 6724–6729.
16 E. Livshits, I. Luzon, K. Gope, R. Baer and D. Strasser, *Commun. Chem.*, 2020, **3**, 49.
17 N. Ekanayake, M. Nairat, N. P. Weingartz, M. J. Michie, B. G. Levine and M. Dantus, *J. Chem. Phys.*, 2018, **149**, 244310.
18 N. Ekanayake, T. Severt, M. Nairat, N. P. Weingartz, B. M. Farris, B. Kaderiya, P. Feizollah, B. Jochim, F. Ziaee, K. Borne, P. K. Raju, K. D. Carnes, D. Rolles, A. Rudenko, B. G. Levine, J. E. Jackson, I. Ben-Itzhak and M. Dantus, *Nat. Commun.*, 2018, **9**, 5186.
19 N. Ekanayake, M. Nairat, B. Kaderiya, P. Feizollah, B. Jochim, T. Severt, B. Berry, K. R. Pandiri, K. D. Carnes, S. Pathak, D. Rolles, A. Rudenko, I. Ben-Itzhak, C. A. Mancuso, B. S. Fales, J. E. Jackson, B. G. Levine and M. Dantus, *Sci. Rep.*, 2017, **7**, 4703.
20 A. Hishikawa, H. Hasegawa and K. Yamanouchi, *J. Electron Spectrosc. Relat. Phenom.*, 2004, **141**, 195–200.
21 P. Farmanara, V. Stert and W. Radloff, *Chem. Phys. Lett.*, 1998, **288**, 518–522.
22 P. López-Tarifa, M.-A. Hervé du Penhoat, R. Vuilleumier, M.-P. Gaigeot, I. Tavernelli, A. Le Padellec, J.-P. Champeaux, M. Alcamí, P. Moretto-Capelle, F. Martín and M.-F. Politis, *Phys. Rev. Lett.*, 2011, **107**, 023202.
23 M. C. Castrovilli, A. Trabattoni, P. Bolognesi, P. O'Keeffe, L. Avaldi, M. Nisoli, F. Calegari and R. Cireasa, *J. Phys. Chem. Lett.*, 2018, **9**, 6012–6016.
24 H. Xu, C. Marceau, K. Nakai, T. Okino, S.-L. Chin and K. Yamanouchi, *J. Chem. Phys.*, 2010, **133**, 071103.
25 T. Okino, A. Watanabe, H. Xu and K. Yamanouchi, *Phys. Chem. Chem. Phys.*, 2012, **14**, 10640–10646.
26 C. E. Liekhus-Schmaltz, I. Tenney, T. Osipov, A. Sanchez-Gonzalez, N. Berrah, R. Boll, C. Bomme, C. Bostedt, J. D. Bozek, S. Carron, R. Coffee, J. Devin, B. Erk, K. R. Ferguson, R. W. Field, L. Foucar, L. J. Frasinski, J. M. Glownia, M. Gühr, A. Kamalov, J. Krzywinski, H. Li, J. P. Marangos, T. J. Martinez, B. K. McFarland, S. Miyabe, B. Murphy, A. Natan, D. Rolles, A. Rudenko, M. Siano, E. R. Simpson, L. Spector, M. Swiggers, D. Walke, S. Wang, T. Weber, P. H. Bucksbaum and V. S. Petrovic, *Nat. Commun.*, 2015, **6**, 8199.
27 H. Xu, T. Okino and K. Yamanouchi, *Chem. Phys. Lett.*, 2009, **469**, 255–260.
28 K. Hoshina, Y. Furukawa, T. Okino and K. Yamanouchi, *J. Chem. Phys.*, 2008, **129**, 104302.
29 T. J. Wasowicz and B. Pranszke, *J. Phys. Chem. A*, 2016, **120**, 964–971.
30 N. G. Kling, S. Díaz-Tendero, R. Obaid, M. R. Disla, H. Xiong, M. Sundberg, S. D. Khosravi, M. Davino, P. Drach, A. M. Carroll, T. Osipov, F. Martín and N. Berrah, *Nat. Commun.*, 2019, **10**, 2813.
31 R. Kushawaha and B. Bapat, *Chem. Phys. Lett.*, 2008, **463**, 42–46.
32 M. D. Burrows, S. R. Ryan, W. E. Lamb and L. C. McIntyre, *J. Chem. Phys.*, 1979, **71**, 4931–4940.

33 Y. Zhang, L. Wei, C.-L. Yang, W. Yu, B. Wang, B. Yan, Y. Zou, L. Chen and B. Wei, *Phys. Rev. A*, 2019, **100**, 052706.
34 Y. Zhang, B. Wang, L. Wei, T. Jiang, W. Yu, R. Hutton, Y. Zou, L. Chen and B. Wei, *J. Chem. Phys.*, 2019, **150**, 204303.
35 Y. Zhang, T. Jiang, L. Wei, D. Luo, X. Wang, W. Yu, R. Hutton, Y. Zou and B. Wei, *Phys. Rev. A*, 2018, **97**, 022703.
36 H. Wu, Y. Xue, J. Wen, H. Wang, Q. Fan, G. Chen, J. Zhu, F. Qu and J. Guo, *RSC Adv.*, 2019, **9**, 16683–16689.
37 M. J. Michie, N. Ekanayake, N. P. Weingartz, J. Stamm and M. Dantus, *J. Chem. Phys.*, 2019, **150**, 044303.
38 Y. Furukawa, K. Hoshina, K. Yamanouchi and H. Nakano, *Chem. Phys. Lett.*, 2005, **414**, 117–121.
39 K. Nakai, T. Kato, H. Kono and K. Yamanouchi, *J. Chem. Phys.*, 2013, **139**, 181103.
40 E. Wang, X. Shan, L. Chen, T. Pfeifer, X. Chen, X. Ren and A. Dorn, *J. Phys. Chem. A*, 2020, **124**, 2785–2791.
41 C. Guo and G. N. Gibson, *Phys. Rev. A: At., Mol., Opt. Phys.*, 2001, **63**, 040701.
42 M. Vafaee, F. Sami, B. Shokri, B. Buzari and H. Sabzyan, *J. Chem. Phys.*, 2012, **137**, 044112.
43 Y.-B. Li, X. Wang, B.-H. Yu, Q.-B. Tang, G.-H. Wang and J.-G. Wan, *Sci. Rep.*, 2016, **6**, 37413.
44 A. Zhao, P. Sándor, V. Tagliamonti, S. Matsika and T. Weinacht, *J. Phys. Chem. A*, 2016, **120**, 3233–3240.
45 T. Shaaran, K. Z. Hatsagortsyan and C. H. Keitel, *Phys. Rev. A*, 2018, **98**, 023410.
46 N. G. Kling, D. Paul, A. Gura, G. Laurent, S. De, H. Li, Z. Wang, B. Ahn, C. H. Kim, T. K. Kim, I. V. Litvinyuk, C. L. Cocke, I. Ben-Itzhak, D. Kim and M. F. Kling, *J. Instrum.*, 2014, **9**, P05005.
47 M. J. Frisch, G. W. Trucks, H. B. Schlegel, G. E. Scuseria, M. A. Robb, J. R. Cheeseman, G. Scalmani, V. Barone, G. A. Petersson, H. Nakatsuji, X. Li, M. Caricato, A. V. Marenich, J. Bloino, B. G. Janesko, R. Gomperts, B. Mennucci, H. P. Hratchian, J. V. Ortiz, A. F. Izmaylov, J. L. Sonnenberg, D. Williams-Young, F. Ding, F. Lipparini, F. Egidi, J. Goings, B. Peng, A. Petrone, T. Henderson, D. Ranasinghe, V. G. Zakrzewski, J. Gao, N. Rega, G. Zheng, W. Liang, M. Hada, M. Ehara, K. Toyota, R. Fukuda, J. Hasegawa, M. Ishida, T. Nakajima, Y. Honda, O. Kitao, H. Nakai, T. Vreven, K. Throssell, J. A. Montgomery Jr, J. E. Peralta, F. Ogliaro, M. J. Bearpark, J. J. Heyd, E. N. Brothers, K. N. Kudin, V. N. Staroverov, T. A. Keith, R. Kobayashi, J. Normand, K. Raghavachari, A. P. Rendell, J. C. Burant, S. S. Iyengar, J. Tomasi, M. Cossi, J. M. Millam, M. Klene, C. Adamo, R. Cammi, J. W. Ochterski, R. L. Martin, K. Morokuma, O. Farkas, J. B. Foresman and D. J. Fox, *Gaussian 16 Revision B.01*, Gaussian Inc., Wallingford CT, 2016.
48 R. Dennington, T. Keith, J. Millam, K. Eppinnett, L. W. Hovell and R. Gilliland, *GaussView, Version 6*, Semichem Inc., Shawnee Mission, 2016.
49 Y. Zhao and D. G. Truhlar, *Theor. Chem. Acc.*, 2008, **120**, 215–241.
50 R. Krishnan, J. S. Binkley, R. Seeger and J. A. Pople, *J. Chem. Phys.*, 1980, **72**, 650–654.
51 C. Y. Legault, *CYLview20*, Université de Sherbrooke, 2020, http://www.cylview.org.

52 L. V. Keldysh, *Zh. Eksp. Teor. Fiz.*, 1964, **47**, 1307–1314.
53 M. Elshakre, *Radiat. Phys. Chem.*, 2015, **112**, 49–55.
54 H. Yazawa, T. Tanabe, T. Okamoto, M. Yamanaka, F. Kannari, R. Itakura and K. Yamanouchi, *J. Chem. Phys.*, 2006, **124**, 204314.
55 E. Wells, K. J. Betsch, C. W. S. Conover, M. J. DeWitt, D. Pinkham and R. R. Jones, *Phys. Rev. A: At., Mol., Opt. Phys.*, 2005, **72**, 063406.
56 V. V. Lozovoy, X. Zhu, T. C. Gunaratne, D. A. Harris, J. C. Shane and M. Dantus, *J. Phys. Chem. A*, 2008, **112**, 3789–3812.
57 K. Hosaka, A. Yokoyama, K. Yamanouchi and R. Itakura, *J. Chem. Phys.*, 2013, **138**, 204301.
58 H. Kono, Y. Sato, N. Tanaka, T. Kato, K. Nakai, S. Koseki and Y. Fujimura, *Chem. Phys.*, 2004, **304**, 203–226.
59 M. Lezius, V. Blanchet, M. Y. Ivanov and A. Stolow, *J. Chem. Phys.*, 2002, **117**, 1575–1588.
60 H. Kang, S. Chen, Y. Wang, W. Chu, J. Yao, J. Chen, X. Liu, Y. Cheng and Z. Xu, *Phys. Rev. A*, 2019, **100**, 033403.
61 B. Walker, E. Mevel, B. Yang, P. Breger, J. P. Chambaret, A. Antonetti, L. F. DiMauro and P. Agostini, *Phys. Rev. A: At., Mol., Opt. Phys.*, 1993, **48**, R894–R897.
62 P. Dietrich, N. H. Burnett, M. Ivanov and P. B. Corkum, *Phys. Rev. A: At., Mol., Opt. Phys.*, 1994, **50**, R3585–R3588.
63 G. D. Gillen, M. A. Walker and L. D. Van Woerkom, *Phys. Rev. A: At., Mol., Opt. Phys.*, 2001, **64**, 043413.
64 F. Mauger, C. Chandre and T. Uzer, *Phys. Rev. Lett.*, 2010, **105**, 083002.
65 A. Galano and J. R. Alvarez-Idaboy, *J. Comput. Chem.*, 2014, **35**, 2019–2026.
66 M. Walker, A. J. A. Harvey, A. Sen and C. E. H. Dessent, *J. Phys. Chem. A*, 2013, **117**, 12590–12600.
67 W. J. Bouma, J. K. MacLeod and L. Radom, *J. Am. Chem. Soc.*, 1982, **104**, 2930–2931.
68 W. J. Bouma, R. H. Nobes and L. Radom, *J. Am. Chem. Soc.*, 1982, **104**, 2929–2930.
69 N. L. Ma, B. J. Smith, J. A. Pople and L. Radom, *J. Am. Chem. Soc.*, 1991, **113**, 7903–7912.

PCCP

PAPER

Check for updates

Cite this: *Phys. Chem. Chem. Phys.*, 2022, **24**, 18306

Strong-field ionization of CH_3Cl: proton migration and association†

Rituparna Das,‡[a] Deepak K. Pandey,[b] Swetapuspa Soumyashree,[a] Madhusudhan P.,‡[a] Vinitha Nimma,[a] Pranav Bhardwaj,‡[a] Muhammed Shameem K. M.,[a] Dheeraj K. Singh[b] and Rajesh K. Kushawaha *[a]

Strong-field ionization of CH_3Cl using femtosecond laser pulses, and the subsequent two-body dissociation of CH_3Cl^{2+} along H_n^+ (n = 1–3) and HCl^+ forming pathways, have been experimentally studied in a home-built COLTRIMS (cold target recoil ion momentum spectrometer) setup. The single ionization rate of CH_3Cl was obtained experimentally by varying the laser intensity from 1.6×10^{13} W cm^{-2} to 2.4×10^{14} W cm^{-2} and fitted with the rate obtained using the MO-ADK model. Additionally, the yield of H_n^+ ions resulting from the dissociation of all charge states of CH_3Cl was determined as a function of intensity and pulse duration (and chirp). Next, we identified four two-body breakup pathways of CH_3Cl^{2+}, which are $H^+ + CH_2Cl^+$, $H_2^+ + CHCl^+$, $H_3^+ + CCl^+$, and $CH_2^+ + HCl^+$, using photoion–photoion coincidence. The yields of the four pathways were found to decrease on increasing the intensity from $I = 4.2 \times 10^{13}$ W cm^{-2} to $2I = 8.5 \times 10^{13}$ W cm^{-2}, which was attributed to enhanced ionization of the dication before it can dissociate. As a function of pulse duration (and chirp), the H_n^+ forming pathways were suppressed, while the HCl^+ forming pathway was enhanced. To understand the excited state dynamics of the CH_3Cl dication, which controls the outcome of dissociation, we obtained the total kinetic energy release distributions of the pathways and the two-dimensional coincidence momentum images and angular distributions of the fragments. We inferred that the H_n^+ forming pathways originate from the dissociation of CH_3Cl dications from weakly attractive metastable excited states having a long dissociation time, while for the HCl^+ forming pathway, the dication dissociates from repulsive states and therefore, undergoes rapid dissociation. Finally, quantum chemical calculations have been performed to understand the intramolecular proton migration and dissociation of the CH_3Cl dication along the pathways mentioned above. Our study explains the mechanism of H_n^+ and HCl^+ formation and confirms that intensity and pulse duration can serve as parameters to influence the excited state dynamics and hence, the outcome of the two-body dissociation of CH_3Cl^{2+}.

Received 1st June 2022,
Accepted 10th July 2022

DOI: 10.1039/d2cp02494b

rsc.li/pccp

The interaction of intense ultrashort laser pulses with atoms and molecules removes electrons from the valence or inner-valence orbitals. This phenomenon, known as strong-field ionization (SFI), has been studied in atoms and molecules for many decades.[1–3] The large number of degrees of freedom in molecules, along with the coupling of the electronic and nuclear motions, renders the understanding of light-induced ultrafast processes in molecules extremely challenging. Once a molecule is ionized, it is transferred from the ground state to either a ground or excited ionic state. These ionic states may be stable, metastable (having a longer lifetime), or dissociative. In the excited dissociative potential energy surfaces (PESs), the molecular ion undergoes structural changes and geometrical deformation as it tries to gain stability. This leads to various ultrafast processes like bond-breaking, association, and isomerization, before fragmentation of the molecule. Using ultrashort pulses (having durations ∼ tens of fs or shorter), it is possible to study the nuclear and electron-nuclear dynamics in real-time, which will enable us to control the reactions. By ionizing the molecules from the valence or inner-valence orbitals and controlling the population of the ionic states, it is possible to control the dissociation pathways of the molecule.

The formation of H_2^+ and H_3^+ ions during the photodissociation of polyatomic molecules is ubiquitous and is of much importance.[4,5] H_3^+ formation involves intramolecular proton migration,[6,7] is complex and has been studied in many hydrocarbons.[3,8–10] In recent studies, it has been found to be a

[a] *Physical Research Laboratory Ahmedabad, Gujarat 380009, India. E-mail: kushawaha@prl.res.in; Tel: +91 07926314560*

[b] *Department of Basic Sciences, Institute of Infrastructure Technology Research And Management, Ahmedabad-380026, India. E-mail: dheerajsingh@iitram.ac.in*

† Electronic supplementary information (ESI) available. See DOI: https://doi.org/10.1039/d2cp02494b

‡ Indian Institute of Technology, Gandhinagar, Gujarat 382355, India.

two-step process. The first step involves the double ionization of the molecule, followed by the breakup of two C–H bonds and the formation of a neutral H_2 molecule. In the next step, the neutral H_2 roams on the PES in the vicinity of the precursor and extracts a proton to form H_3^+.[11–17] H_2^+, on the other hand, is formed by the long-range electron transfer from the neutral H_2 to the parent dication by a process known as "inverse harpooning".[11] The timescale of such intramolecular hydrogen migration has been reported to be ~100 fs.[18,19]

Methyl chloride (CH_3Cl) is one of the most significant contributors (15%, according to the World Meteorological Organization) of stratospheric ozone depletion among the various chloride compounds present in the atmosphere, originating from both natural[20,21] and anthropological[22] sources. In the stratosphere, photodissociation of methyl chloride generates chlorine radicals (which lead to ozone depletion) and numerous fragments like H_n^+ (n = 1–3), Cl^+, HCl^+, CH_2Cl^+, $CHCl^+$, and CCl by various dissociation pathways. In addition, methyl chloride has been found in a stable form in the interstellar medium.[23]

The fragmentation of CH_3Cl has been studied extensively using ion bombardment,[24,25] synchrotron radiation,[26–29] and femtosecond lasers.[30–32] H_n^+ (n = 1–3) and HCl^+ formation during the photodissociation of CH_3Cl has been of interest for many years. Duflot *et al.* studied the various two- and three-body dissociation channels of the CH_3Cl dication using the complete active space self-consistent field (CASSCF) method.[33] A similar study was performed by Ruhl *et al.*[34] on the cleavage of the CH_3Cl dication by the PEPIPICO method. In ref. 10, H_3^+ formation from the CH_3Cl dication was proposed by three C–H bond breakups followed by the three H atoms coming close to each other and forming H_3^+ ions, in contrast to the roaming mechanism of H_3^+ formation proposed by Ekanayake *et al.*[15] The mechanism by which the stable HCl^+ ion is formed in CH_3Cl following Auger decay has also been studied.[35] Additionally, two-color asymmetric fields have been used to study the angle- and momentum-resolved ionization and Coulomb explosion of CH_3Cl.[36] The head-to-tail ionization asymmetry in the ejection of CH_3^+ and X^+ from methyl halide dications (CH_3X^{2+}, X = F, Cl, Br, and I) was investigated experimentally by controlling the phase between the fundamental and second-harmonic fields. Furthermore, Ma *et al.* used 800 nm and 400 nm pulses of duration 50 fs to study the ultrafast H migration and Coulomb explosion (CE) in CH_3Cl along various two-body breakup channels of the parent dication and trication.[31]

In this work, we have investigated the strong-field ionization of the CH_3Cl molecule. The effect of intensity and pulse duration on the single and double ionization of CH_3Cl has been determined. To understand the effect of these parameters on the fragmentation of CH_3Cl^{2+} and the formation of H_n^+ (n = 1–3) and HCl^+ ions, photoion–photoion coincidence has been performed. This has further helped us to understand the contribution of the singly and doubly ionized CH_3Cl molecules in producing these fragments. We have also identified four two-body breakup channels of CH_3Cl^{2+} as follows: $H^+ + CH_2Cl^+$, $H_2^+ + CHCl^+$, $H_3^+ + CCl^+$, and $CH_2^+ + HCl^+$. The yield, kinetic energy releases, and two-dimensional coincidence momentum distribution of the fragments (H_n^+ and HCl^+) have been measured as a function of pulse duration. Furthermore, the anisotropy $\langle\cos\theta\rangle$ in the angular distribution of H_n^+ and HCl^+ ions has been obtained, which helped us to understand the lifetime of the precursor. Our study suggests that it is possible to control the ultrafast dynamics of the parent dication in the excited potential energy surfaces and hence, the outcome of its dissociation by using laser intensity and pulse duration.

1 Experimental methodology

The setup consists of a Ti:sapphire laser (Coherent), which produces 29 fs, 10 mJ pulses at 1 kHz, having a central wavelength of 800 nm. A portion of the beam (~1.5 mJ) is used for performing photodissociation experiments in a home-built cold target recoil ion momentum spectrometer (COLTRIMS) setup. The schematic diagram of the experimental setup is shown in Fig. 1. A commercial SPIDER setup (APE Germany) was used for pulse characterization. A half-waveplate (Altechna) and polarizer (Altechna) combination was used for controlling the laser power. The polarization of the beam was kept parallel (y-axis) to the detector throughout the experiment. A 2-inch concave mirror (effective focal length = −10 cm, Newport) mounted inside the COLTRIMS chamber was used to focus the pulses on the molecular beam at the ionization region. The beam diameter at the focus was measured to be 38 μm using a Beamage-4M, Gentec-EO. The intensity of the beam was estimated using the average power, pulse duration, and spot size. SF11 glass plates with thicknesses of 5 mm, 10 mm, and 20 mm were used in various combinations to perform photoionization experiments with stretched pulses of different durations.

The COLTRIMS setup is operated under the Wiley McLaren condition.[37] It consists of 9 electrodes (annular rings) on either side of the ionization region. A weak homogeneous electric field (35 V cm^{-1}) directs the positive and negatively charged ions and electrons, respectively, to the opposite ends of the setup. MCP detectors (Roentdek, Germany) on both ends of the setup were used to determine the times-of-flight (TOFs) of

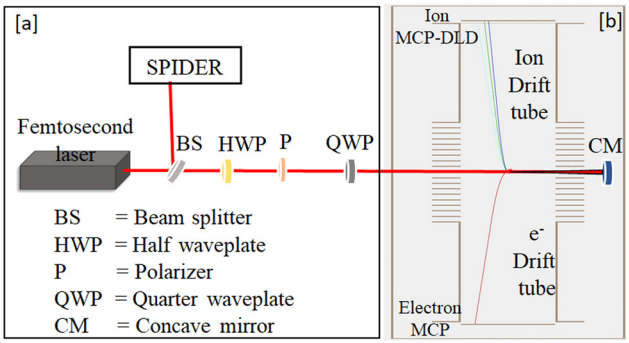

Fig. 1 Schematic diagram of the experimental setup and the femtosecond pulse characterization (SPIDER) unit.

the ions and electrons. A position-sensitive delay line detector (DLD) determines their (x, y) positions on the ion side.

CH_3Cl (Sigma Aldrich, purity of $\geq$99.5%) in the gas-phase was effused into the COLTRIMS chamber using a needle having an orifice diameter of 250 μm. The COLTRIMS chamber pressure was maintained at $\sim 9 \times 10^{-8}$ torr at room temperature. This ensured that the event rate was less than 300 Hz, which is essential for avoiding false coincidences and the space charge effect.

For intensity and pulse duration-dependent studies, the TOFs and (x, y) positions on the detector of the fragments were recorded ($>10^6$ counts), while keeping all other laser parameters constant, using a TDC8HP card (Roentdek). The MCP and DLD signals were first sent to an ATR-19 (preamplification and CFD). NIM signals generated by the ATR-19 were then sent to the TDC8HP card. The COBOLD PC software was used for both data acquisition and analysis (offline mode).

2 Theoretical methodology

The theoretical ionization rate of CH_3Cl^+ was obtained using the molecular Ammosov–Delone–Krainov (MO-ADK) theory and compared with experimental results. The details of this theory are given in ref. 38 and 39. Here, we briefly introduce the essential equations used for getting the theoretical ionization rate.

Assuming the molecular axis to be aligned parallel to the external field, the rate of tunnelling ionization for a molecule can be expressed as:[38–40]

$$\omega_{\text{MO-ADK}}(F,0) = \frac{B^2(m)}{2^{|m|}|m|!}\frac{1}{\kappa\frac{2Z_c}{\kappa-1}}\left(\frac{2\kappa^3}{F}\right)^{\frac{2Z_c}{\kappa-|m|-1}} \times \exp\left(\frac{-2\kappa^3}{3F}\right) \tag{1}$$

where,

$$B(m) = \sum_l C_l Q(l,m), \tag{2}$$

F is the laser field strength, l is the azimuthal quantum number, m is the magnetic quantum number along the molecular axis, Z_c is the effective Coulomb charge, and $\kappa = \sqrt{I_p}$ where I_p denotes the ionization potential for the given valence orbital. C_l is the structure co-efficient for the valence orbital whose values are tabulated in Table 1.[41]

Table 1 C_{lm} structure coefficients for the HOMO of CH_3Cl used in the theoretical model from ref. 41

Molecule	I_p (eV)	$C_{1\pm1}$	$C_{2\pm1}$	$C_{2\pm2}$
CH_3Cl (HOMO1)	11.3	0.58i	1.72i	0.21
		$C_{3\pm1}$	$C_{3\pm2}$	$C_{4\pm1}$
		−0.36i	−0.27	0.54i
		$C_{4\pm2}$	$C_{5\pm1}$	$C_{5\pm2}$
		0.24	−0.13i	0.17
		$C_{6\pm1}$	$C_{6\pm2}$	
		0.06i	0.09	

For an arbitrary alignment, $\mathbf{R}$ of the molecular axis with respect to the laser field, $B(m)$ can be expressed as:

$$B(m') = \sum_l C_l D^l_{m',m}(\mathbf{R}) Q(l,m) \tag{3}$$

where $D^l_{m',m}(\mathbf{R})$ is the rotation matrix, and $\mathbf{R}$ represents the Euler angles between the molecular axes and the laser field direction. Therefore, the ionization rate in a static field is given by:[38–40]

$$\omega_{\text{MO-ADK}}(F,\mathbf{R}) = \sum_{m'} \frac{B^2(m')}{2^{|m'|}|m'|!}\frac{1}{\kappa\frac{2Z_c}{\kappa-1}}\left(\frac{2\kappa^3}{F}\right)^{\frac{2Z_c}{\kappa-|m'|-1}} \times \exp\left(\frac{-2\kappa^3}{3F}\right) \tag{4}$$

In a pulsed laser field, the electric field has the form of:

$$F(\mathbf{t}, r, z) = F_0 \exp(-2\ln 2t^2/\tau^2)\exp(-2\ln 2r^2/W(z)^2) \tag{5}$$

where F_0 is the laser field peak strength and τ is the FWHM of the pulse. $W(z)$ is given by $w_0\sqrt{(1+z^2/z_R{}^2)}$, where w_0 is the beam spot size and z_R is the Rayleigh range, given by $\pi w_0{}^2/\lambda$. λ is the laser wavelength. Ionisation rate is given by the following equation:

$$P(F,\mathbf{R}) = 1 - \exp\int w(F,\mathbf{R})\mathrm{d}t \tag{6}$$

Theoretical ionization rate is obtained using the in-house developed program in MATLAB. The laser electric field strength was calculated from the experimental intensity value varying from 1.4 x 10^{13} to 24.2 × 10^{13} W cm^{-2}. The focal volume average was taken into account by integrating over the spatial components (*i.e.*, integrating over r and z). r was integrated from −45 μm to 45 μm, and z was integrated over 0 to z_R. The measured w_0 was 19 μm. The Rayleigh range for this case was calculated to be 1.42 mm. The ionization rate was calculated using eqn (6) integrating over t from −29 fs to 29 fs. The obtained MO-ADK curve is discussed in the results section.

3 Computational methods

GaussView 6 software was used to create initial input geometries for all molecular ions (CH_2^+, CH_2Cl^+, HCl^+, $CHCl^+$, CCl^+, H^+, H_2^+, and H_3^+), intermediate complexes, and multiple transition states (TSs) of CH_3Cl and doubly ionized chloromethane.[42] To acquire a better understanding of the probable mechanism of hydrogen migration and dissociation processes in the chlromethane dication (CH_3Cl^{2+}) and produce various molecular ions (H^+, H_2^+, H_3^+, and CH_2^+), density functional theory (DFT) calculations were executed using the Gaussian 16 quantum chemistry package.[43] DFT calculations have recently been employed to assess the characteristics of several chemical entities and their potential uses in diverse fields.[44,45] The meta-generalized gradient approximation-based

global Minnesota hybrid functional (M06-2X) with the 6-311++G(d,p) basis set was used to fully optimize the geometries of different monomers of CH_3Cl^{2+}, multiple fragmented products, and TSs without any constraint at the PES.[46,47] The same level of theory has previously also produced reliable and accurate results by supporting the experimentally observed results for dissociation processes.[3] In order to understand the intramolecular hydrogen migration process in CH_3Cl^{2+}, four different pathways were designed and then further computed on the CH_3Cl^{2+} PES in which CH_3Cl^{2+} can be dissociated into multiple fragments. Furthermore, vibrational frequencies were computed at the same level of theory (M06-2X/6-311++G(d,p)) to confirm that the resulting geometries correspond to minima or TSs on the PES and to attain zero-point energies. The presence of one imaginary frequency throughout the specified dissociation reaction routes confirms the presence of TSs, whereas the optimized geometries were confirmed as minima without imaginary frequencies. Furthermore, the transition states were evaluated using the intrinsic reaction coordinate (IRC) method at the same level of theory to compute the connection between the reactants and intermediates/products on the potential energy diagrams (PEDs). The optimized ground state/transition state geometries of all the computed structures were visualized using GaussView 6 software.[42]

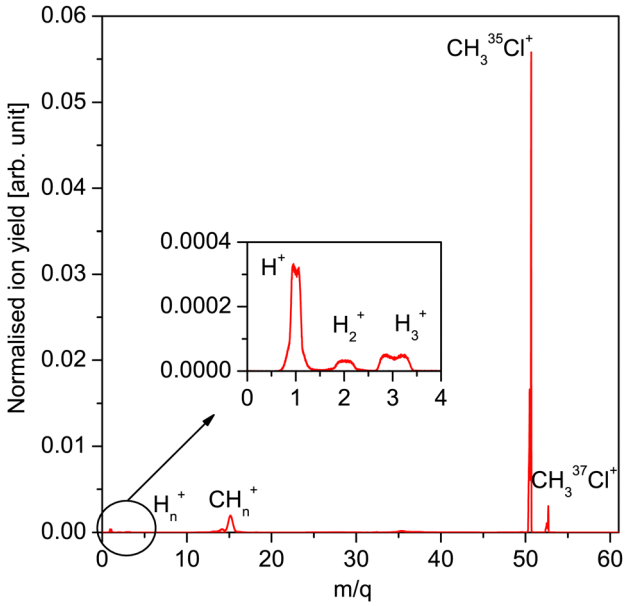

Fig. 2 The normalized TOF spectrum of CH_3Cl recorded for 29 fs, 800 nm, and linearly polarized pulses having an intensity of 4.2×10^{13} W cm^{-2}. Normalization has been performed with respect to the total counts in the spectrum.

4 Results and discussion

4.1 Experimental results

The TOF spectrum of CH_3Cl recorded using 29 fs, 800 nm, and linearly polarized pulses having an intensity of 4.2×10^{13} W cm^{-2} is shown in Fig. 2. The yield of CH_3Cl^+ ions is the maximum, which indicates that for the moderately intense pulses (10^{13} W cm^{-2}) used here, the single ionization of CH_3Cl is predominant. In addition, there is a small yield of smaller fragments like H_n^+ (n = 1–3, shown in the inset) and CH_n^+ (n = 0–3) for the given laser parameters. These fragments are formed from the dissociation of both CH_3Cl^+ and CH_3Cl^{2+} ions. Among the H_n^+ ions, H^+ has the highest yield (the ratio of the H^+ yield with respect to the CH_3Cl yield is 11%), which is expected due to the ease of C–H bond breakup. H_2^+ (1%) and H_3^+ (2%) formation has a lower cross-section as they require bond association and, therefore, have a comparatively much lower yield. It is also interesting to note that despite H_3^+ formation being a complex process requiring bond association between three H atoms, its yield is slightly higher than H_2^+. This observation is in contrast to previous studies on H_n^+ formation in other hydrocarbons.[48,49] Duflot *et al.* reported that H_3^+ formation is energetically easier (potential barrier is lower) compared to H_2^+ in the two-body breakup of CH_3Cl^{2+}. In fact, the potential energy of the final state (H_3^+ + CCl^+) is lower than the energy required for the double ionization of CH_3Cl. This was even confirmed in our theoretical calculations, as seen in Fig. 14 and 15. Duflot *et al.* also suggested that the second ionization occurs from the Rydberg states of CH_3Cl^+, resulting in the lower potential energy barrier for the H_3^++ CCl^+ pathway, and hence, the H_3^+ yield is higher than that of H_2^+.

Firstly, we have investigated the effect of laser intensity on (a) the strong-field single ionization of CH_3Cl and (b) the yield of H_n^+ ions, by varying the intensity from 1.6×10^{13} W cm^{-2} to 2.4×10^{14} W cm^{-2}, while keeping all other parameters constant. Fig. 3(a) shows the experimental (blue) intensity-dependent yield of CH_3Cl cations compared with the ionization rate predicted by the MO-ADK theory (red). It can be seen from the figure that as the intensity is increased from 1.6×10^{13} W cm^{-2} to 8×10^{13} W cm^{-2}, the yield of CH_3Cl cations increases monotonically. At these moderate intensities, ionization of the molecule takes place in the MPI (multiphoton ionization, Keldysh parameter $\gamma > 1$) regime[50] by the absorption of multiple photons. In this regime, the rate of single ionization of CH_3Cl is higher than that of double or triple ionization. As the intensity is increased, the single ionization rate increases monotonically and then saturates at intensities beyond 1.2×10^{14} W cm^{-2} (in agreement with Grugan *et al.*[51]). This saturation intensity I_{sat}, which can be attributed to the depletion of ground states at high intensities,[52] depends on the ionization potential (I_p) of the molecule. For the photoionization of CH_3Cl (I_p = 11.28 eV), saturation in the ionization rate occurs at intensities above 1.2×10^{14} W cm^{-2}, which lie in the tunneling regime ($\gamma < 1$). Although the single ionization rate saturates in this regime, the tunnel electron recollision produces highly charged states (2+, 3+, 4+, *etc.*) of CH_3Cl. The ionization rate predicted by the MO-ADK theory (red curve) scaled with a factor of 0.12 agrees well with the experimental result at high intensities (above 1×10^{14} W cm^{-2}), but shows some deviation at low intensities (MPI regime). Since the

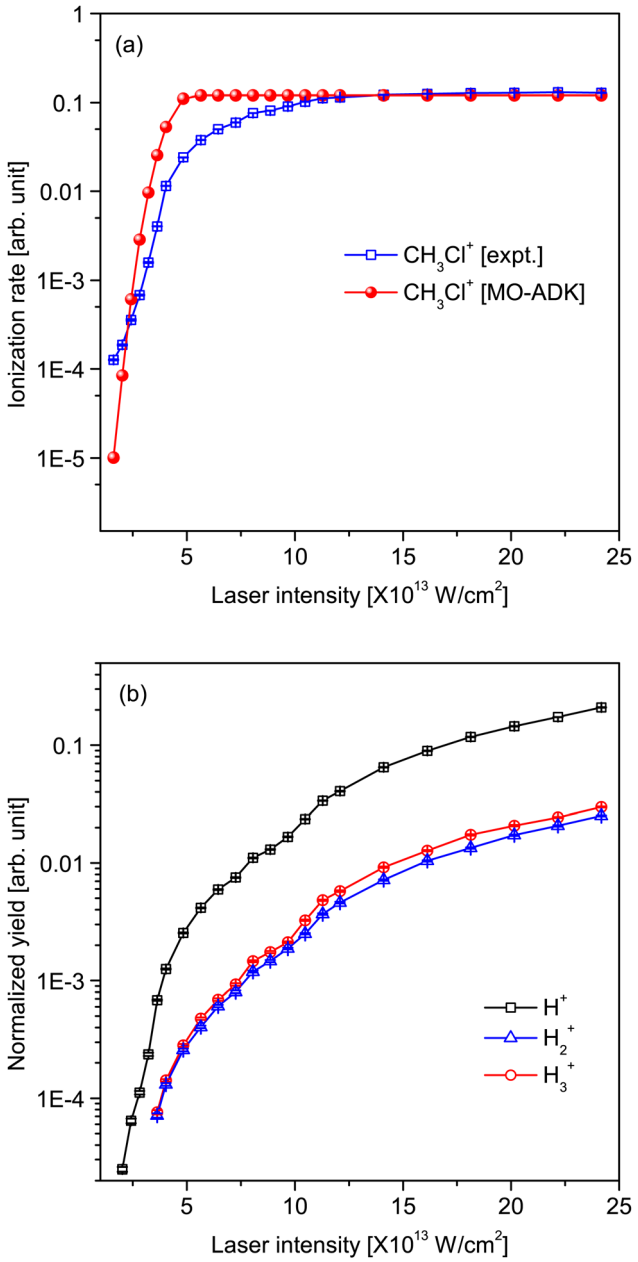

Fig. 3 Intensity-dependent yield of (top) CH_3Cl cations (maximum error is 2% for $CH_3{}^{35}Cl^+$) and (bottom) $H_n{}^+$ (n = 1–3) ions (maximum errors are 5% for H^+ and 4% for $H_2{}^+$ and $H_3{}^+$) for 29 fs, 800 nm, and linearly polarized pulses. The ion yields were normalized by the total counts of all ions in each TOF spectrum.

MO-ADK theory gives us the tunnelling ionization rate, the theory breaks down in the low-intensity multiphoton absorption regime, which explains the deviation. Tong *et al.*[39] have reported a similar discrepancy between the ionization rates of SO molecules obtained experimentally and using MO-ADK theory at low intensities.

Fig. 3(b) shows the variation in the $H_n{}^+$ (n = 1–3) yield as a function of laser intensity. It should be noted that these ions are formed by the fragmentation of CH_3Cl cations, dications, and all highly charged ions. The H^+ yield is 10 times lower than the CH_3Cl^+ yield up to 8×10^{13} W cm^{-2}. In fact, the $H_2{}^+$ and $H_3{}^+$ ions have a negligible yield below an intensity of 3.6×10^{13} W cm^{-2}. The low $H_n{}^+$ yield in the MPI regime can be ascribed to the low rates of fragmentation of the cation and double ionization of the parent. Single ionization of CH_3Cl from the HOMO by the absorption of multiple photons is prevalent here and the resulting cations populate the CH_3Cl^+ ground state, which is highly stable, and do not fragment much. However, some molecules are singly ionized by the absorption of an excess number of photons, leading to the removal of an electron from the HOMO−1 or HOMO−2 (inner valence) orbitals. The resulting ions populate the excited states of CH_3Cl^+, which are repulsive in nature. Furthermore, few molecules are doubly ionized and it is these CH_3Cl dications and the cations populating the excited states that dissociate to produce $H_n{}^+$ ions in the MPI regime. For intensities beyond 1.2×10^{14} W cm^{-2}, CH_3Cl is ionized by tunneling, as mentioned above. Multiply charged molecules are produced, which are highly unstable in nature and undergo fragmentation. As a result, the $H_n{}^+$ yield increases steadily as a function of intensity in this regime, and continues rising even after the CH_3Cl^+ yield saturates.

To ascertain the different fragmentation pathways of CH_3Cl^{2+} contributing to the formation of $H_n{}^+$ ions, we have obtained the photoion–photoion coincidence (PIPICO) of CH_3Cl for 29 fs, 800 nm pulses at an intensity of $I = 4.2 \times 10^{13}$ W cm^{-2} in Fig. 4(a). Various islands corresponding to the two- and three-body dissociation channels can be seen in the figure. The two-body fragmentation of CH_3Cl^{2+} results in the two fragments having anti-correlated momenta and they are characterized by islands having a slope of −1 (due to momentum conservation).[53] Here, we have investigated the effects of intensity and pulse duration variations on the following two-body breakup channels of CH_3Cl^{2+}:

$$CH_3{}^{35}Cl^{2+} \Rightarrow H^+ + CH_2{}^{35}Cl^+ \quad (7)$$

$$CH_3{}^{35}Cl^{2+} \Rightarrow H_2{}^+ + CH^{35}Cl^+ \quad (8)$$

$$CH_3{}^{35}Cl^{2+} \Rightarrow H_3{}^+ + C^{35}Cl^+ \quad (9)$$

$$CH_3{}^{35}Cl^{2+} \Rightarrow CH_2{}^+H^{35}Cl^+ \quad (10)$$

While eqn (7)–(9) show the $H_n{}^+$-forming pathways, eqn (10) corresponds to the $H^{35}Cl^+$ formation pathway. HCl^+ is formed by the intramolecular hydrogen migration from C to Cl atoms, followed by H–Cl bond formation before the C–H bond breakup occurs (shown in the inset of Fig. 4(a). From here on, we shall refer to the $H^{35}Cl^+$ ion as HCl^+. The islands corresponding to all the four pathways in the PIPICO have a slope of −1, thereby, confirming the two-body breakup of CH_3Cl^{2+}. Fig. 4(b) shows the PIPICO obtained for 510 fs pulses of intensity I. We shall discuss the effects of pulse stretching on the two-body fragmentation of CH_3Cl^{2+} later.

We discussed the variation in the normalized $H_n{}^+$ yield from all CH_3Cl ions (1+, 2+, 3+, *etc.*) as a function of laser intensity in Fig. 3(b). We now use the photoion–photoion coincidence to determine the contribution of CH_3Cl cations (red) and

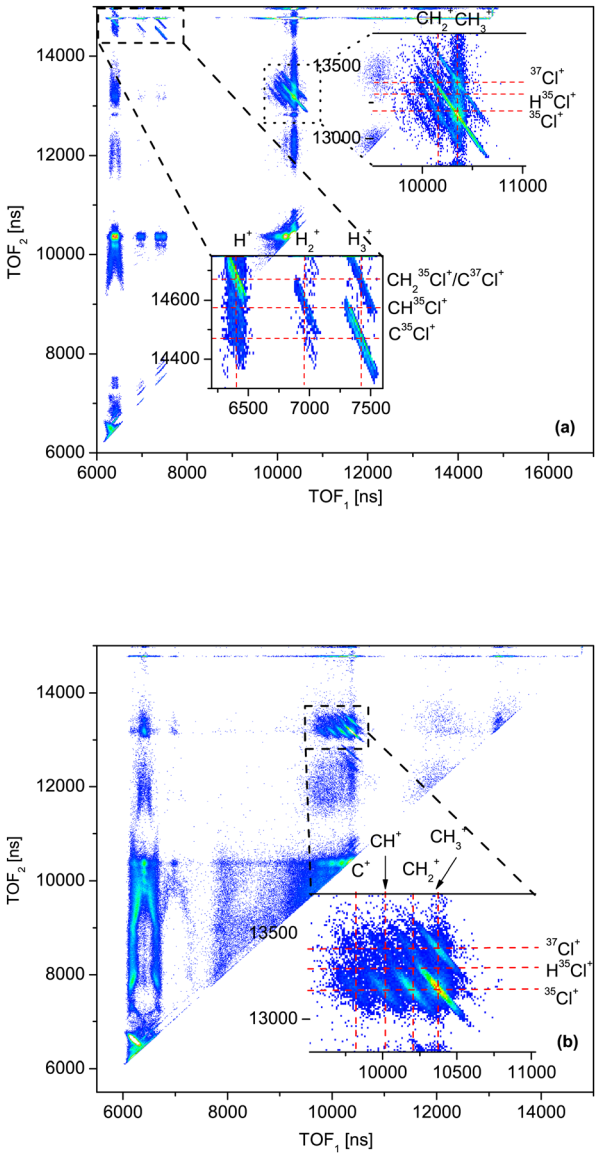

Fig. 4 Photoion–photoion coincidence plots of CH_3Cl recorded for 800 nm, linearly polarized pulses of intensity 4.2 × 10^{13} W cm^{-2} and durations (a) 29 fs and (b) 510 fs. The dissociation pathways (7)–(10) are shown in expanded form in both (a and b). However, as seen in (b), the pathways (7)–(9) are completely suppressed, while the yield of pathway (10) is enhanced for 510 fs pulses.

dications (blue) in the normalized H_n^+ yield as a bar plot in Fig. 5. The *y*-axis represents the normalized yield of H_n^+ ions and the *x*-axis represents the ions. As seen in the figure, CH_3Cl dications have a higher contribution to the H_n^+ yield (∼2 times for H^+ and H_2^+ and 1.4 times for H_3^+ ions) than the cations. As previously mentioned, the PESs predominantly populated by the CH_3Cl^+ ions are stable and have a long lifetime, so they do not fragment much and have very little contribution to H_n^+ formation. On the other hand, the CH_3Cl^{2+} ions are unstable (confirmed from the very low yield of CH_3Cl dications experimentally) because the populated dication states are primarily repulsive and they undergo fragmentation. Therefore, the parent dications have a higher contribution to the H_n^+ yield.

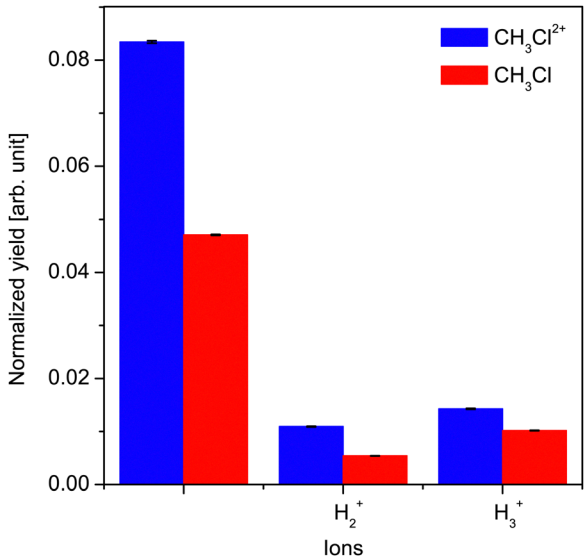

Fig. 5 Comparative yields of H_n^+ (n = 1–3) ions and CH_3Cl mono- and dications. The yield of the H_n^+ ions has been normalized with respect to the total ion yield in each case.

Finally, to examine the effect of laser intensity on the yield of the dissociative pathways (7)–(10) and investigate if intensity can serve as a parameter to control the dissociation of CH_3Cl, we have obtained the yields of the channels as a function of intensity in Fig. 6. The *x*-axis represents the four fragmentation pathways, while the *y*-axis represents the normalized yield of the pathways. The yields for three values of intensity are

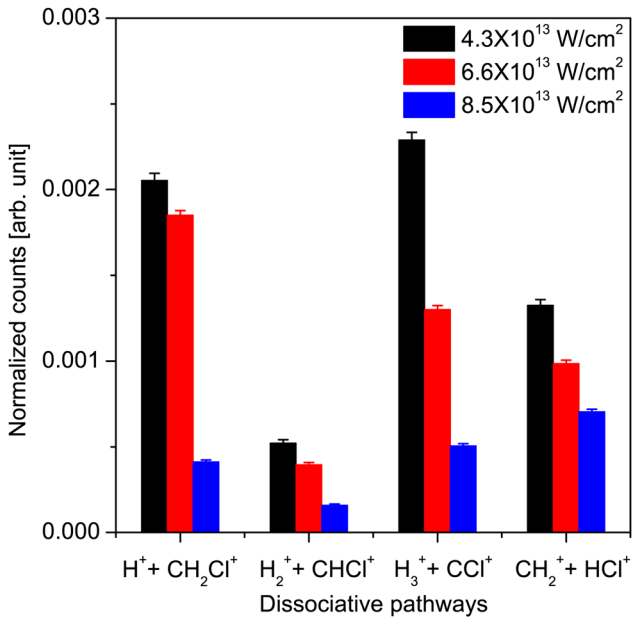

Fig. 6 Normalized yields of the dissociation pathways (7)–(10) for the intensities 4.2 × 10^{13} W cm^{-2}, 6.6 × 10^{13} W cm^{-2}, and 8.5 × 10^{13} W cm^{-2}. The other laser parameters like pulse duration (29 fs), polarization (linear), and wavelength (800 nm) were maintained constant in all three cases. The % yield represents the ratio of the number of counts in a particular pathway and the total number of coincidence events.

considered -4.2×10^{13} W cm^{-2} (black), 6.6×10^{13} W cm^{-2} (red), and 8.5×10^{13} W cm^{-2} (blue) – and shown as bar plots. It is evident from the figure that as the intensity is doubled, all four pathways are suppressed (the reduction in H^+ yield is 5 times, 3 times for H_2^+, 4 times for H_3^+, and 2 times for HCl^+). The three intensity values chosen in this experiment are in the MPI regime, so the double ionization of CH_3Cl takes place essentially by multiphoton absorption in all cases. At high intensities, the rate of ionization of molecules is higher than that of dissociation.[54] It is known that the ionization rate of molecules depends on the internuclear separation[54,55] and at separations much larger than the equilibrium separation, the ionization rate has been found to be enhanced by a few times. This phenomenon known as charge resonance-enhanced ionization (CREI) is attributed to the coupling of pairs of electronic states by the laser field, leading to charge localization and enhanced ionization. As the laser intensity is increased to 8.5×10^{13} W cm^{-2}, the dication evolving on the excited PES undergoes further ionization at a critical internuclear separation (R_c) before the dication can dissociate, thereby producing triply ionized molecules. As a result, the yield of the dissociation pathways decreases with increasing intensity. This observation suggests that varying the intensity leads to changes in the excited state dynamics of the parent ion, which in turn, affects the yield of the pathways.

Next, we passed the beam through SF11 plates of different thicknesses, while maintaining a constant intensity, which introduced pulse stretching and a positive chirp. Due to the chirp, the red frequency components travel faster and are present in the leading edge of the pulse, while the blue components are present in the trailing edge. Since SF11 plates produce positively-chirped pulses only, we did not study the negative chirp-dependence of the fragmentation of CH_3Cl^{2+}. We show here that by controlling the pulse duration and the chirp of the pulses, it is possible to control the dynamics of CH_3Cl^{2+} and its fragmentation. To estimate the amount of chirp, we have calculated the group delay dispersion for SF11 of different thicknesses, which are displayed in Table 2. The fragmentation of atoms[56–58] and polyatomic molecules[59–61] has been found to be strongly affected by chirp and its control using shaped pulses has been demonstrated in earlier experiments. In addition, the laser pulse duration affects the ultrafast excited state dynamics of the parent ion and its subsequent fragmentation.[60,62–64] For pulses with durations of ~100 fs or more, ionization and the subsequent nuclear dynamics occur in the presence of the field. This leads to a more significant stretching of the bond lengths, affecting the molecular restructuring and fragmentation dynamics. Enhanced ionization of polyatomic molecules at long internuclear distances has been observed due to an energy upshift of the inner-valence shells leading to larger coupling of multiple orbitals.[63,65,66]

Fig. 7 shows the yields of the CH_3Cl cations and dications for different values of chirp and pulse duration. As seen in the figure, photoionization by 29 fs unchirped pulses primarily produces CH_3Cl cations. It should be emphasized that the dication yield shown here corresponds to the ions populating the metastable dicationic states, while the majority of the dications are unstable and undergo fragmentation. However, the low fragment yield seen in the TOF spectrum in Fig. 2 for 29 fs pulses indicates the low double ionization rate. Positively chirping the pulses shows a reduction in the yields of both the cations and dications. This trend can be attributed not only to the chirp, but also the pulse stretching. Photoionization by stretched pulses leads to larger stretching of the bonds. As the cations and dications evolve on the excited PESs and the internuclear separations increase, at a critical internuclear separation (R_c), pairs of charge resonant states are coupled by the laser field, due to which the ion is further excited or ionized to higher charge states.[55,63,65] These multiply-charged ions are unstable and undergo fragmentation along various pathways, as indicated by a high fragment yield in the TOF spectrum obtained for chirped pulses. Furthermore, we investigate the

Table 2 Group delay dispersion (GDD) and stretching of the laser pulses for different thicknesses of SF11

Thickness of SF11 (mm)	GDD (fs^2)	P.D. (fs)
0	0	29
5	600	64
10	1650	160
15	2390	230
20	3120	300
25	4380	420
30	5330	510

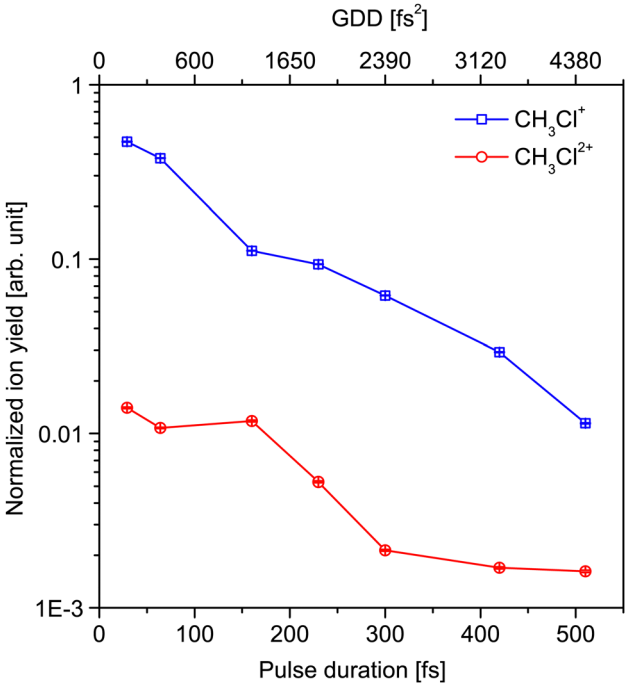

Fig. 7 Pulse durations and chirp-dependent yields of CH_3Cl cations and dications (maximum errors are 0.1% for $CH_3{}^{35}Cl^+$ and 0.01% for $CH_3{}^{35}Cl^{2+}$). The other laser parameters like intensity (4.2×10^{13} W cm^{-2}), wavelength (800 nm), and polarization (linear) of the pulses were maintained constant throughout the measurements. The ion yields were normalized by the total ion yield in each TOF spectrum.

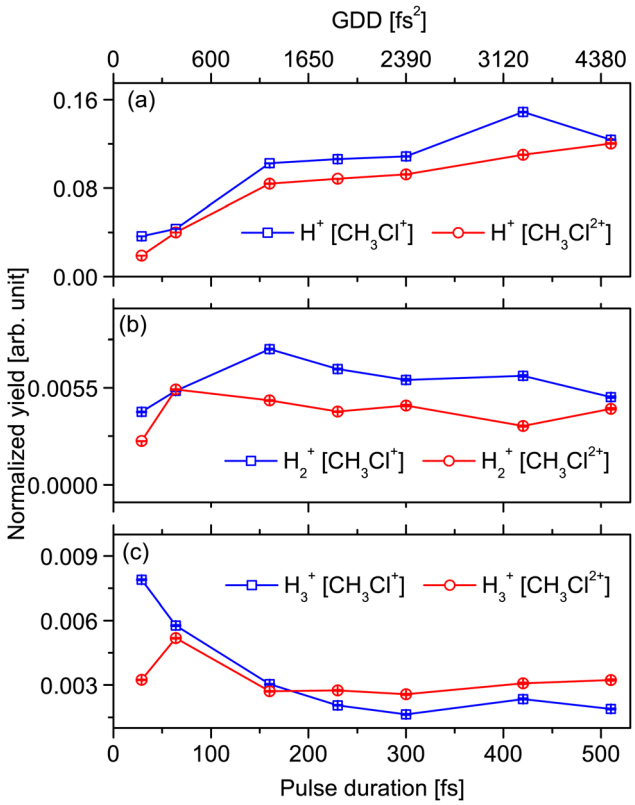

Fig. 8 Normalized (a) H^+, (b) H_2^+, and (c) H_3^+ yields as a function of pulse duration and chirp. The other laser parameters like intensity (4.2×10^{13} W cm^{-2}), wavelength (800 nm), and polarization (linear) of the pulses were maintained constant throughout the measurements. Normalization was done by the total ion yield in each TOF spectrum. The total H_n^+ yield is shown in blue, while the H_n^+ ions contributed by CH_3Cl cations and dications are shown in black and red, respectively. The maximum error in all the cases is less than 1%.

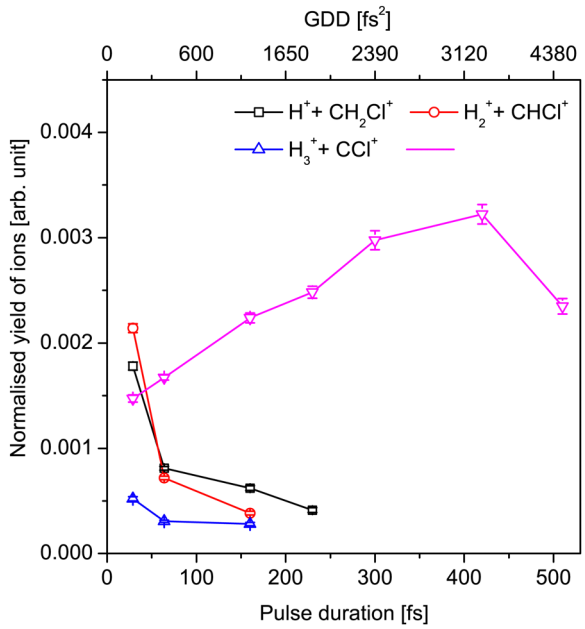

Fig. 9 Normalized yields of the dissociation channels (7)–(10) as a function of pulse duration and chirp. The other laser parameters like intensity (4.2×10^{13} W cm^{-2}), wavelength (800 nm), and polarization (linear) of the pulses were maintained constant throughout the measurements. The maximum errors are 6%, 5%, 5%, and 3% for the channels (7), (8), (9), and (10), respectively.

effect of chirp on the fragmentation of the parent cations and dications, and the H_n^+ yield. The chirp and pulse stretching-dependent normalized yields of (a) H^+, (b) H_2^+, and (c) H_3^+ ions are shown in Fig. 8. The blue curves in each case represent the H_n^+ ions produced by the fragmentation of CH_3Cl cations, while the red curves represent the fragments produced from the parent dications. As evident from the figures, while the H^+ ion yield has an increasing trend as a function of chirp and pulse duration, the H_2^+ and H_3^+ ion yields show a decreasing trend. Duflot *et al.* showed that H^+ is formed from the dissociation of the most stable isomer H_2CClH^{2+} (the $^1A'$ state of this isomer lies 34.83 kcal mol^{-1} below the $^1A'$ state of CH_3Cl^{2+}).[67] This means that the H^+-forming pathways are energetically favoured compared to the H_2^+ and H_3^+ forming pathways. Our study shows that photoionizing CH_3Cl by chirped pulses further favours the H^+ forming pathways compared to the H_2^+ and H_3^+ forming pathways for larger positive chirps.

Next, we have focused on the double ionization of CH_3Cl and tried to understand the influence of the chirp and pulse stretching on the excited state dynamics of CH_3Cl^{2+} and the subsequent two-body breakup of the CH_3Cl dication. The variation in the yield of the dissociation pathways (7)–(10) is shown in Fig. 9. Pathways (7)–(9), which involve H_n^+ (n =1–3) formation, have a decreasing trend as the pulses are stretched and chirped. These pathways are suppressed for pulses beyond 160 fs and their yields are negligible. In contrast, pathway (10) shows an enhancement in the fragments' yield for stretched and positively chirped pulses. This is an isomerization pathway involving an intramolecular migration of the H atom to the Cl atom, H–Cl bond formation, and finally, C–Cl bond breakup. To explain the observed trends in the overall yields of the four pathways, we have tried to understand the excited state dynamics of CH_3Cl^{2+} by determining the kinetic energies, two-dimensional momenta, and angular distributions of the fragments in each pathway.

Firstly, we discuss the kinetic energy release (KER) distributions of the pathways. The kinetic energy of fragments has information about the potential energy surface on which the molecular wavepacket evolution took place, the molecular geometry, and the charge distribution on the ions just before it underwent dissociation. Fig. 10 shows the KER (sum of kinetic energies of the fragments in a particular channel) distributions for the channels (7)–(10) for various chirps and pulse durations. The KER distributions for pathways (7)–(10) peak at 0.2 eV, 0.4 eV, and 0.6 eV, respectively. The KER peaks and the FWHM values of the distributions of the pathways (7)–(9) do not change as the pulses are chirped. However, the KER peak for the pathway 10 shows a shift to lower energy values (from 1.6 eV to 1 eV) as the pulses are chirped. This is accompanied by a decrease in the FWHM value of the KER distribution. Earlier studies have shown that a shift in the KER

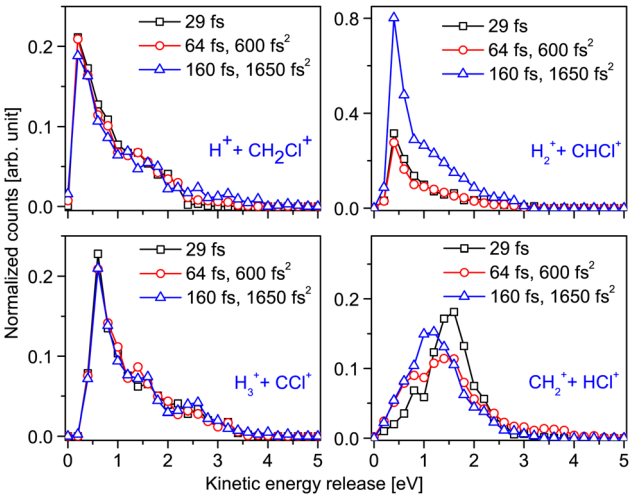

Fig. 10 Kinetic energy releases of the dissociation channels (7)–(10) for various pulse durations and chirps. The other laser parameters like intensity (4.2×10^{13} W cm^{-2}), wavelength (800 nm), and polarization (linear) of the pulses were maintained constant throughout the measurements.

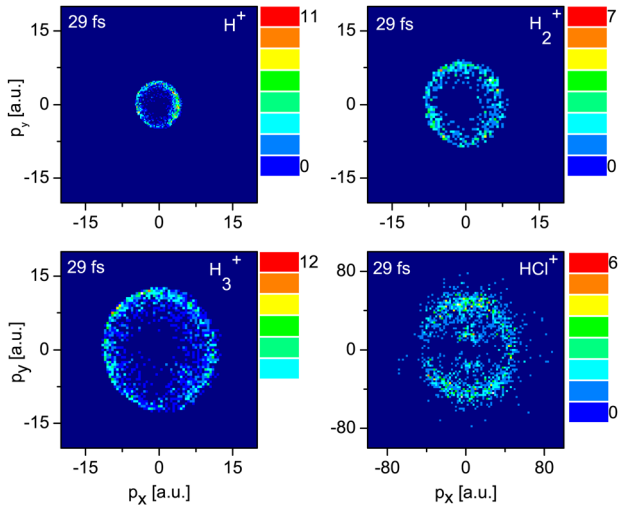

Fig. 11 The two-dimensional coincidence momentum images of H^+, H_2^+, H_3^+, and HCl^+ ions produced by the two-body breakup of CH_3Cl^{2+} along the pathways (7)–(10) obtained with 29 fs, 800 nm, linearly polarized pulses of intensity 4.2×10^{13} W cm^{-2}.

of a dissociation pathway with increasing pulse duration is due to the parent ion dissociating from a Coulombic (or repulsive) PES, where the bond length maps onto the total KER.[55,68] Therefore, for pathway (10), the dication must dissociate from a repulsive PES and therefore, has a rapid dissociation time. On the contrary, the pathways (7)–(9) originate from non-Coulombic (metastable) weakly attractive PESs having lifetimes of the order of the rotational period of the dication, due to which their KER distributions do not show a shift to lower energies with pulse stretching; that is, the bond length does not map onto the KER in this case. At the same time, the FWHM values of the KER distributions for all the pathways are broad. However, the FWHM value of the KER distribution for the $CH_2^+ + HCl^+$ pathway is reduced with increasing chirp. A broad KER distribution suggests the contribution of multiple excited electronic states[69] in a dissociation pathway. Therefore, some of the electronic states participating in the case of unchirped pulses are suppressed with increased positive chirps. The KER distributions of the four pathways as a function of intensity ($I = 4.2 \times 10^{13}$ W cm^{-2} and $2I = 8.5 \times 10^{13}$ W cm^{-2}) are not shown here. For the H_n^+ forming pathways (7)–(9), the KER peaks showed no variation as a function of intensity. However, there was a shift in the KER peak observed in the HCl^+ forming pathway (10) from 1.6–1.4 eV as the intensity was increased from I to $2I$. The KER values reported by Ma *et al.* for the same pathways are significantly higher than those observed here.[31] It must be noted that the intensity used in our experiment is $\sim 10^{13}$ W cm^{-2}, which is an order of magnitude less than that used by Ma *et al.*[31] A previous study on the ultrafast dynamics of H_2^+ ions by He *et al.* reported a shift in the KER distribution of the Coulomb explosion channel to higher energies as the intensity was increased from 7.7×10^{13} W cm^{-2} to 2.5×10^{14} W cm^{-2}.[70] Therefore, the discrepancy in the KER values may be attributed to the low intensity used in our study.

Furthermore, we have plotted the two-dimensional coincidence momentum images of H_n^+ (n = 1–3) and HCl^+ ions (Fig. 11). The polarization direction is parallel to the p_y axis. As seen in the figure, the momentum of H^+ is the least (5 a.u.), followed by H_2^+ (9 a.u.) and H_3^+ (14 a.u.) ions. The distribution of HCl^+ has a lower momentum component (14 a.u.) and a higher momentum component (27 a.u.). The two components indicate the involvement of two excited states (PESs) in the HCl^+ formation. The momentum distributions of the H_n^+ ions are nearly isotropic, while that of HCl^+ is anisotropic. To quantify the anisotropy in the ejection direction of the fragments, we have obtained their angular distribution. It is known that the ionization rate of a molecule depends on the relative orientation of the molecular axis with respect to the laser polarization direction and it maps the shape of the molecular orbital from which ionization takes place.[71,72] Since the molecular orbitals of polyatomic molecules are very closely spaced, the interaction of the molecules with intense fs lasers removes electrons not only from the HOMO but also the HOMO−1 and the HOMO−2 orbitals (the inner-valence orbitals).[73–75] Therefore, the angular distribution of the ejected fragments also depends on whether the molecule was ionized from the valence or inner-valence orbitals. In addition, the lifetime of the precursor ion affects the extent of anisotropy in the ejection direction of the fragments.[6,7,30,76]

The angular distributions of the pathways (7)–(10) are shown in Fig. 12. Here, θ is the angle between the laser polarization direction and the momentum vector of the fragment. I_1 and I_2 stand for the intensities 4.2×10^{13} W cm^{-2} and 8.5×10^{13} W cm^{-2}, respectively. The experimentally obtained distributions were then fitted with the equation:

$$I(\theta) = 1 + \sum_i a_i \mathbf{P}_i(\cos(\theta)) \quad (i = 2, 4, 6) \qquad (11)$$

where a_i represents the expansion coefficients, $\mathbf{P}_i(\cos(\theta))$ are the Legendre polynomials, and $I(\theta)$ represents the angular distribution. The expansion coefficients a_i for the various pathways are summarized in Table 3 for varying pulse durations and

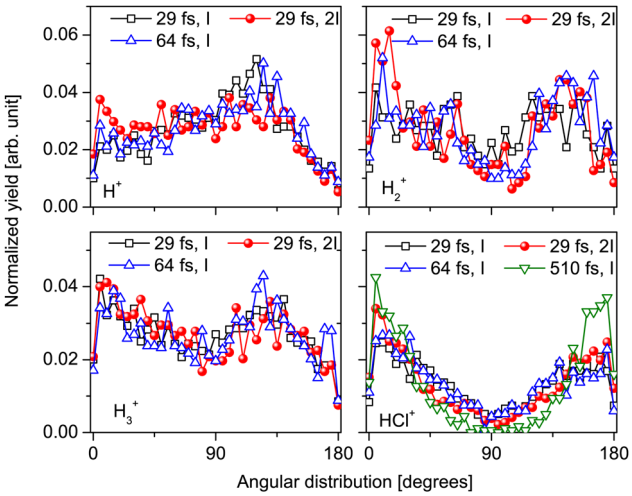

Fig. 12 Angular distributions of H_n^+ and HCl^+ ejected during the two-body breakup of CH_3Cl^{2+} along the pathways (7)–(10) as a function of intensity (I and $2I$, at a constant pulse duration of 29 fs) and pulse duration (at a constant intensity of I). Here, θ is the angle between the polarization direction and the momentum vector of the fragment.

Table 3 Coefficients of Legendre polynomial a_i (i = 2, 4, and 6) for the angular distributions of the fragments formed in the two-body breakup of the CH_3Cl^{2+} ion. I_1 and $2I$ stand for the intensities 4.2×10^{13} W cm^{-2} and 8.5×10^{13} W cm^{-2}, respectively, and P.D. represents pulse duration

Dissociation pathways	P.D. (fs)	I (W cm^{-2})	a_2	a_4	a_6
$H^+ + CH_2Cl^+$	29	I	−0.4	−0.2	0.1
	64	I	−0.2	−0.2	0
	29	$2I$	−0.2	−0.2	0
$H_2^+ + CHCl^+$	29	I	0.2	−0.5	0.2
	64	I	0.7	−0.6	0
	29	$2I$	0.7	−0.5	0
$H_3^+ + CCl^+$	29	I	0	−0.2	0
	64	I	0	−0.2	0.1
	29	$2I$	0.1	−0.2	0
$CH_2^+ + HCl^+$	29	I	1.0	−0.1	−0.2
	64	I	1.2	−0.2	−0.1
	160	I	2.3	0.6	−0.1
	230	I	2.4	0.8	−0.2
	300	I	2.4	0.9	−0.4
	420	I	2.4	1.0	0.0
	510	I	2.8	1.0	−0.5
	29	$2I$	1.5	0.2	−0.1

intensities. For the H_n^+ forming pathways, the angular distribution plots show that these ions are ejected in all directions (also at 90° with respect to the polarization direction) with respect to the polarization direction. The Legendre coefficients a_2 for the H_n^+ ions are ≤ 0, indicating their nearly uniform angular distributions, including at 90° with respect to the polarization direction. As discussed earlier, in the case of dissociation along the H_n^+ forming pathways, the CH_3Cl dication dissociates from non-Coulombic PESs and therefore have a long dissociation time. The rotation of the precursor with respect to the polarization direction destroys the anisotropy in the ejection directions of the fragments and we observe a nearly uniform angular distribution. On the other hand, the HCl^+ fragments are distributed primarily close to 0° and 180°. The HCl^+ ions are formed from repulsive PESs and have a fast dissociation time, so the anisotropy in their ejection direction is not destroyed by the rotation of the molecule.[6,30] On using chirped pulses, the angular distribution of the H_n^+ ions remains nearly unchanged, while that of the HCl^+ ions becomes more anisotropic. For stretched pulses, electrons are removed not from the HOMO−1 and HOMO−2 orbitals,[55,63,76] due to the coupling of electronic states by the laser field at large internuclear distances. Thus, the increased anisotropy in the HCl^+ ejection direction is due to (i) the symmetry of the inner valence orbitals from which ionization takes place and (ii) the rapid dissociation of the dication from the excited PESs, thereby preserving the anisotropy. On the contrary, the slow dissociation of the dication along the H_n^+ forming pathways is responsible for the isotropic distribution of the fragments even for chirped pulses. At this point, we can explain the results of Fig. 9. Due to the long dissociation time of CH_3Cl^{2+} along the H_n^+ forming pathways, we expect that the dication absorbs more energy from the field (which is still present in the case of stretched pulses) and is further excited or ionized. Thus, the yields of the pathways (7)–(10) are suppressed on stretching the pulses. On the other hand, the $CCl^+ + HCl^+$ pathway is favoured over the H_2^+ and H_3^+ forming pathways because its precursor (H_2CClH^{2+}) is highly stable. The increased yield of the HCl^+ pathway with increased chirp can be attributed to the dications populating the PESs, which dissociate along this pathway. The angular distribution of the H_n^+ ions for the pathways (7)–(9) reported by Ma *et al.*[31] differ from our findings. The H_n^+ and HCl^+ ions have an anisotropic angular distribution in their study, suggesting that the CH_3Cl^{2+} ions populate high energy repulsive PESs. This observation may be due to the high intensity (10^{14} W cm^{-2}) used by Ma *et al.* On increasing the intensity from I to $2I$, while keeping all other laser parameters constant, we do not observe very significant changes in the angular distributions of the H_n^+ fragments. On the other hand, the HCl^+ fragments show a slightly increased anisotropy at the intensity $2I$. Therefore, the intensity and pulse duration control the excited dynamics of the parent dication and the orbitals contributing to the double ionization, which in turn, control the outcome of dissociation and the overall yield.

4.2 Quantum chemical calculations

In the present study, further, comprehensive quantum chemical calculations were conducted to have an in-depth insight into the possible reaction mechanism of various possible dissociative channels leading to the fragmentation process of the CH_3Cl dication, intramolecular hydrogen migration, and yielding of multiple fragmented ions (H_n^+ (n = 1–3)). The M06-2X hybrid functional was used to improve the precision since it provides high-quality kinetic data when compared to the well-known and accepted Beckes three-parameter hybrid method using the LYP correlation functional (B3LYP).[77,78] Before delving into the dissociation channels that lead to the generation of H_n^+ ions, it is necessary to first understand the initial geometries of neutral

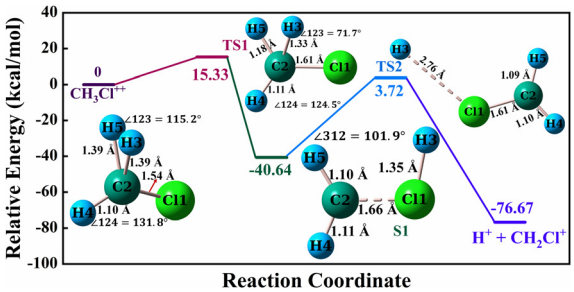

Fig. 13 The potential energy diagram along with the optimized structures of the CH_3Cl^{2+}, TS1, S1, and TS2 for the dissociation of doubly ionized CH_3Cl into H^+ and CH_2Cl^+ at the M06-2X/6-311++G(d,p) level of theory. The energies in the figure are relative to the total energy of CH_3Cl^{2+}.

and doubly ionized CH_3Cl on their singlet potential energy surfaces. The optimized ground state geometry of neutral CH_3Cl with the C_{3v} symmetry was calculated at the M06-2X/6-311++G(d,p) level of theory and is depicted in Fig. S1 (ESI†). Because both bond distances (C–H = 1.086 Å and C–Cl = 1.787 Å) and bond angles (HCCl = 108.3°, HCH = 110.5°) are identically the same as the experimental values (C–H = 1.086 Å and C–Cl = 1.778 Å), our estimated geometric data for CH_3Cl are in great agreement with the experimental results.[79,80] Furthermore, this fact ensures the accuracy of the selected level of theory. Furthermore, at the same level of theory, the CH_3Cl^{2+} dication arrangement is optimized and its ground state geometry is depicted in Fig. 13. The CH_3 fragment acts as an electron donor in doubly ionized CH_3Cl, while chlorine acts as an acceptor, causing a significant redistribution of charge partition. There are significant differences in the ground state geometry of doubly ionized CH_3Cl^{2+} in comparison to the neutral CH_3Cl (see Fig. S1, ESI† and Fig. 13). The length of the C–Cl bond contracted to 1.54 Å from 1.78 Å in CH_3Cl. In substituted methylene dications, this latter value, which is very short, has already been detected.[80–83]

The conjugative interaction between the chlorine atom (electron donor) and the dicationic carbon atom (electron acceptor), according to Wong *et al.*, is responsible for this feature.[83] The shape of the occupied MOs can be used to illustrate the decrease in the C–Cl bond length in the dication (Fig. S1, ESI†). The HOMO is slightly delocalized on chlorine in CH_3Cl^{2+}, resulting in a higher electron density between the C and Cl and a shorter C–Cl bond length. Another obvious feature of the optimized geometry of the CH_3Cl dication is the weakening of the C–H bonds, which is understandable given the loss of electrons on the methyl fragment. In CH_3Cl^{2+}, the C–H bond distance is 1.39 Å for C2–H3 and C2–H5 bonds and 1.10 Å for the C2–H4 bond, which is nearly equal to the case of neutral CH_3Cl (see Fig. S1, ESI†). The H3–H5 distance (0.88 Å) is close to the experimental H_2 internuclear distances (0.74 Å).[84] As a result, this structure can be thought of as H_2 weakly bound to the methyl group's carbon atom. Following a brief look at the ground state structures of neutral and doubly ionized CH_3Cl, we will look at the possible dissociation routes that can help us to understand the yields of various fragments. The unimolecular dissociation reaction of doubly ionized CH_3Cl can take four different routes, which have been described as pathways (7)–(10). In this process, first, we have attempted to understand the dissociation and intramolecular hydrogen migration processes by designing pathway (7). The local minima, intermediate complexes, and TSs of CH_3Cl^{2+} engaged in this dissociation process are all located at the same level of theory in this pathway, and their structures and potential energy diagrams (PED) are shown in Fig. 13. We estimated the transition state geometries produced by removing one hydrogen atom from the equilibrium geometry of the doubly ionized CH_3Cl^{2+} to form the H^+/CH_2Cl^+ pair. This leads to TS1 (Fig. 13), in which the H3 atom appears to shift towards the Cl1 atom. At *i*1411 cm^{-1}, TS1 has one imaginary frequency, which corresponds to the hydrogen atom positioned between the carbon atoms C2 and Cl1 with the C–Cl bond extended to 1.61 Å (Fig. 13). Following the crossing of TS1, the system reaches intermediate S1, where H3 moves towards the Cl1 atom. The C2–H3 bond entirely dissociates in this process and the H3 atom forms a new H3–Cl1 bond that separates from the methyl group, changing the C–Cl bond distance to 1.66 Å. The H3 atom moves away from the Cl1 atom in the next transition stage and S1 overcomes the second transition state TS2 with an activation energy of 3.72 kcal mol^{-1}, resulting in H^+/CH_2Cl^+ complexes.

Now we will look at another essential dissection pathway (8) that reveals information about the formation of H_2^+. According to Ruhl *et al.*, in their PEPIPICO experiments the weakest two-body process was the formation of a $H_2^+/HCCl^+$ ion pair.[34] On the potential energy map in Fig. 14, the optimized structures of pathway (8)'s reaction coordinate are plotted. These fragments could be created theoretically by eliminating the two hydrogen atoms from the geometry of CH_3Cl^{2+}, where the H_2 pair is weakly linked to the $HCCl^+$, making it easier to produce the H_2^+ ion. The H3 atom migrated slightly towards the Cl1 atom in this dissociation channel ($CH_3Cl^{2+} \rightarrow H_2^+ + CHCl^+$), without disrupting the C2–H3 bond *via* transition state TS1, which is comparable to the first transition state in path (7) with a minor energy variation of 0.01 kcal mol^{-1}. The formation of TS1 is endothermic approximately by 15.34 kcal mol^{-1}. It then moves on to the first intermediate S1, where the bond angle of the H3–H5 atoms is ∠125 = 115.2° and the bond distance of the

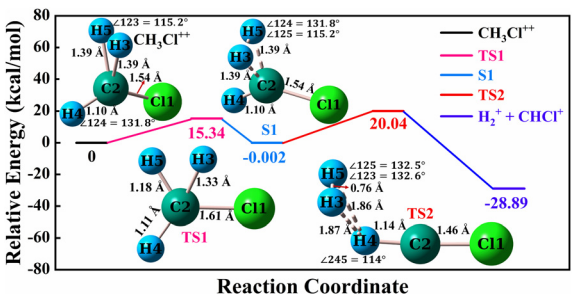

Fig. 14 The potential energy diagram along with the optimized structures of the CH_3Cl^{2+}, TS1, S1, and TS2 for the dissociation of doubly ionized CH_3Cl into H_2^+ and $CHCl^+$ at the M06-2X/6-311++G(d,p) level of theory. The energies in the figure are relative to the total energy of CH_3Cl^{2+}.

H3–H5 atoms is 0.88 Å, which is close to the observed H_2 internuclear distance (0.741 Å). Additionally, the H3–H5 moiety continues to migrate towards the H4 atom, resulting in the second transition state TS2, in which the H3–H5 moiety is found just above the H4 atom connected to the C–Cl bond. In comparison to the doubly ionized CH_3Cl^{2+} ground state geometry, we can find significant variations in the geometric data of TS2.

In contrast to the S1 structure, the angle between H4, C2, and Cl1 decreased to 114° from 131.8°, while the ∠124 increased to 132.5° from 115.2°. This intermediate dissociates into H_2^+ and $CHCl^+$ fragmented ions after breaking through an energy barrier of 20.04 kcal mol^{-1}.

The most unexpected mechanism in the fragmentation of CH_3–X^{2+} molecules is the formation of H_3^+.[34,85] It does, after all, need the dissolution of all the three C–H bonds and the production of new H–H bonds. According to Thissen *et al.*, the production of the dication results in the development of a weakly attached H_2 molecule to the carbon atom. Furthermore, Thissen *et al.* demonstrated that the H_3^+ ion in methylamine was derived from the methyl group rather than the amine group through work with deuterated species.[85] The production of CNH_2^+ and H_3^+ would result from the dissociation of methylamine, which would provide the $HCNH_2^+/H_2$ fragment pair and owe to the strong protonic affinity of H_2 (4 eV).[85] As a result, since the ground state of doubly ionized CH_3Cl is a weakly bound complex of H_2 and $HCCl_2^+$, such a process might potentially occur. To test this assumption and explain the existence of H_3^+, the geometry of a putative transition state between CH_3Cl^{2+} and CCl^+:H_3^+ must be determined. This is a tough endeavor since, unlike the other mechanisms investigated in this study, this geometry cannot be simply predicted. We arranged the two hydrogen atoms in such a way that they could be rotated around the hydrogen atom connected to the C–Cl bond to determine the initial transition state. In this way, we were able to create a structure A with one imaginary frequency, *i*298.58 cm^{-1}, which corresponds to the H3H5 group's out-of-plane rotation. Fig. S1 (ESI†) depicts this structure A. We obtained structure B, which has a C_{2v} symmetric planar structure as illustrated in Fig. S1 (ESI†), by increasing the H4C2Cl1 angle. It also has an imaginary frequency of *i*1018.48 cm^{-1}, which corresponds to H3 vibrations between H4 and H5. Our SCF calculations, however, failed to produce any stable geometry employing these structures. As a result, it appears that following these structures will not result in the formation of the H_3^+ ion. However, while investigating the PES of CH_3Cl^{2+}, we observed that the linear structure of CH_3Cl^{2+} is a potential transition state because it has a vibrational frequency, indicating that it is a saddle point with a doubly degenerated imaginary mode at *i*756 cm^{-1}, which corresponds to the rotation of the H3H5 group. CH_3Cl^{2+} and TS1 have an energy barrier of 17.08 kcal mol^{-1} (see Fig. 15). It is feasible to form the CCl^+/H_3^+ pair from this structure by raising the C2–H4 bond distance, as shown in Fig. 15, which depicts the PED of the dissociation process of CH_3Cl^{2+} into H_3^+ and CCl^+. The energy gap between these two structures is relatively small, under

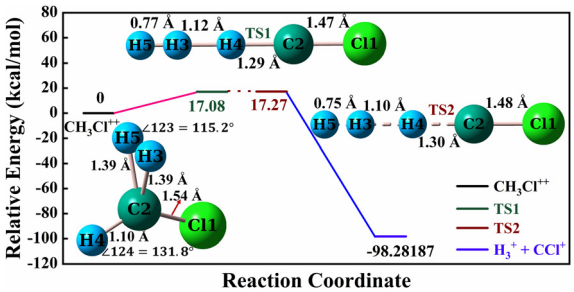

Fig. 15 The potential energy diagram along with the optimized structures of the CH_3Cl^{2+}, TS1, and TS2 for the dissociation of doubly ionized chloromethane into H_3^+ and CCl^+ at the M06-2X/6-311++G(d,p) level of theory. The energies in the figure are relative to the total energy of CH_3Cl^{2+}.

0.20 kcal mol^{-1}, implying that a barrier-free reaction process can be achieved. Further, tentative calculations were done by moving the H3H5 group in TS2, which failed or led to the structure B in Fig. S1 (ESI†) to produce more intermediates/TSs.

In this regard, our findings indicate that the formation of H_3^+ is a highly complex process compared to the formation of other H_n^+ ions. Furthermore, when pulse duration was considered as a measure to understand the H_n^+ (n = 1, 2) ion production, identical results were found. Fig. 8 depicts that the yield of H_3^+ ions is much lower than that of H^+ ions and that the yield decreases as the pulses are stretched. As a result, our theoretically designed pathway (9) fully reflects the experimental findings, implying that the formation of H_3^+ is slightly difficult and the yields are lower than for other hydrogen ions.

After the preliminary isomerization of doubly ionized CH_3Cl, the breakdown of CH_2ClH^{2+} produces the HCl^+/CH_2^+ pair (S1 structure in Fig. 16). In the next dissociation channel (10), we obtained the first transition state (Fig. 16), which has only one imaginary frequency of *i*1295 cm^{-1} and corresponds to the vibration of H5 between Cl1 and C2 atoms. The formation of TS1 is approximately 50.99 kcal mol^{-1} endothermic. The system approaches the intermediate S1 after overcoming the TS1 due to the migration of the H3 atom towards the Cl1 atom, where the system is stabilized by the isomerization process. The CCl bond becomes weaker in this isomer as the bond distance

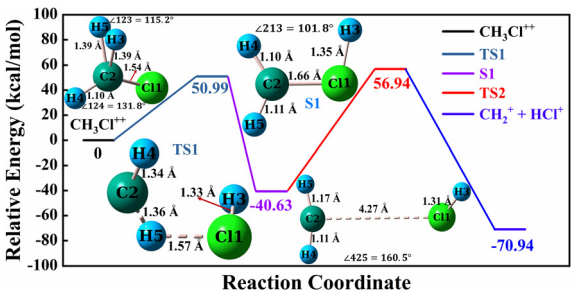

Fig. 16 The potential energy diagram along with the optimized structures of the CH_3Cl^{2+}, TS1, S1, and TS2 for the dissociation of doubly ionized chloromethane into CH_2^+ and HCl^+ at the M06-2X/6-311++G(d,p) level of theory. The energies in the figures are relative to the total energy of CH_3Cl^{2+}.

increases to 1.66 Å from 1.54 Å (CH_3Cl^{2+}). The distance between the CCl bond continues to grow in the next point of dissociation and the CH_2 group was found 4.27 Å atoms away from the Cl1 atom *via* transition state TS2. This process overcame a 56.94 kcal mol^{-1} energy barrier, resulting in the production of CH_2^+ and HCl^+ fragmented ions.

Based on the comparison of the different dissociation routes, it seems that all the ions can be achieved by the intramolecular hydrogen migration process, which is also shown by our experimental results. Even without the excited state calculations, DFT calculations employing the M06-2X functional appear to be highly beneficial in providing essential understanding into the dissociation mechanisms in CH_3Cl^{2+} and further providing assistance to interpret the experimentally observed findings.

5 Conclusions

In conclusion, we have demonstrated the effects of laser intensity and pulse duration on the strong-field ionization and two-body fragmentation of CH_3Cl. The single ionization rate of CH_3Cl was obtained experimentally and fitted with the rate obtained using MO-ADK theory, which agreed well at intensities above 1.2×10^{14} W cm^{-2} but showed some deviation in the multiphoton regime. Firstly, increasing the intensity from $I = 4.2 \times 10^{13}$ W cm^{-2} to $I = 8.5 \times 10^{13}$ W cm^{-2} suppressed the yields of the four pathways, which was attributed to an increased ionization of the parent dication compared to dissociation. On the other hand, stretching the pulses (introducing a positive chirp) from 29 fs to 510 fs enhanced the HCl^+ forming pathway, while suppressing the H_n^+ forming pathways. The KER distributions, two-dimensional coincidence momentum distribution and angular distributions of the H_n^+ and HCl^+ ions revealed that the H_n^+ ions are formed by the dissociation of CH_3Cl^{2+} from non-Coulombic metastable PESs, so their bond lengths do not map onto the KER. These pathways have a long dissociation time (of the order of ps) and the anisotropy in their ejection direction is destroyed by the rotation of the dication. Conversely, the HCl^+ forming pathways arise from the dissociation of CH_3Cl^{2+} from Coulombic (repulsive) PESs, due to which their KER distribution shows a shift to lower energies with increased pulse stretching. Since this pathway has a rapid dissociation time, the HCl^+ ions have an anisotropic distribution. Finally, quantum chemical calculations helped us to understand the mechanism of the H_n^+ and HCl^+ formation along the selected pathways. Therefore, combining experiment and theory, we have successfully demonstrated the fragmentation of the CH_3Cl dication. Furthermore, we demonstrated the control of the ultrafast fragmentation dynamics of CH_3Cl^{2+} and the resulting dissociation pathways using laser intensity, pulse duration and chirp.

Author contributions

The research was planned by RKK and RD. RD, MP, VN, PB, MSKM, and RKK have worked on the experiments. DKP and DKS have worked on the quantum chemical calculations. The MO-ADK theory calculations were done by SS. The first draft was prepared by RD and DKP and others contributed to the final manuscript. The research was conducted under the supervision of RKK.

Conflicts of interest

There are no conflicts to declare.

Acknowledgements

RD, PM, VN, PB, SS, KMMS and RKK acknowledge PRL's support in the research activities of Femtolab, AMOPH division. We also acknowledge the workshop for their support and fabrication of the COLTRIMS setup. We acknowledge Vimlesh Kumar, Photonics Sciences Lab, AMOPH Division for designing the COLTRIMS setup. DKP acknowledges DST, India, for providing financial support under the INSPIRE Fellowship No. IF170625. DKS acknowledges financial support from SERB-DST ECR Project "ECR/2016/001289".

References

1 S. Matsika, M. Spanner, M. Kotur and T. C. Weinacht, *J. Phys. Chem. A*, 2013, **117**, 12796–12801.
2 L. Holmegaard, J. L. Hansen, L. Kalhøj, S. L. Kragh, H. Stapelfeldt, F. Filsinger, J. Küpper, G. Meijer, D. Dimitrovski and M. Abu-Samha, *et al.*, *Nature Physics*, 2010, **6**, 428–432.
3 R. Das, D. K. Pandey, V. Nimma, P. Madhusudhan, P. Bhardwaj, P. Chandravanshi, M. S. KM, D. K. Singh and R. K. Kushawaha, *Faraday Discuss.*, 2021, **228**, 432–450.
4 M. Garg, A. K. Tiwari and D. Mathur, *J. Chem. Phys.*, 2012, **136**, 024320.
5 N. Ekanayake, T. Severt, M. Nairat, N. P. Weingartz, B. M. Farris, B. Kaderiya, P. Feizollah, B. Jochim, F. Ziaee and K. Borne, *et al.*, *Nat. Commun.*, 2018, **9**, 1–11.
6 T. Okino, Y. Furukawa, P. Liu, T. Ichikawa, R. Itakura, K. Hoshina, K. Yamanouchi and H. Nakano, *Chem. Phys. Lett.*, 2006, **423**, 220–224.
7 T. Okino, A. Watanabe, H. Xu and K. Yamanouchi, *Phys. Chem. Chem. Phys.*, 2012, **14**, 10640–10646.
8 P. M. Kraus, M. C. Schwarzer, N. Schirmel, G. Urbasch, G. Frenking and K.-M. Weitzel, *J. Chem. Phys.*, 2011, **134**, 114302.
9 S. Kaziannis, I. Liontos, G. Karras, C. Corsi, M. Bellini and C. Kosmidis, *J. Chem. Phys.*, 2009, **131**, 144308.
10 J. Palaudoux and M. Hochlaf, *ACS Earth Space Chem.*, 2019, **3**, 980–985.
11 E. Livshits, I. Luzon, K. Gope, R. Baer and D. Strasser, *Commun. Chem.*, 2020, **3**, 1–6.
12 K. Gope, E. Livshits, D. M. Bittner, R. Baer and D. Strasser, *J. Phys. Chem. Lett.*, 2020, **11**, 8108–8113.

13 N. Ekanayake, M. Nairat, N. P. Weingartz, M. J. Michie, B. G. Levine and M. Dantus, *J. Chem. Phys.*, 2018, **149**, 244310.
14 E. Wang, X. Shan, L. Chen, T. Pfeifer, X. Chen, X. Ren and A. Dorn, *J. Phys. Chem. A*, 2020, **124**, 2785–2791.
15 N. Ekanayake, M. Nairat, B. Kaderiya, P. Feizollah, B. Jochim, T. Severt, B. Berry, K. R. Pandiri, K. D. Carnes and S. Pathak, *et al.*, *Sci. Rep.*, 2017, **7**, 1–12.
16 T. Ando, A. Shimamoto, S. Miura, A. Iwasaki, K. Nakai and K. Yamanouchi, *Commun. Chem.*, 2018, **1**, 1–7.
17 F. Ota, S. Abe, K. Hatada, K. Ueda, S. Daz-Tendero and F. Martn, *Phys. Chem. Chem. Phys.*, 2021, **23**, 20174–20182.
18 S. Maclot, D. G. Piekarski, A. Domaracka, A. Méry, V. Vizcaino, L. Adoui, F. Martn, M. Alcam, B. A. Huber and P. Rousseau, *et al.*, *J. Phys. Chem. Lett.*, 2013, **4**, 3903–3909.
19 M. Castrovilli, A. Trabattoni, P. Bolognesi, P. OaKeeffe, L. Avaldi, M. Nisoli, F. Calegari and R. Cireasa, *J. Phys. Chem. Lett.*, 2018, **9**, 6012–6016.
20 Y. Yokouchi, M. Ikeda, Y. Inuzuka and T. Yukawa, *Nature*, 2002, **416**, 163–165.
21 R. C. Rhew, B. R. Miller and R. F. Weiss, *Nature*, 2000, **403**, 292–295.
22 S. Li, M.-K. Park, C. O. Jo and S. Park, *J. Atmos. Chem.*, 2017, **74**, 227–243.
23 K. Acharyya and E. Herbst, *Astrophys. J.*, 2017, **850**, 105.
24 M. Monce, A. Edwards, R. Wood, M. Steuer, A. Shah and P. Tabor, *J. Chem. Phys.*, 1981, **74**, 2860–2865.
25 M. Monce, A. Edwards, R. Wood, M. Steuer and A. Shah, *J. Chem. Phys.*, 1983, **78**, 597–598.
26 R. Bohinc, M. Žitnik, K. Bučar, M. Kavčič, L. Journel, R. Guillemin, T. Marchenko, M. Simon and W. Cao, *J. Chem. Phys.*, 2013, **139**, 134302.
27 C. Miron, P. Morin, D. Céolin, L. Journel and M. Simon, *J. Chem. Phys.*, 2008, **128**, 154314.
28 L. El Khoury, L. Journel, R. Guillemin, S. Carniato, W. C. Stolte, T. Marin, D. W. Lindle and M. Simon, *J. Chem. Phys.*, 2012, **136**, 024319.
29 D. Ceolin, M. N. Piancastelli, R. Guillemin, W. C. Stolte, S.-W. Yu, O. Hemmers and D. W. Lindle, *J. Chem. Phys.*, 2007, **126**, 084309.
30 S. Sun, Y. Yang, J. Zhang, H. Wu, Y. Chen, S. Zhang, T. Jia, Z. Wang and Z. Sun, *Chem. Phys. Lett.*, 2013, **581**, 16–20.
31 P. Ma, C. Wang, X. Li, X. Yu, X. Tian, W. Hu, J. Yu, S. Luo and D. Ding, *J. Chem. Phys.*, 2017, **146**, 244305.
32 P. Grugan, N. Ekanayake, S. White, S. Luo, P. Ruan and B. Walker, *J. Phys. B: At., Mol. Opt. Phys.*, 2018, **51**, 165601.
33 D. Duflot, J.-M. Robbe and J.-P. Flament, *Int. J. Mass Spectrom. Ion Processes*, 1997, **171**, 215–230.
34 E. Ruhl, S. Price, S. Leach and J. Eland, *Int. J. Mass Spectrom. Ion Processes*, 1990, **97**, 175–201.
35 E. Kokkonen, M. Vapa, K. Bučar, K. Jänkälä, W. Cao, M. Žitnik and M. Huttula, *Phys. Rev. A*, 2016, **94**, 033409.
36 S. G. Walt, N. Bhargava Ram, A. von Conta, O. I. Tolstikhin, L. B. Madsen, F. Jensen and H. J. Wörner, *J. Phys. Chem. A*, 2015, **119**, 11772–11782.
37 W. Wiley and I. H. McLaren, *Rev. Sci. Instrum.*, 1955, **26**, 1150–1157.
38 M. V. Ammosov, N. B. Delone and V. P. Krainov, *High Intensity Laser Processes SPIE Proceedings*, 1986.
39 X. M. Tong, Z. X. Zhao and C. D. Lin, *Phys. Rev. A: At., Mol., Opt. Phys.*, 2002, **66**, 033402.
40 C. D. Lin, A.-T. Le, C. Jin and H. Wei, *Attosecond and Strong-Field Physics: Principles and Applications*, Cambridge University Press, 2018.
41 S.-F. Zhao, J. Xu, C. Jin, A.-T. Le and C. D. Lin, *J. Phys. B: At., Mol. Opt. Phys.*, 2011, **44**, 035601.
42 R. Dennington, K. Todd, J. Millam, K. Eppinnett, W. L. Hovell and R. Gilliland, *GaussView, Version 6*, 2016, Semichem, Inc., Shawnee Mission, KS.
43 M. J. Frisch, G. W. Trucks, H. B. Schlegel, G. E. Scuseria, M. A. Robb, J. R. Cheeseman, G. Scalmani, V. Barone, G. A. Petersson, H. Nakatsuji, X. Li, M. Caricato, A. V. Marenich, J. Bloino, B. G. Janesko, R. Gomperts, B. Mennucci, H. P. Hratchian, J. V. Ortiz, A. F. Izmaylov, J. L. Sonnenberg, D. Williams-Young, F. Ding, F. Lipparini, F. Egidi, J. Goings, B. Peng, A. Petrone, T. Henderson, D. Ranasinghe, V. G. Zakrzewski, J. Gao, N. Rega, G. Zheng, W. Liang, M. Hada, M. Ehara, K. Toyota, R. Fukuda, J. Hasegawa, M. Ishida, T. Nakajima, Y. Honda, O. Kitao, H. Nakai, T. Vreven, K. Throssell, J. A. Montgomery, Jr., J. E. Peralta, F. Ogliaro, M. J. Bearpark, J. J. Heyd, E. N. Brothers, K. N. Kudin, V. N. Staroverov, T. A. Keith, R. Kobayashi, J. Normand, K. Raghavachari, A. P. Rendell, J. C. Burant, S. S. Iyengar, J. Tomasi, M. Cossi, J. M. Millam, M. Klene, C. Adamo, R. Cammi, J. W. Ochterski, R. L. Martin, K. Morokuma, O. Farkas, J. B. Foresman and D. J. Fox, *Gaussian 16, Revision B.01*, Gaussian Inc., Wallingford CT, 2016.
44 D. K. Pandey, H. L. Kagdada, A. Materny and D. K. Singh, *J. Phys. Chem. A*, 2021, **125**, 2653–2665.
45 P. Sanchora, D. K. Pandey, H. L. Kagdada, A. Materny and D. K. Singh, *Phys. Chem. Chem. Phys.*, 2020, **22**, 17687–17704.
46 Y. Zhao and D. G. Truhlar, *Theor. Chem. Acc.*, 2008, **120**, 215–241.
47 R. Krishnan, J. S. Binkley, R. Seeger and J. A. Pople, *J. Chem. Phys.*, 1980, **72**, 650–654.
48 R. Kushawaha and B. Bapat, *Chem. Phys. Lett.*, 2008, **463**, 42–46.
49 Y. Malakar, W. Pearson, M. Zohrabi, B. Kaderiya, F. Ziaee, S. Xue, A. Le, I. Ben-Itzhak, D. Rolles and A. Rudenko, *et al.*, *Phys. Chem. Chem. Phys.*, 2019, **21**, 14090–14102.
50 L. V. Keldysh, *Zh. Eksp. Teor. Fiz.*, 1964, **47**, 1307–1314.
51 P. D. Grugan, N. Ekanayake, S. White, S. Y. Luo, P. Ruan and B. C. Walker, *J. Phys. B: At., Mol. Opt. Phys.*, 2018, **51**, 165601.
52 B. Wolter, M. G. Pullen, M. Baudisch, M. Sclafani, M. Hemmer, A. Senftleben, C. D. Schröter, J. Ullrich, R. Moshammer and J. Biegert, *Phys. Rev. X*, 2015, **5**, 021034.
53 J. Eland, *Laser Chem.*, 1991, **11**, 259–263.
54 T. Zuo and A. D. Bandrauk, *Phys. Rev. A: At., Mol., Opt. Phys.*, 1995, **52**, R2511.
55 I. Bocharova, R. Karimi, E. F. Penka, J.-P. Brichta, P. Lassonde, X. Fu, J.-C. Kieffer, A. D. Bandrauk, I. Litvinyuk and J. Sanderson, *et al.*, *Phys. Rev. Lett.*, 2011, **107**, 063201.

56 M. Krug, T. Bayer, M. Wollenhaupt, C. Sarpe-Tudoran, T. Baumert, S. Ivanov and N. Vitanov, *New J. Phys.*, 2009, **11**, 105051.
57 M. Wollenhaupt, A. Präkelt, C. Sarpe-Tudoran, D. Liese and T. Baumert, *Appl. Phys. B: Lasers Opt.*, 2006, **82**, 183–188.
58 B. D. Bruner, H. Suchowski, N. V. Vitanov and Y. Silberberg, *Phys. Rev. A: At., Mol., Opt. Phys.*, 2010, **81**, 063410.
59 A. Vredenborg, C. S. Lehmann, D. Irimia, W. G. Roeterdink and M. H. Janssen, *Chem. Phys. Chem.*, 2011, **12**, 1459–1473.
60 T. Goswami, S. K. Kumar, A. Dutta and D. Goswami, *Chem. Phys.*, 2009, **360**, 47–52.
61 T. Townsend, C. J. Schwartz, B. Jochim, T. Severt, N. Iwamoto, J. Napierala, P. Feizollah, S. Tegegn, A. Solomon and S. Zhao, *et al.*, *Frontiers in Physics*, 2021, **9**, 691727.
62 X. Xie, E. Lötstedt, S. Roither, M. Schöffler, D. Kartashov, K. Midorikawa, A. Baltuška, K. Yamanouchi and M. Kitzler, *Sci. Rep.*, 2015, **5**, 1–11.
63 A. Sen, S. Mandal, S. Sen, B. Bapat, R. Gopal and V. Sharma, *Phys. Rev. A*, 2021, **103**, 043107.
64 X. Li, L. Inhester, S. Robatjazi, B. Erk, R. Boll, K. Hanasaki, K. Toyota, Y. Hao, C. Bomme and B. Rudek, *et al.*, *Phys. Rev. Lett.*, 2021, **127**, 093202.
65 S. Erattupuzha, C. L. Covington, A. Russakoff, E. Lötstedt, S. Larimian, V. Hanus, S. Bubin, M. Koch, S. Gräfe and A. Baltuška, *et al.*, *J. Phys. B: At., Mol. Opt. Phys.*, 2017, **50**, 125601.
66 E. Lötstedt, T. Kato and K. Yamanouchi, *J. Chem. Phys.*, 2013, **138**, 104304.
67 D. Duflot, J.-M. Robbe and J.-P. Flament, *J. Chem. Phys.*, 1995, **103**, 10571–10579.
68 H. Xu, T. Okino and K. Yamanouchi, *Chem. Phys. Lett.*, 2009, **469**, 255–260.
69 S. Falcinelli, M. Rosi, F. Pirani, D. Bassi, M. Alagia, L. Schio, R. Richter, S. Stranges, N. Balucani and V. Lorent, *et al.*, *Front. Chem.*, 2019, 7, 621.
70 H. He, R. Lu, P. Zhang, Y. Guo, K. Han and G. He, *Phys. Rev. A: At., Mol., Opt. Phys.*, 2011, **84**, 033418.
71 D. Pavičić, K. F. Lee, D. M. Rayner, P. B. Corkum and D. M. Villeneuve, *Phys. Rev. Lett.*, 2007, **98**, 243001.
72 S.-F. Zhao, J. Xu, C. Jin, A.-T. Le and C. Lin, *J. Phys. B: At., Mol. Opt. Phys.*, 2011, **44**, 035601.
73 B. K. McFarland, J. P. Farrell, P. H. Bucksbaum and M. Gühr, *Science*, 2008, **322**, 1232–1235.
74 P. Von den Hoff, I. Znakovskaya, S. Zherebtsov, M. F. Kling and R. de Vivie-Riedle, *Appl. Phys. B: Lasers Opt.*, 2010, **98**, 659–666.
75 H. Akagi, T. Otobe, A. Staudte, A. Shiner, F. Turner, R. Dörner, D. Villeneuve and P. Corkum, *Science*, 2009, **325**, 1364–1367.
76 X. Xie, S. Roither, M. Schöffler, E. Lötstedt, D. Kartashov, L. Zhang, G. G. Paulus, A. Iwasaki, A. Baltuška and K. Yamanouchi, *et al.*, *Phys. Rev. X*, 2014, **4**, 021005.
77 A. Galano and J. R. Alvarez-Idaboy, *J. Comput. Chem.*, 2014, **35**, 2019–2026.
78 M. Walker, A. J. Harvey, A. Sen and C. E. Dessent, *J. Phys. Chem. A*, 2013, **117**, 12590–12600.
79 M. D. Harmony, V. W. Laurie, R. L. Kuczkowski, R. Schwendeman, D. Ramsay, F. J. Lovas, W. J. Lafferty and A. G. Maki, *J. Phys. Chem. Ref. Data*, 1979, **8**, 619–722.
80 P. Jensen, S. Brodersen and G. Guelachvili, *J. Mol. Spectrosc.*, 1981, **88**, 378–393.
81 K. Lammertsma, *et al.*, *JACS*, 1983, **105**, 5252–5257.
82 W. Koch and G. Frenking, *Chem. Phys. Lett.*, 1985, **114**, 178–181.
83 M. W. Wong, B. F. Yates, R. H. Nobes and L. Radom, *J. Am. Chem. Soc.*, 1987, **109**, 3181–3187.
84 K. Huber, *Molecular Spectra and molecular Structure Constants of Diatomic molecules*, 1979.
85 R. Thissen, M. Simon and M.-J. Hubin-Franskin, *J. Chem. Phys.*, 1994, **101**, 7548–7553.

